Helsinki University of Technology Laboratory of Steel Structures Publications 30
Teknillisen korkeakoulun teräsrakennetekniikan laboratorion julkaisuja 30
Espoo 2004 TKK-TER-30

WEB CRIPPLING OF COLD-FORMED THIN-WALLED STEEL CASSETTES

Olli Kaitila

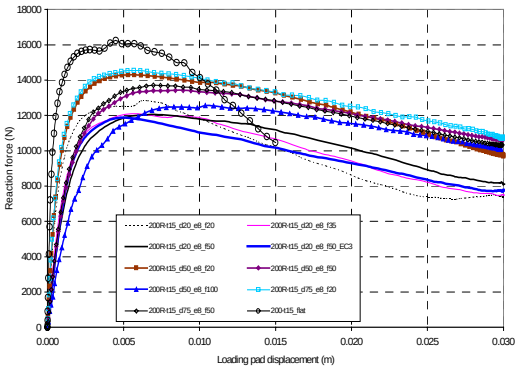

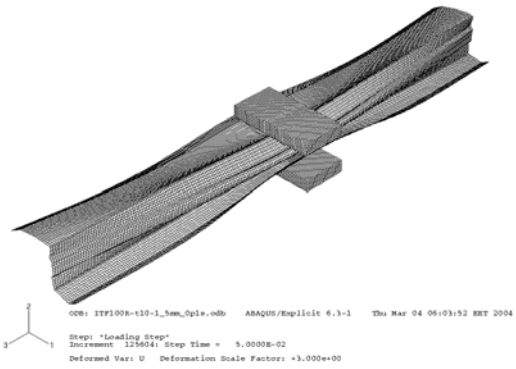

TEKNILLINEN KORKEAKOULU
TEKNISKA HÖGSKOLAN
HELSINKI UNIVERSITY OF TECHNOLOGY
TECHNISCHE UNIVERSITÄT HELSINKI
UNIVERSITE DE TECHNOLOGIE D'HELSINKI

Helsinki University of Technology Laboratory of Steel Structures Publications 30
Teknillisen korkeakoulun teräsrakennetekniikan laboratorion julkaisuja 30
Espoo 2004 TKK-TER-30

WEB CRIPPLING OF COLD-FORMED THIN-WALLED STEEL CASSETTES

Olli Kaitila

Dissertation for the degree of Doctor of Science in Technology to be presented with due permission of the Department of Civil and Environmental Engineering for public examination and debate in Auditorium R1 at Helsinki University of Technology (Espoo, Finland) on the 22nd of October, 2004, at 12 o'clock noon.

Helsinki University of Technology
Department of Civil and Environmental Engineering
Laboratory of Steel Structures

Teknillinen korkeakoulu
Rakennus- ja ympäristötekniikan osasto
Teräsrakennetekniikan laboratorio

Distribution:
Helsinki University of Technology
Laboratory of Steel Structures
P.O. Box 2100
FIN-02015 HUT
Tel. +358-9-451 3701
Fax. +358-9-451 3826
E-mail: srt-sihteerit@hut.fi

ISBN 951-22-7270-9
ISSN 1456-4327
Otamedia Oy
Espoo 2004

Kaitila, O. 2004, Web Crippling of Cold-Formed Thin-Walled Steel Cassettes, Helsinki University of Technology Laboratory of Steel Structures Publications 30, TKK-TER-30, Espoo. 189 p. + annexes 24 p. ISBN 951-22-7270-9, ISSN 1456-4327.

Keywords: cold-formed steel, cassette, liner tray, web crippling, local transverse forces, parametric study

ABSTRACT

The resistance of cold-formed thin-walled cassettes against local transverse forces, i.e. the web crippling capacity, was investigated. The web crippling of cassettes, or liner trays as they are also called, was studied both experimentally and numerically using finite element modelling. Both unreinforced (flat) cassette webs and webs with longitudinal stiffeners situated on only one side of the web mid-line were studied.

The calculation of the web crippling capacity of this type of stiffened webs is not included in current design codes. However, if cassettes are designed as continuous over two or more spans, the resistance against local transverse forces has to be verified. It should be noted that the original purpose of the stiffener in cassette webs is to increase the bending moment capacity by increasing the effective area of the compressed part of the web when cassettes are designed as single-span structures, in which case web crippling does not usually become critical.

A total of 52 structural tests were carried out on specially manufactured single cassette web sections and built-up cassette structures. Both interior two-flange and interior one-flange loading were considered. The calculation rules for unreinforced webs given in current design codes were found to be relatively conservative in comparison to the test results.

Finite element models were developed and validated on the basis of the test results and very good agreement was achieved. These models were used as a starting point for a parametric study of the influence of different cross-sectional parameters on the resistance against local transverse forces of longitudinally stiffened webs. Also the influence of the load bearing length was included in the study. Recommendations concerning the design of the cassette web section are given based on the results.

It was shown that the use of a longitudinal stiffener of the studied type in fact reduces the web crippling capacity by at least 10 % in comparison to a similar cassette with an unreinforced web. Depending on the stiffener's geometry, the reduction can be considerably larger. A reduction factor equal to 0.7 - 0.9 should be used for the type of longitudinally stiffened webs considered in this study in connection with the design code formulae for the resistance of unreinforced webs against local transverse forces, depending on the cross-section geometry.

PREFACE

This research was carried out in the Laboratory of Steel Structures, Department of Civil and Environmental Engineering, at Helsinki University of Technology between January 2002 and May 2004. The work has been financially supported by the following institutions and foundations: The Academy of Finland (Project number 47454 (Development of Design Methods for Light-Weight Steel Structures, 2001-2003)), RIL-Säätiö, Emil Aaltosen Säätiö, Tekniikan edistämissäätiö and Honkasen säätiö. Their support is gratefully acknowledged with the sincere hope that this finished work can be considered worthy of it.

I would like to thank my supervisor, Prof D.Sc.(Tech.) Pentti Mäkeläinen, head of the Laboratory of Steel Structures at HUT, for his support and encouragement, not only during this research, but also during the whole time I worked as a researcher in his laboratory (1998-2003).

My current employer, VTT Building and Transport, and especially Group Manager D.Sc.(Tech.) Esko Mikkola, are warmly thanked for their support of researchers' further studies and for believing in this particular work enough to allow me to use regular work time to finish the dissertation. Given the limited amount of hours in a day, this proved to be invaluable for the completion of the work.

Many thanks also to D.Sc.(Tech) Jyrki Kesti of Rautaruukki Oyj for initiating my interest in this particular problem concerning cold-formed steel structures by commissioning the test series presented in this dissertation and allowing the publication of the results so that they are available to the whole academic community. Thanks also for the discussions and comments.

Many thanks to Mr. Reijo Lindgren of CSC (Centre for Scientific Computing) for his support and advice on the finite element modelling.

Warm thanks to my colleagues, past and present, and the staffs at the HUT Laboratory of Steel Structures and VTT Building and Transport, Fire Research, for their support and discussions. Sincere thanks also to Mr. Veli-Antti Hakala and the skilled staff at the Testing Hall of the HUT Department of Civil and Environmental Engineering.

A very special thank you goes, once more, to Mr. Paavo Hassinen of the HUT Laboratory of Structural Mechanics, whose scrutinized comments, discussions and humane encouragement were of great help in wrapping up the research.

The preliminary examiners of the thesis, Professor Torsten Höglund from the Royal Institute of Technology, Sweden, and Professor Teoman Peköz of Cornell University, N.Y., U.S.A., are also gratefully acknowledged. Professor J. Michael Davies from the University of Manchester is warmly thanked for agreeing to act as opponent during the defense of the thesis.

The greatest thanks, however, go to my wife Dorothee, who never ceases to believe in me, even when I myself am ready to throw in the towel, and to our newborn son, Leo, who gave a big push to the research work in the end of last year by announcing his arrival.

Olli Kaitila
Espoo, August 30, 2004

CONTENTS

NOTATIONS

A	cross-sectional area
B	half of the width of the wider flange
B_{m1}	effective width of the wide flange
C_2	non-dimensional coefficient
C_9	non-dimensional coefficient
D	flexural stiffness of the plate
D_x	bending stiffness across the wider flange
D_y	bending stiffness along the wider flange
E	modulus of elasticity
E_{st}	modulus of elasticity of the steel sheet
F	load
F_{di}	failure load at value of d equal to i
F_{ei}	failure load at value of e equal to i
F_{fi}	failure load at value of f equal to i
F_R	capacity against local transverse forces
F_{test}	failure load obtained in test
F_u	ultimate load
$F_{FE\text{-}PRE}$	ultimate load obtained from preliminary FE-analysis
H	height of the web
I_a	second moment of area of the wide flange about its own centroid
K	non-dimensional buckling coefficient
L	span length of the cassette, total length of test specimen
L_{lb}	load bearing plate width
L_{span}	span of cassette in interior one-flange tests
N	actual bearing length
P_n	nominal strength of a single web
R	inside bend radius
R_b	nominal strength of a single web
R_s	corner radius of stiffener fold
$R_{w,Rd}$	local transverse resistance of a single unreinforced web
RF	reduction factor
S_v	shear stiffness per unit length
$T_{v.Rd}$	ultimate shear flow
$V_{Sd,1}$	transverse shear force
$V_{Sd,2}$	transverse shear force
a	height of the web opening, length of the plate
a_1	distance between fasteners in the top (narrow) flange
b	width of the plate
b_1	partial flange width of cassette in interior one-flange tests on built-up sections
b_2	flange width of cassette in interior one-flange tests on built-up sections
b_3	partial flange width of cassette in interior one-flange tests on built-up sections
$b_{bf,fl}$	width of bottom flange
$b_{bf,fl}$	flat width of bottom flange
b_d	developed width of the loaded flange

b_{tf}	width of top flange
$b_{tf.st}$	width of flange stiffener fold
b_u	width of the wider flange
b_w	width of web
b_{wfl}	flat web width
$b_{w.fl}$	flat web width
$b_{w.st}$	exterior in-plane height of web stiffener
$b_{w.st.fl}$	interior in-plane height of web stiffener
c	clear distance from free end to location of transverse load
$curv_{bf}$	curvature of bottom flange
$curv_{tf}$	curvature of top flange
$curv_w$	curvature of web
$curv_{w.vert}$	vertical curvature of web
d	top flange displacement, distance of the longitudinal stiffener from the wide flange
d_1	depth of the flat portion of the web measured along the plane of the web
$d_{w.st}$	distance of web stiffener from wide flange
e	Neper's number, e = 2.718281…, out-of-plane height (eccentricity) of the longitudinal stiffener
e_{max}	larger eccentricity of the folds relative to the system line of the web
e_{min}	smaller eccentricity of the folds relative to the system line of the web
e_o	distance from the top (narrow) flange to the mass centre of the cross-section
e_s	distance between seam fasteners through the web
f	in-plane height (width) of the longitudinal stiffener
f_{Go}	initial deformation of the wide flange
$f_{p0.1}$	mean yield strength corresponding to 0.1 % plastic strain
$f_{p0.2}$	mean yield strength corresponding to 0.2 % plastic strain
$f_{u.test}$	yield strength obtained from material tests
f_y	yield strength of steel
f_{yb}	basic yield strength of steel
h	height of the web
h	depth of the flat portion of the web measured along the plane of the web
h_w	web height between the midlines of the flanges
$h_{w.st}$	out-of-plane height (eccentricity) of web stiffener
Δh_w	web crippling deformation at ultimate load
k	non-dimensional coefficient
k_1	non-dimensional coefficient
k_2	non-dimensional coefficient
k_3	non-dimensional coefficient
k_F	force increase factor
k_{TF}	top flange displacement increase factor
k_{WC}	web crippling deformation increase factor
l_a	effective bearing length
l_b	actual length of bearing
r	internal radius of corners
r_{bf}	mid-surface bottom flange corner radius
r_{ebf}	exterior bottom flange corner radius
r_{ibf}	interior bottom flange corner radius
r_{etf}	exterior top flange corner radius
r_{itf}	interior top flange corner radius

r_{tf}	mid-surface top flange corner radius
s_p	slant height of the plane web element nearest to the loaded flange
s_s	actual length of the stiff bearing
t	thickness of the steel sheet
t_{eq}	equivalent thickness of the stiffened lower (wider) flange
t_{nom}	nominal steel thickness
t_w	thickness of the web
w	beam deflection at ultimate load
wcd	web crippling deformation
x	distance from the outer edge of an opening to the interior edge of the bearing plate
α	non-dimensional coefficient, width reduction factor
α_M	mechanical interaction coefficient
α_G	geometrical factor
β	coefficient depending on the boundary conditions of the plate
β_v	non-dimensional coefficient
γ_{M1}	partial safety factor
γ_{M2}	partial safety factor
γ_m	material design safety factor
$\varepsilon_{fu.test}$	strain corresponding to failure load in material test
ε_{break}	ultimate strain
θ_w	angle between web and flange
μ	Poisson's ratio, $\mu = 0.3$
τ_{cr}	local shear buckling stress
ϕ	slope of the web relative to the flanges
ϕ_w	factor of safety

1. Introduction

1.1 Background

Over the last few decades, lightweight steel framing construction has been a serious competitor to the more traditional wood frame construction and has gained ground all over the world, especially in Europe, U.S.A. and Australia. Cassette wall structures provide an alternative to the more common type of light-weight steel wall framing based on individual stub columns connected to each other at both flanges with the help of e.g. gypsum wall boards.

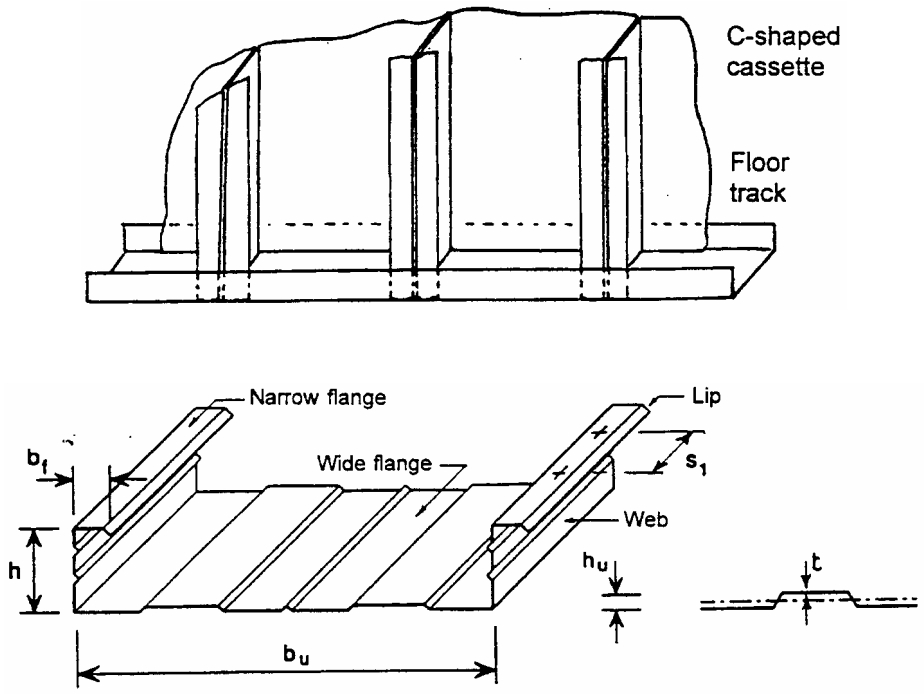

Fig. 1.1 Cassette wall construction (Davies 1998).

Cassettes are large U- or C-shaped cross-sections that have two webs connected with a wide flange and a lip-stiffened narrow flange on the other side, as shown in Figure 1.1. Different types of stiffeners can be used also along the wider flange and in the webs in order to increase the effective width of section parts in compression. Cassettes are installed as wall structures so that they span either vertically of horizontally. They have also been used as roof structures. They are fastened using screws to columns and beams or purlins. The sections can be installed so that the wider flange is on the outer or on the inner side of the wall. If the wider flange is

on the outer side, it immediately provides a weather-proof shell for the building and the insulation materials can be installed inside the cassette while other work is being continued on the outside of the wall. In some cases, the thermal insulation can also act compositely with the steel member and provide support against local buckling of the wider flange.

Cassettes, or liner trays as they often are called, have so far usually been designed as single-span structures connected to columns or beams at both ends. In this case, sagging bending moment acting together with curling of the wide flange has usually become critical in design. However, interest in installing cassettes as continuous structures over two or more spans has recently emerged. Current design codes provide formulae for the resistance of webs against local transverse forces present at the interior support area, but the codes fail to consider the type of longitudinally stiffened webs often used in cassette cross-sections. In these, the stiffener has been designed with bending moment resistance in mind, and the stiffener folds are situated on one side of the mid-line of the web only.

1.2 Objectives of research

The primary objective of the research is to gain an improved understanding of the behaviour of both unreinforced (flat) and longitudinally stiffened cassette webs under local transverse loading by using experimental and numerical methods. The main task is to examine the behaviour of longitudinally stiffened cassette webs, for which there are no design rules currently available. Also the verification of the validity of existing design rules, where applicable, is set as an objective.

The influence of the cross-section geometry of longitudinally stiffened cassette webs on the resistance against local transverse forces is to be investigated by carrying out a substantial numerical parametric study, with the objective of providing design recommendations on the optimal shape of the cross-section.

1.3 Scope of the research

An early objective of the research was to include all four commonly defined local transverse loading conditions (interior two-flange, interior one-flange, end two-flange and end one-flange, see Section 2.3) in the study and to provide suitable design formulae for possible implementation in design codes. Unfortunately, this proved to be an overwhelming task once the experimental part of the research had been carried out and the cost in computation time and the laboriousness of model editing was established. Therefore the study was mainly limited to interior two-flange and interior one-flange loading and the provision of design recommendations for the studied structures.

Experimental research included both flat and longitudinally stiffened webs with web heights 100 mm, 150 mm and 200 mm and nominal steel thicknesses 1.0 mm and 1.5 mm tested under interior two-flange and interior one-flange conditions. Also built-up constructions were tested.

Numerical studies concentrated on longitudinally stiffened cassette web sections under interior two-flange loading, although finite element models of structures with flat webs, structures under interior one-flange loading and steel sheeting based on tests found in literature were also created.

1.4 Outline of the dissertation

In order to obtain a basic understanding concerning the design of cassettes, a literature survey was carried out in Chapter 2. The existing research on the behaviour of cassette structures in bending, in-plane shear and under local-transverse forces is presented. The current European, American (U.S.A.), Australian and Finnish design regulations concerning resistance to local transverse forces are reviewed.

Chapter 3 presents the experimental research carried out during this study. A total of 52 tests on single web sections and built-up sections under interior two-flange or interior one-flange loading were carried out. Both flat and longitudinally stiffened web sections were included.

The test results are compared to nominal design values calculated according to currently used design codes.

Chapter 4 presents the development of the numerical models and their validation against test results. Some of the numerical analyses were carried out before the experimental testing and were used in the planning of testing. Chapter 5 presents the results of a parametric numerical study on the web crippling capacity of longitudinally stiffened thin-walled cassette webs. Design recommendations are given based on the results. Finally, the full results are discussed and final conclusions are given in Chapter 6.

2. STATE OF THE ART

2.1 Design of cassette structures

Cassettes have commonly been designed as single-span structures. In this case, the sagging bending moment is usually critical in design and vertical shear forces and transverse forces at supports can often be ignored. The bending moment resistance is critical for instance when the structure is submitted to a large wind load. Moreover, the membrane action created by the interaction of the cassettes and the frame of the building can be used beneficially in design.

When cassettes are designed to have two or more spans, the structural behaviour at the interior support has to be studied carefully. The design calculations have to take into account the shear strength of the webs and web crippling at support areas. The resistance against the combined actions of hogging bending moment and local transverse forces has to verified. This chapter presents existing research work on cassette structures in general and web crippling in particular. Different design codes dealing with resistance to local transverse forces are also reviewed.

2.2 Bending and in-plane shear

When the cassette is under bending action, the wider flange tends to deflect towards the neutral axis of the cross-section. This phenomenon is known as flange curling and has the effect of reducing the bending capacity as the distance of the flange from the neutral axis is reduced. The phenomenon can be seen in Figure 2.1. A relatively large part of the wide flange has to be considered ineffective in design. One way to prevent the considerable ineffectiveness of the wide flange is suggested by steel manufacturer Rannila, who say that when the webs of adjacent cassettes are connected close to the wide flange as shown in Figure 2.2, flange curling cannot take place and the whole flange can be considered effective (Rannila Steel 2001). Although this procedure will reduce the curling of the wide flange, it is most likely that it will not prevent it completely. The effectiveness of the procedure is in fact literally put to the test in this study as reported in Chapter 3.

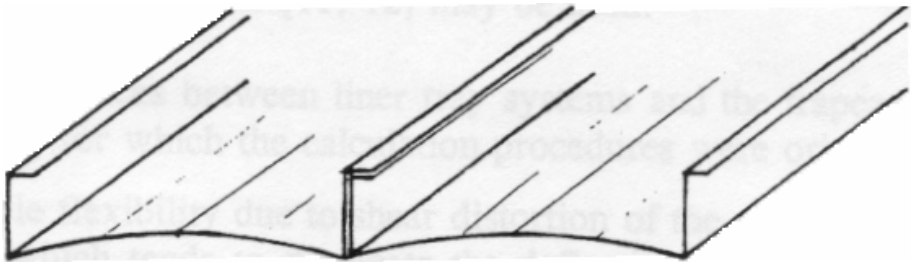

Fig. 2.1 Flange curling (Davies (1998)).

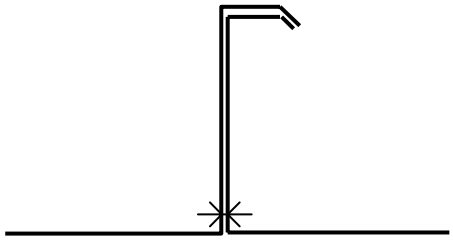

Fig. 2.2 Connection of webs close to the wide flange.

According to Davies (1998), the idea of cassette wall construction was first developed by Rolf Baehre in the late 1960's. Baehre worked at the time in Stockholm, Sweden and later at the Universität Fridericiana in Karlsruhe, Germany. He published several papers, which presented the results of experimental and theoretical studies and were used as the basis of the design rules in ENV 1993-1-3: 1996 (Eurocode 3: Part 1.3). Baehre's results were published in the German journal Stahlbau between 1986 and 1988.

In Baehre & Buca (1986), the effective width of the tension flange of thin-walled C-shaped panels is investigated. They carried out an experimental research on bended cassettes with the wide flange in tension. The length of the tested specimens was 3.0 metres and it was loaded at four cross-sections at locations 1/4, 3/8, 5/8, and 7/8 along the length. Three different total load levels, i.e. 1.7 kN, 2.7 kN and 3.1 kN, were used. These total loads include a preload of 0.7 kN and a variable load of 1.0 kN, 2.0 kN and 2.4 kN, respectively.

The curling of the wide flange was measured as the difference between the deflections at mid-span so that the mean of the flange edge deflections was subtracted from the deflection at the flange midpoint, as shown in the insert of Figure 2.3. The figure also shows the load-deflection curve of a test with the highest load level.

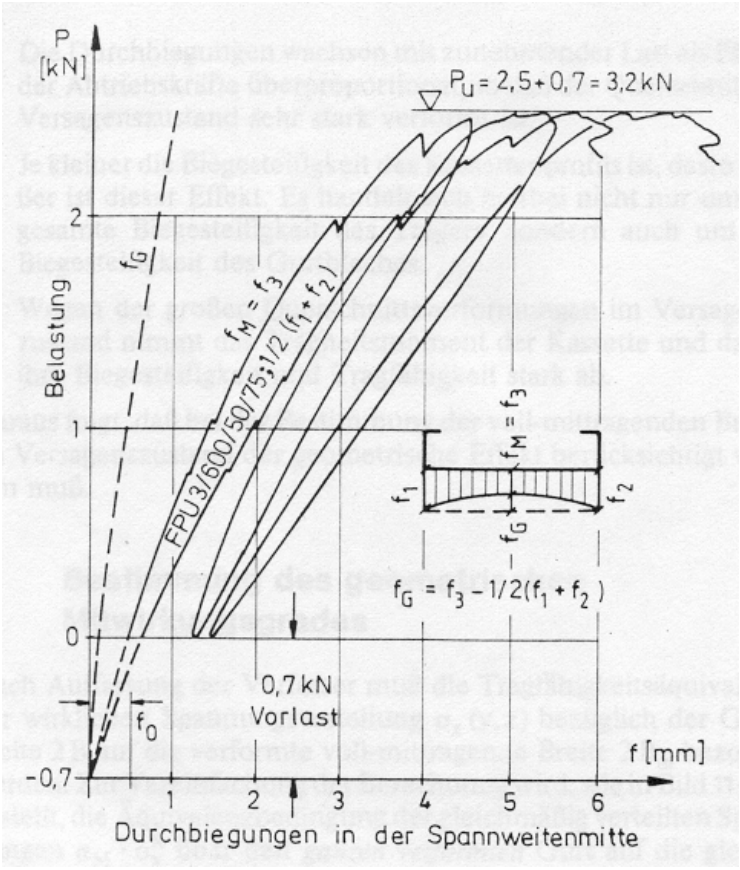

Fig. 2.3 Load-deflection curve of cassette under bending (Baehre & Buca 1986).

Baehre and Buca introduced a width reduction factor α that is comprised of a mechanical interaction coefficient α_M and a geometrical factor α_G. The mechanical interaction coefficient is due to the uneven stress distribution in the cross-section and the geometrical reduction factor to the curling of the wider flange. These two factors are multiplied in order to obtain α:

$$\alpha = \alpha_M \cdot \alpha_G \tag{2.1}$$

Baehre and Buca presented a design method for the calculation of the effective width of the wide flange. The procedure includes an appreciation of the distance between connectors in the narrow flanges, which has an effect on the failure load and mode and also on the width reduction factor α. The mechanical interaction coefficient α_M takes into account the shear lag phenomenon and is determined as a function of $(2B/L)$, where B is one half of the width of the wider flange and L is the span length of the cassette according to Figure 2.4. $B_{m1} = \alpha_M \cdot B$ in the Figure is the effective width of the wide flange.

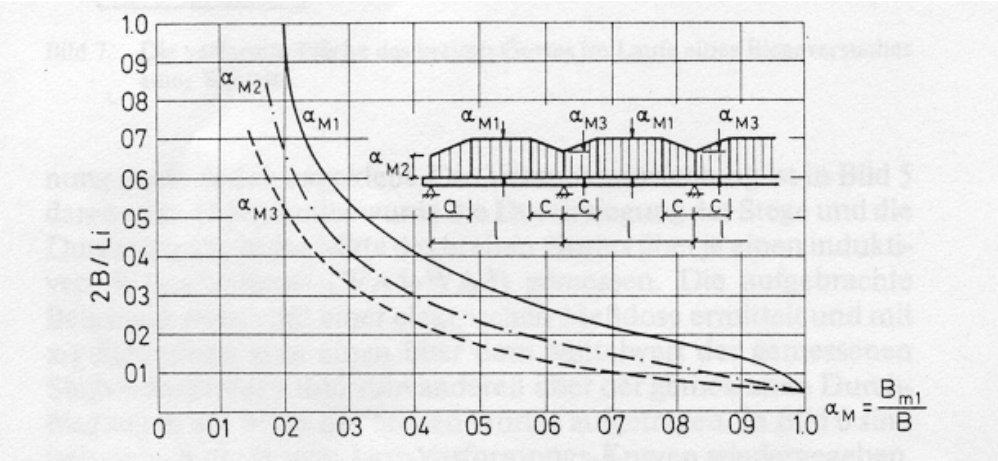

Fig. 2.4 Mechanical interaction coefficient according to DIN 1073 (Baehre & Buca (1986)).

The geometrical interaction coefficient α_G, on the other hand, appears to reflect the bending stiffness of the cross-sections and is determined as

$$\alpha_G = \frac{1}{30}\beta \cdot 10^{12} \tag{2.2}$$

where $$\beta = \left(\frac{E}{E_{st}}\right)\left(\frac{e_o^2 t^3 t_{eq}}{HLB^4}\right)\left(\frac{300}{a_1}\right)\left(1 - \frac{6 f_{Go}}{B}\right) \tag{2.3}$$

E is the modulus of elasticity of the cassette material [N/mm^2],
E_{st} is the modulus of elasticity of the steel sheet [N/mm^2],
e_o is the distance from the top (narrow) flange to the mass centre of the cross-section [mm],
t is the thickness of the steel sheet [mm],
t_{eq} is the equivalent thickness of the stiffened lower (wider) flange [mm],
H is the height of the web [mm],
B is the one half of the width of the wider flange [mm],
L is the span length of the cassette [mm],
a_1 is the distance between fasteners in the top (narrow) flanges [mm],
f_{Go} is the initial deformation of the wide flange [mm].

The effective width of the wider flange can then be calculated as

$$B_m = \alpha B = \alpha_M \alpha_G B\,. \tag{2.4}$$

The mechanical interaction coefficient is independent of the load level, but the geometrical interaction coefficient is not. Figure 2.5 shows the qualitative interdependence between the

interaction coefficients and the moment relative to ultimate moment. Up to about 2/3 of the failure load, the interaction coefficient α is approximately constant.

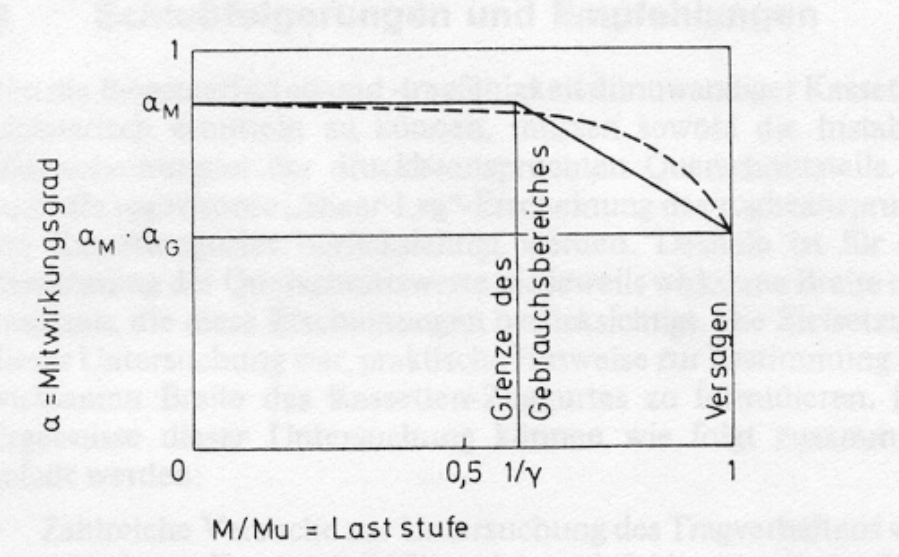

Fig. 2.5 Graphical representation of the interdependence between the interaction coefficients and external load (Baehre & Buca (1986)).

Baehre then turned his attention to the tension field (longitudinal shear, in-plane shear) analysis of cassette structures (Baehre 1987). He carried out a total of 24 structural tests in order to establish a design procedure for the longitudinal and transverse shear capacity of cassette structures and included the effects of thermal insulation on the load-carrying capacity. Bare cassettes (no foamed thermal insulation) usually experience local buckling of the wide flange, whereas this phenomenon is prevented in insulation-filled cassettes due to the support given by the rigid foam. The ultimate limit state, however, was first reached at the fastenings between cassettes or at the support due to longitudinal and lateral shear effects.

Baehre differentiated between “local” shear buckling that takes place in the wider flange of just one cassette and “global” shear buckling that happens continuously over several adjoining cassettes, as shown in Figure 2.6.

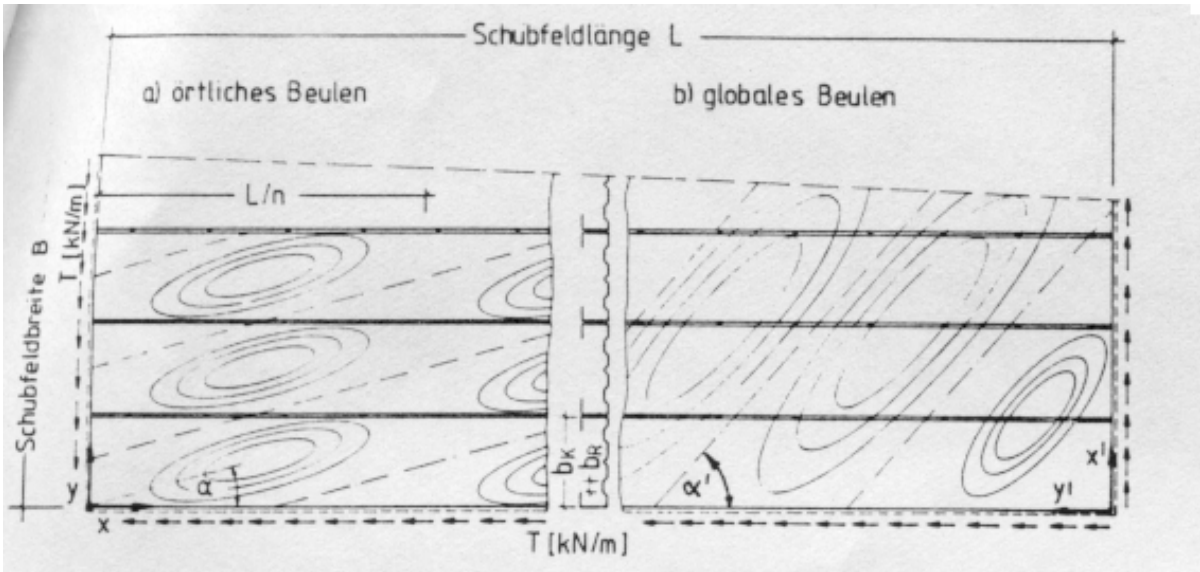

Fig. 2.6 Buckling formation in case of local shear buckling (a) and global shear buckling (b) (Baehre 1987).

Baehre showed that the ultimate shear flow $T_{v.Rd}$ can be calculated as

$$T_{v.Rd} = \frac{36 \cdot \sqrt[4]{D_x D_y^3}}{b_u^2} \tag{2.5}$$

where D_x is the bending stiffness across the wider flange, $D_x \approx \dfrac{EI_a}{b_u}$,

D_y is the bending stiffness along the wider flange, $D_y = \dfrac{Et^3}{12(1-\mu^2)}$,

I_a is the second moment of area of the wide flange about its own centroid,
E is the modulus of elasticity,
b_u is the width of the wider flange,
μ is Poisson's ratio.

This equation basically deals with the shear buckling of an orthotropic slab. When the usual value for Poisson's ratio, $\mu = 0.3$, is inserted and the equation is simplified, we obtain

$$T_{v.Rd} = 6E \cdot \sqrt[4]{I_a \left(\frac{t}{b_u}\right)^9} \tag{2.6}$$

which is the equation given in ENV 1993-1-3:1996. As Davies & Fragos (2001) point out, this equation was printed incorrectly in earlier versions of ENV 1993-1-3.

The design capacities of the fastenings were also discussed in Baehre's paper and design formulae for the connections between adjacent cassettes and the connections to the underlying frame structure were given.

The deformations of cassettes due to shear were taken into account in Baehre's article through the introduction of four spring constants, which describe the shear flexibility of the diaphragm due to different effects. The method is in accordance with the instructions given in ECCS (1978). These effects include shear strain, flexibility of the sheet end fasteners, flexibility of the seam fasteners and flexibility of the shear connector fasteners along the longitudinal edge. Furthermore, Baehre pointed out that the resulting stiffness from the different effects could be approximated as

$$S_v = \frac{2000 L b_u}{e_s (B - b_u)} \tag{2.7}$$

where e_s is the distance between seam fasteners through the web (max. 300 mm).

This equation is included in ENV 1993-1-3:1996 as well.

The fastening of trapezoidal sheeting to thin-walled C-shaped panels was discussed by Baehre, Holz & Voß (1988). They made the following main points in their paper:

A. The distance between fasteners must be kept below a prescribed maximum value,
B. The trapezoidal profile must be fastened at every second trough, at least, and
C. The individual fasteners must withstand the tension and shear forces they are submitted to.

Salonen (1988) presented a calculation method for the calculation of the deflection of the wide flange in tension. The method is based on an analogy with the theory of a beam on an elastic foundation. The results of the calculation method were compared to the mean result from a test series comprised of 13 tests and the difference between the two was found to be only 0.25 %. Salonen concluded that the effect of shear lag is small in the case of a single-span cassette. In a continuous cassette, shear lag has to be taken into account because of the concentrated load on the internal support. Moreover, according to Salonen, web crippling is more critical in a continuous than in a single-span cassette. The ultimate load capacity of a

continuous cassette may in some cases be smaller than that of a single-span cassette of the same length.

After Baehre, probably the most prominent researcher interested in cassette structures has been Professor J. Michael Davies of the University of Manchester in the U.K. In addition to his work on stressed skin diaphragm design (e.g. Davies & Bryan (1981), ECCS (1978) and ECCS (1995)), he has been the author or co-author of several articles specifically on cassettes during recent years.

Davies (1998) provided a general presentation on lightweight steel cassette wall construction including a discussion of different construction methods, a historical overview of the development of design methods and applications, an appreciation of the different design cases commonly occurring and a presentation of a few realised projects. Davies pointed out that because of the relatively high material factor $\gamma_{M2} = 1.25$ prescribed in ENV 1993-1-3:1996 for the moment resistance of cassettes, significantly better bending strengths can be obtained by testing than by calculation, and therefore design supported by testing is recommended.

The basic load systems for a cassette wall installed with cassettes spanning vertically are shown in Figure 2.7. Davies (1998) discussed each of these different design cases separately. The axial compressive load capacity can be determined using essentially the design procedure given in ENV 1993-1-3:1996, bearing in mind that buckling in the plane of the wall is prevented. This procedure includes the determination of the effective area of the cross-section using the iterative method given in ENV 1993-1-3:1996 and should also consider distortional buckling.

When the narrow flange is in compression and the wide flange is in tension, the design for bending should consider local buckling of the web and the narrow flange, distortional buckling of the narrow flange/lip combination and flange curling of the wide flange. Distortional buckling can be prevented by regular and sufficiently spaced fastenings of the narrow flanges, but Davies suggested that distortional buckling could be checked separately for an unbraced cassette using e.g. the Second-Order Generalized Beam Theory as given in Davies, Leach & Heinz (1994) or the method proposed by Serrette & Peköz (1995).

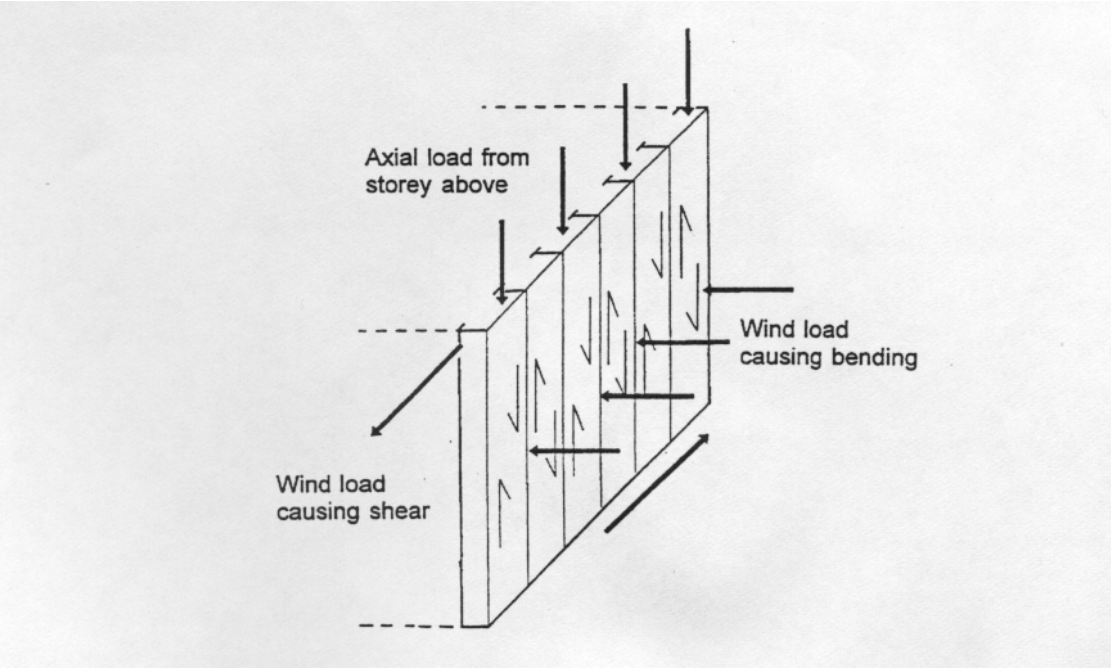

Fig. 2.7 Load system in a cassette wall with cassettes spanning vertically (Davies 1998).

The behaviour of a cassette wall in shear was considered with reference to stressed skin design as prescribed in ENV 1993-1-3:1996 and ECCS (1995). However, Davies pointed out three important differences in the behaviour of cassette systems and trapezoidally profiled sheeting and decking. Firstly, the flexibility due to shear distortion is negligible in cassettes. Secondly, the strength calculation is often dominated by the tendency of the wide flange to buckle locally in shear. Thirdly, there is usually no separate longitudinal edge member, because the other web of the outermost cassettes serves this purpose.

Davies repeated the equations (2.6) and (2.7) originally presented by Baehre (1987) and remarked that the stiffness could be calculated using the more fundamental approach given in ECCS (1995) instead of the simplified method (Equation (2.7). He emphasized that fastener failure can also be critical and criticizes the “excessive simplicity in the approach of EC3”, which is likely “to lead to a lack of fundamental understanding and over-confidence”. Another important point made in the paper is that resisting the uplift forces at the ends of the diaphragm walls can often be a critical factor in design. The corresponding axial compressive forces should also be considered in combination with other axial loads due to the overlaying structures and effects.

The shear buckling strength of empty and insulation-filled cassettes was discussed in more detail in Davies & Fragos (2001). They again pointed out that the method given in ENV 1993-1-3:1996 for the calculation of local buckling due to shear (Equation 2.6) is safe but also quite inaccurate due to the neglect of the influence of boundary conditions and post-buckling behaviour. A test programme was carried out in order to account for these phenomena in plane unstiffened flanges.

The accurate buckling load was difficult to ascertain from the tests, but it became clear that there is considerable post-buckling strength. The results showed also that the influence of the foam filling is important, especially for very thin walled elements and/or high grades of foam. The local shear buckling stress was evaluated by using the equation

$$\tau_{cr} = K\frac{\pi^2 D}{b^2 t} \tag{2.8}$$

where D is the flexural stiffness of the plate, $D = \frac{Et^3}{12\left(1-\nu^2\right)}$,

K is a non-dimensional buckling coefficient, $K = \alpha + e^{\beta\left(\frac{b}{a}\right)}$,
α, β are coefficients depending on the boundary conditions of the plate,
e is Neper's number, e = 2.718281…,
a is the length of the plate,
b is the width of the plate,

and by using finite element analysis. Values for the coefficients α and β for different boundary conditions are given in Table 2.1.

Table 2.1 Values of coefficients α and β (Davies & Fragos 2001).

Boundary condition	α	β
All edges simply supported	4.188	1.64
All edges rigidly clamped	7.868	1.92
Two long edges clamped, two short edges simply supported	7.980	1.53
Two long edges simply supported, two short edges clamped	4.089	2.14
One long edge rigidly clamped, other edges simply supported	6.209	1.56
One short edge rigidly clamped, other edges simply supported	4.262	1.90

Davies & Fragos found that although the buckled shapes obtained in finite element analyses were invariably similar to those observed in tests, there was much more theoretical post-buckling strength than was reached in the tests. The explanation to this was that the longitudinal boundary condition deteriorated during the post-buckling phase, leading to premature failure.

In addition to the general presentation of test results and finite element analyses on empty and infilled cassettes, Davies & Fragos (2001) also discussed briefly the use of differential equations in the analysis of this type of structures.

2.3 Crippling of thin-walled webs

2.3.1 General

Web crippling is a significant problem in thin-walled structures that are subjected to local transverse external loads or support reactions. Cold-formed thin-walled members are usually unstiffened against this type of loading and sometimes additional members with high stiffness are added at the support area to provide the needed extra strength.

Web crippling of thin-walled webs is a complicated phenomenon that is quite difficult to study theoretically, although attempts toward this exist and are also currently in development. Web crippling behaviour includes the influences of (Yu 2000):

- non-uniform stress distribution under the applied load,
- elastic and inelastic stability of the web,
- local yielding at the area of load application,
- bending produced by eccentric loading,
- initial out-of-plane imperfections of the plate elements,
- various edge restraints due to the flanges,
- possible inclined webs.

The ultimate web crippling capacity is a function of several parameters, i.e. the web slenderness ratio H, the inside bend radius ratio R, the bearing length ratio N, the angle of web inclination θ, and the yield strength f_y. Also the distance between the bearing edges of adjacent opposite concentrated loads or reactions has an effect on load capacity (Yu 2000).

Because of the many factors influencing the ultimate web crippling strength of cold-formed steel sections, the majority of research has been experimental, but also finite element modelling has been used to model web crippling behaviour. Some authors have also created so-called mechanical models for web crippling (Bakker 1992, Hofmeyer 2000).

The current design methods are based on curve-fitting of experimental results, which has been criticised for two main reasons (Rhodes & Nash 1998): "(i) the rules are strictly confined to the range for which they have been proven, and (ii) it is often difficult to ascertain the engineering reasoning behind the different parts of the rather complex equations". The same criticism has been made by Hofmeyer (2000). For these reasons, a number of researchers have worked to create mechanical models that could be used to produce more accurate and descriptive design methods for web crippling. Although promising results have been achieved, especially at the University of Eindhoven in the Netherlands (Bakker 1992, Hofmeyer 2000), these methods have not yet been incorporated in design practice.

In general, current design rules provide empirically defined formulae for the calculation of web crippling strength of cold-formed steel members. Four different loading conditions as shown in Figure 2.8 can generally be distinguished:

- EOF = End One-Flange loading
- IOF = Interior One-Flange loading
- ETF = End Two-Flange loading
- ITF = Interior Two-Flange loading

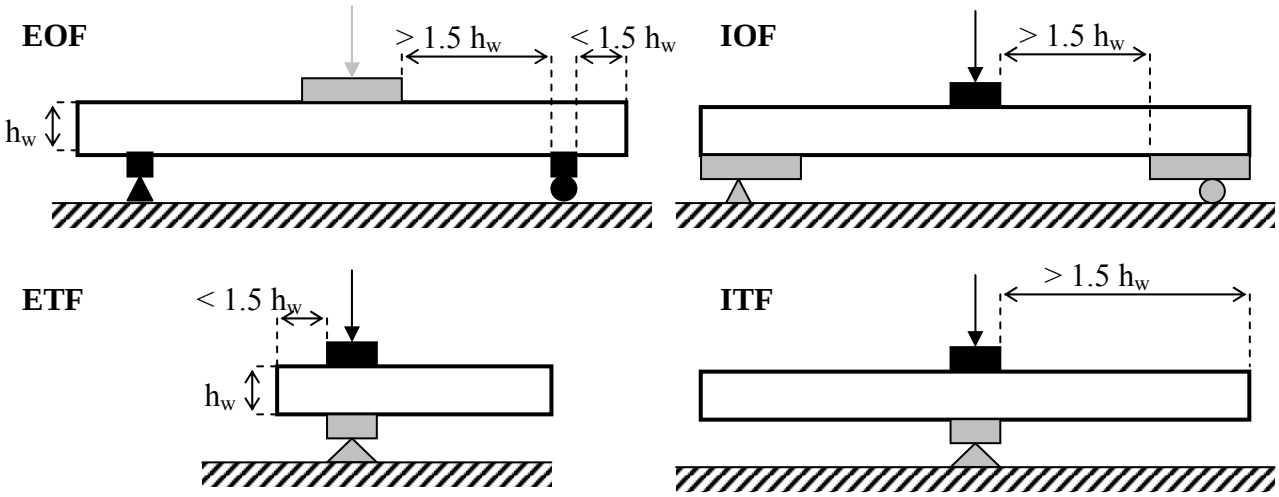

Fig. 2.8 Different web loading conditions (h_w = height of web).

If the distance between the edges of the bearing plates on opposite sides of the web is more than 1.5 times the web height h_w, one-flange loading is assumed to govern. If the distance is less than 1.5 times the web height, two-flange loading is assumed. Moreover, if the distance from the end of the member to the outer edge of the bearing or support plate is less than 1.5

times the web height, the loading is assumed to be end loading. If the distance is more than 1.5 times the web height, interior loading is assumed.

Web crippling quite often occurs together with a bending moment, especially for one-flange loading. However, Baehre (1975) showed that the influence of the bending moment is negligible if the applied bending moment is less than or equal to one third of the ultimate bending moment capacity of the section. Other authors have since confirmed this result (e.g. Wing and Schuster 1986, Studnička 1990).

2.3.2 Existing design rules

2.3.2.1 Eurocode 3: Part 1.3

The web crippling equations in the European design code ENV 1993-1-3:1996 (also known simply as Eurocode 3: Part 1.3) are based on the Swedish code for cold-formed thin-walled steel structures StBK-N5 (1980). ENV 1993-1-3:1996 considers the web crippling of cross-sections with single unstiffened webs (Figure 2.9), cross-sections with two or more unstiffened webs (Figure 2.10) and cross-sections with stiffened webs of the type shown in Figure 2.11. Cassette sections with unstiffened webs can be paralleled with C- and Z-sections with unstiffened webs (Figure 2.9). However, the web stiffeners used in common cassette sections, like that seen in Figure 1.1, are different from those shown in Figure 2.11. The procedure given in ENV 1993-1-3:1996 for stiffened webs only concern webs with "longitudinal web stiffeners folded in such a way that the two folds in the web are on opposite sides of the system line of the web joining the points of intersection of the midline of the web with the midlines of the flanges". However, in common cassette sections, this condition is not satisfied. In fact, ENV 1993-1-3:1996 does not provide any rules for the calculation of the web crippling capacity of webs with one-sided longitudinal stiffeners. However, the design rules for cross-sections with two of more unstiffened webs or stiffened webs are given below for comparison of different methods.

An interesting remark can be made on the European design code for aluminium structures (ENV 1999-1-1:1998), more generally known as Eurocode 9: Part 1.1. In the section dealing with the resistance of webs to transverse forces, it is written that the "resistance of a

longitudinally stiffened web is increased due to the presence of the stiffeners but no rules about this are given here". No background to this statement is given either, so it is assumed that the resistance of such webs should be found out experimentally.

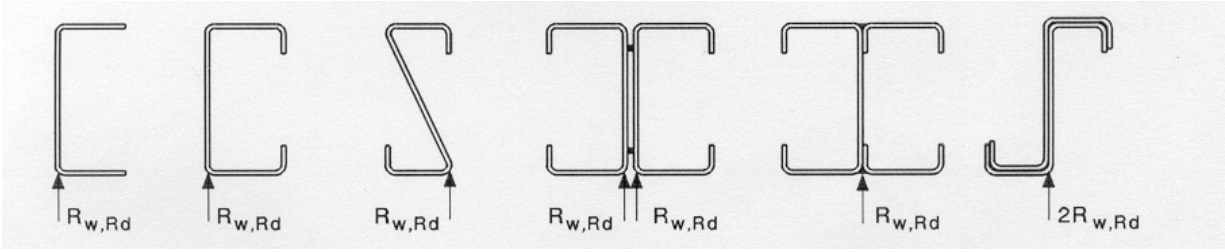

Fig. 2.9 Cross-sections with single unstiffened webs (ENV 1993-1-3:1996).

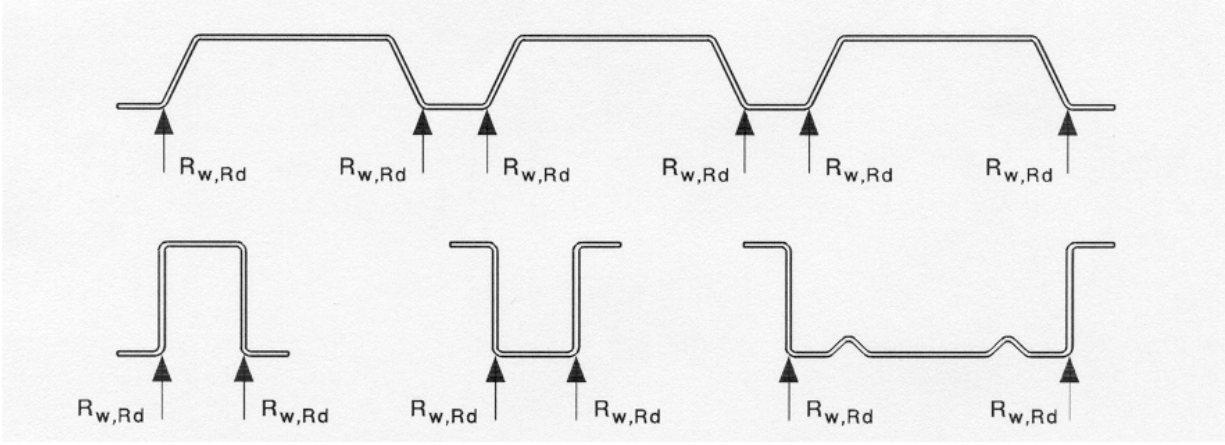

Fig. 2.10 Cross-sections with two or more unstiffened webs (ENV 1993-1-3:1996).

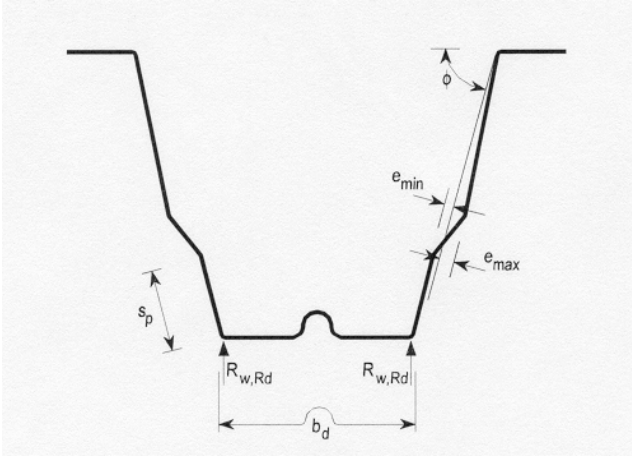

Fig. 2.11 Cross-section with stiffened webs (ENV 1993-1-3:1996).

Cross-sections with a single unstiffened web

According to Equation (5.18g) of ENV 1993-1-3:1996, the local transverse resistance $R_{w,Rd}$ of a single unstiffened web in the case of ITF-loading can be determined from:

$$R_{w,Rd} = \frac{k_3 k_4 k_5 \left[21.0 - \frac{h_w / t}{16.3} \right] \left[1 + 0.0013 \frac{s_s}{t} \right] t^2 f_{yb}}{\gamma_{M1}} \tag{2.9}$$

where h_w is the web height between the midlines of the flanges,
t is the design wall thickness equal to the nominal core thickness of the steel material before cold forming, exclusive of zinc or organic coatings,
s_s is the actual length of the stiff bearing,
f_{yb} is the yield strength of steel,
γ_{M1} is the partial safety factor, $\gamma_{M1} = 1.00$.

The values of the factors k_3 to k_5 should be determined using the equations:

$$k_3 = 0.7 + 0.3 \left(\frac{\phi}{90} \right)^2 \tag{2.10a}$$

$$k_4 = 1.22 - 0.22k \tag{2.10b}$$

$$k_5 = 1.06 - 0.06 \frac{r}{t} \leq 1.0 \tag{2.10c}$$

where $k = f_{yb} / 228$, with f_{yb} in N/mm^2,
ϕ is the slope of the web relative to the flanges (in degrees),
r is the internal radius of corners.

The above design equation is valid if the cross-section satisfies the following criteria:

$$r / t \leq 6 \tag{2.11a}$$

$$h_w / t \leq 200 \tag{2.11b}$$

$$r / t \leq 6 \tag{2.11c}$$

In the case of IOF-loading, Equation (5.18e) of ENV 1993-1-3:1996 should be used:

$$R_{w,Rd} = \frac{k_3 k_4 k_5 \left[14.7 - \frac{h_w / t}{49.5} \right] \left[0.75 + 0.011 \frac{s_s}{t} \right] t^2 f_{yb}}{\gamma_{M1}} \tag{2.12}$$

Cross-sections with two of more unstiffened webs

According to Equation (5.20) of ENV 1993-1-3:1996, the local transverse resistance $R_{w,Rd}$ per web of a cross-section with two or more unstiffened webs can be determined from:

$$R_{w,Rd} = \frac{\alpha \cdot t^2 \sqrt{f_{yb} E}\left(1 - 0.1\sqrt{\frac{r}{t}}\right)\left[0.5 + \sqrt{0.02 \cdot \frac{l_a}{t}}\right]\left(2.4 + \left(\frac{\phi}{90}\right)^2\right)}{\gamma_{M1}} \tag{2.13}$$

where α is a non-dimensional coefficient,
E is the modulus of elasticity of steel, $E = 210\,000$ N/mm^2,
l_a is the effective bearing length, $l_a \le 200$ mm.

The values of α and l_a depend on the loading category and the type of cross-section. Loading Category 1 effectively covers loading conditions EOF, ETF and ITF, while Category 2 corresponds to IOF-loading (see Figure 2.8):

- for cassettes (liner trays) in Category 1:

  - $\alpha = 0.057$
  - $l_a = 10$ mm,

- for cassettes (liner trays) in Category 2:

  - $\alpha = 0.115$
  - $l_a = s_s$ for $\beta_v \le 0.2$
  - $l_a = 10$ mm for $\beta_v \ge 0.3$

    where $\beta_v = \dfrac{|V_{Sd,1}| - |V_{Sd,2}|}{|V_{Sd,1}| + |V_{Sd,2}|}$,

    $|V_{Sd,1}|$ and $|V_{Sd,2}|$ are the absolute values of the transverse shear forces on each side of the local load or support reaction, $|V_{Sd,1}| \ge |V_{Sd,2}|$,

    s_s is the actual bearing length.
  - for values $0.2 \le \beta_v \le 0.3$, l_a is linearly interpolated.

The above design equation is valid if the clear distance c from the actual bearing length for the support reaction or local load to a free end is at least 40 mm and the cross-section satisfies the following criteria:

$$r/t \le 10 \tag{2.14a}$$

$$h_w/t \le 200 \sin\phi \tag{2.14a}$$

$$45° \le \phi \le 90° \tag{2.14a}$$

It is interesting to see that Eq. (2.13) is not dependent on the height of the cross-section, but only on the wall thickness of the steel sheet and the corner radius. Also, the α-factor causes a

relatively large change (α = 0.057 vs. α = 0.115) in the calculated resistance value in cases where the distance from the end of the beam to an end support changes from c = 1.5 h_w to c > 1.5 h_w, because this is set as a limit value between Categories 1 and 2 according to more specific category definitions in ENV1993-1-3:1996. In principle, this is true even when the distance is increased even slightly (say, 1 mm) past the value c = 1.5 h_w. The value of the effective bearing length l_a can also be either 10 mm or equal to the actual bearing length s_s depending on the value of β_v in Category 2, which causes more variance.

Cross-sections with stiffened webs

For cross-sections of the type in Figure 2.11 satisfying the condition

$$2 \le \frac{e_{\max}}{t} \le 12\,, \tag{2.15}$$

where e_{max} is the larger eccentricity of the folds relative to the system line of the web as shown in Figure 2.11, the local transverse resistance of the web can be determined by multiplying the corresponding value for a similar unstiffened web by the factor $\kappa_{a,s}$ given by

$$\kappa_{a,s} = 1.45 - 0.05\frac{e_{\max}}{t} \le 0.95 + \frac{35000 \cdot t^2 \cdot e_{\min}}{b_d^2 \cdot s_p} \tag{2.16}$$

where e_{min} is the smaller eccentricity of the folds relative to the system line of the web,
b_d is the developed width of the loaded flange,
s_p is the slant height of the plane web element nearest to the loaded flange.

2.3.2.2 AISI Specification

The design code currently in use in the United States is the 2001 edition of the Specification for the Design of Cold-Formed Steel Members published by the American Iron and Steel Institute. However, this edition was not available to the author during this research, so the text here is based on the 1996 edition (AISI 1996). The Specification gives design expressions to determine the web crippling strength of flexural members having flat single webs and I-beams made of two channels connected back to back, by welding two angles to a channel, or by connecting three channels, as shown in Figure 2.12. Stiffened webs are thus completely neglected.

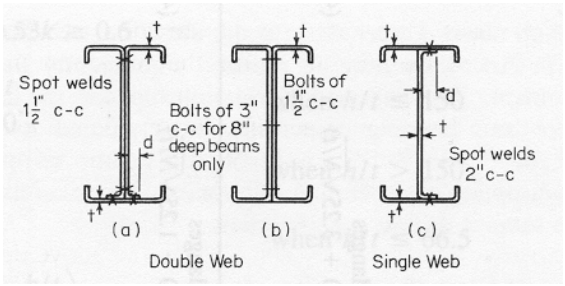

Fig. 2.12 Built-up sections considered in AISI (1996) (Yu 2000).

AISI (1996) gives a total of 12 different design expressions to be used in different design cases depending on the type of cross-section, spacing of opposing loads, whether end or interior loading is considered and if the flanges of the cross-section are stiffened or not. The equations are presented in a form that includes many different coefficients, but for the equations given below, some of the factors have been incorporated into the formula in order to simplify the presentation. The equations are valid for beams when $R/t \le 6$ and to decks when $R/t \le 7$, $N/t \le 210$ and $N/h \le 3.5$. For the case of interior two-flange loading, the design expression is

$$P_n = t^2 \cdot 894 \frac{f_y}{E} \cdot \left(1.22 - 0.22 \cdot 894 \frac{f_y}{E}\right) \cdot C_2 \cdot C_9 \cdot \left(0.7 + 0.3\left(\frac{\phi}{90}\right)^2\right)\left(771 - 2.26\frac{h}{t}\right)\left(1 + 0.0013\frac{N}{t}\right) \tag{2.17}$$

where $C_2 = 1.06 - 0.06\frac{R}{t} \le 1.0$,

R is the inside bend radius,
C_9 = 6.9 for metric units (N and mm),
h is the depth of the flat portion of the web measured along the plane of the web,
N is the actual bearing length.

For the case of cassette structures continuous over two spans, the interior one-flange - situation is valid. The nominal strength of a single web, P_n, at a concentrated load or reaction for this design case is given by Eq. (2.18).

$$P_n = t^2 \cdot 894\frac{f_y}{E} \cdot \left(1.22 - 0.22 \cdot 894\frac{f_y}{E}\right) \cdot C_2 \cdot C_9 \cdot \left(0.7 + 0.3\left(\frac{\phi}{90}\right)^2\right)\left(538 - 0.74\frac{h}{t}\right)\left(1 + 0.007\frac{N}{t}\right) \tag{2.18}$$

When $N/t > 60$, the factor $(1 + 0.007(N/t))$ may be increased to $(0.75 + 0.011(N/t))$.

In the case of EOF-loading, the design value for a Z-section that has its flange bolted to the section's end support member may be multiplied by 1.3, if the following conditions are met:

- $h/t \leq 150$,
- $R/t \leq 4$,
- cross-section base metal thickness ≥ 1.52 mm,
- support member thickness ≥ 4.76 mm.

The design value of the strength of a single web is obtained by multiplying the value of P_n by the factor of safety $\phi_w = 0.75$ in the case of single unreinforced webs and $\phi_w = 0.80$ in the case of I-sections. It should be noted that the value of the modulus of elasticity is taken as $E = 203\,000$ N/mm^2 in AISI (1996).

2.3.2.3 Australian / New Zealand Standard

The Australian / New Zealand Standard for Cold-Formed Steel Structures (AS/NZS 4600 (1996)) gives design equations that are similar to the AISI (1996) equations, although their formulation is slightly different and different symbols have been used for some variables. The modulus of elasticity is taken as $E = 200\,000$ N/mm^2 in AS/NZS 4600 (1996). For ITF-loading, the equation is

$$R_b = 23.3 \cdot t^2 f_y \cdot \left(1.22 - 0.22 \cdot \frac{f_y}{228}\right) \cdot C_2 \cdot \left(0.7 + 0.3\left(\frac{\phi}{90}\right)^2\right)\left(1 - 0.00292\frac{d_1}{t_w}\right)\left(1 + 0.0013\frac{l_b}{t_w}\right) \tag{2.19}$$

where d_1 is the depth of the flat portion of the web measured along the plane of the web,
t_w is the thickness of the web,
l_b is the actual length of bearing (smaller value of l_b is used for two opposite concentrated loads).

For IOF-loading, the design expression is

$$R_b = 16.3 \cdot t^2 f_y \cdot \left(1.22 - 0.22 \cdot \frac{f_y}{228}\right) \cdot C_2 \cdot \left(0.7 + 0.3\left(\frac{\phi}{90}\right)^2\right)\left(1 - 0.00138\frac{d_1}{t_w}\right)\left(1 + 0.007\frac{l_b}{t_w}\right) \tag{2.20}$$

As in AISI (1996), when $l_b/t_w > 60$, the factor $(1 + 0.007(l_b/t_w))$ may be increased to $(0.75 + 0.011(l_b/t_w))$. Also otherwise, the same conditions, limits and capacity (safety) factors for the use of the equations apply, as in the AISI (1996) specification.

2.3.2.4 The National Building Code of Finland

The National Building Code of Finland for cold-formed steel structures, RakMK B6 (1989), gives a design expression not dissimilar to the ENV 1993-1-3:1996 equations. The code considers only one-flange loading. When the support or the load-bearing plate is situated further away than the distance $1.5 \cdot h_w$ from the end of the member, the capacity F_R of one web against the concentrated load is given by Equation (2.21). Some of the symbols used in RakMK B6 (1989) have been modified from the original to correspond to the symbols used in ENV 1993-1-3:1996.

$$F_R = k_1 \cdot k_2 \cdot k_3 \cdot f_y \cdot t^2 \cdot \left(4.3 - 765\frac{f_y}{E}\right)\left(1 - 0.1\sqrt{\frac{r}{t}}\right)\left(2.4 + \left(\frac{\phi}{90}\right)^2\right) \tag{2.21}$$

where k_1
- $k_1 = 1$ for an unstiffened web,
- k_1 is the smaller of the values $k_1 = 1.74 - 0.06\,e_{\max}/t$ and $k_1 = 0.95 + 50000t^2 e_{\min}/(b_d^2 \cdot s_p)$ for a stiffened web,

k_2
- $k_2 = 1 + 0.01 \cdot l_a / t$, when $l_a \le 100 \cdot t$,
- $k_2 = 1 + 0.01 \cdot l_a / t - 0.1(l_a/(100 \cdot t)^2$, when $100 \cdot t < l_a \le 500 \cdot t$,
- $k_2 = 3.6$, when $l_a > 500 \cdot t$,

k_3
- $k_3 = 1.0$ for unreinforced webs of steel sheeting,
- $k_3 = 0.8$ for stiffened webs of steel sheeting and for cassette sections,

f_y is the yield strength of steel,
E is the modulus of elasticity, E = 210000 N/mm^2,
l_a is the length of the bearing plate (when a steel sheet is supported/loaded by a C- or Z-section, the value $l_a = 2b/3$ is used, where b is the width of the flange as shown in Figure 2.13,
ϕ, s_p, e_{max}, e_{min} and b_d are as defined in Figure 2.11.

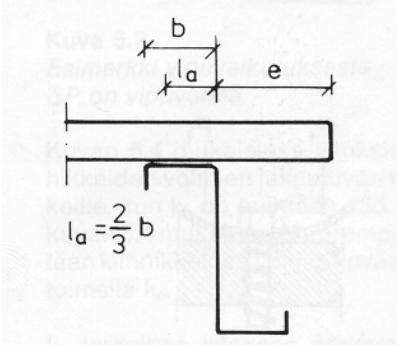

Fig. 2.13 Value of l_a when steel sheeting is loaded through a C- or Z-section (RakMK B6 (1989)).

When the support or the load-bearing plate is situated closer than the distance $1.5 \cdot h_w$ from the end of the member, the capacity F_R of one web against the concentrated load is one half of the value calculated above. By "stiffened web" in the calculation of k_1, the same type of stiffening as in ENV 1993-1-3:1996 is meant, as shown in Figure 2.11. The material design safety factor used for cold-formed steel in RakMK B6 (1989) is $\gamma_m = 1.0$.

It is most interesting to note that the Finnish code includes the factor $k_3 = 0.8$ for cassettes. However, there is no mention about exactly what type of cassette is meant by the Finnish code in this case. The value 0.8 should also be used for profiled steel sheeting with stiffened webs, but the only type of stiffener mentioned in RakMK B6 (1989) is that shown in Figure 2.11. The explanatory document to RakMK B6 (1989), TRY (1989), does not clarify this matter either. What is surprising is that cassettes, regardless of web type, appear to be grouped together with profiled steel sheeting with stiffened webs. On the other hand, also factor k_1 is meant to take the stiffener into account.

2.3.2.5 Comparisons of design codes from literature

Laine (1997) compared the values given by ENV 1993-1-3:1996 and RakMK B6 (1989) for different types of steel sheeting sections. He found that for an inside radius $r = 5$ mm, the values given by ENV 1993-1-3:1996 are, for the most part, slightly higher than the RakMK B6 (1989) values. He also compared the values to results from tests carried out by the sheet manufacturer Rannila and found that both codes give slightly higher capacities than the tests, except for high sheet thicknesses and when the load is applied at the narrow flange.

However, Laine points out that it is not possible to predict which code gives a higher capacity value for a particular design case, because of the many factors involved.

Hofmeyer (2000) compared the AISI (1996) predictions with the Eurocode 3 (1996) values and various test data and found that the AISI code gives results that are from -22 % lower to +18 % higher than the Eurocode 3 values. These differences are not correlated to the web width, the span length or the bottom flange width, but they are larger for small plate thicknesses.

A new comparison of design codes has not been carried out here, but comparisons have been carried out on the basis of test results at the end of Chapter 3.

2.3.3 Existing research work

There is a vast amount of research on the behaviour of thin-walled webs under local transverse loading. Most published articles are concerned with web crippling of unstiffened webs of channel or Z-sections, or corrugated steel sheets.

The author has not been able to find articles dealing specifically with web crippling of cassette sections. In practice, however, cassettes with unstiffened webs can in this respect be fairly directly paralleled with common C- and Z-sections. Many research projects have dealt with trapezoidal steel sheeting or hat sections that can have inclined webs, while the webs of cassette sections normally form a 90° angle with both flanges.

Cassettes normally have either unstiffened webs or webs that are stiffened in such a way that the stiffener is only on one side of a line drawn between the endpoints of the web. This is somewhat similar to the web of a Sigma-section shown in Figure 2.14. The author has not been able to find research results dealing with webs stiffened in this manner, which is unfortunate, because this section presents the most relevant case related to the present study. On the other hand, there is no theoretical reason why also cassette webs could not be stiffened using the type of folds shown in Figure 2.11. However, practical problems that prevent this may arise during the manufacturing process depending on the limitations of the production line.

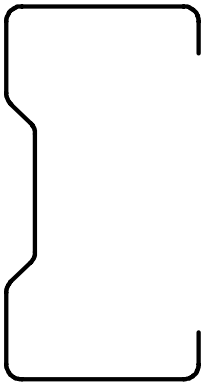

Fig. 2.14 Sigma-section.

Web crippling behaviour can generally be studied in three different ways. Testing is the fundamental research method for all empirical sciences. However, testing is rather expensive, which prevents research establishments from carrying out extensive experimental research programs. Therefore testing is quite often limited to a more or less representative sampling of design cases or specific orders from manufacturers. In spite of this, it is clear that when a new type of cross-section and/or design case is studied, testing is absolutely necessary in order to obtain reliable information about the different aspects of structural behaviour.

A powerful and significantly less expensive research method is finite element modelling, which can provide additional information about structural behaviour and more insight into the test results. Finite element modelling makes it possible to "look inside" a structure and study internal stresses, strains and deformations. However, all finite element modelling should have a basis in the real behaviour of structures and numerical models should be validated by testing. Therefore, finite element modelling is usually used alongside testing. It can also be used to study the structural behaviour in design cases for which testing would be virtually impossible or cases that have very little practical application but are interesting theoretically.

A third way to study web crippling is by the construction of mechanical models that use mathematical formulae to describe the cross-section geometry at the larger scale of e.g. web height and corner radius, while finite element models are constructed by much smaller elements whose stresses and strains are mathematically interdependent.

The experimental investigation of web crippling behaviour of thin-walled cross-sections was first started at Cornell University in the 1940's and 1950's by Winter & Pian, followed by

Zetlin (Yu 2000). Also Hetrakul & Yu carried out a large number of tests in the 1970's. These tests provided the foundation of the AISI (1996) design expressions. Later numerous other researchers have returned to the topic in order to provide more specific information on different types of sections or sections with different cross-sectional parameters.

In 1982, Wing & Schuster (1982) presented results of a study on the web crippling of decks (steel sheeting) subjected to either interior or end two-flange loading. The webs were unreinforced and their spreading was prevented by bolting the lower flanges to the bearing plate. New design expressions were developed for the ultimate web crippling load using a statistical program. The test results were found to fall within 20 % of the values predicted using the design expression.

Four years later, Wing & Schuster (1986) continued the publication of research results on the topic of web crippling, this time concentrating on interior one-flange loading. Similarly to their previous study, they formulated a design expression, which predicts the failure load with 20 % accuracy. This new expression for unstiffened webs was adopter for use in the Canadian design standard. According to Hofmeyer (2000), the Canadian Standard design expression has since evolved further and in the 1995 Edition of the standard, it is in the form:

$$R_u = 21 \cdot t^2 \cdot f_y \cdot \sin\phi \left(1 - 0.12\sqrt{\frac{r_{ibf}}{t}}\right)\left(1 + 0.065\sqrt{\frac{L_{lb}}{t}}\right)\left(1 - 0.04\sqrt{\frac{b_{wfl}}{t}}\right) \tag{2.22}$$

where r_{ibf} is the interior bottom flange corner radius,
L_{lb} is the load bearing plate width,
b_{wfl} is the flat web width.

The formula is valid for

$$r_{ibf} / t \le 10 \tag{2.23a}$$
$$L_{lb} / t \le 200 \tag{2.23b}$$
$$b_{wfl} / t \le 200 \tag{2.23c}$$
$$L_{lb} / b_{wfl} \le 2 \tag{2.23d}$$

The web crippling of wide deck sections was also studied experimentally by Studnička (1990), who found that for interior loading, the ultimate load is almost directly influenced by the width of the bearing plate and that the behaviour of the deck was not substantially changed when its loading direction was reversed. For end loading, Studnička

found, in addition to the above, that when the free distance at the end of the member extending beyond the bearing plate is increased, the ultimate load is also increased, but that the influence is not very strong.

Langan, LaBoube & Yu (1994) studied the behaviour of perforated webs subjected to end one-flange loading. They used a reduction factor *RF* to modify the ultimate web crippling capacity given by the AISI design code expression for unreinforced webs. *RF* includes the influence of web opening width and height and also the position of the opening along the vertical direction:

$$RF = 1.08 - 0.630\frac{a}{h} + 0.120\frac{x}{h} \leq 1.00 \qquad (2.24)$$

where a is the height of the web opening,
h is the height of the web,
x is the distance from the outer edge of the opening to the interior edge of the support bearing plate.

The reduction factor may be used when the section is single-web and meets the requirements for application of the current AISI design code. The method of Lagan, LaBoube & Yu provides a simple and directly applicable way to take account of web openings in the case of end one-flange loading. Similarly, appropriate strength increase factors may be usable in the case of stiffened webs.

Fox & Schuster (2000) studied the lateral strength of wind load bearing wall stud-to-track connections concentrating on web crippling failure and punch-through shear failure of the track. While the loading corresponds to end one-flange loading, it is different from the conditions given in design codes in that the bearing supports cannot be considered rigid (Figure 2.15). Fox and Schuster concluded that to ensure that web crippling of the stud is the critical design criterion, the track should be made of material of at least the same thickness as the stud.

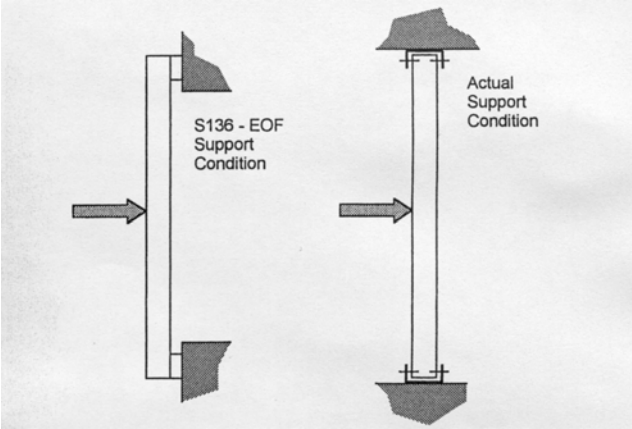

Fig. 2.15 Idealised web crippling compared to stud-to-track connection (Fox & Schuster 2000).

A large body of work on web crippling of cold-formed steel members has been carried out at the Technical University of Eindhoven in the Netherlands since the early 1990's. Bakker (1992) presented a mechanism model for the web crippling behaviour of unstiffened web elements in hat sections and first generation deck panels (Figure 2.16) when a negligibly small bending moment is present alongside the compressive concentrated load. This situation refers generally to IOF-loading when the distances between load and support bearing plates are not very large.

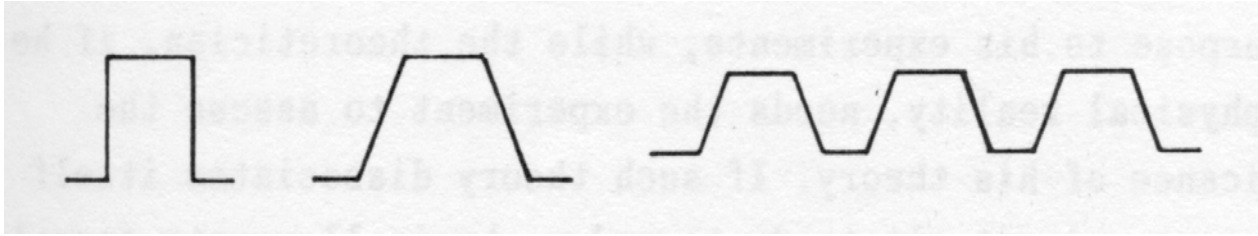

Fig. 2.16 Section types included in Bakker's (1992) research.

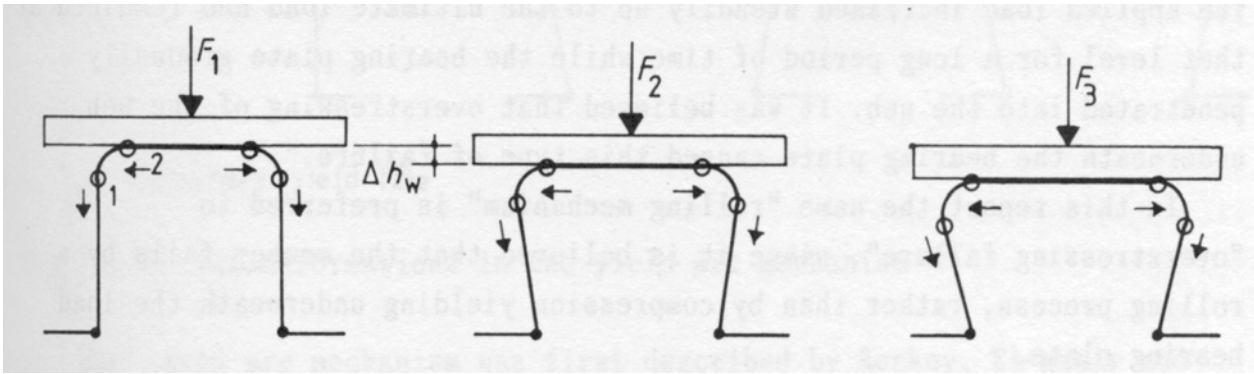

Fig. 2.17 Rolling mechanism modelled with moving yield lines (Bakker 1992).

The mechanical models were based on yield line theory with the objective of creating simplified and generalised expressions for web crippling strength. Based on previous work by other researchers, Bakker distinguished between two different web crippling mechanisms. In the rolling mechanism, the corner radius moves in a rolling manner down the web as shown in Figure 2.17. In the yield arc mechanism, web crippling is caused by a yield arc in the web underneath the load bearing plate (Figure 2.18). All deformations are assumed to be concentrated in the yield lines and other dimensions remain unchanged. For large corner radius, the rolling mechanism is governing; for small corner radius, the yield arc mechanism occurs. Bakker developed a mechanism model only for the rolling mechanism, not for the yield arc mechanism.

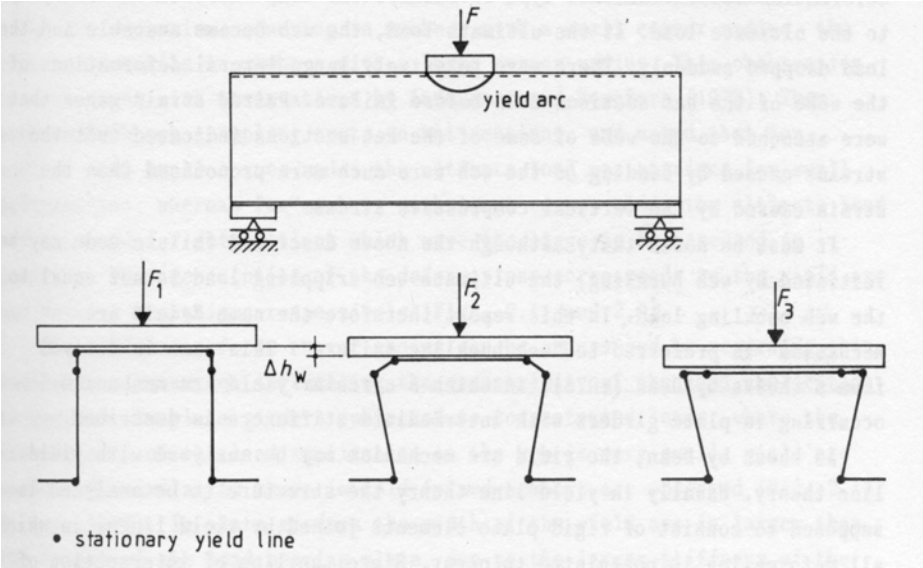

Fig. 2.18 Yield arc mechanism (Bakker 1992).

The model concentrates on the determination of the mechanism initiation load, whereas generally used design rules give the ultimate load. The mechanism initiation load is defined as the point of intersection of an elastic curve and a rigid-plastic mechanism initiation curve. The elastic curve is simply taken based on the initial stiffness observed in tests and the rigid-plastic curve is based on generalized yield-line theory. According to Bakker, however, "the difference between the ultimate load and the mechanism initiation load may be so small, that it would not be unduly conservative to base design rules on the determination of the mechanism initiation load". The difference is smaller for larger span lengths. The prediction of the ultimate load using a mechanism model is much more difficult than that of the mechanism initiation load. In its presented form, the model by Bakker (1992) gives promising

results, although it is not given in a very user-friendly form, but it has to be remembered that it was only a first attempt at creating such a model.

Hofmeyer (2000) continued Bakker's work and studied the combined web crippling and bending moment failure of first-generation trapezoidal steel sheeting. First-generation trapezoidal sheeting refers to cross-sections with unstiffened webs and flanges. Second-generation sheeting includes longitudinal stiffeners and third-generation sheeting has both longitudinal and transversal stiffeners. The different sheeting generation types are shown in Figure 2.19.

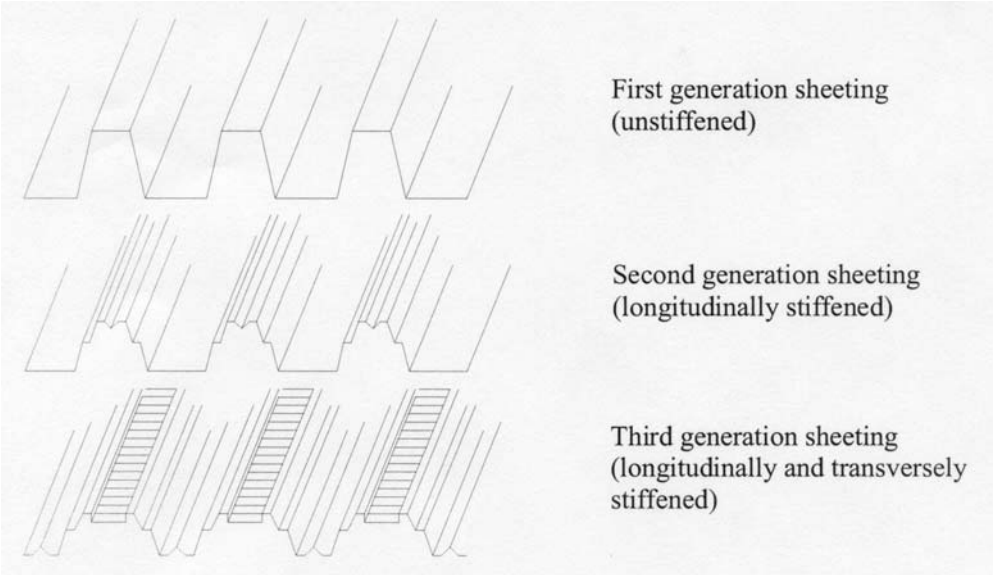

Fig. 2.19 Generations of sheeting (Hofmeyer 2000).

Hofmeyer carried out three-point bending tests on sheet sections and recognised a third post-failure mode in addition to the two described by Bakker (1992). This third failure mode is an unsymmetrical variant of the yield arc mechanism and was named the yield eye post-failure mode. Hofmeyer's tests showed that the rolling mechanism only occurs for impractically short span lengths (~ 600 mm) or impractically short load bearing plates. Therefore only the yield arc and yield eye mechanism are relevant for practical considerations.

As defined by Hofmeyer (2000), the yield eye mode describes a situation, where buckles in the flange adjacent to the load-bearing plate become more pronounced after elastic deformations, and ultimately the failure load is thus reached. Just before the failure load is

reached, a yield eye occurs near one edge of the load-bearing plate. A schematic view of the yield eye mode is given in Figure 2.20.

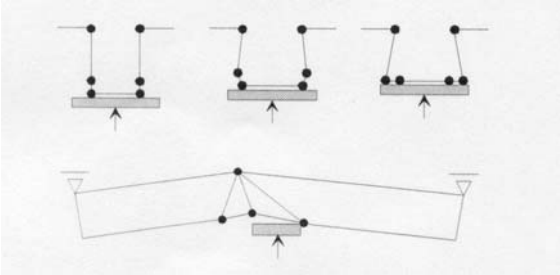

Fig. 2.20 Yield eye mode (Hofmeyer 2000).

In addition to the experimental research, Hofmeyer developed finite element models for each of the three post-failure modes on finite element code ANSYS 5.4 (1999) using linear shell elements SHELL43. According to Hofmeyer, the elements are capable of describing plasticity, large deflections and large strains. For the rolling and yield arc modes, the load bearing plate was modelled using a solid steel block and the contact between the nodes of the block and the sheet section was modelled using special contact elements. The same approach was attempted for the yield eye mode, but this lead to convergence problems. Therefore the loading was instead applied via two point loads placed at the corners of the load bearing plate. Displacement control and a Newton-Raphson procedure were used for the yield arc and rolling mechanisms, while the arc-length method was applied to the yield eye mechanism problem. Because the rolling and yield arc modes are symmetrical, it was sufficient to use a quarter model, while a half model was needed for the yield eye mode. Hofmeyer reported reasonably good correspondence between the analysis and test results and the yield line patterns could be distinguished in most cases.

Hofmeyer discussed the choice of the correct finite element model and concluded that a study should be started using the rolling model, which is a quarter model unable to describe the unsymmetrical yield eye mode. If a rolling post-failure mode appears, this is the correct mode. If a yield arc post-failure mode occurs, this is the correct mode. If the model seems to predict a mode similar to the yield eye mode (i.e. a yield eye develops, but because of the symmetry condition of the model, it cannot describe the unsymmetrical yield eye mode), another analysis should be run using the yield eye finite element model. A single model able to describe all three modes was not developed.

On the basis of the experiments and the finite element modelling, Hofmeyer developed an ultimate failure mechanical model and three post-failure mechanical models for each of the three modes. These models are too complicated for hand calculation, and will not be presented here as they are outside the main scope of the present work, but according to Hofmeyer's comparisons, the results given by the models are promising, although more model development may be appropriate. Hofmeyer also concluded that the Eurocode 3 predictions for the studied cases were quite good.

3. EXPERIMENTAL RESEARCH

3.1 General

A total of 52 tests were carried out on cassettes with different cross-sections. All cassettes were manufactured by Rannila Steel Oy and were chosen from the palette of Casetti cross-sections normally in production at their factories. The test specimens were made from hot-dipped zinc covered steel coils on a cold-forming line in Kaarina, Finland, and cut to the desired length directly on the production line. All longitudinal cutting required to prepare the final test specimens was done at the testing hall of the HUT Department of Civil and Environmental Engineering using a manually operated cutting blade. All testing was carried out at the same testing hall.

The first phase of testing was divided into three groups depending on the loading conditions and the type of test specimen. The first of the three groups consisted of ITF (interior two-flange) -tests on single web sections cut from factory-produced cassettes. The second group included IOF (interior one-flange) -tests on similar web sections using two different span lengths for the three-point bending tests. Finally, the third group consisted of IOF-tests on built-up sections where a small structural entity was constructed using two cassette sections for each specimen as explained in Section 3.5.

Three different web heights (100 mm, 150 mm and 200 mm) and two different nominal wall thicknesses (1.0 mm and 1.5 mm) were chosen for testing. The IOF-tests were carried out only on 200 mm high sections with nominal wall thickness 1.5 mm.

The naming convention for the test specimens is the following:

$$\begin{Bmatrix} ITF \\ IOF \\ S-IOF \end{Bmatrix} \begin{Bmatrix} 100 \\ 150 \\ 200 \end{Bmatrix} \begin{Bmatrix} \\ R \end{Bmatrix} - \begin{Bmatrix} t10 \\ t15 \end{Bmatrix} - \begin{Bmatrix} \\ S600 \\ S1000 \end{Bmatrix} - \{\#\}$$

1st term: test type: *ITF* for interior two-flange loading of single web specimens, *IOF* for interior one-flange loading of single web specimens, *S-IOF* for interior one-flange loading with built-up sections.

2nd term: web height: *100*, *150* or *200* [mm].

3rd term: section type: [blank] for flat web sections,
R for longitudinally stiffened web sections.

4th term: wall thickness: *t10* for t_{nom} = 1.0 mm,
t15 for t_{nom} = 1.5 mm.

5th term: span length: [blank] for ITF tests,
S600 for IOF-tests with span length L_{span} = 600 mm,
S1000 for IOF-tests with span length L_{span} = 1000 mm.

6th term: sequence number of test in test series.

For example, IOF200R-t15-S600-2 stands for the second test in the series of IOF-tests on 200 mm high longitudinally stiffened webs with nominal wall thickness 1.5 mm and span length 600 mm. The main results of the tests have been previously published in the test report Kaitila & Mäkeläinen (2003).

3.2 Material properties

The material used in the manufacturing of the test specimens was S350GD-Z275MA (SFS-EN 10147, 2000). The material properties were determined by carrying out standardized tensile tests on test pieces cut out in both longitudinal and perpendicular directions relative to the direction of cold forming (SFS-EN 10 002-1, 2002). A total of ten different material test series had to be carried out, because the test specimens with different heights and thicknesses were manufactured from different steel coils. All coil materials had to be tested in both longitudinal and perpendicular directions relative to the direction of cold forming. The pieces tested longitudinally to the direction of cold forming were cut from the flat parts of the wide flange of cassette sections. The pieces tested perpendicularly to the direction of cold forming were cut from the cassettes' web part. Before testing, the protective zinc coating was removed and the tests were carried out on the base steel material. Tables 3.1-3.5 show the main parameters for the different steel materials with nominal thicknesses 1.0 mm and 1.5 mm and different web heights. The material test specimen tag numbers were chosen during testing and their sole purpose was to distinguish the different test series and specimens from each other.

As is usually the case, the strength of the material is a little higher in the direction perpendicular to the cold forming direction. This is also the direction in which the loading is

mostly applied in the web crippling tests, especially in the ITF-tests. The development of plastic areas, the redistribution of stresses and the bending in IOF-tests naturally leads to stresses in the axial direction as well, i.e. the direction of cold forming.

Some variations can be seen in the results of the material tests. The mean yield strength corresponding to 0.2 % plastic strain $f_{p0.2}$ varies between a low of 390.1 N/mm^2 and a high of 446.6 N/mm^2. The mean ultimate strength varies between 493.7 N/mm^2 and 522.0 N/mm^2. The mean modulus of elasticity varies between 167028 N/mm^2 and 205364 N/mm^2.

The values the moduli of elasticity have been determined from the straight parts of the stress-strain curves between data points corresponding approximately to stress values 30 N/mm^2 and 250 N/mm^2 in the present tests. The exact determination of the modulus of elasticity is quite difficult for thin-walled steel sheets, because the material test specimens may have an initial curvature and the straightness of the initial part of the stress-strain curve may be difficult to ascertain. Therefore the values of E given in Tables 3.1-3.5 should not be taken as precise data.

The material values given in Tables 3.3 and 3.5 for specimens with b_w = 150 mm and b_w = 200 mm, respectively (t_{nom} = 1.5 mm in both cases), are all actually from the same steel coil (KH089002). When the data is carefully inspected, some differences in values of both strength and modulus of elasticity can be observed. The strength variations are thought to be due to the local residual stresses caused by the cold forming and the initial imperfections in the specimens (see section 3.3.1).

The stress-strain curves corresponding to all the material test series presented in Tables 3.1-3.5 are given in ANNEX A.

Table 3.1a Material test results for specimens with t_{nom} = 1.0 mm and b_w = 100 mm cut longitudinally to the direction of cold forming (steel coil number FT019002).

Specimen tag	t mm	b mm	A mm^2	E N/mm^2	$f_{p0.1}$ N/mm^2	$f_{p0.2}$ N/mm^2	$f_{u.test}$ N/mm^2	$\varepsilon_{fu.test}$ %	ε_{break} %
CC-1	0.953	12.51	11.92	171432	379.9	394.0	492.4	16.40	24.34
CC-2	0.951	12.51	11.90	192518	379.7	396.1	494.0	16.55	25.22
CC-3	0.951	12.51	11.90	176978	382.2	397.3	494.8	16.61	25.68
Mean	**0.952**	**12.51**	**11.91**	**180309**	**380.6**	**395.8**	**493.7**	**16.5**	**25.1**
St. deviation	0.00	0.00	0.01	10930.6	1.39	1.67	1.22	0.11	0.68

Table 3.1b Material test results for specimens with t_{nom} = 1.0 mm and b_w = 100 mm cut perpendicularly to the direction of cold forming (steel coil number FT019002).

Specimen tag	t mm	b mm	A mm^2	E N/mm^2	$f_{p0.1}$ N/mm^2	$f_{p0.2}$ N/mm^2	$f_{u.test}$ N/mm^2	$\varepsilon_{fu.test}$ %	ε_{break} %
CCP-1	0.952	12.51	11.91	177226	422.0	462.2	501.4	15.54	23.42
CCP-2	0.951	12.51	11.90	173847	427.8	424.1	500.6	15.72	22.58
CCP-3	0.954	12.51	11.93	178137	429.6	424.8	500.6	15.92	24.91
Mean	**0.952**	**12.51**	**11.91**	**176403**	**426.5**	**437.0**	**500.9**	**15.7**	**23.6**
St. deviation	0.00	0.00	0.02	2260.2	3.97	21.80	0.46	0.19	1.18

Table 3.2a Material test results for specimens with t_{nom} = 1.0 mm and b_w = 150 mm cut longitudinally to the direction of cold forming (steel coil number J6503002).

Specimen tag	t mm	b mm	A mm^2	E N/mm^2	$f_{p0.1}$ N/mm^2	$f_{p0.2}$ N/mm^2	$f_{u.test}$ N/mm^2	$\varepsilon_{fu.test}$ %	ε_{break} %
A1-1	0.937	12.51	11.72	189097	383.3	395.3	501.4	14.84	21.11
A1-2	0.940	12.51	11.76	188930	385.6	396.7	501.0	14.02	20.82
A1-3	0.938	12.51	11.73	190735	380.2	393.4	498.6	14.15	20.19
A1-4	0.934	12.51	11.68	177739	383.0	394.7	500.8	14.32	20.97
A1-5	0.935	12.51	11.70	177360	382.0	392.8	499.5	14.36	21.88
Mean	**0.937**	**12.51**	**11.72**	**184772**	**382.8**	**394.6**	**500.3**	**14.34**	**20.99**
St. deviation	0.00	0.00	0.03	6632.4	1.97	1.55	1.17	0.31	0.61

Table 3.2b Material test results for specimens with t_{nom} = 1.0 mm and b_w = 150 mm cut perpendicularly to the direction of cold forming (steel coil number J6503002).

Specimen tag	t mm	b mm	A mm^2	E N/mm^2	$f_{p0.1}$ N/mm^2	$f_{p0.2}$ N/mm^2	$f_{u.test}$ N/mm^2	$\varepsilon_{fu.test}$ %	ε_{break} %
B1-1	0.936	12.51	11.71	198936	387.5	421.6	503.3	13.53	15.95
B1-2	0.936	12.51	11.71	209738	389.1	423.4	502.8	13.54	16.78
B1-3	0.929	12.51	11.62	206748	387.9	420.9	502.5	12.92	16.60
B1-4	0.928	12.51	11.61	200975	388.9	420.3	498.3	10.69	13.03
B1-5	0.929	12.51	11.62	210423	382.9	417.0	501.3	12.75	15.55
Mean	**0.932**	**12.51**	**11.65**	**205364**	**387.3**	**420.6**	**501.6**	**12.69**	**15.58**
St. deviation	0.00	0.00	0.05	5177.43	2.53	2.34	2.01	1.17	1.51

Table 3.3a Material test results for specimens with t_{nom} = 1.5 mm and b_w = 150 mm cut longitudinally to the direction of cold forming (steel coil number KH089002).

Specimen tag	t mm	b mm	A mm^2	E N/mm^2	$f_{p0.1}$ N/mm^2	$f_{p0.2}$ N/mm^2	$f_{u.test}$ N/mm^2	$\varepsilon_{fu.test}$ %	ε_{break} %
A2-1	1.437	12.51	17.98	202449	390.4	407.4	506.0	12.75	17.49
A2-2	1.443	12.51	18.05	188848	387.8	405.0	505.3	12.59	18.26
A2-3	1.443	12.51	18.05	189132	389.9	407.6	507.5	12.61	17.71
A2-4	1.440	12.51	18.01	189946	389.6	408.2	507.6	12.70	18.50
A2-5	1.438	12.51	17.99	187627	390.9	408.5	509.3	12.76	19.61
Mean	**1.440**	**12.51**	**18.02**	**191600**	**389.7**	**407.3**	**507.1**	**12.68**	**18.31**
St. deviation	0.00	0.00	0.03	6121.39	1.18	1.38	1.56	0.08	0.83

Table 3.3b Material test results for specimens with t_{nom} = 1.5 mm and b_w = 150 mm cut perpendicularly to the direction of cold forming (steel coil number KH089002).

Specimen tag	t mm	b mm	A mm^2	E N/mm^2	$f_{p0.1}$ N/mm^2	$f_{p0.2}$ N/mm^2	$f_{u.test}$ N/mm^2	$\varepsilon_{fu.test}$ %	ε_{break} %
B2-1	1.433	12.51	17.93	196575	414.0	446.7	520.9	9.70	11.93
B2-2	1.431	12.51	17.90	187337	412.7	445.7	520.5	11.81	15.33
B2-3	1.428	12.51	17.86	181071	417.8	447.2	522.5	10.95	13.34
B2-4	1.429	12.51	17.88	201371	413.4	446.5	522.0	11.18	14.16
B2-5	1.437	12.51	17.98	184891	415.9	447.1	524.2	12.11	17.49
Mean	**1.432**	**12.51**	**17.91**	**190249**	**414.8**	**446.6**	**522.0**	**11.15**	**14.45**
St. deviation	0.00	0.00	0.04	8443.06	2.07	0.60	1.46	0.94	2.10

Table 3.4a Material test results for specimens with t_{nom} = 1.0 mm and b_w = 200 mm cut longitudinally to the direction of cold forming (steel coil number KF943005).

Specimen tag	t mm	b mm	A mm^2	E N/mm^2	$f_{p0.1}$ N/mm^2	$f_{p0.2}$ N/mm^2	$f_{u.test}$ N/mm^2	$\varepsilon_{fu.test}$ %	ε_{break} %
BB-1	0.958	12.51	11.98	173891	377.8	390.3	496.8	15.15	22.89
BB-2	0.954	12.51	11.93	180800	373.2	389.5	497.8	14.96	22.16
BB-3	0.962	12.51	12.03	192256	379.4	390.5	497.9	15.54	23.51
Mean	**0.958**	**12.51**	**11.98**	**182316**	**376.8**	**390.1**	**497.5**	**15.2**	**22.9**
St. deviation	0.00	0.00	0.05	9275.8	3.22	0.53	0.61	0.30	0.68

Table 3.4b Material test results for specimens with t_{nom} = 1.0 mm and b_w = 200 mm cut perpendicularly to the direction of cold forming (steel coil number KF943005).

Specimen tag	t mm	b mm	A mm^2	E N/mm^2	$f_{p0.1}$ N/mm^2	$f_{p0.2}$ N/mm^2	$f_{u.test}$ N/mm^2	$\varepsilon_{fu.test}$ %	ε_{break} %
BBP-1	0.949	12.51	11.87	190408	372.8	408.4	501.5	15.03	23.19
BBP-2	0.949	12.51	11.87	198170	375.3	410.6	501.5	14.66	21.17
BBP-3	0.948	12.51	11.86	198612	372.9	409.3	501.8	15.16	21.97
Mean	**0.949**	**12.51**	**11.87**	**195730**	**373.7**	**409.4**	**501.6**	**15.0**	**22.1**
St. deviation	0.00	0.00	0.01	4614.3	1.42	1.11	0.17	0.26	1.02

Table 3.5a Material test results for specimens with t_{nom} = 1.5 mm and b_w = 200 mm cut longitudinally to the direction of cold forming (steel coil number KH089002).

Specimen tag	t mm	b mm	A mm^2	E N/mm^2	$f_{p0.1}$ N/mm^2	$f_{p0.2}$ N/mm^2	$f_{u.test}$ N/mm^2	$\varepsilon_{fu.test}$ %	ε_{break} %
AA-1	1.446	12.51	18.09	166452	381.4	396.8	506.4	14.13	23.62
AA-2	1.448	12.51	18.11	159190	378.3	393.8	503.4	14.51	22.72
AA-3	1.451	12.51	18.15	175443	376.9	400.2	503.3	13.61	22.78
Mean	**1.448**	**12.51**	**18.12**	**167028**	**378.9**	**396.9**	**504.4**	**14.1**	**23.0**
St. deviation	0.00	0.00	0.03	8141.8	2.30	3.20	1.76	0.45	0.50

Table 3.5b Material test results for specimens with t_{nom} = 1.5 mm and b_w = 200 mm cut perpendicularly to the direction of cold forming (steel coil number KH089002).

Specimen tag	t mm	b mm	A mm^2	E N/mm^2	$f_{p0.1}$ N/mm^2	$f_{p0.2}$ N/mm^2	$f_{u.test}$ N/mm^2	$\varepsilon_{fu.test}$ %	ε_{break} %
AAP-1	1.436	12.51	17.96	215585	394.9	427.8	520.5	13.27	20.71
AAP-2	1.440	12.51	18.01	209294	396.8	429.0	520.4	13.12	20.63
AAP-3	1.437	12.51	17.98	185375	399.2	431.3	522.4	12.64	18.08
Mean	**1.438**	**12.51**	**17.98**	**203418**	**397.0**	**429.4**	**521.1**	**13.0**	**19.8**
St. deviation	0.00	0.00	0.03	15939.2	2.15	1.78	1.13	0.33	1.50

3.3 ITF-tests on single webs

3.3.1 Test arrangement

The first series of tests was carried out on 1200 mm long single web sections that had been cut from factory-produced Rannila Casetti sections. This resulted in nominal cross-sections of the type shown in Figure 3.1 for unstiffened web sections and Figure 3.2 for stiffened web sections. The figures also show the measurements taken from each tested specimen before testing. The most important nominal dimensions are given in Tables 3.6a and 3.6b. The actual measured values are given in ANNEX B.

Table 3.6a Most important nominal cross-sectional dimensions for flat and longitudinally stiffened web profiles (t = wall thickness).

	b_{tf}	$b_{tf.st}$	b_w	$b_{bf.fl}$	r_{itf}	r_{etf}	r_{tf}	r_{ibf}	r_{ebf}	r_{bf}
ITF100			100 + t							
ITF150	93.7	30.3	150 + t	36.7	2.4	3.6	3.0	2.4	3.6	3.0
ITF200			200 + t							

Table 3.6b Additional nominal cross-sectional dimensions for webs with longitudinal stiffeners (t = wall thickness).

	$b_{w.st}$	$b_{w.st.fl}$	$d_{w.st}$	$h_{w.st}$
ITF100R ITF150R ITF200R	30.7	49.3	27.0 - t	8.0

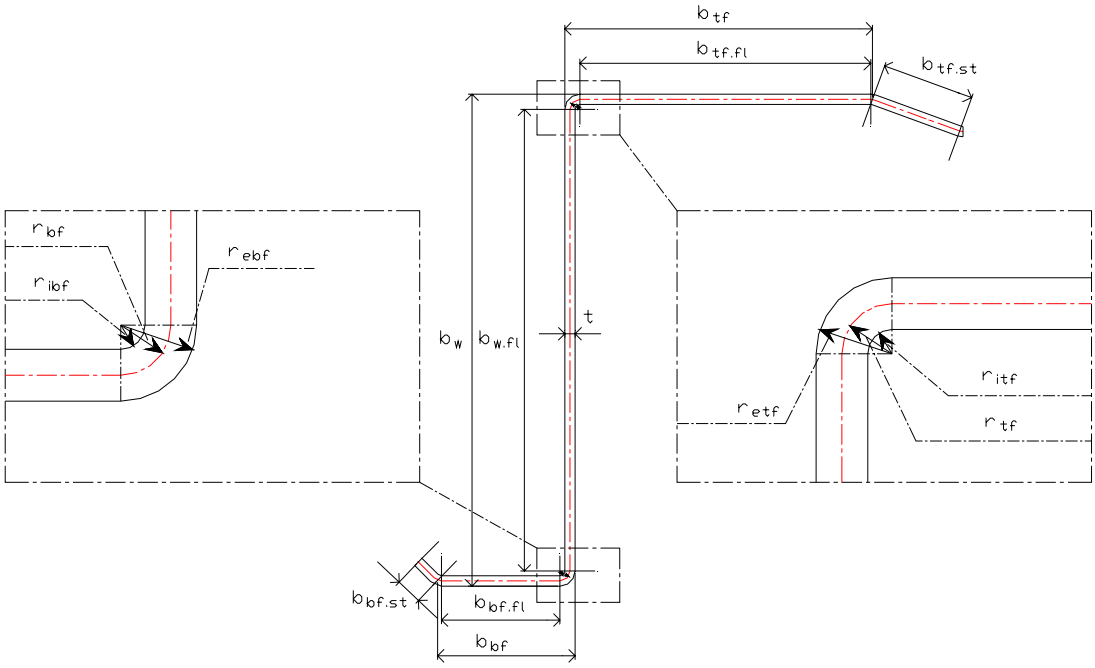

Fig. 3.1 Nominal flat web cross-section for ITF- and IOF-tests.

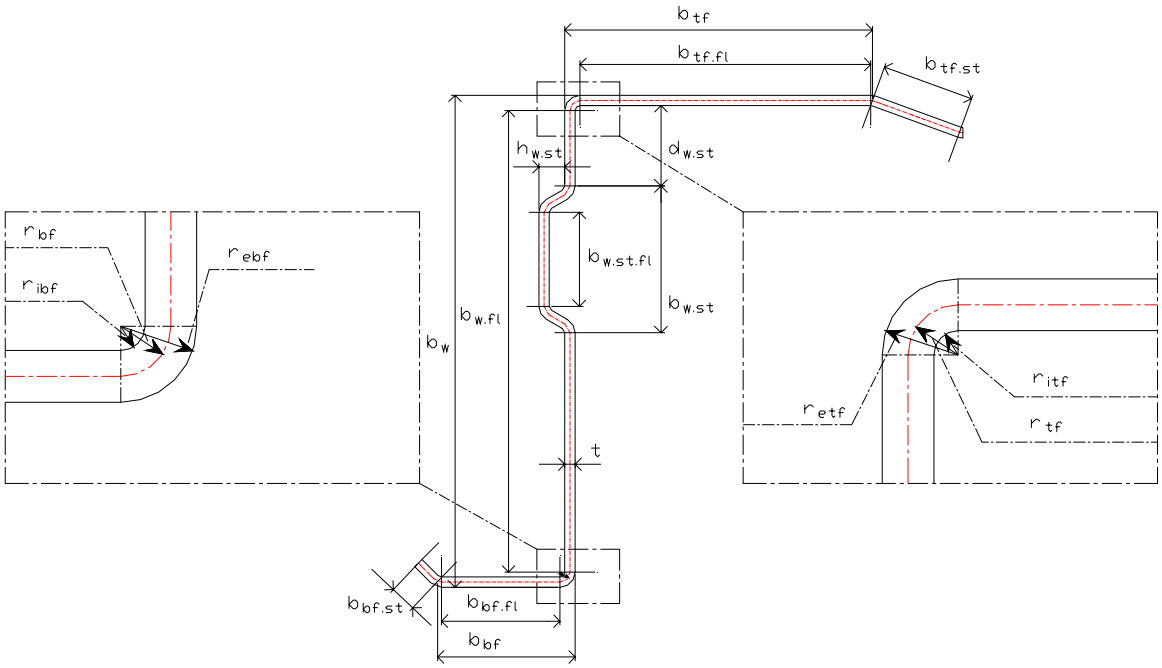

Fig. 3.2 Nominal longitudinally stiffened web cross-section for ITF- and IOF-tests.

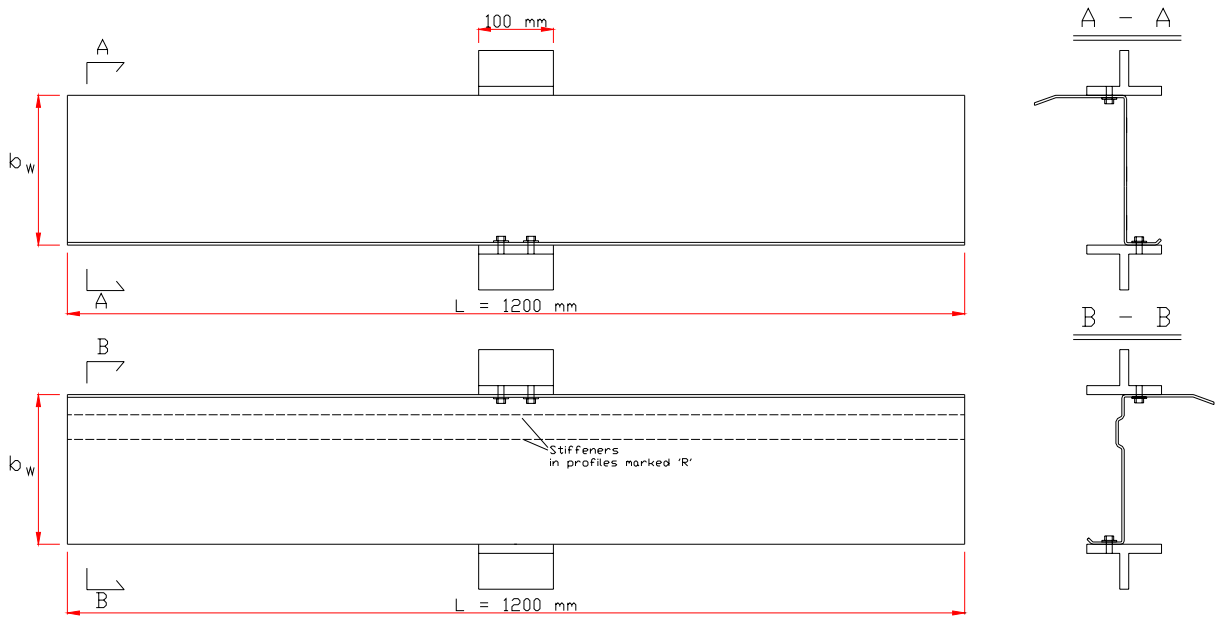

Fig. 3.3 Schematic view of general ITF test set-up.

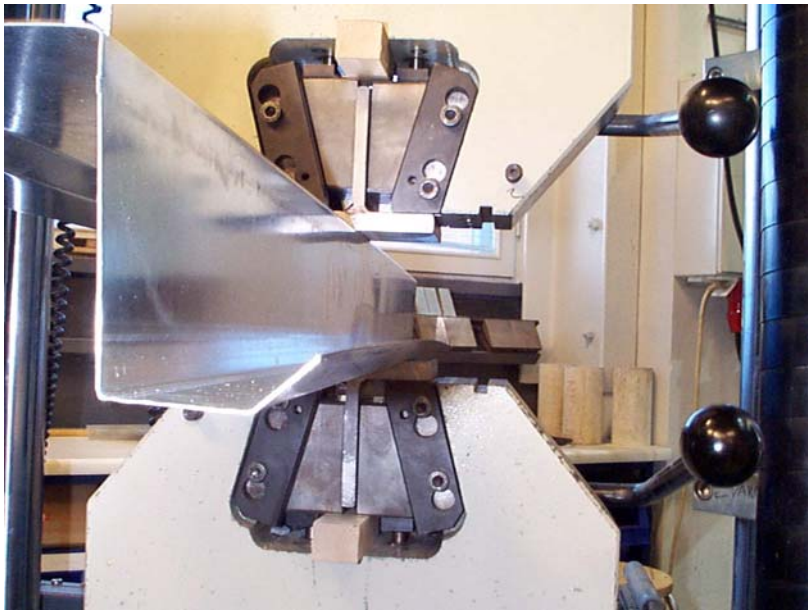

Fig. 3.4 General view of test set-up (test ITF100-t10-1).

As can be seen from Figure 3.4, specially manufactured welded T-shaped steel sections were used to connect the specimen to the Roell+Koerthaus universal testing rig. The T-shaped sections were attached to the flanges of the test specimen using two 8 mm diameter screws and 20 mm diameter washers situated at 20 mm distance from the centre line of the web. The connection can be seen in the photo on the right in Figure 3.11a. This test set-up provided

laterally braced connections at the top and bottom flanges and did not allow curling of the flanges at the loading area. Although this arrangement may not be directly comparable to all practical situations, it nevertheless provides unambiguously determined boundary conditions, which is important in the comparison of test results and numerical analysis results.

The test specimen was placed between the jaws of the testing machine and attached via the T-shaped sections. The loading was applied using displacement control. In the first two tests (ITF100-t10-1 and ITF100-t10-2), the load application speed was chosen as 0.5 mm/min, but was thereafter increased to 1.0 mm/min for all subsequent ITF- and IOF-tests in order to speed up the testing procedure while still keeping the loading speed relatively low.

There were noteworthy and sometimes important deviations in the initial shape of a number of test specimens in comparison to the nominal cross-section dimensions. Many test specimens were also rather curved along their length. These initial imperfections were measured along the length of the specimens using a three-point measuring rod whose end points were at a 1100 mm distance from each other and at equal (approximately 50 mm) distances from the ends of the specimen. The difference from the zero-value was measured at mid-span. Measurements were taken at both flanges and at the mid-height of the web as shown in Figure 3.5. In some specimens, also the shape of the web at mid-span was curved vertically, which obviously had a direct influence on some of the test results. The vertical curvature of the web at mid-span was evaluated in a similar way as shown in Figure 3.6. All the measurements shown in the Figures are given for each test specimen in ANNEX B. The +- and –-signs in the figures indicate the sign of the measured curvature.

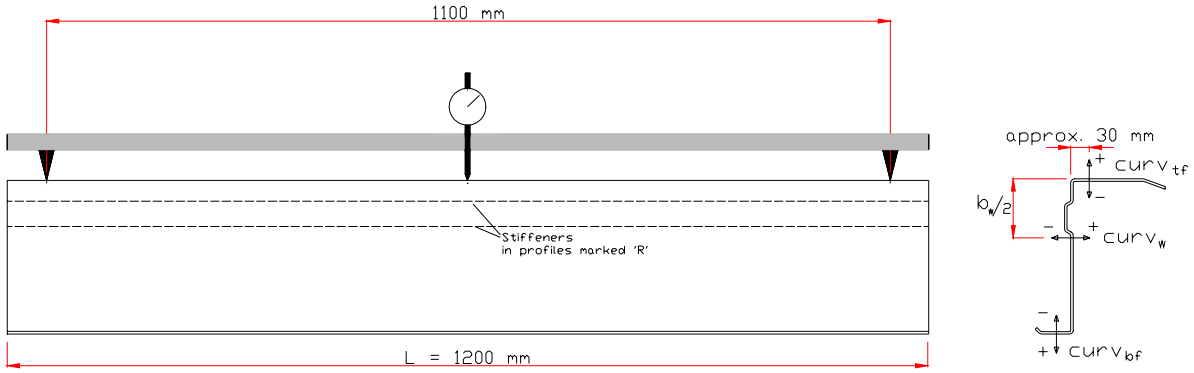

Fig. 3.5 Principle of longitudinal curvature measurement for ITF- and IOF- test specimens.

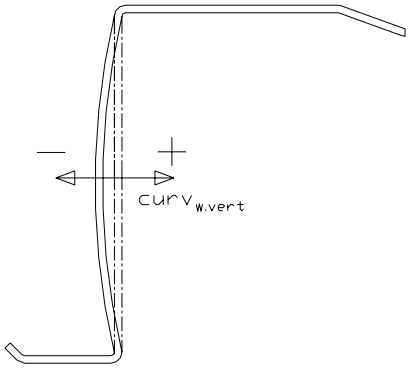

Fig. 3.6 Principle of vertical curvature measurement of the web at mid-span.

3.3.2 Test results

The results of all ITF-tests are summarized in Table 3.7 and the results of all individual tests are given in Tables 3.8-3.17 and Figures 3.7-3.25.

Table 3.7 Summary of test results from ITF-tests.

Test series	Average F_u [kN]	Average load displacement at F_u [mm]
ITF100-t10	7.45	3.08
ITF100R-t10	6.02	7.52
ITF150-t10	6.34	5.34
ITF150R-t10	5.27	8.68
ITF150-t15	16.56	3.42
ITF150R-t15	12.90	7.34
ITF200-t10	6.51	6.16
ITF200R-t10	5.14	8.94
ITF200-t15	16.24	4.67
ITF200R-t15	12.71	7.70

One of the main conclusions from the results of the ITF-tests is that the presence of a longitudinal web stiffener reduces the web crippling strength of the profile by about 17-22 % in comparison to the corresponding section with a flat web. Also the initial stiffness of the web is reduced when a stiffener is present as can be seen from the load-displacement graphs of individual tests shown below.

The influence of web height on the section's resistance against local transverse forces does not appear to be very important, although the average failure loads for the 100 mm high section with t_{nom} = 1.0 mm are slightly higher than those for 150 mm and 200 mm high sections with

the same steel thickness. The differences between 150 mm and 200 mm high sections are smaller still.

The behaviour of cross-sections with flat webs is remarkably different from that of cross-sections with stiffened webs. As could be expected, the flat webs collect a higher amount of potential energy during the first part of loading. This energy is then freed when the ultimate load bearing capacity is reached and the web buckles. However, in most of the ITF-tests herein, the buckling of the web was not very notable, probably due to the initial imperfections and curvatures of the profiles. However, tests on the most slender flat webs, the 200 mm high 1.0 mm thick sections, were an exception to this rule. Here the buckling was pronounced and happened suddenly leading to an immediate fall of the applied load. The redistribution of stresses still led to a further increase of the load after the buckling, but subsequent buckling still occurred later on in the tests.

By looking at the development of the buckling and plastic deformations in the profiles, it can be seen how the stresses are redistributed to sections of the beam further away from the loading area as the test progresses.

The different test series are discussed below in separate sections. The individual test results are given in tables and the load-displacement curves are shown. Photographs showing the deformation modes are given and the test results are discussed. The load-displacement curves from all ITF-tests are also collected in ANNEX C in order to show the differences in the results depending on web height and steel thickness.

Test series ITF100-t10 and ITF100R-t10

Table 3.8 Results of ITF-tests on 100 mm high unstiffened single webs with t_{nom} = 1.0 mm.

Specimen code	F_u [kN]	Load displacement at F_u [mm]
ITF100-t10-1	7.30	3.17
ITF100-t10-2	7.34	3.10
ITF100-t10-3	7.7	2.98
Mean	**7.45**	**3.08**
Standard deviation	0.220	0.096

Table 3.9 Results of ITF-tests on 100 mm high stiffened single webs with t_{nom} = 1.0 mm.

Specimen code	F_u [kN]	Load displacement at F_u [mm]
ITF100R-t10-1	6.01	7.47
ITF100R-t10-2	6.05	7.53
ITF100R-t10-3	6.00	7.55
Mean	**6.02**	**7.52**
Standard deviation	0.027	0.040

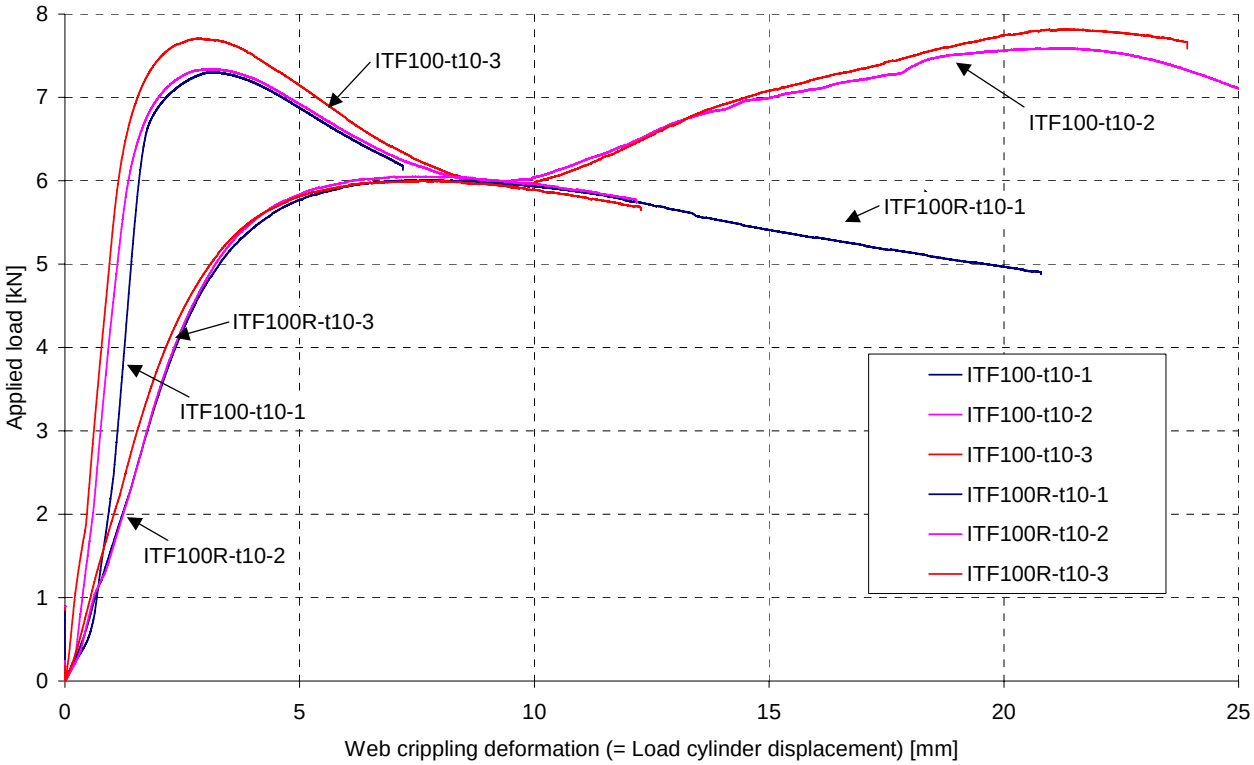

Fig. 3.7 Load-deformation curves for ITF-tests on 100 mm high single webs with t_{nom} = 1.0 mm.

The failure load of the unstiffened webs of 100 mm high sections with t_{nom} = 1.0 mm is on average 23.8 % higher than the failure load of corresponding stiffened webs. The failure load for unstiffened webs is taken as the first local maximum in the load-displacement curve. Interestingly for these specimens, an even higher load magnitude is reached later in the test.

After the failure load, the load magnitude is reduced by about 20-30 %, but after this the load starts to increase again and the profile is able to carry load for a long time even though the plastic web crippling process continues. However, only for these first tests did the second local maximum reach an even higher value than the failure load. The webs with longitudinal stiffeners showed fundamentally different behaviour. The load-displacement curve is smoother and no sudden changes are observed. After the failure load is reached, the load continues to decrease rather slowly without any further post-failure stiffening occurring.

As explained above, the load was applied using displacement control with a load application speed of 0.5 mm/min for the first two tests and 1.0 mm/min for all subsequent tests. This explains the slightly higher ultimate load and stiffness of test ITF100-t10-3 when compared with the first two tests, because the increase of load application speed is known to cause this type of effect.

The stiffened webs are not as much affected by initial form imperfections as the nominally flat webs, because the non-symmetry of the stiffener causes a spring-like effect that is not too sensitive to minor variations in the cross-section. This is shown by the practically overlapping load-displacement curves. As the load is applied, the stiffened web simply starts to displace out-of-plane in the direction of the stiffener. The unstiffened web, on the other hand, behaves more like a simply supported plate loaded in the plane and undergoes buckling when the load reaches a certain level.

Figures 3.8a and 3.8b show the progression of the deformations in the web of the specimen as seen from either side of the web, respectively. It can be seen that the first deformations constitute of a clear arc-shaped curve under the loading pad. As the test is continued, the deformed area widens as plastic deformations are born and the stresses are redistributed. Nevertheless, in all the tests, the deformed area remained relatively local in the longitudinal direction of the specimen and the ends of the 1200 mm long specimens were not seen to be affected by the local transverse forces applied at mid-span.

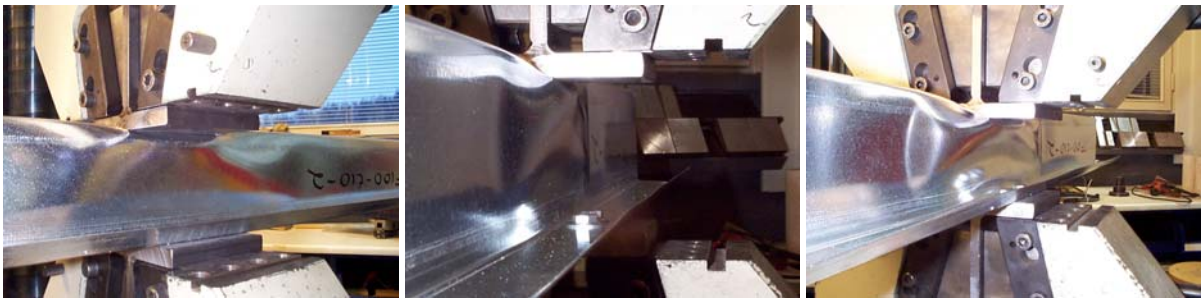

Fig. 3.8a Web crippling progression in test ITF100-t10-2 as seen from the "outside".

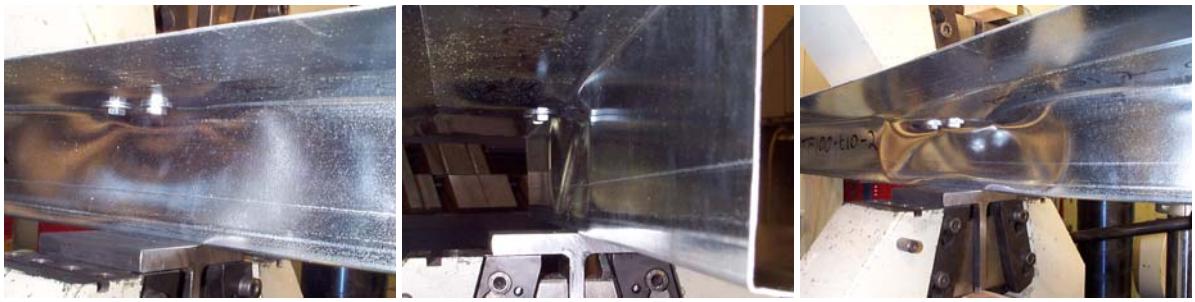

Fig. 3.8b Web crippling progression in test ITF100-t10-2 as seen from the "underside".

Fig. 3.9 Web crippling progression in test ITF100R-t10-1.

Figure 3.9 shows the progression of the deformations for 100 mm high webs with stiffeners. The first arc-shaped deformations can be seen at the stiffener level in the photo on the left. In the other two photos, the further yield deformations are shown. The deformations were concentrated on the lower part of the web and the bottom flange.

Test series ITF150-t10 and ITF-150R-t10

Table 3.10 Results of ITF-tests on 150 mm high unstiffened single webs with t_{nom} = 1.0 mm.

Specimen code	F_u [kN]	Load displacement at F_u [mm]
ITF150-t10-1	6.17	5.54
ITF150-t10-2	6.53	5.79
ITF150-t10-3	6.19	5.21
ITF150-t10-4	6.47	4.86
ITF150-t10-5	6.35	5.31
Mean	**6.34**	**5.34**
Standard deviation	0.163	0.352

Table 3.11 Results of ITF-tests on 150 mm high stiffened single webs with t_{nom} = 1.0 mm.

Specimen code	F_u [kN]	Load displacement at F_u [mm]
ITF150R-t10-1	5.33	8.60
ITF1500R-t10-2	4.78	9.68
ITF150R-t10-3	5.70	7.75
Mean	**5.27**	**8.68**
Standard deviation	0.467	0.970

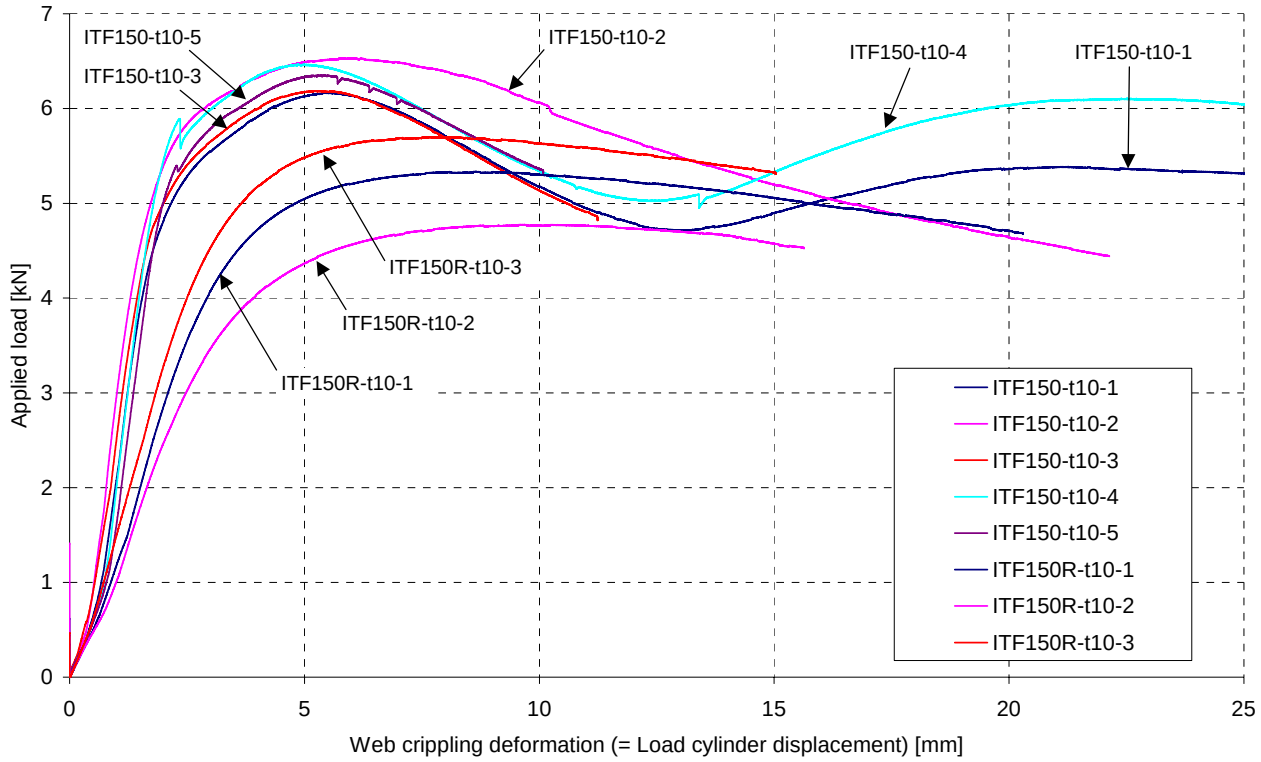

Fig. 3.10 Load-deformation curves for ITF-tests on 150 mm high single webs with t_{nom} = 1.0 mm.

The 150 mm high flat web specimens with t_{nom} = 1.0 mm all behaved qualitatively similarly to the 100 mm high flat web specimens with the exception of the second test specimen as can be seen from the load-displacement curves in Figure 3.10. The deformation mode in this test was

quite different as well, as can be seen when the web crippling progression in Figure 3.12 for specimen ITF150-t10-2 is compared to the one in Figures 3.11a and 3.11b for specimen ITF150-t10-1. In four of the five tests, the deformation started off as a local arc-shaped mode at the location of the loading pad, as was observed in the ITF100-t10 tests as well. This arc was then transformed into a rolling deformation mode as seen most clearly from the photo on the right in Figure 3.11a. The widening of the yielding area can also be clearly observed. However, in test ITF150-t10-2, the web buckled towards the right (in Figure 3.12) at its mid-height, while creating a large arc-like buckled shape in the lower part of the web. When the initial imperfections of the tested specimens measured before testing are studied closely, it can be seen that the vertical curvature of test specimen ITF150-t10-2 was larger in magnitude (-0.64 mm) than for any of the other specimens in this category (see ANNEX B). This may have partly contributed to the change of behaviour. Test specimen ITF150-t10-4, which has a similar load-displacement curve during the start of the test, has the second-highest magnitude of initial vertical curvature (-0.54 mm). In these cases this initial imperfection appears to be beneficial to the resistance of the cross-section. However, the differences are relatively small.

Fig. 3.11a Web crippling progression in test ITF150-t10-1 as seen from the "outside".

Fig. 3.11b Web crippling progression in test ITF150-t10-1 as seen from the "underside".

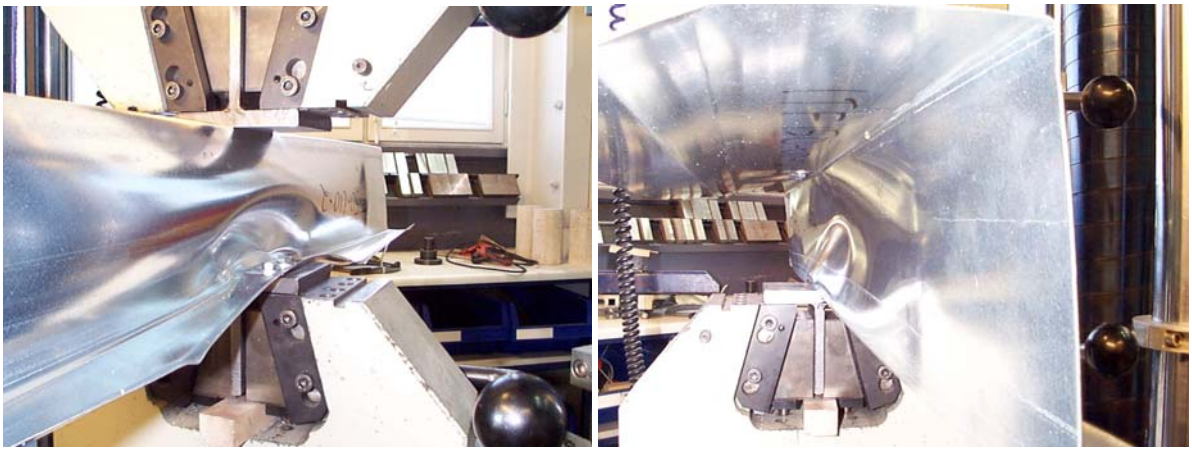

Fig. 3.12 Web crippling progression in test ITF150-t10-2.

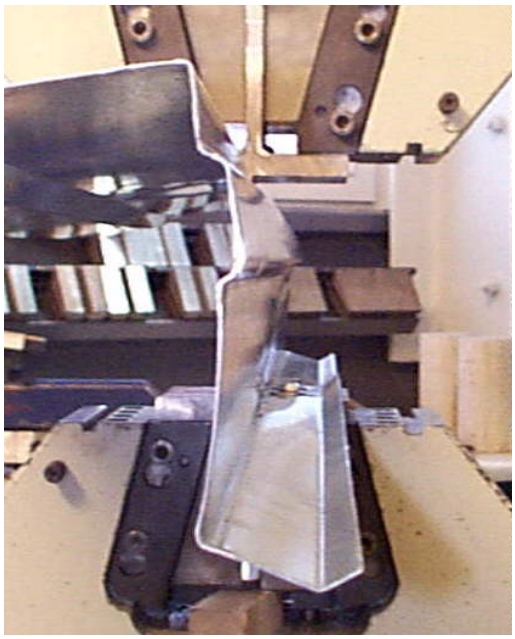

Fig. 3.13 Web deformation in test ITF150R-t10-2.

It is also interesting to note that while the failure load of specimen ITF150-t10-2 is somewhat higher than for the other specimens, the test load for this specimen appears to decrease monotonously after its first maximum, while for the other specimens, a further increase is observed similarly to the ITF100-t10 tests. This is qualitatively similar to the behaviour of web sections with longitudinal stiffeners, which is explained by the similarity of the initial web deformation of specimen ITF150-t10-2 with the eccentricity caused by the longitudinal stiffener in tests ITF150R.

Test series ITF150-t15 and ITF-150R-t15

Table 3.12 Results of ITF-tests on 150 mm high unstiffened single webs with t_{nom} = 1.5 mm.

Specimen code	F_u [kN]	Load displacement at F_u [mm]
ITF150-t15-1	16.73	3.10
ITF150-t15-2	16.73	3.41
ITF150-t15-3	16.20	3.76
Mean	**16.56**	**3.42**
Standard deviation	0.306	0.331

Table 3.13 Results of ITF-tests on 150 mm high stiffened single webs with t_{nom} = 1.5 mm.

Specimen code	F_u [kN]	Load displacement at F_u [mm]
ITF150R-t15-1	12.87	7.45
ITF150R-t15-2	13.00	6.75
ITF150R-t15-3	12.84	7.82
Mean	**12.90**	**7.34**
Standard deviation	0.082	0.544

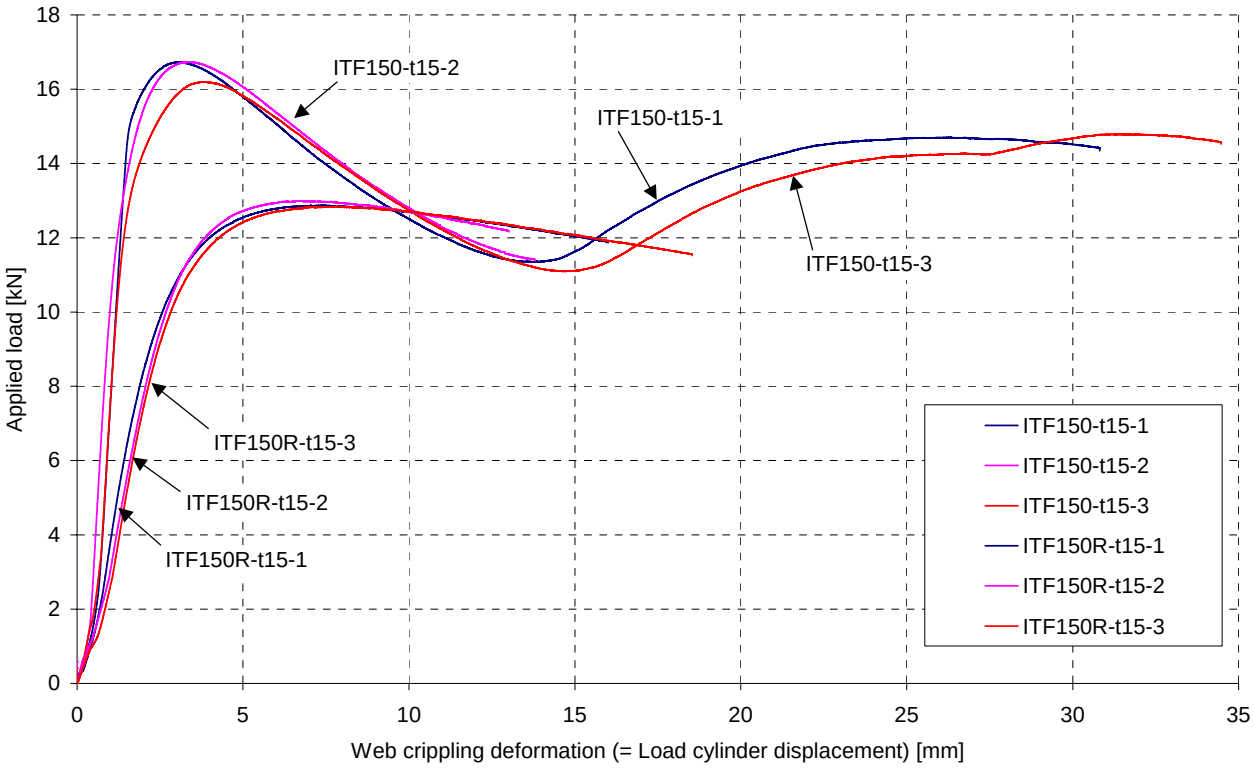

Fig. 3.14 Load-deformation curves for ITF-tests on 150 mm high single webs with t_{nom} = 1.5 mm.

The results of the ITF-tests on 150 mm high specimens with t_{nom} = 1.5 mm do not show any unexpected behaviour when compared to the previous results. The web crippling progression was similar to the corresponding 1.0 mm thick sections, as can be seen from Figures 3.15 and 3.16. For the flat webs, an arc-shaped deformation first appeared, and a rolling web crippling

deformation followed later on in the test. For the web with a longitudinal stiffener, the deformations first concentrated at the mid-height of the web, close to the lower edge of the stiffener, and soon thereafter the web was simply bulged toward the "outside" as seen in previous tests, with the deformed area widening as the test progressed.

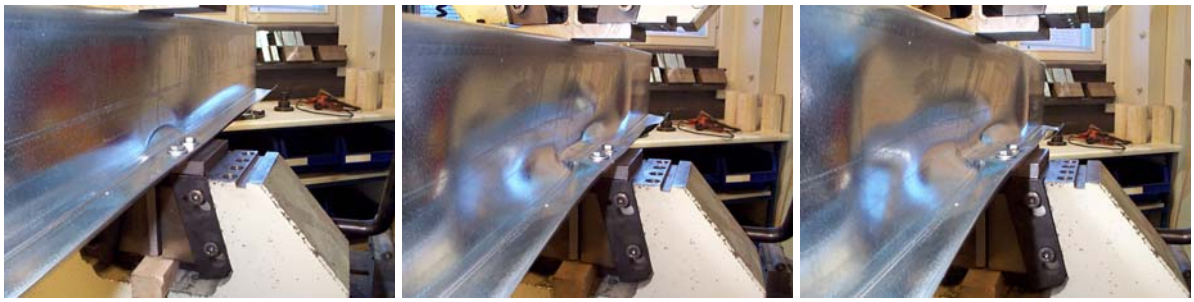

Fig. 3.15 Web crippling progression in test ITF150-t15-1 as seen from the "outside".

Fig. 3.16 Web crippling progression in test ITF150R-t15-1 as seen from the "underside".

Test series ITF200-t10 and ITF-200R-t10

Table 3.14 Results of ITF-tests on 200 mm high unstiffened single webs with t_{nom} = 1.0 mm.

Specimen code	F_u [kN]	Load displacement at F_u [mm]
ITF200-t10-1	7.16	5.96
ITF200-t10-2	6.25	6.51
ITF200-t10-3	6.13	6.00
Mean	**6.51**	**6.16**
Standard deviation	0.567	0.308

Table 3.15 Results of ITF-tests on 200 mm high stiffened single webs with t_{nom} = 1.0 mm.

Specimen code	F_u [kN]	Load displacement at F_u [mm]
ITF200R-t10-1	5.08	9.62
ITF200R-t10-2	5.08	8.80
ITF200R-t10-3	5.27	8.39
Mean	**5.14**	**8.94**
Standard deviation	0.107	0.626

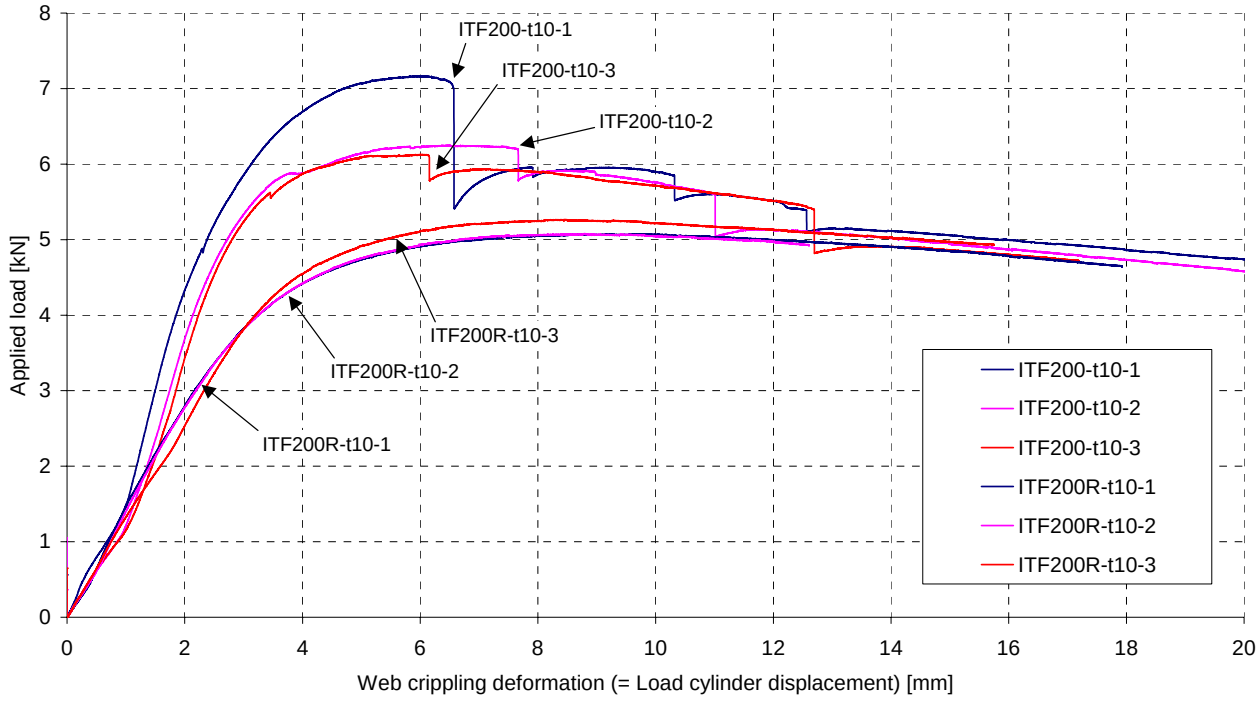

Fig. 3.17 Load-deformation curves for ITF-tests on 200 mm high single webs with t_{nom} = 1.0 mm.

The load-displacement curves of test specimens in series ITF200-t10 (Figure 3.17) show a somewhat different behaviour from all the other specimens. In these specimens, the web buckling was much more pronounced than in the others due obviously to the higher slenderness of the web. The buckling load corresponds to the failure load. A loud noise could

be heard at the moment of buckling and a sudden drop in load can be seen. After the drop, the load continued to increase slightly until a further buckling occurred.

The higher slenderness of these webs makes them also prone to the effects of initial imperfections. It should be pointed out that of all those tested, these specimens were the most curved initially as can be seen from the measurements given in ANNEX B. The higher failure load of specimen ITF200-t10-1 can probably be attributed to the magnitude of the vertical curvature, which was -3.13 mm, while for specimens ITF200-t10-2 and ITF200-t10-3 the values were -2.15 and -1.93, respectively. The negative sign of the initial curvature seems therefore to increase the load bearing capacity of this type of section, at least in the inspected range. The same effect was witnessed in test series ITF150-t10 above.

The web crippling progression for the flat web specimens is shown in Figures 3.18 and 3.19 for tests ITF200-t10-1 and ITF200-t10-2, respectively. The deformation starts again as a yield-arc mode followed by the bulging of the whole web. The photo on the right in Figure 3.18 includes a vertically placed member to help show the magnitude of the lateral web deformation.

The photo on the left in Figure 3.19 shows specimen ITF200-t10-2 in its initial state. It can be seen that there are several wave-like deformations in the web profile.

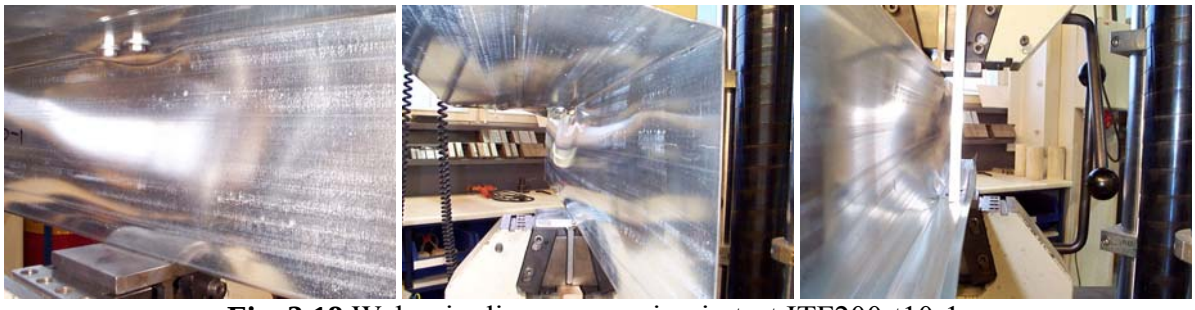

Fig. 3.18 Web crippling progression in test ITF200-t10-1.

Fig. 3.19 Web crippling progression in test ITF200-t10-2.

Fig. 3.20 Web crippling progression in test ITF200R-t10-1.

The basic deformation mode of test series ITF200R-t10 was similar to the other webs with longitudinal stiffeners, i.e. the web bulged towards the stiffener side, as seen in Figure 3.20. However, probably due to the higher slenderness value of these sections, a yield-arc pattern could also be more clearly recognized at areas adjacent to the loading pads.

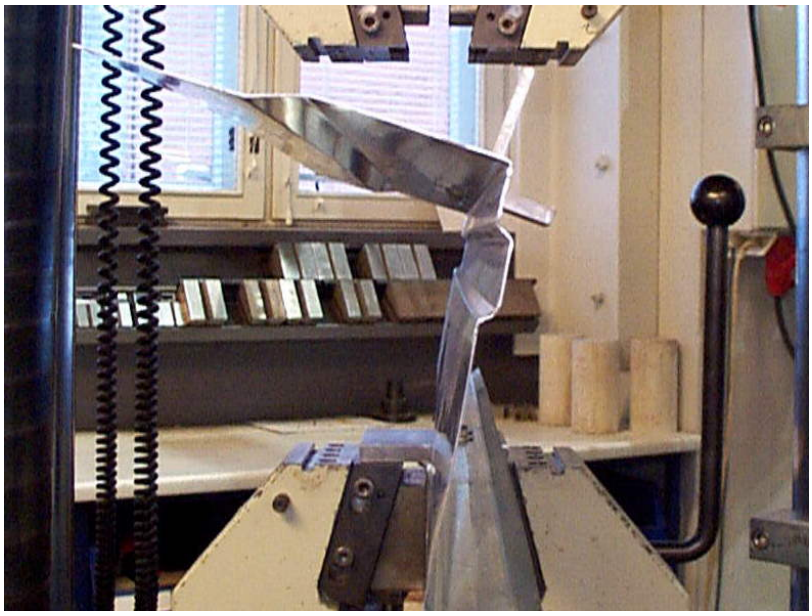

Fig. 3.21 Initial form of test specimen ITF200R-t10-3 forcing the top flange T-section into the jaws of the loading cylinder.

To give a better idea of the initial curvatures present in the test specimens, Figure 3.21 shows a photo of test specimen ITF200R-t10-3 before testing with the lower flange connected to the testing rig and the top flange free with the T-section connected. In the top part of the figure, the opening of the loading cylinders jaws can be seen. The specimen had to be forced into the vertical position before testing could be started. It is clear that the initial stresses thus created will have some effect on the test results. However, it should be noted that the photo presents the most pronounced case and that the initial curvatures were not as large as this in all the specimens.

Test series ITF200-t15 and ITF-200R-t15

Table 3.16 Results of ITF-tests on 200 mm high unstiffened single webs with t_{nom} = 1.5 mm.

Specimen code	F_u [kN]	Load displacement at F_u [mm]
ITF200-t15-1	14.30	4.32
ITF200-t15-2	17.39	4.64
ITF200-t15-3	16.99	4.73
ITF200-t15-4	16.27	5.00
Mean of all tests	**16.24**	**4.67**
Standard deviation of all tests	1.370	0.278
Mean of tests 2-4	**16.88**	**4.79**
Standard deviation of tests 2-4	0.571	0.185

Table 3.17 Results of ITF-tests on 200 mm high stiffened single webs with t_{nom} = 1.5 mm.

Specimen code	F_u [kN]	Load displacement at F_u [mm]
ITF200R-t15-1	12.18	8.69
ITF200R-t15-2	13.26	6.66
ITF200R-t15-3	12.69	7.74
Mean	**12.71**	**7.70**
Standard deviation	0.538	1.013

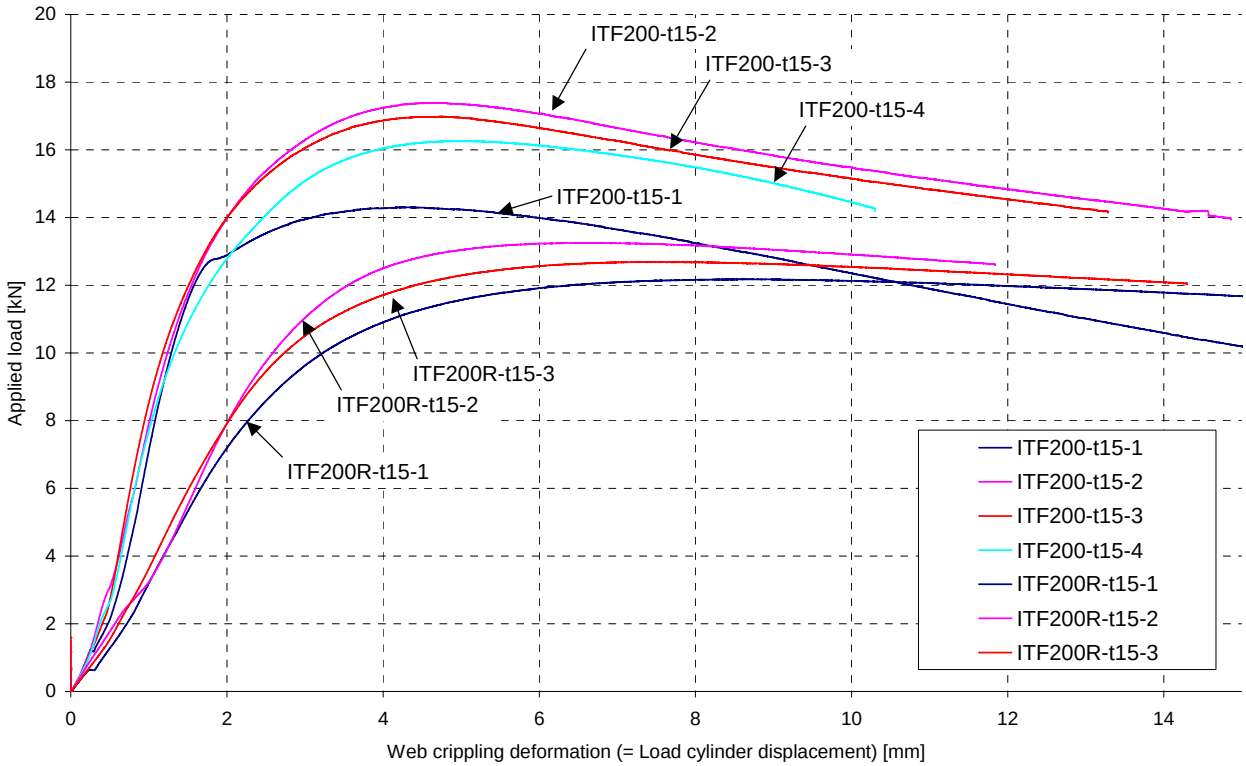

Fig. 3.22 Load-deformation curves for ITF-tests on 200 mm high single webs with t_{nom} = 1.5 mm.

As can be seen in Figure 3.22, the load-displacement curve of test ITF200-t15-1 runs lower than those of the other tests in the same series. No clear reason for this behaviour could be

found. The photos in Figure 3.23 show that the web bulged towards the left in this test, while for the other three tests in the series, the web bulged towards the right, as shown in Figure 3.24. However, the initial vertical curvatures fail to explain this difference, as can be concluded when comparing the values given in Table 3.18. The value for ITF200-t15-1 (-0.56 mm) falls between the extreme values recorded (-0.31 mm and -0.74 mm). It can be seen from the load-displacement curve that just before a deflection of 2 mm was reached, the web buckled, which was not as clearly observed for any of the other three tests in this series. This type of snap-through behaviour may have been due to the initial stresses caused by having to force the web section between the jaws of the testing rig in a situation similar to that shown in Figure 3.21.

Table 3.18 Initial vertical web curvature values for specimens in test series ITF200-t15.

Test specimen	Value of vertical web curvature [mm]
ITF200-t15-1	-0,56
ITF200-t15-2	-0,71
ITF200-t15-3	-0,74
ITF200-t15-4	-0,31

It is possible that test ITF200-t15-1 was simply an exception, but it is obviously impossible to discuss the statistical importance of this exception with such a small amount of test results. Nevertheless, Table 3.16 also shows the calculated mean values of tests 2-4 in this series. These tests give results comparable to each other.

Fig. 3.23 Web crippling progression in test ITF200-t15-1.

Once again, the webs with a longitudinal stiffener showed no great surprises in their behaviour. The failure mode constituted of the slowly progressing web bulging as shown in Figure 3.25. Here, the initial vertical curvature appears to have a straightforward influence on the failure load, as can be concluded by comparing the curvature values in Table 3.19 with the test results in Table 3.17.

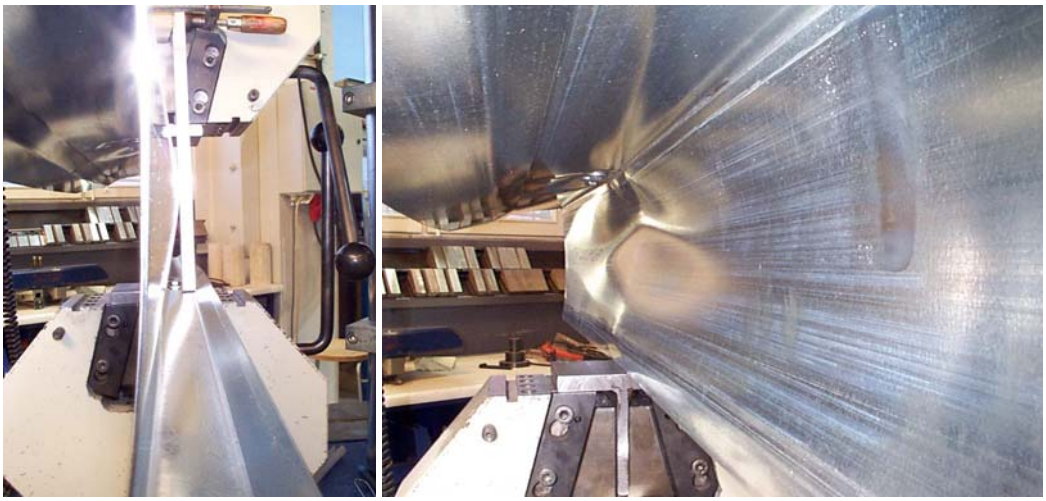

Fig. 3.24 Web crippling progression in test ITF200-t15-2.

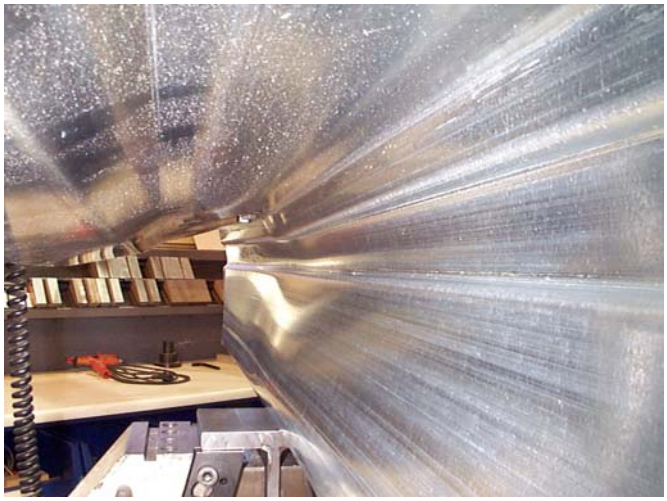

Fig. 3.25 Web crippling in test ITF200R-t15-1.

Table 3.19 Initial vertical web curvature values for specimens in test series ITF200R-t15.

Test specimen	Value of vertical web curvature [mm]
ITF200R-t15-1	-1,98
ITF200R-t15-2	-0,28
ITF200R-t15-3	-1,08

3.4 IOF-tests on single webs

3.4.1 Test arrangement

The second group of tests consisted of three-point bending tests carried out on similar 1200 mm long single-web sections as those used for the ITF-tests above. Two different span lengths were considered, i.e. 600 mm and 1000 mm. Strictly speaking, the shorter span does not correspond to the commonly used definition of IOF-loading (ENV 1993-1-3:1996), which requires the distance between the edges of the loading and support pads to be at least 1.5 times the height of the web. However, the term IOF is used for these tests as well, in order to distinguish them from the ITF-tests. The test type definitions (ITF and IOF) are conventional and based on earlier empirical information and cannot be considered to be physically confining definitions.

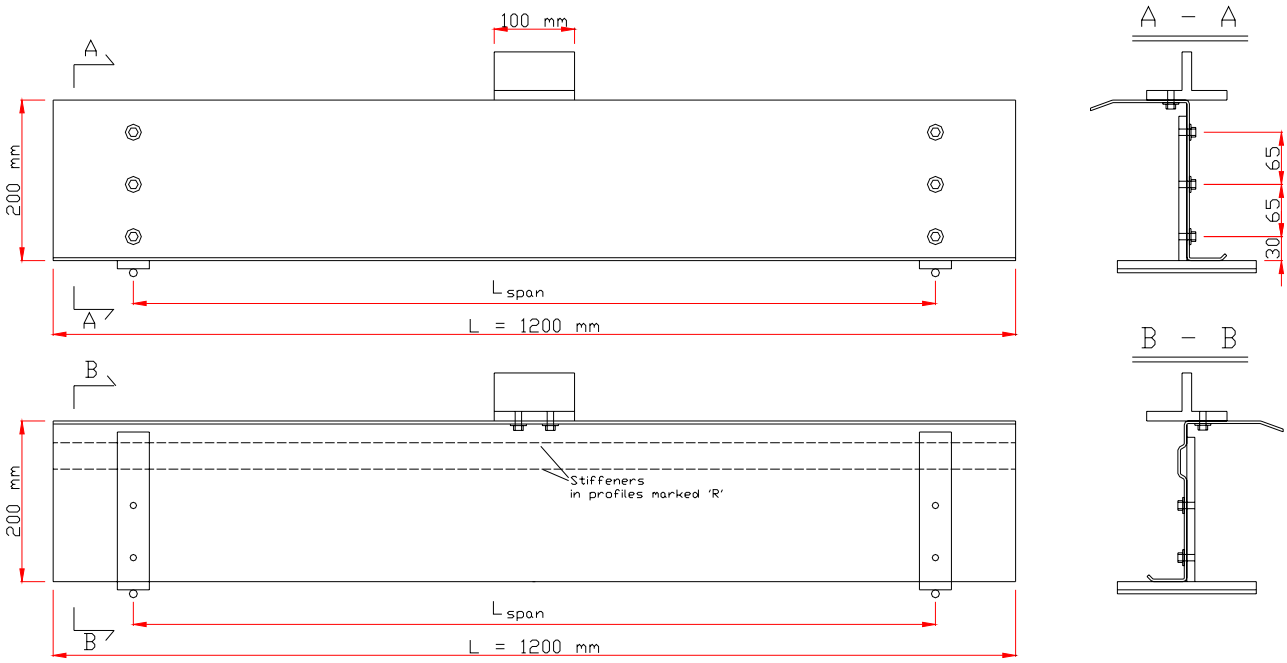

Fig. 3.26 General test set-up for IOF-tests. L_{span} was set as either 600 mm or 1000 mm.

Figure 3.26 shows a sketch of the general test set-up for the IOF-tests. Specially manufactured welded T-sections were used at the supports and at the loading area at mid-span. The support conditions included rollers that allowed the free rotation of the supports. A photograph of test specimen IOF200-t15-S600-1 ready for testing is shown in Figure 3.27. The clamps shown in

the picture were used to keep the specimen in place and removed at the start of the test once the applied load had reached a value of about 8 kN. The clamps were necessary, because the test specimens were not ideally straight.

At the supports, the test specimen was connected with bolts to the vertical support plate as shown in the sketch. Three bolts were used for the flat web sections, while for the longitudinally stiffened web sections, the uppermost bolt had to be omitted because it would have had to be placed at the height of the stiffener. This support arrangement was used in order to have the web crippling phenomena take place at mid-span. The arrangement proved successful and no notable deformations occurred at the support areas. The loading pad connection at mid-span was the same as that used for the ITF-tests. The lateral displacement and the rotation about the longitudinal (x) axis of the specimen was restrained at the connected flanges at mid-span and at the supports.

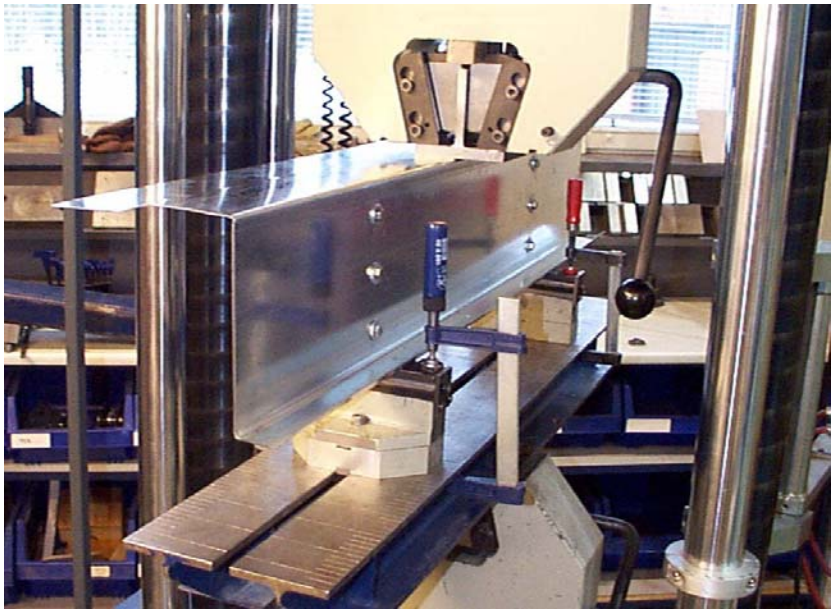

Fig. 3.27 General view of test arrangement.

The nominal cross-sectional dimensions of the specimens were the same as for the ITF-tests (cf. Section 3.3.1). All the same measurements as for the ITF-tests were also carried out before testing and the measured values can be found in ANNEX B.

3.4.2 Test results

The results of all IOF-tests are summarized in Table 3.20 and the results of all individual tests are given in Tables 3.21-3.24 and Figures 3.29-3.51, which show load-displacement curves, load-web crippling curves and photographs of the test specimens.

Table 3.20 Summary of test results from IOF-tests.

Test series	Average F_u [kN]	Average load displacement at F_u [mm]	Average web crippling deformation at F_u [mm]
IOF200-t15-S600	17.14	3.43	2.42
IOF200R-t15-S600	13.99	7.93	7.34
IOF200-t15-S1000	15.91	4.30	2.41
IOF200R-t15-S1000	12.23	8.34	5.92

The presence of a longitudinal stiffener in the web decreases the resistance to concentrated lateral loading by about 18-23 % in these tests. These results and the overall behaviour are quite similar to those seen in the ITF-tests.

It was expected that the ultimate load be reduced when the effect of bending moment comes to play, but this was not necessarily the case in these tests. The mean ultimate load of tests ITF200-t15 was 16.24 kN, less than the 17.14 kN recorded for the corresponding IOF-tests with L_{span} = 600 mm. For L_{span} = 1000 mm, the load was reduced, but not by very much. However, the displacement of the load cylinder was a little less at the time of ultimate load for the IOF-tests.

Similar behaviour can be observed for the IOF-tests on longitudinally stiffened web sections. When L_{span} = 600 mm, the ultimate load is a little higher than it was for the ITF-tests, while the increase of L_{span} to 1000 mm causes a slight decrease in the ultimate load value. The displacement at the time of reaching the ultimate load is again a little higher than for the ITF-tests. The web crippling deformation in the IOF-tests on flat webs is only about half of that recorded for the ITF-tests. For the IOF-tests with longitudinally stiffened webs, the web crippling deformation is not reduced quite as rapidly.

The load and displacement values for all tests were measured directly from the load cylinder using a very short data saving interval. In addition, the vertical displacement of the bottom flange was measured using a gauge (cf. Figure 3.28), which recorded displacement values at

about 0.125 kN intervals. In order to use a spreadsheet to calculate the web crippling deformation, i.e. the difference in vertical displacements between the top and bottom flanges, the data points from the load cylinder data corresponding to the more scarcely recorded data points from the gauge data had to be identified. A special macro was developed in Microsoft Excel (2000) for this purpose. Because the results in Table 3.20 are based on the load cylinder data and the load-displacement and load-web crippling deformation curves in Figures 3.27-3.28, 3.33-3.34, 3.40-3.41 and 3.46-3.47 are based on the gauge data, some minor differences in values may occur. The problem of having to transform the data in order to calculate the web crippling deformation was avoided in the four tests (tests IOF200-t15-S1000-2 and -3 and IOF200R-t15-S1000-2 and -3) that were the last to be carried out by adding a second gauge on the top flange.

Fig. 3.28 Displacement measurement gauge at bottom flange.

The load-displacement curves of IOF-tests with a span of 1000 mm are compared with the corresponding ITF-tests on 200 mm high specimens with t_{nom} = 1.5 mm in ANNEX D and ANNEX E for flat webs and longitudinally stiffened webs, respectively. It can be seen from the graphs that the ITF-curves showing the displacement of the load cylinder at the top flange are located between the IOF-curves for load cylinder displacement and IOF-curves for web

crippling deformation (= the difference between top and bottom flange displacements). The stiffness of the section subjected to ITF-loading thus appears to be slightly higher than when IOF-loading is applied, which is intuitively correct because of the influence of the bending moment.

Test series IOF200-t15-S600

Table 3.21 Results of IOF-tests on 200 mm high unstiffened single webs with t_{nom} = 1.5 mm and L_{span} = 600 mm.

Specimen code	F_u [kN]	Load displacement at F_u [mm]	Web crippling deformation at F_u [mm]
IOF200-t15-S600-1	16.09	3.42	2.44
IOF200-t15-S600-2	17.52	3.52	2.52
IOF200-t15-S600-3	17.43	3.42	2.22
IOF200-t15-S600-4	17.53	3.35	2.52
Mean	**17.14**	**3.43**	**2.42**
Standard deviation	0.705	0.070	0.143

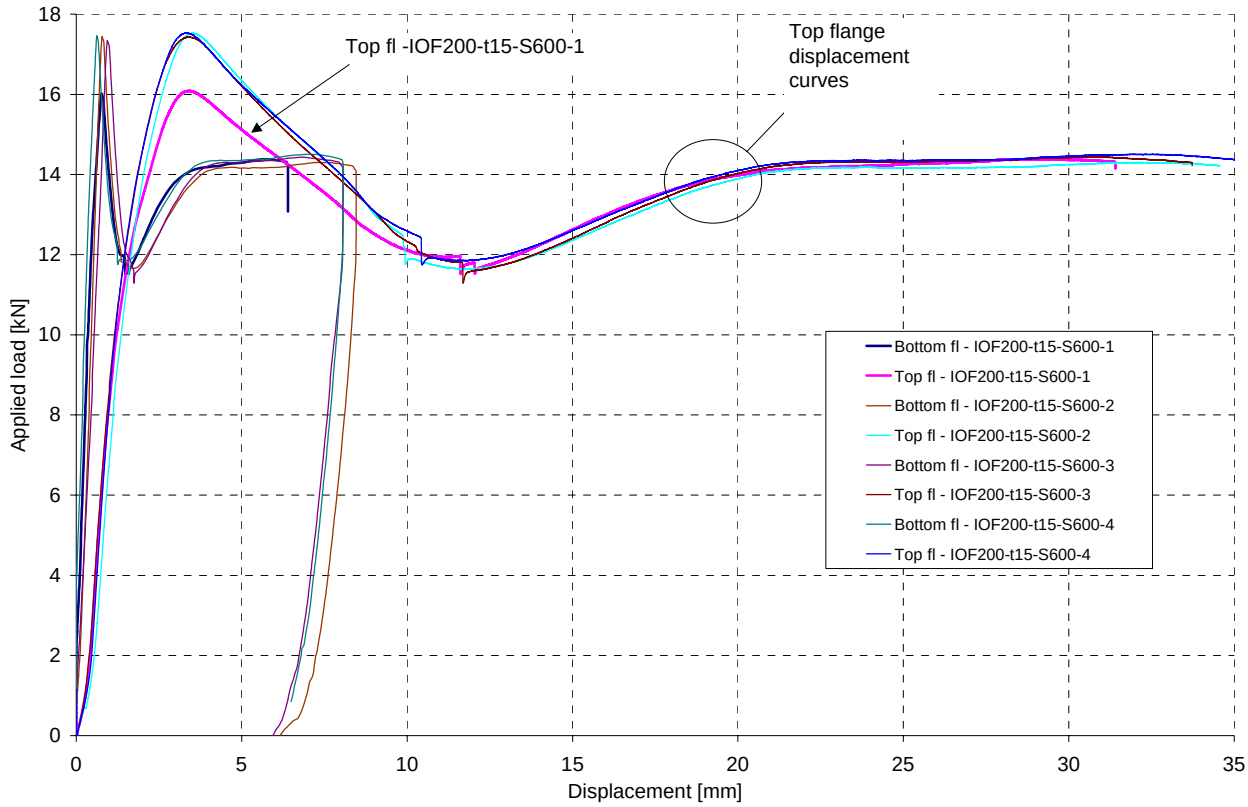

Fig. 3.27a Load-displacement curves for IOF-tests on 200 mm high flat single webs with t_{nom} = 1.5 mm and L_{span} = 600 mm.

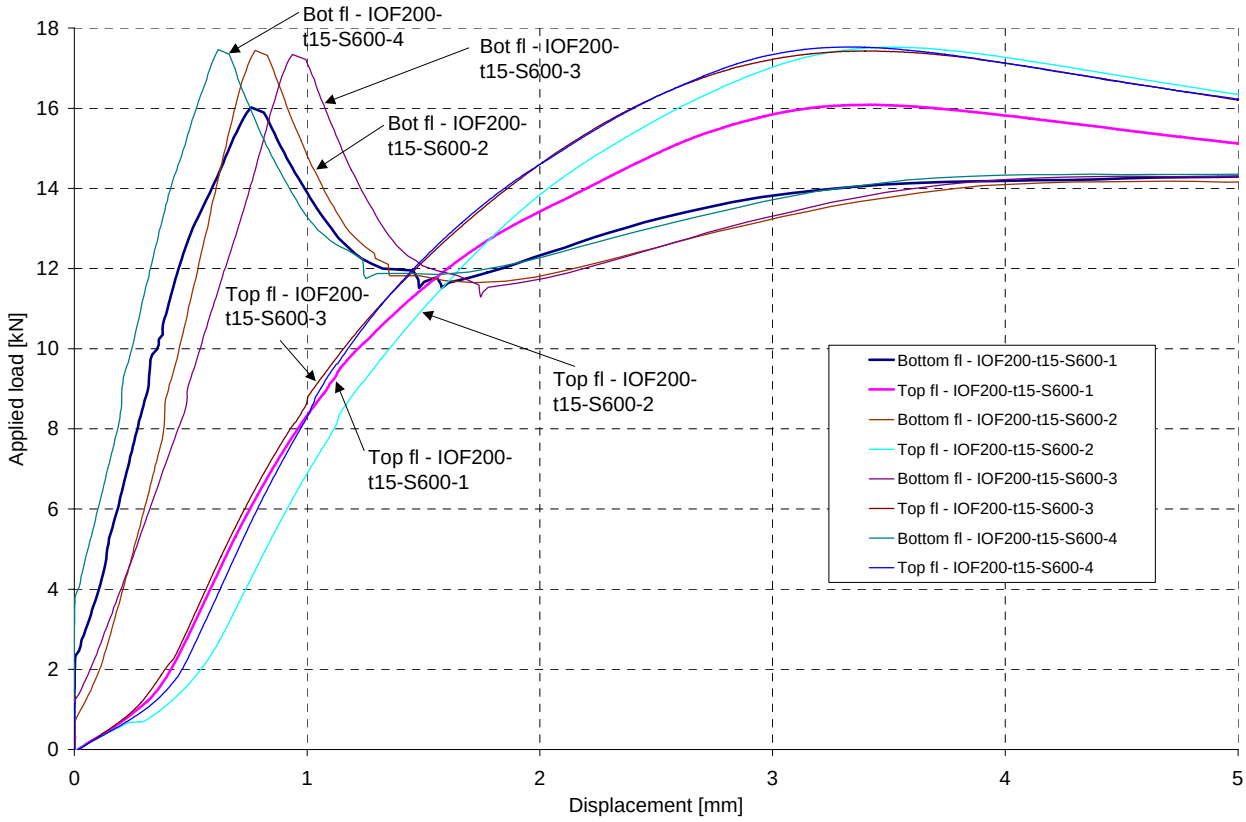

Fig. 3.27b Load-displacement curves for IOF-tests on 200 mm high flat single webs with t_{nom} = 1.5 mm and L_{span} = 600 mm, detailed view of initial phase.

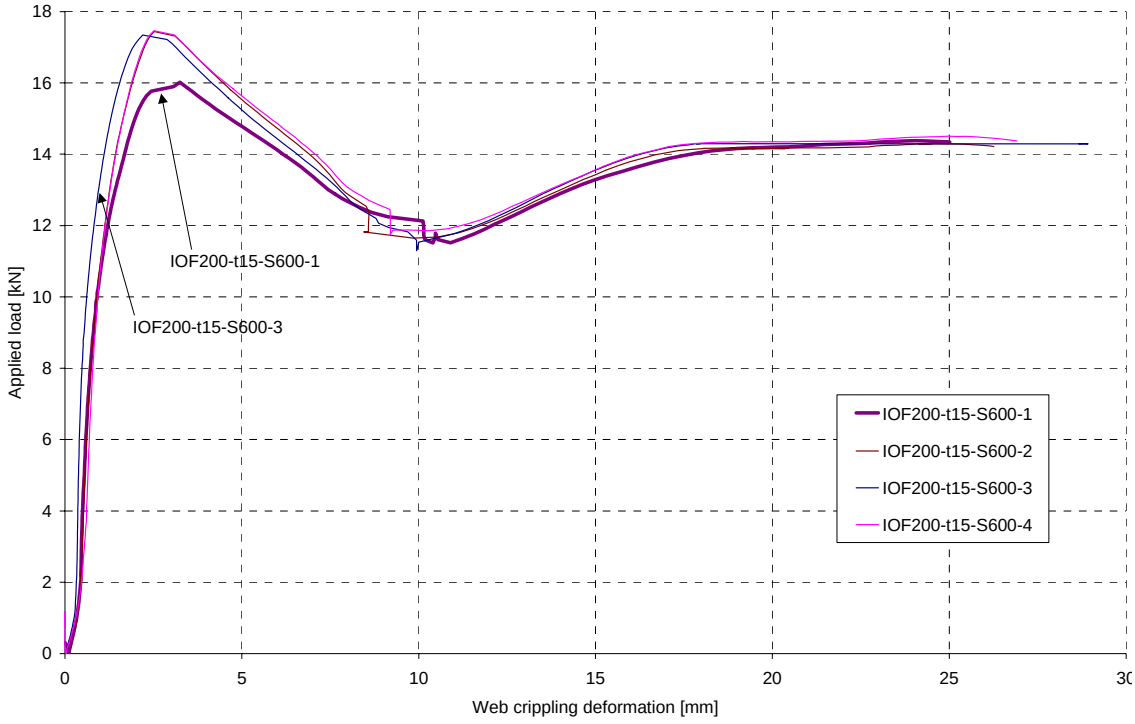

Fig. 3.28 Load-web crippling deformation curves for IOF-tests on 200 mm high flat single webs with t_{nom} = 1.5 mm and L_{span} = 600 mm.

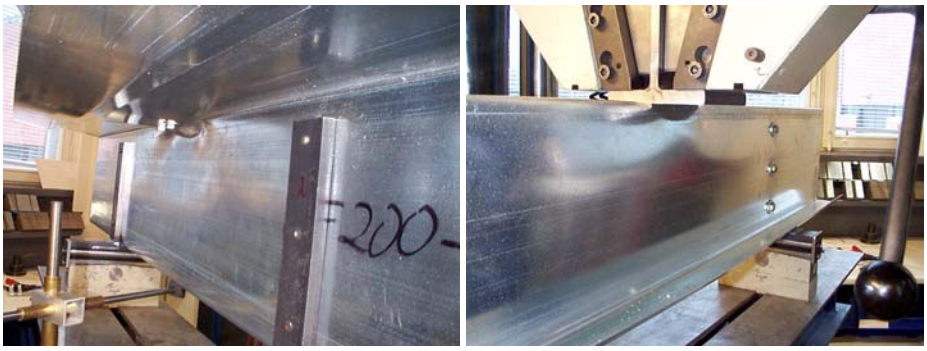

Fig. 3.29 Deformations in specimen IOF200-t15-S600-1 at load $F = F_u$, views from left and right side.

Fig. 3.30 Deformations in specimen IOF200-t15-S600-1 at time when top flange displacement is equal to 10 mm, views from left and right side.

Fig. 3.31 Deformations in specimen IOF200-t15-S600-1 at time when top flange displacement is equal to 20 mm, views from left and right side.

Fig. 3.32 Deformations in specimen IOF200-t15-S600-1 at time when top flange displacement is equal to 30 mm, views from left and right side.

Test series IOF200R-t15-S600

Table 3.22 Results of IOF-tests on 200 mm high longitudinally stiffened single webs with t_{nom} = 1.5 mm and L_{span} = 600 mm.

Specimen code	F_u [kN]	Load displacement at F_u [mm]	Web crippling deformation at F_u [mm]
IOF200R-t15-S600-1	13.99	8.01	7.89
IOF200R-t15-S600-2	13.93	8.01	6.23
IOF200R-t15-S600-3	14.05	7.77	7.90
Mean	**13.99**	**7.93**	**7.34**
Standard deviation	0.060	0.138	0.963

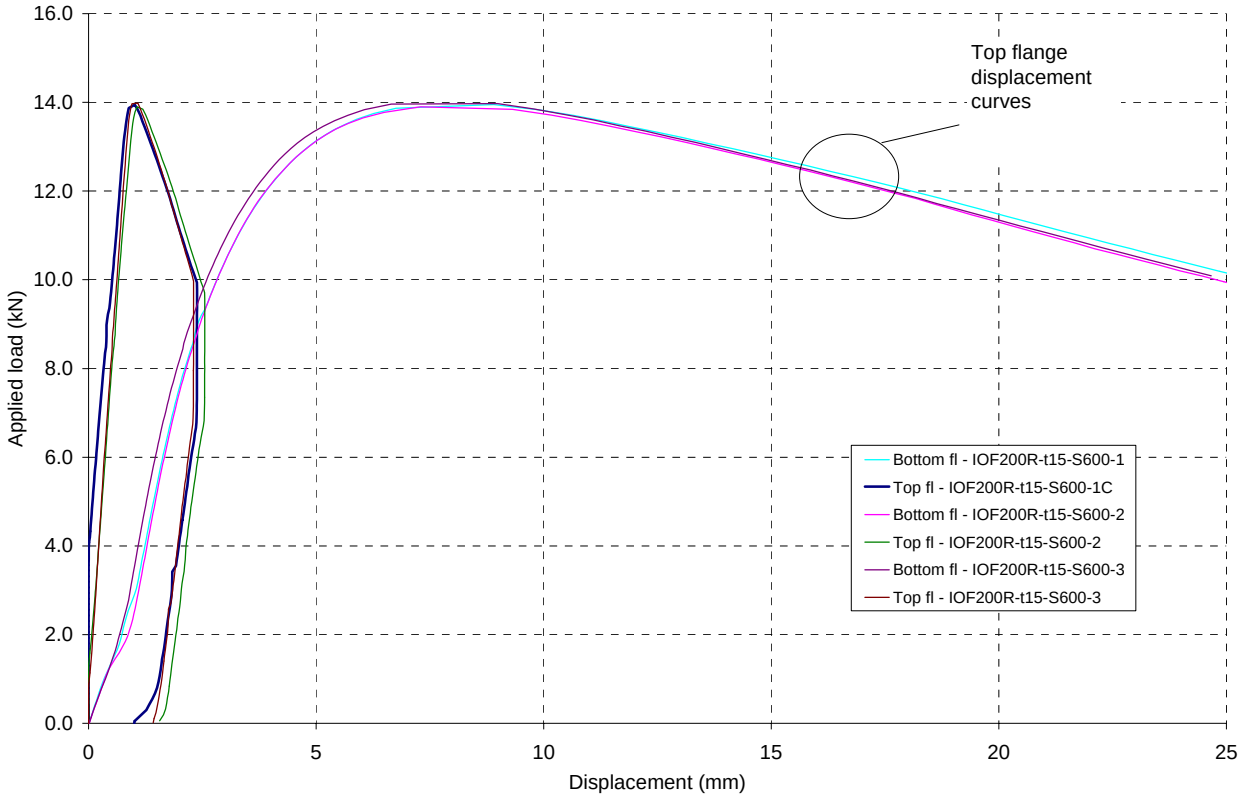

Fig. 3.33 Load-displacement curves for IOF-tests on 200 mm high longitudinally stiffened single webs with t_{nom} = 1.5 mm and L_{span} = 600 mm.

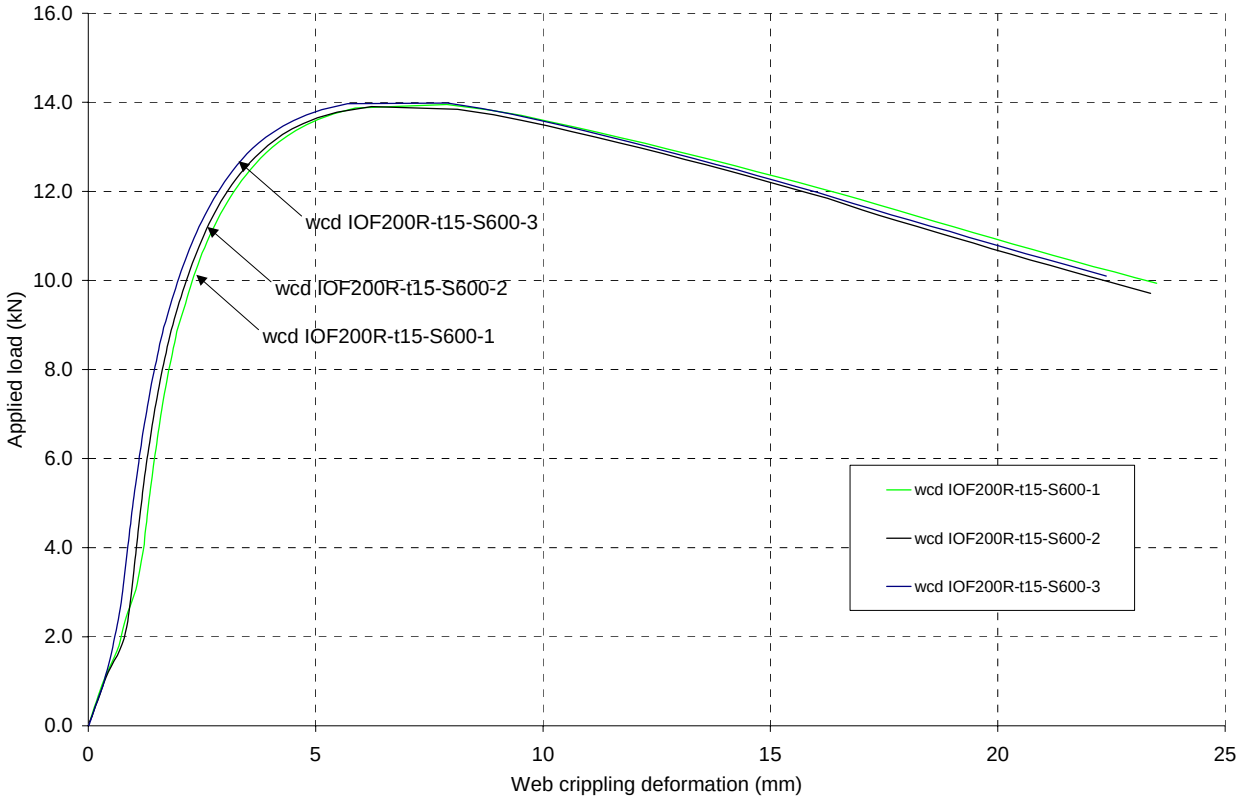

Fig. 3.34 Load-web crippling deformation curves for IOF-tests on 200 mm high longitudinally stiffened single webs with t_{nom} = 1.5 mm and L_{span} = 600 mm.

Fig. 3.35 Deformations in specimen IOF200R-t15-S600-1 at load $F = F_u$, views from left and right side.

Fig. 3.36 Deformations in specimen IOF200R-t15-S600-1 at time when top flange displacement is equal to 15 mm, views from left and right side.

Fig. 3.37 Deformations in specimen IOF200R-t15-S600-1 at time when top flange displacement is equal to 20 mm, views from left and right side.

Fig. 3.38 Deformations in specimen IOF200R-t15-S600-1 at time when top flange displacement is equal to 25 mm, views from left and right side.

Fig. 3.39 Deformations in specimen IOF200R-t15-S600-1 at time when top flange displacement is equal to 20 mm, axial view from end of beam.

Test series IOF200-t15-S1000

Table 3.23 Results of IOF-tests on 200 mm high unstiffened single webs with t_{nom} = 1.5 mm and L_{span} = 1000 mm.

Specimen code	F_u [kN]	Load displacement at F_u [mm]	Web crippling deformation at F_u [mm]
IOF200-t15-S1000-1	15.80	4.31	2.29
IOF200-t15-S1000-2	16.06	4.34	2.48
IOF200-t15-S1000-3	15.85	4.24	2.46
Mean	**15.91**	**4.30**	**2.41**
Standard deviation	0.138	0.050	0.104

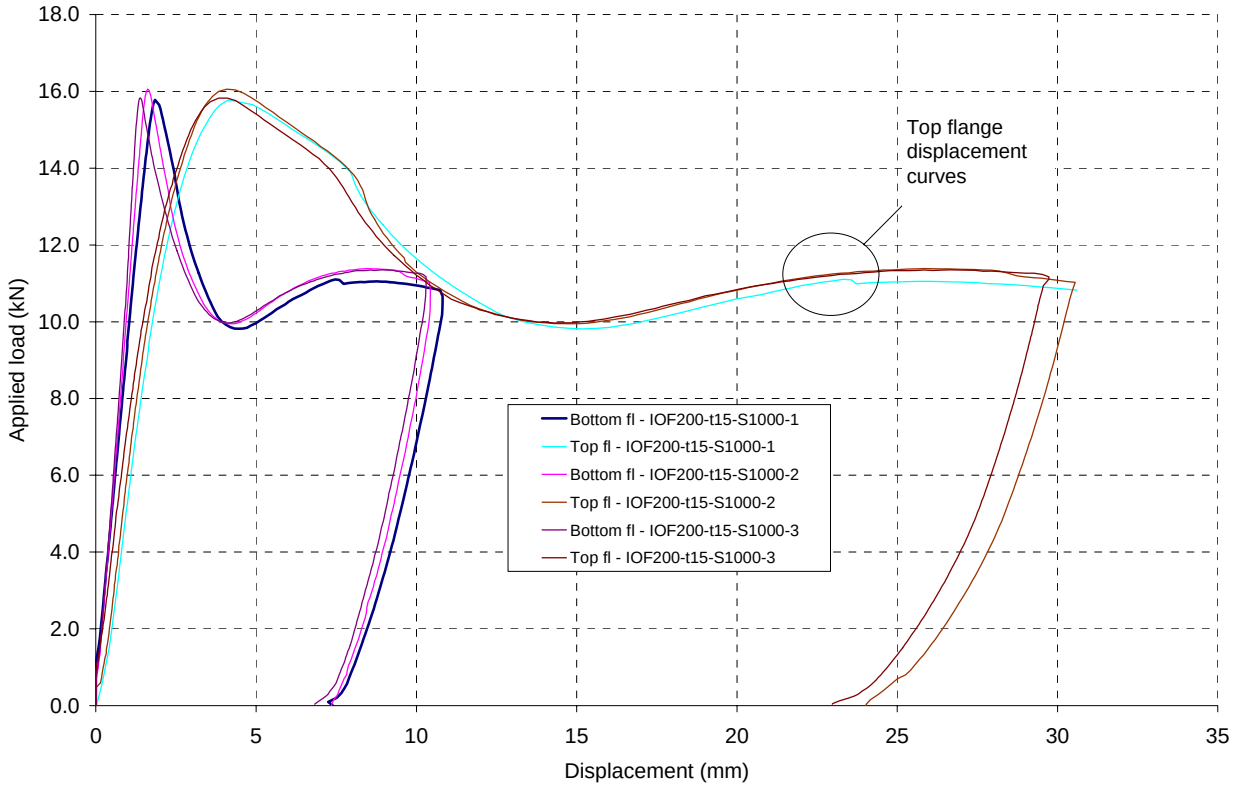

Fig. 3.40a Load-displacement curves for IOF-tests on 200 mm high flat single webs with t_{nom} = 1.5 mm and L_{span} = 1000 mm.

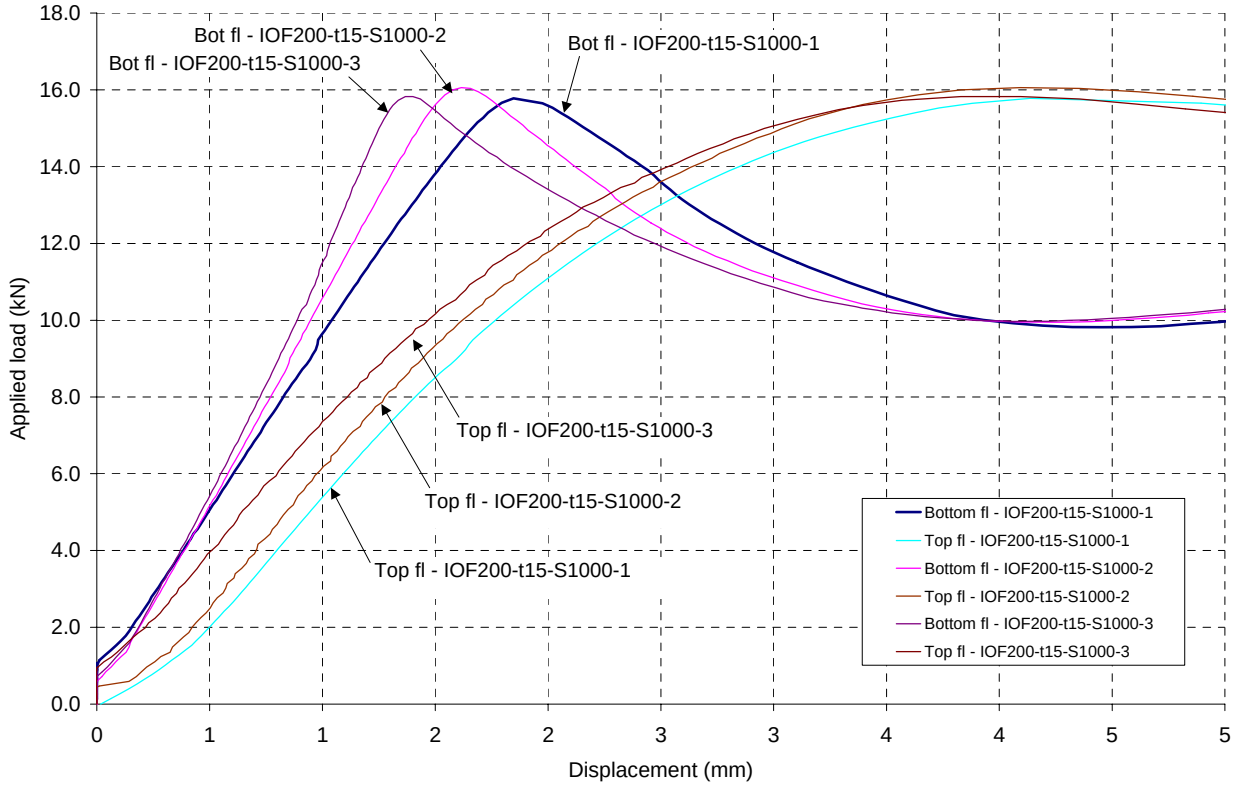

Fig. 3.40b Load-displacement curves for IOF-tests on 200 mm high flat single webs with t_{nom} = 1.5 mm and L_{span} = 1000 mm, detailed view of initial phase.

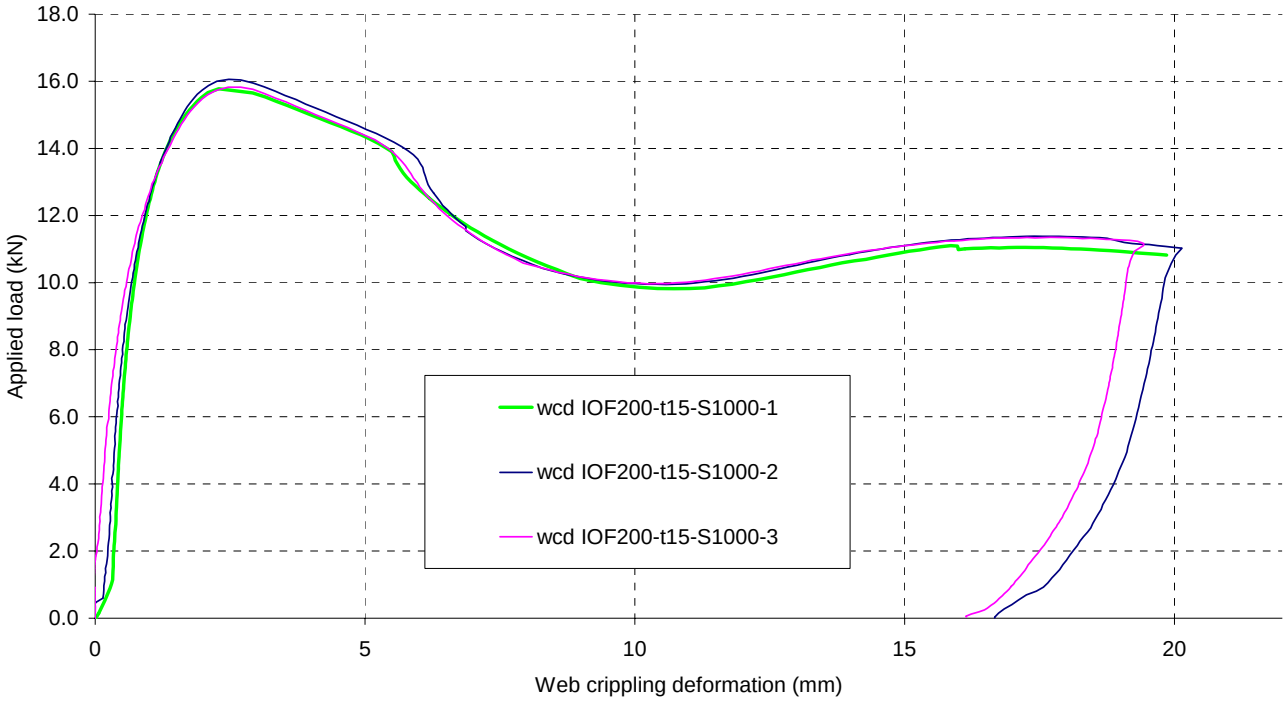

Fig. 3.41 Load-web crippling deformation curves for IOF-tests on 200 mm high flat single webs with t_{nom} = 1.5 mm and L_{span} = 1000 mm.

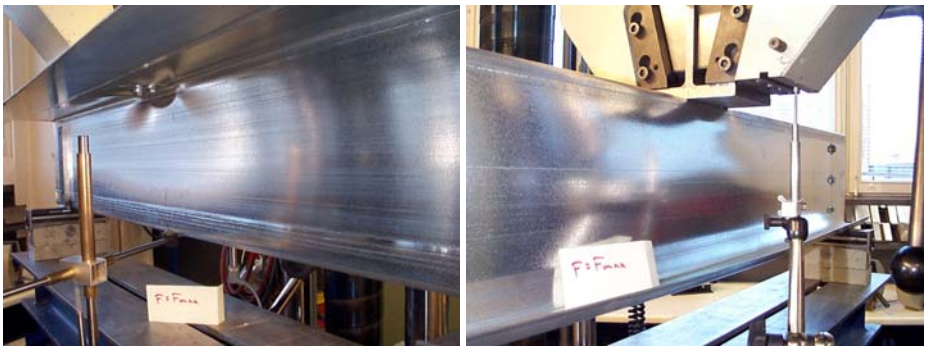

Fig. 3.42 Deformations in specimen IOF200-t15-S1000-2 at load $F = F_u$, views from left and right side.

Fig. 3.43 Deformations in specimen IOF200-t15-S1000-2 at time when top flange displacement is equal to 10 mm, views from left and right side.

Fig. 3.44 Deformations in specimen IOF200-t15-S1000-2 at time when top flange displacement is equal to 20 mm, views from left and right side.

Fig. 3.45 Deformations in specimen IOF200-t15-S1000-2 at time when top flange displacement is equal to 30 mm, views from left and right side.

Test series IOF-200R-t15-S1000

Table 3.24 Results of IOF-tests on 200 mm high longitudinally stiffened single webs with t_{nom} = 1.5 mm and L_{span} = 1000 mm.

Specimen code	F_u [kN]	Load displacement at F_u [mm]	Web crippling deformation at F_u [mm]
IOF200R-t15-S1000-1	12.03	9.22	6.56
IOF200R-t15-S1000-2	12.39	7.76	6.05
IOF200R-t15-S1000-3	12.27	8.03	5.15
Mean	**12.23**	**8.34**	**5.92**
Standard deviation	0.186	0.777	0.716

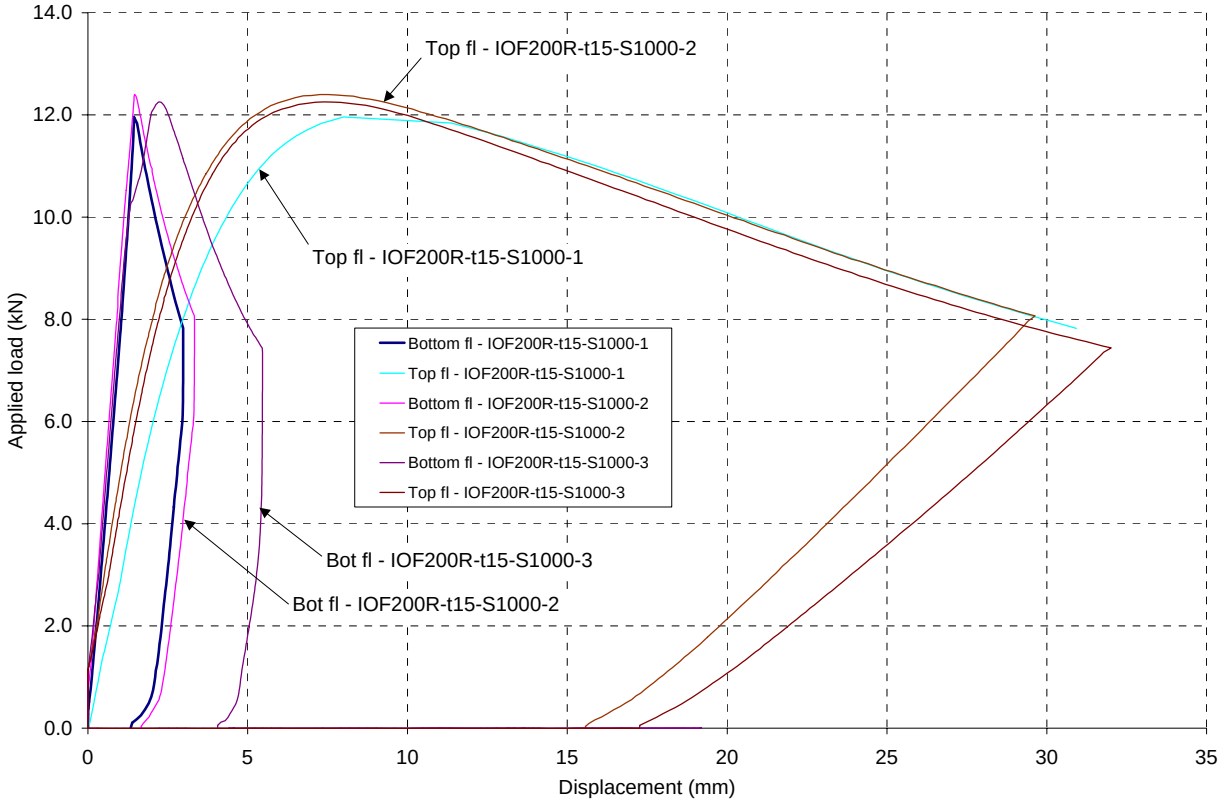

Fig. 3.46 Load-displacement curves for IOF-tests on 200 mm high longitudinally stiffened single webs with t_{nom} = 1.5 mm and L_{span} = 1000 mm.

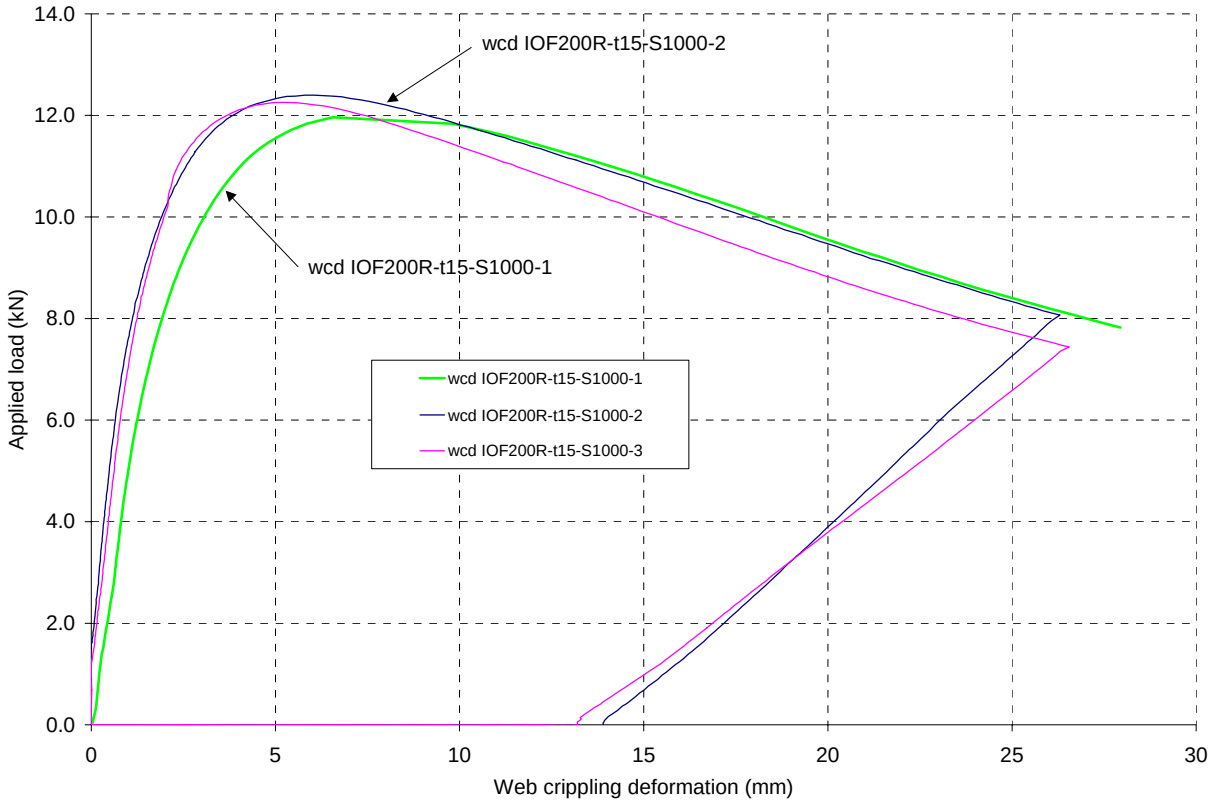

Fig. 3.47 Load-web crippling deformation curves for IOF-tests on 200 mm high longitudinally stiffened single webs with t_{nom} = 1.5 mm and L_{span} = 1000 mm.

Fig. 3.48 Deformations in specimen IOF200R-t15-S1000-1 at load $F = F_u$, views from left side, beam end and right side.

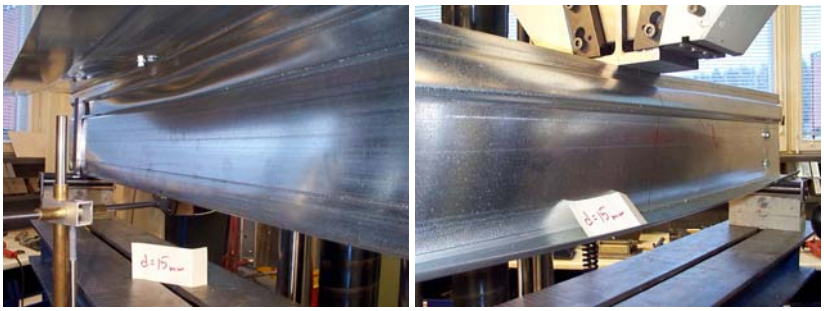

Fig. 3.49 Deformations in specimen IOF200R-t15-S1000-1 at time when top flange displacement is equal to 15 mm, views from left and right side.

Fig. 3.50 Deformations in specimen IOF200R-t15-S1000-1 at time when top flange displacement is equal to 20 mm, views from left and right side.

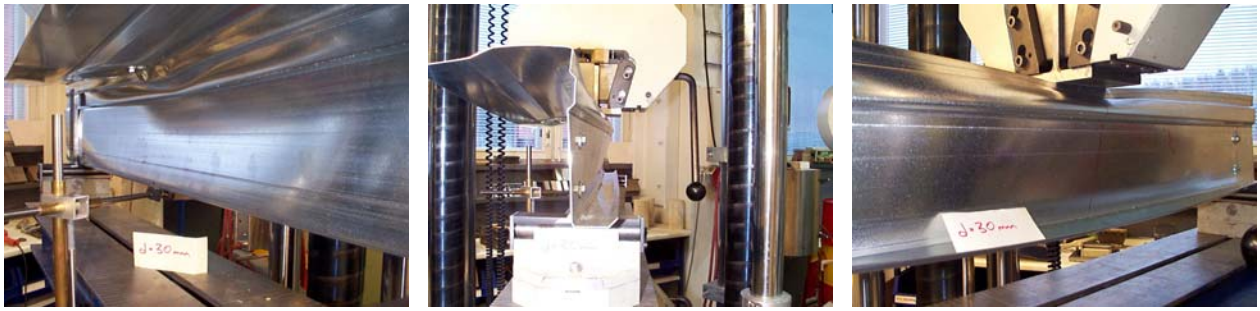

Fig. 3.51 Deformations in specimen IOF200R-t15-S1000-1 at time when top flange displacement is equal to 30 mm, views from left side, beam end and right side.

3.5 IOF-tests on built-up sections

3.5.1 Test arrangement

The short-span bending tests carried out on built-up cassette sections were similar in arrangement to the IOF-tests on single webs. Due to the greater width of the test pieces, the tests were moved away from the Roell+Koerthaus testing machine to a separate hydraulic loading cylinder as shown in Figure 3.52. The loading beam was tied to the displacement cylinders at the sides to obtain forced displacement control.

Fig. 3.52 General view of test set-up for S-IOF-tests on built-up specimens.

The general test arrangement, support conditions and naming conventions for the webs are shown in Figure 3.53. A 45 mm thick piece of wood was cut to shape and placed tightly between the two sets of webs at the supports as shown in Figures 3.52 and 3.53. The webs were connected to the piece of wood using wood screws through drilled holes. A 35 mm wide

steel batten connected with screws to the piece of wood was placed between the bottom flanges and the 30 mm diameter steel tube at the supports. The adjacent webs were furthermore connected to one another using self-drilling screws at 250 mm intervals as shown in Figure 3.53. The top flange was connected with screws to the loading beam on both sides of the webs at 30 mm distances from the mid-line of the web. The lateral displacement of the specimen was thus prevented during the test, but the rollers allowed for free longitudinal displacement at the supports.

The load was applied using displacement control at a speed of 2 mm/minute. The vertical displacements at top and bottom flange locations of both sets of webs were measured using four separate displacement gauges. The load value was recorded directly from the load cylinder.

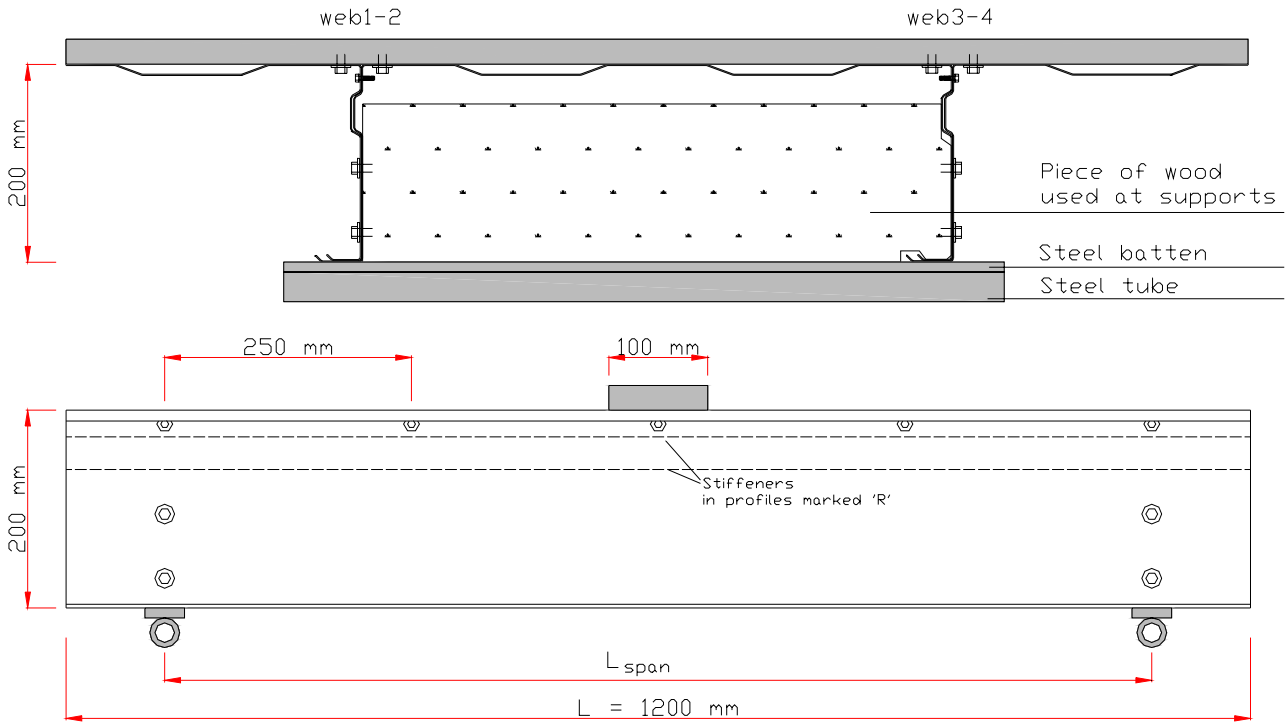

Fig. 3.53 General test set-up for S-IOF-tests. L_{span} was set as 1000 mm.

All the most important cross-sectional dimensions were measured as for the earlier tests as shown in Figures 3.1, 3.2 and 3.5. In addition, the total widths b_1, b_2 and b_3 of the different parts of the top flange were measured. The vertical curvatures of the four webs were measured at mid-span using the sign rules shown in Figure 3.54. The measurements are given in ANNEX B.

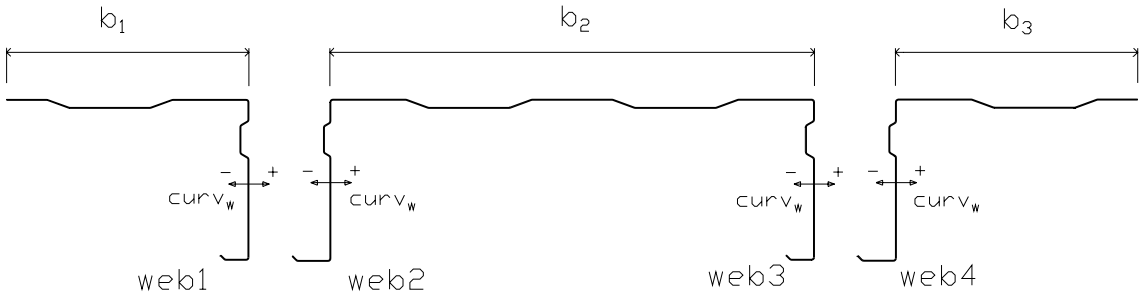

Fig. 3.54 Additional measurements for built-up specimens.

3.5.2 Test results

3.5.2.1 Test series S-IOF200-t15-S1000

The results of test series S-IOF200-t15-S1000 on built-up specimens with flat web sections are summarized in Table 3.25, Figure 3.55 (average top and bottom flange displacement curves) and Figure 3.56 (average web crippling deformation curves).

Table 3.25 Results of S-IOF-tests on 200 mm high built-up specimens with flat webs and t_{nom} = 1.5 mm and L_{span} = 1000 mm.

Specimen code	F_u [kN]	Load displacement at F_u [mm]	Web crippling deformation at F_u [mm]
S-IOF200-t15-S1000-1	84.06	6.30	2.28
S-IOF200-t15-S1000-2	77.83	7.34	3.43
S-IOF200-t15-S1000-3	81.67	7.68	3.41
Mean	**81.19**	**7.11**	**3.04**
Standard deviation	3.143	0.719	0.658

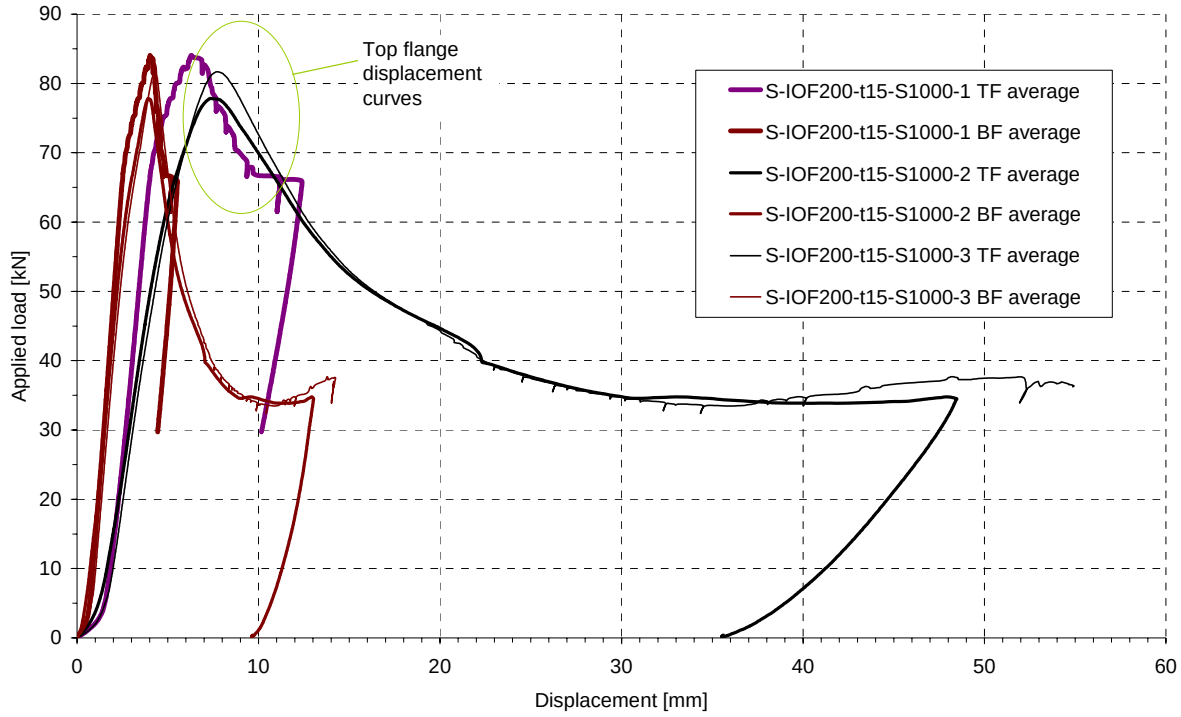

Fig. 3.55 Calculated average top and bottom flange displacement curves for test series S-IOF200-t15-S1000.

The ultimate load reached in the present test series S-IOF200-t15-S1000 was 81.19 kN on average, which is equal to 5.1 times the ultimate load reached in test series IOF200-t15-S1000 on single flat webs (15.91 kN), although there were only 4 similar webs in the present test series. This shows that the adjacent webs do give support to each other and that the total

resistance of the built-up structure against concentrated loads is higher than the sum of the individual web resistances. The failure load calculated per web was thus increased by a factor k_F = 5.1 / 4 = 1.28. This and similar factors k_{TF} *and* k_{WC} for top flange displacement and web crippling deformation, respectively, are calculated in Table 3.26.

Table 3.26 Factors *k* for comparison of flat single webs with built-up structures.

	S-IOF200-t15-S1000	IOF200-t15-S1000	Ratio *k*
Ultimate load F_u per web	81.19 / 4 = 20.30	15.91	k_F = 20.30 / 15.91 = 1.28
Top flange displacement at F_u	7.11	4.30	k_{TF} = 7.11 / 4.30 = 1.65
Web crippling deformation at F_u	3.04	2.41	k_{WC} = 3.04 / 2.41 = 1.26

The top flange displacement corresponding to the ultimate load in the present test series S-IOF200-t15-S1000 was 7.11 mm, which is 1.65 times the corresponding value (4.30 mm) for test series IOF200-t15-S1000. Because this factor is higher than the relative increase of the ultimate load, it can be concluded there was relatively more flexibility per web in the built-up structure than in the single-web specimen. However, the web crippling deformation corresponding to the ultimate load was 3.04 mm for the built-up sections, which is only 1.26 times the corresponding value (2.41 mm) for test series IOF200-t15-S1000. This factor is close to the relative increase of the ultimate load (factor 1.275), so the stiffness per web is about the same in both cases.

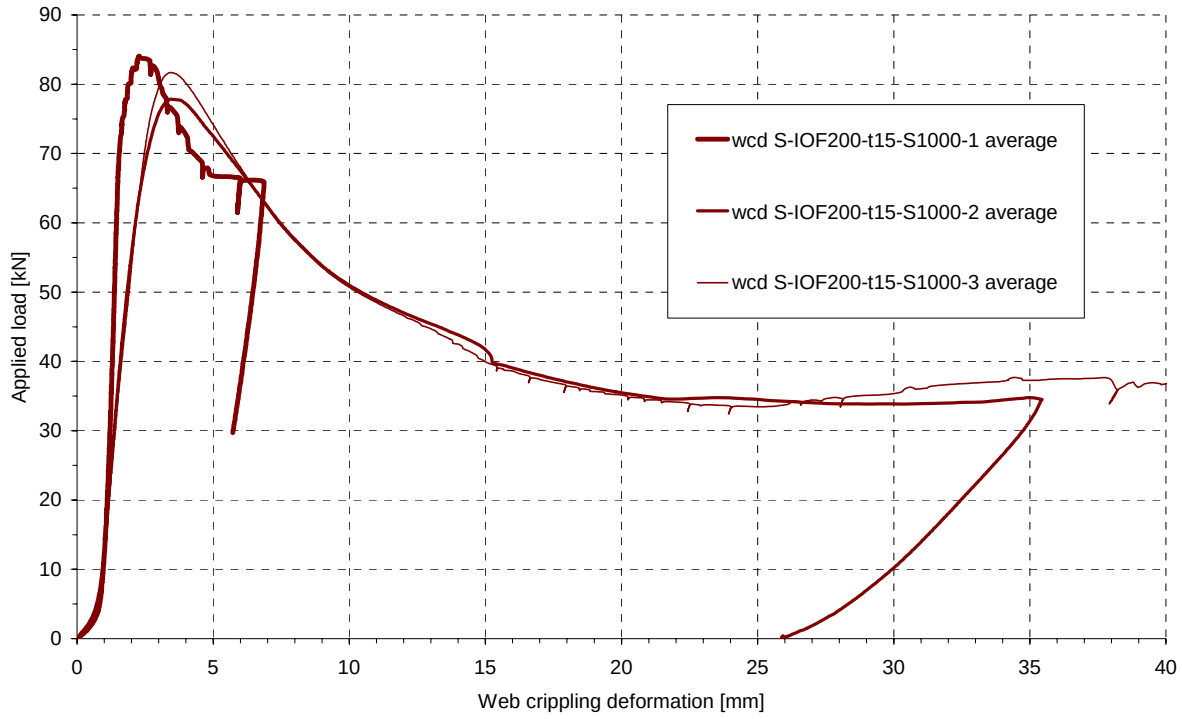

Fig. 3.56 Calculated average web crippling deformation curves for test series S-IOF200-t15-S1000.

The deformation modes were generally quite similar to those observed in test series IOF200-t15-S1000. This is demonstrated in the photos under the sections on individual tests (see below).

Test S-IOF200-t15-S1000-1

Test S-IOF200-t15-S1000-1 was the first to be carried out in this test series. Some problems were experienced during this test concerning both the displacement measurements and the forced displacement control. When the test was first begun, the displacement gauges did not start measuring correctly and the applied load reached a value of about 49 kN before the test was interrupted. After the load was brought back down, a small residual displacement remained in the specimen due mostly to the closure of gaps and other tolerances present in the built-up specimen. No noticeable plastic deformations could be observed in the web or at the loading and support areas. When the test was restarted, the displacements were reset to zero as seen in Figure 3.57. However, it is likely that this unplanned preloading of the specimen had some influence on the final results especially regarding the displacement values. The ultimate load reached in the test, however, is close to the values obtained in the other two similar tests. It can be seen in Figures 3.55 and 3.56 that the stiffness of test specimen S-IOF200-t15-S1000-1 was a little higher before reaching the ultimate load than for the other specimens.

Figure 3.57 shows the top and bottom flange displacement curves for the different webs and their calculated averages. Figure 3.58 shows the web crippling deformation curves and their average calculated on the basis of the measurements. It can be seen that the deformations in web1-2 were throughout larger than those in web3-4. This is mainly due to the failure of the loading beam to distribute the load evenly on both sets of webs. When web1-2 started to give in, the beam became inclined and practically started to rotate around the top flange intersection of web3-4. This is demonstrated by the large differences in deformations between the two sets of webs as seen in Figure 3.57.

For the reasons explained above, the results of test S-IOF200-t15-S1000-1 should be considered to be suggestive at best. For the remaining five tests on built-up sections, the side

supports of the loading beam were made considerably stronger and the stability of the beam was secured. This can be observed in the symmetry of the displacement-load curves of the remaining tests.

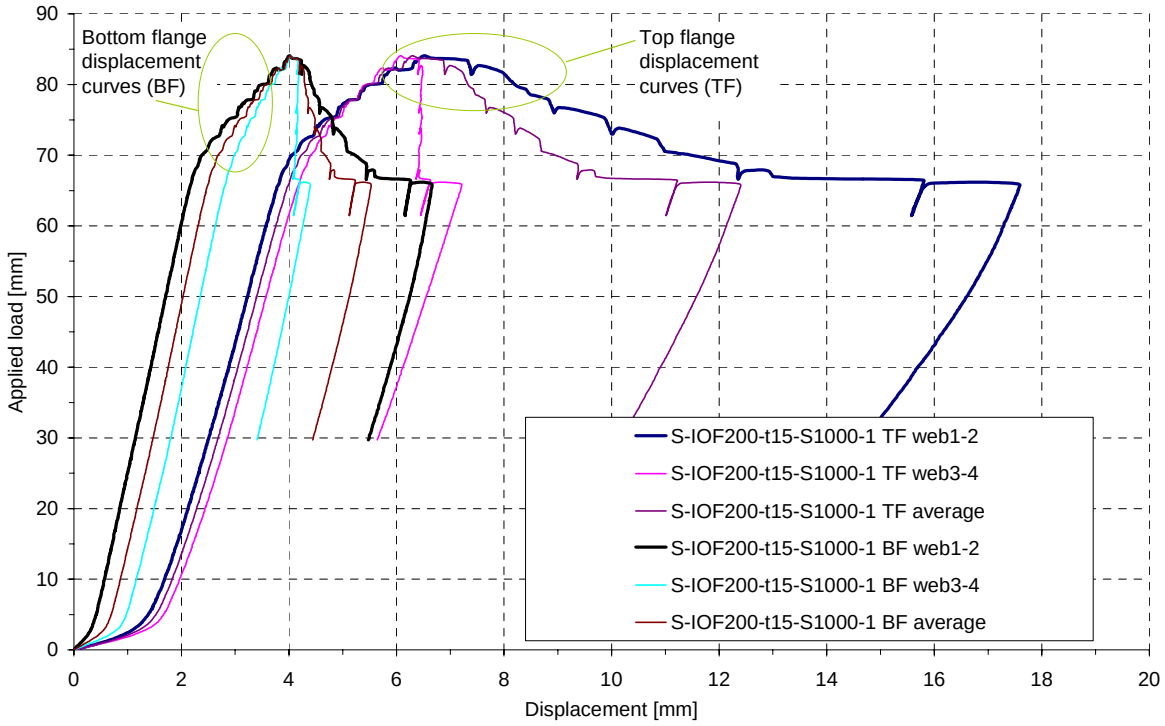

Fig. 3.57 Top and bottom flange displacement curves for test S-IOF200-t15-S1000-1.

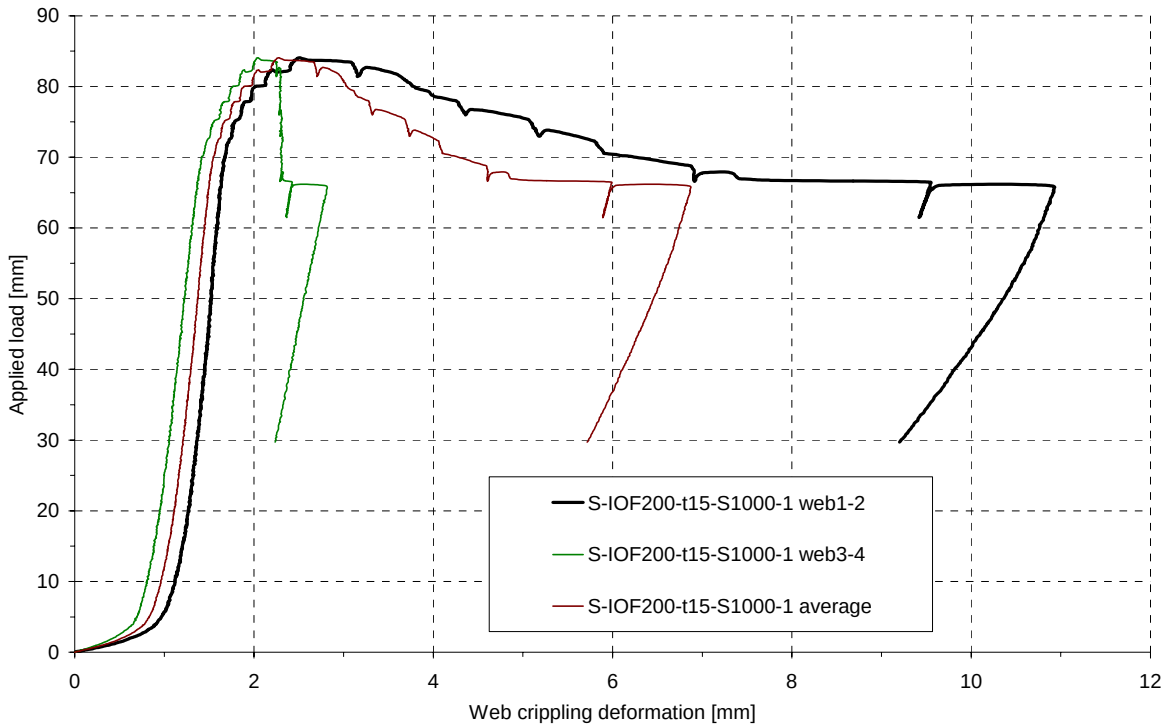

Fig. 3.58 Web crippling deformation curves for test S-IOF200-t15-S1000-1.

Test S-IOF200-t15-S1000-2

Figure 3.59 shows the top and bottom flange displacement curves for the different webs and their calculated averages for test S-IOF200-t15-S1000-2. Figure 3.60 shows the web crippling deformation curves and their average calculated on the basis of the measurements. Figures 3.61-3.63 show photos of the deformations during the test.

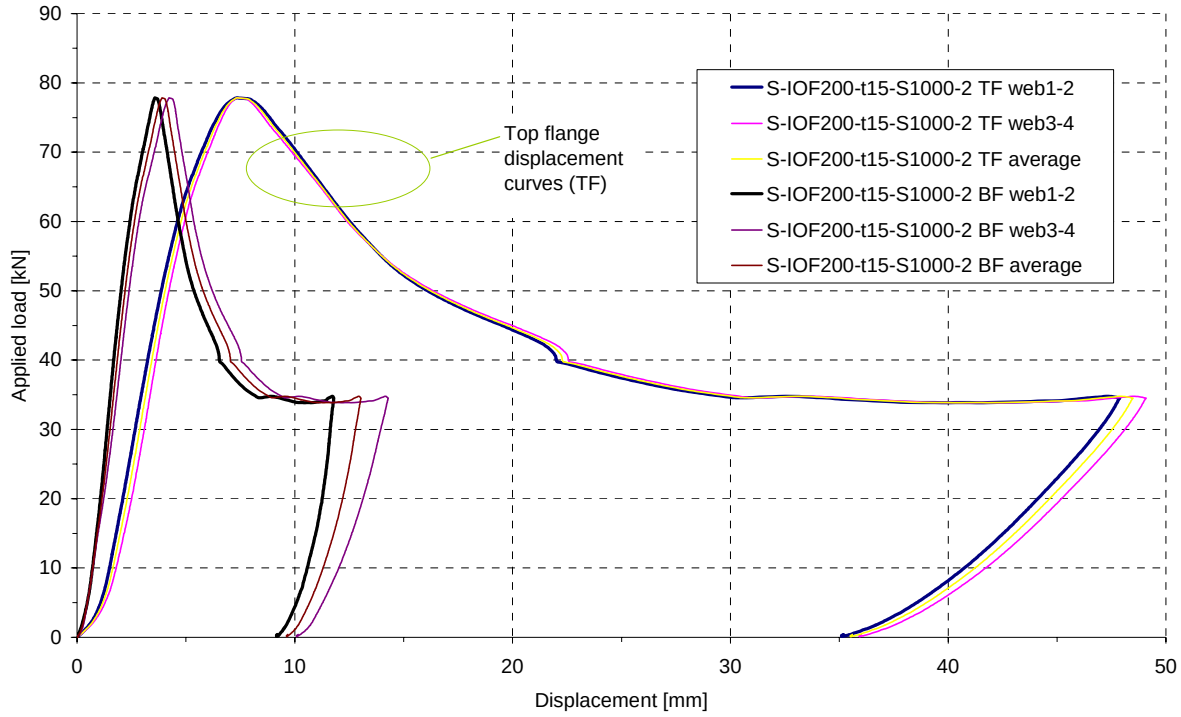

Fig. 3.59 Top and bottom flange displacement curves for test S-IOF200-t15-S1000-2.

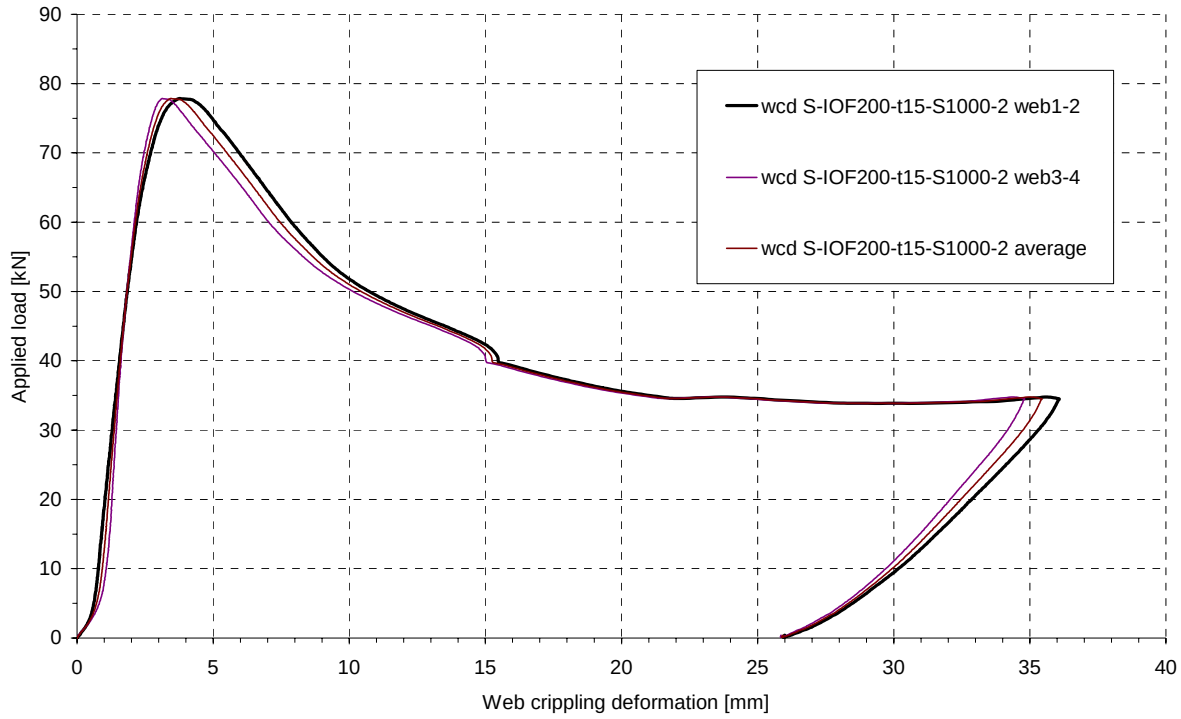

Fig. 3.60 Web crippling deformation curves for test S-IOF200-t15-S1000-2.

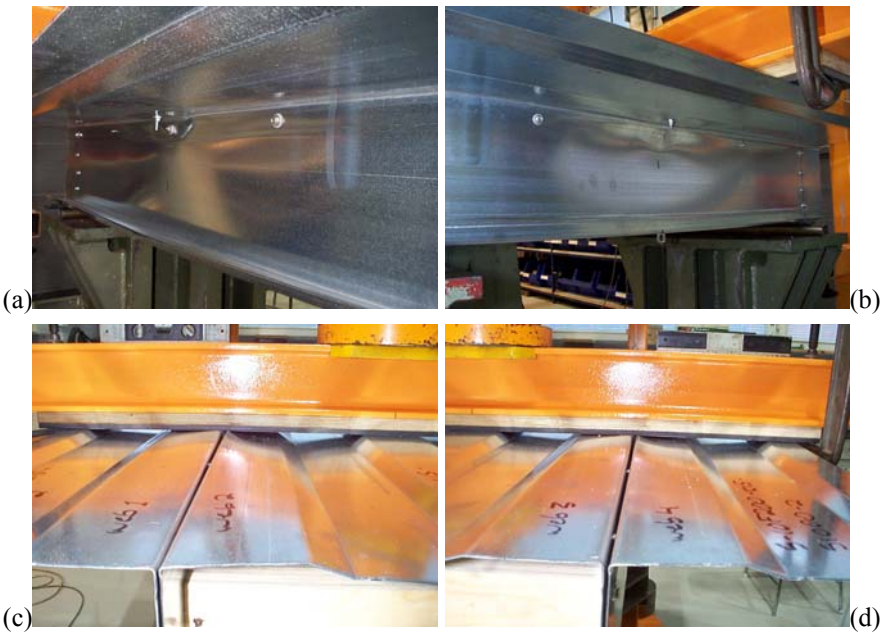

Fig. 3.61 Deformations in test S-IOF200-t15-S1000-2 at load $F = F_u$: web1-2 (a), web3-4 (b), top flange at web1-2 (c), top flange at web3-4 (d).

Fig. 3.62 Deformations in web1-2 in test S-IOF200-t15-S1000-2 at top flange displacements d = 15 mm (left), d = 24 mm (centre) and d = 35 mm (right).

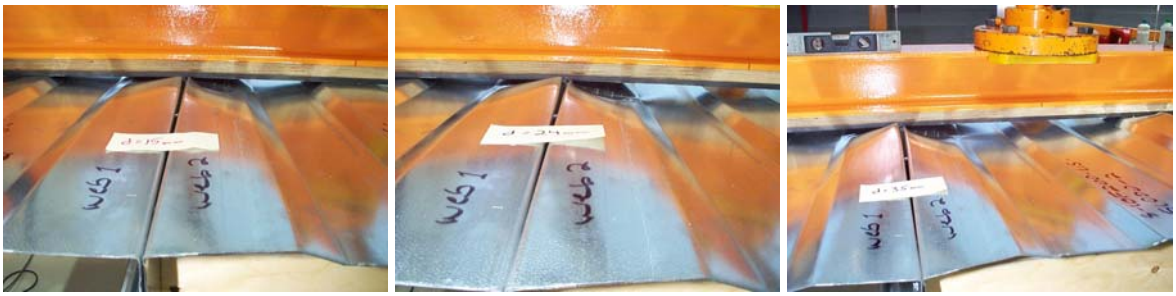

Fig. 3.63 Deformations in top flange above web1-2 in test S-IOF200-t15-S1000-2 at top flange displacements d = 15 mm (left), d = 24 mm (centre) and d = 35 mm (right).

The wide flange experienced some flange curling as can be seen in Figure 3.63. The maximum deflection of the flange in relation to the loading beam was about 20 mm when the displacement of the loading beam was d = 35 mm (photo on the right in Figure 3.63). This shows that having the adjacent webs connected to each other near the wide flange, as explained in Chapter 2, is not able to completely prevent flange curling from taking place, although it probably reduces it.

Test S-IOF200-t15-S1000-3

Figure 3.64 shows the top and bottom flange displacement curves for the different webs and their calculated averages for test S-IOF200-t15-S1000-3. Figure 3.65 shows the web crippling deformation curves and their average calculated on the basis of the measurements. The photos in Figures 3.61-3.63 are demonstrative of the deformations in test S-IOF200-t15-S1000-3 as well.

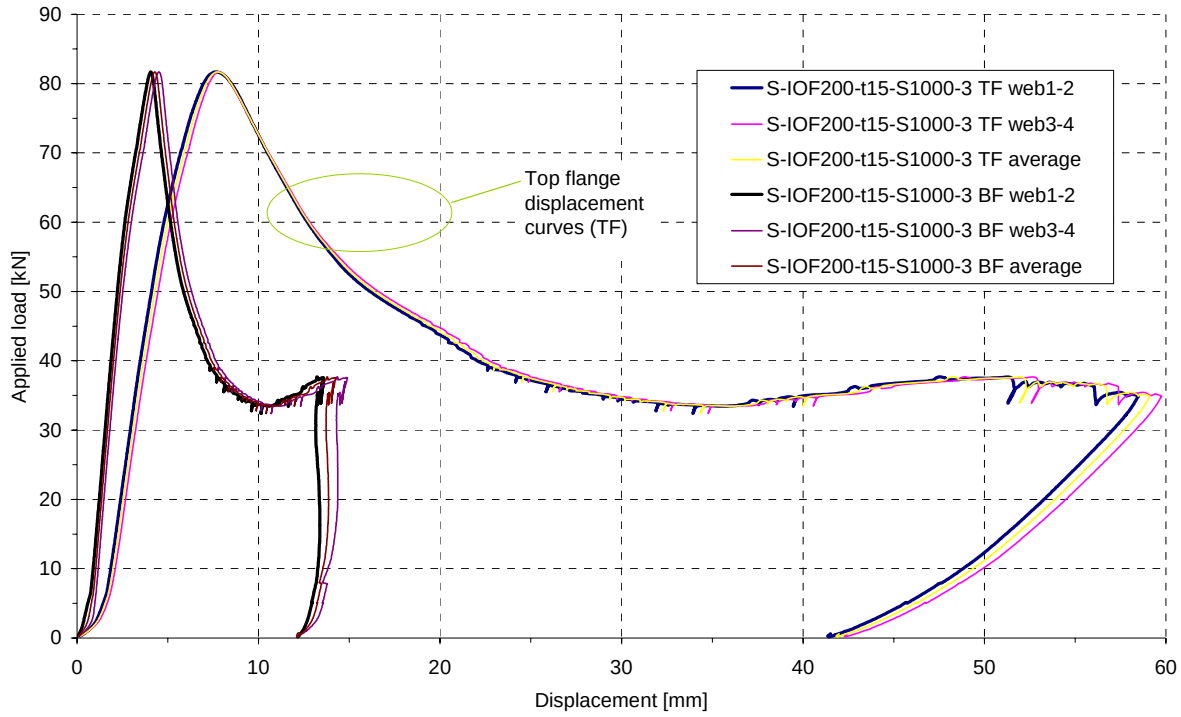

Fig. 3.64 Top and bottom flange displacement curves for test S-IOF200-t15-S1000-3.

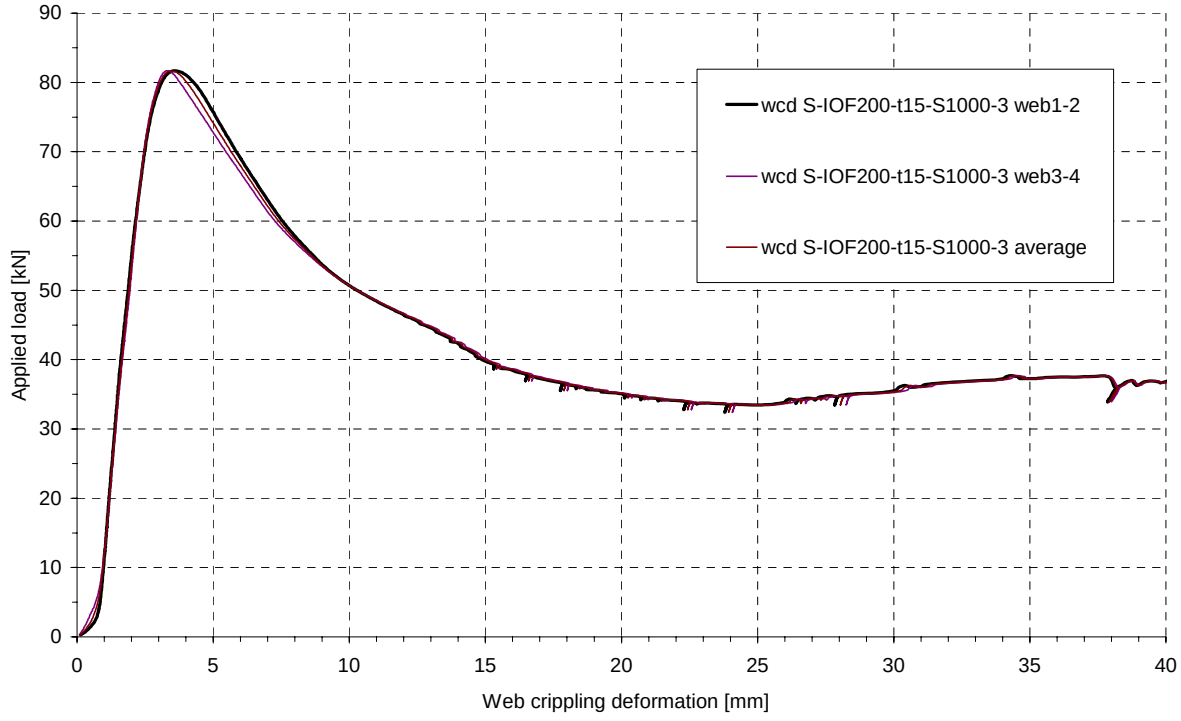

Fig. 3.65 Web crippling deformation curves for test S-IOF200-t15-S1000-3.

Test series S-IOF200R-t15-S1000

The results of test series S-IOF200R-t15-S1000 on built-up specimens with longitudinally stiffened web sections are summarized in Table 3.27, Figure 3.66 (average top and bottom flange displacements curves) and Figure 3.67 (average web crippling deformation curves).

Table 3.27 Results of S-IOF-tests on 200 mm high built-up specimens with longitudinally stiffened webs, t_{nom} = 1.5 mm and L_{span} = 1000 mm.

Specimen code	F_u [kN]	Load displacement at F_u [mm]	Web crippling deformation at F_u [mm]
S-IOF200R-t15-S1000-1	55.68	9.11	5.98
S-IOF200R-t15-S1000-2	54.20	9.52	6.62
S-IOF200R-t15-S1000-3	54.97	10.00	6.71
Mean	**54.95**	**9.54**	**6.44**
Standard deviation	0.740	0.445	0.398

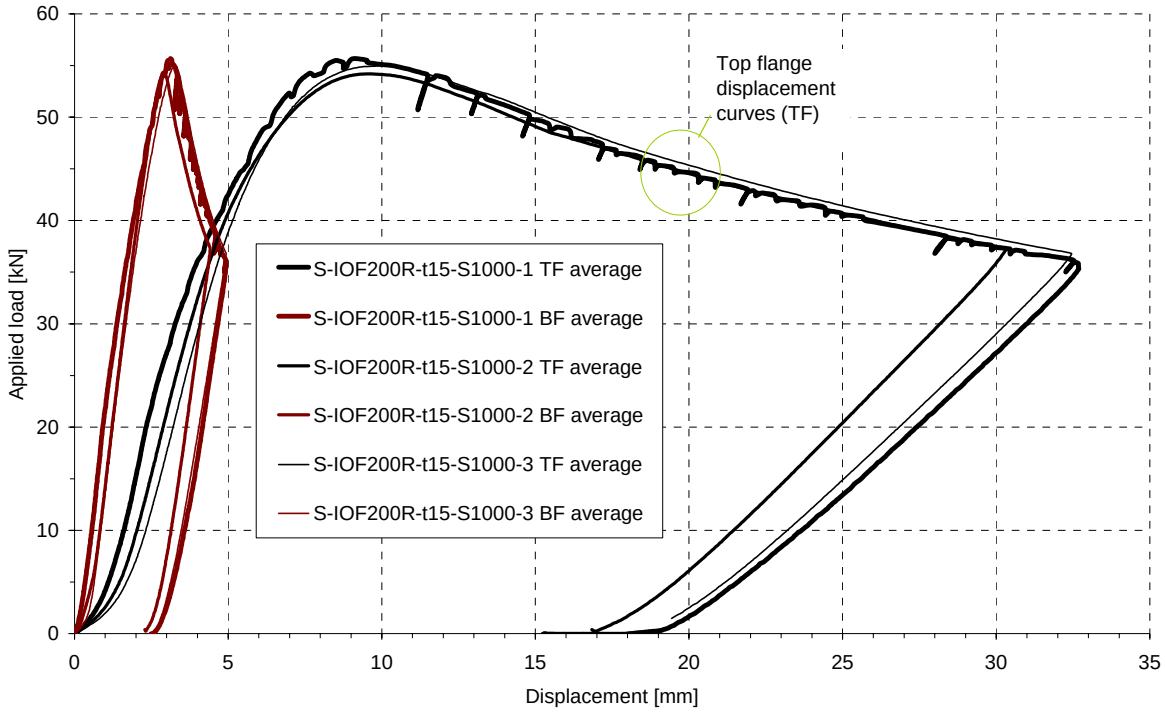

Fig. 3.66 Calculated average top and bottom flange displacement curves for test series S-IOF200R-t15-S1000.

The ultimate load reached in the present test series S-IOF200R-t15-S1000 was 54.95 kN on average, which is equal to 4.5 times the ultimate load reached in test series IOF200R-t15-S1000 on single longitudinally stiffened webs (12.23 kN). This result is similar to that obtained with built-up specimens with flat webs and shows that some extra strength is

provided by the interaction and interconnection of adjacent cassette profiles. The increase factor per web is smaller here than it was for flat webs, but it is still equal to $k_F = 4.5 / 4 = 1.12$, i.e. the ultimate load per web is increased by an average of 12 % per web in the built-up structure. This and similar factors k_{TF} *and* k_{WC} for top flange displacement and web crippling deformation, respectively, are calculated in Table 3.28.

Table 3.28 Factors k for comparison of longitudinally stiffened single webs with built-up structures.

	S-IOF200R-t15-S1000	IOF200R-t15-S1000	Ratio k
Ultimate load F_u per web	54.95 / 4 = 13.74	12.23	$k_F = 13.74 / 12.23 = 1.12$
Top flange displacement at F_u	9.54	8.34	$k_{TF} = 9.54 / 8.34 = 1.14$
Web crippling deformation at F_u	6.44	5.92	$k_{WC} = 6.44 / 5.92 = 1.09$

The top flange displacement corresponding to the ultimate load in the present test series S-IOF200R-t15-S1000 was 1.14 times and the web crippling deformation 1.09 times the corresponding values for test series IOF200R-t15-S1000 with single webs. It can be concluded that the flexibility of the top flange and the stiffness per section are about the same as in the single web tests, because the values of k_F, k_{TF} *and* k_{WC} are close to each other.

The deformation modes were again generally quite similar to those observed in test series IOF200R-t15-S1000. This is demonstrated in the photos under the sections on individual tests (see below).

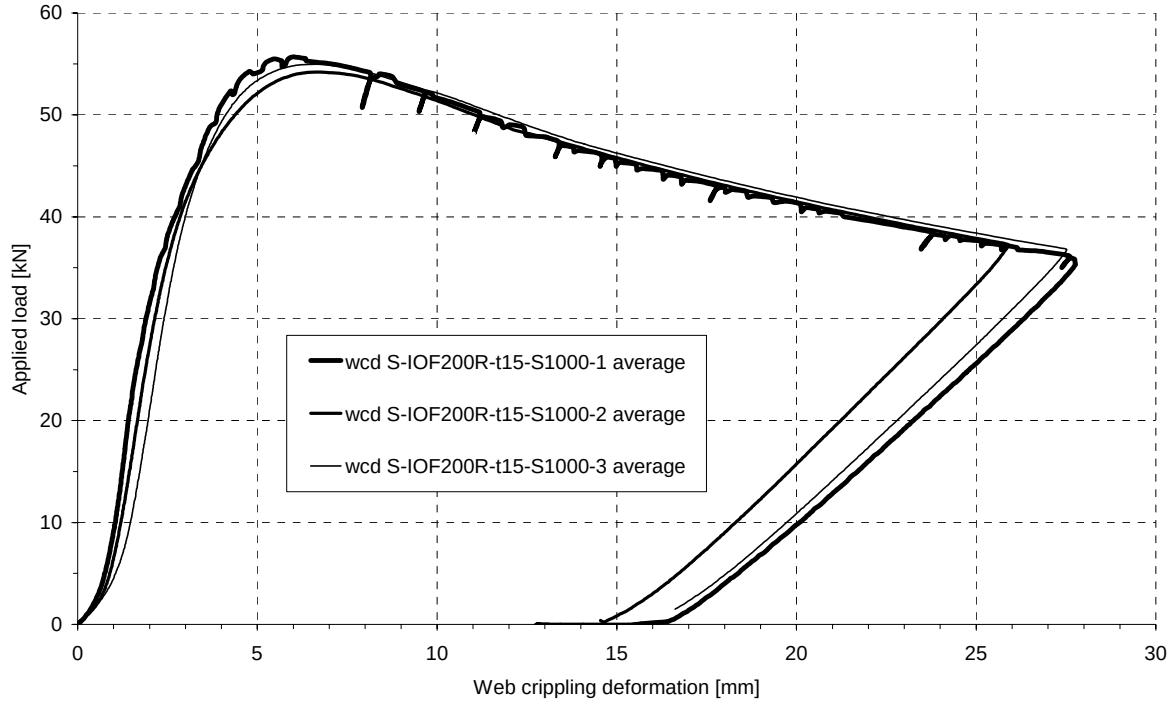

Fig. 3.67 Calculated average web crippling deformation curves for test series S-IOF200R-t15-S1000.

Test S-IOF200R-t15-S1000-1

Figure 3.68 shows the top and bottom flange displacement curves for the different webs and their calculated averages for test S-IOF200R-t15-S1000-1. Figure 3.69 shows the web crippling deformation curves and their average calculated on the basis of the measurements. Figures 3.72-3.73 show photos of the deformations of test specimen S-IOF200R-t15-S1000-2 during the test. These deformations are demonstrative of the deformations in specimen S-IOF200R-t15-S1000-1 as well.

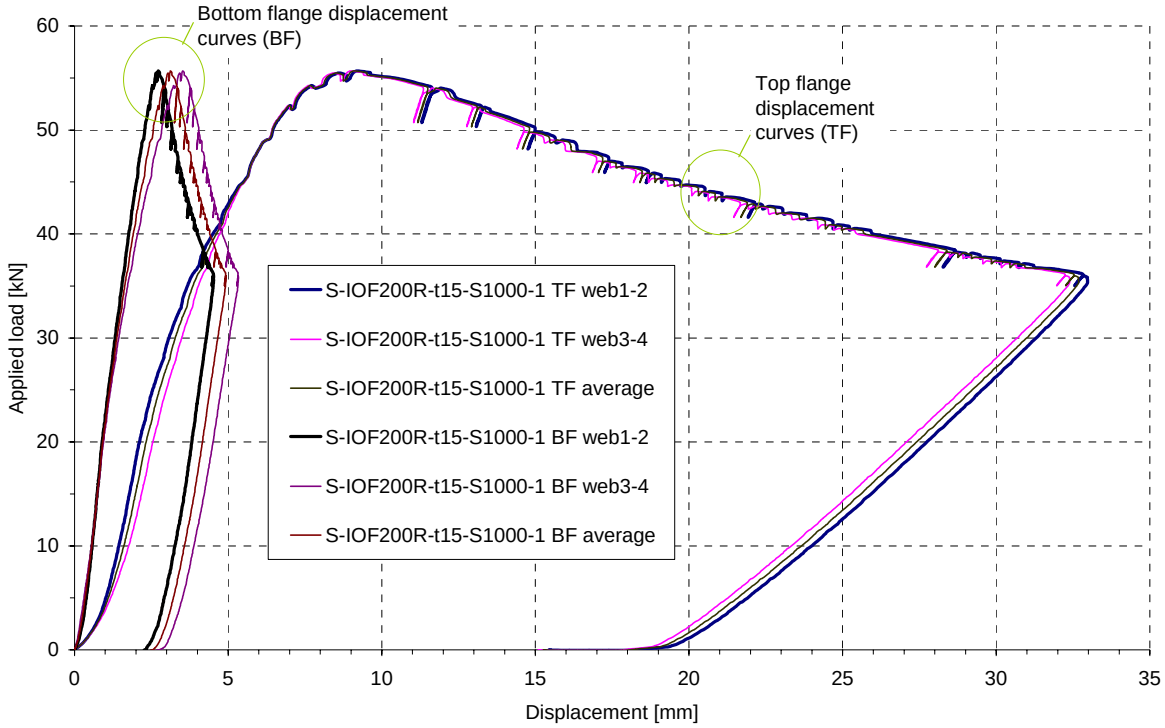

Fig. 3.68 Top and bottom flange displacement curves for test S-IOF200R-t15-S1000-1.

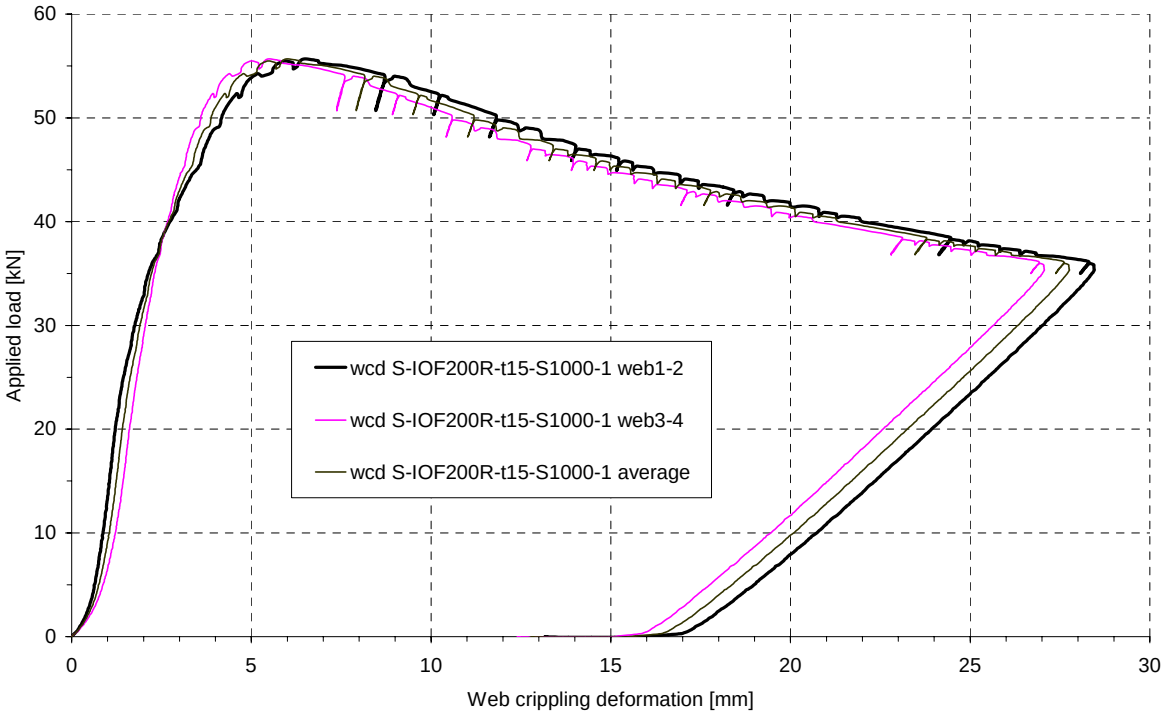

Fig. 3.69 Web crippling deformation curves for test S-IOF200R-t15-S1000-1.

Test S-IOF200R-t15-S1000-2

Figure 3.70 shows the top and bottom flange displacement curves for the different webs and their calculated averages for test S-IOF200R-t15-S1000-2. Figure 3.71 shows the web crippling deformation curves and their average calculated on the basis of the measurements. Figures 3.72-3.73 show photos of the deformations during the test.

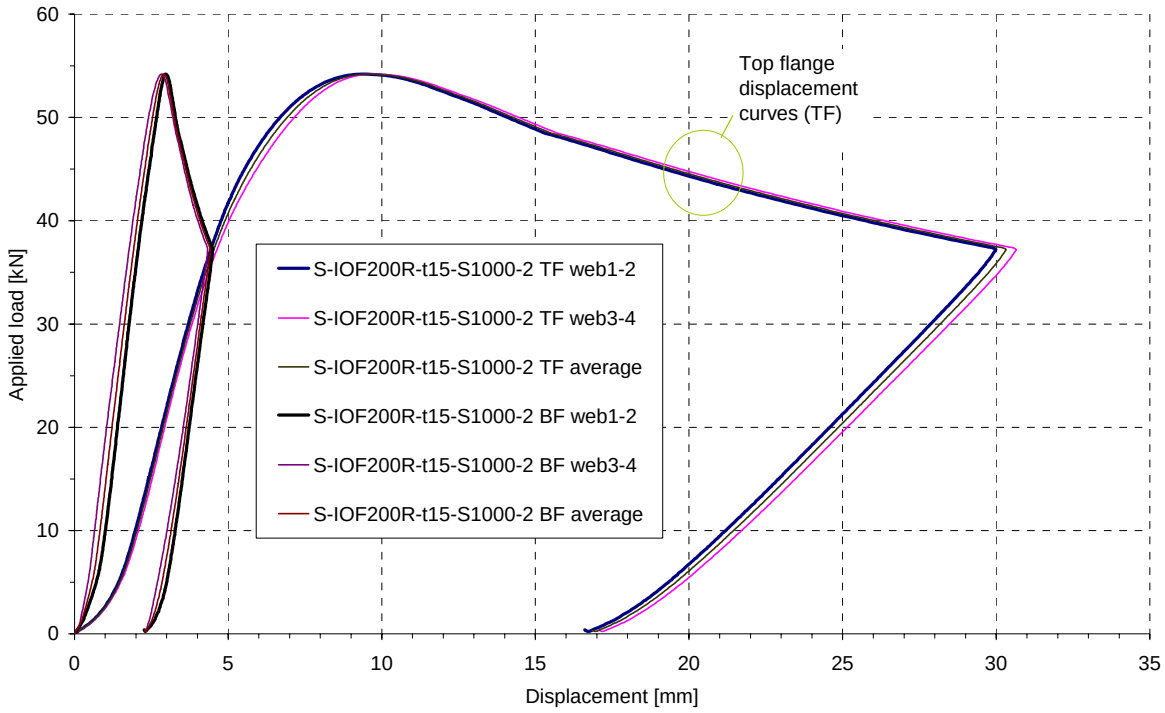

Fig. 3.70 Top and bottom flange displacement curves for test S-IOF200R-t15-S1000-2.

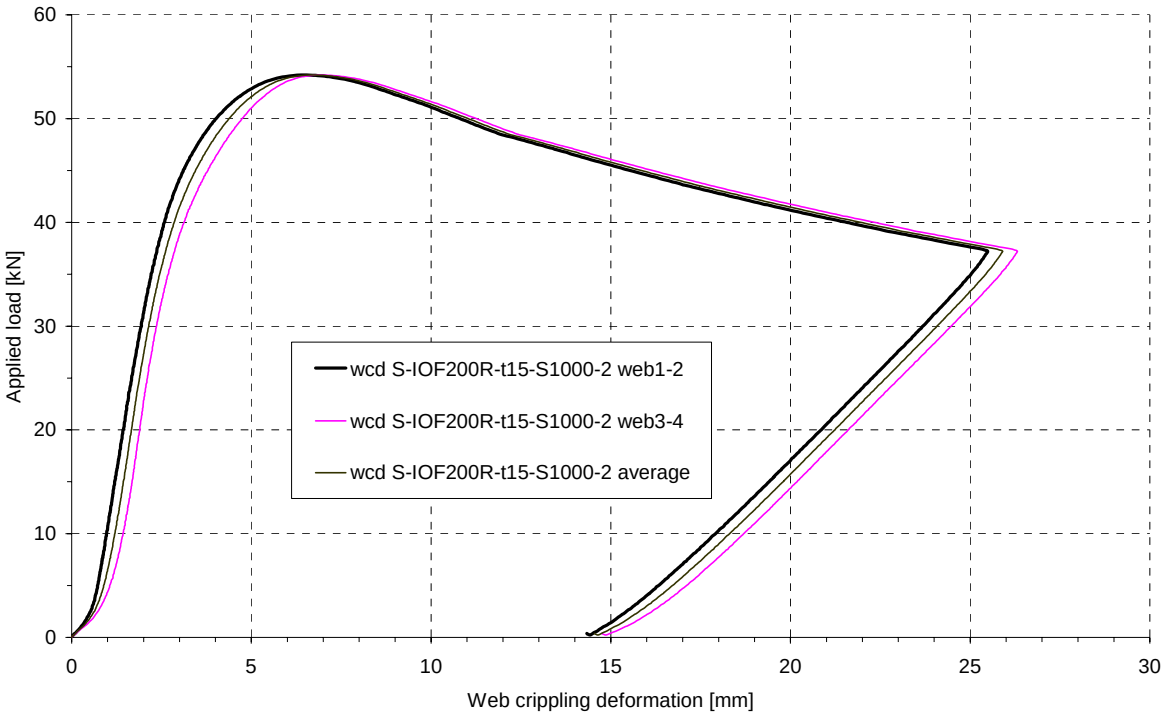

Fig. 3.71 Web crippling deformation curves for test S-IOF200R-t15-S1000-2.

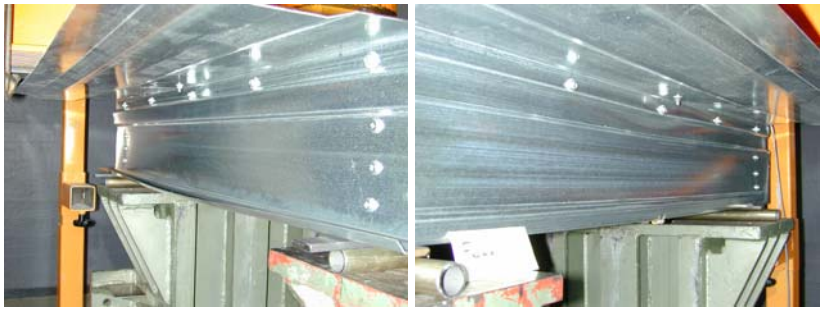

Fig. 3.72 Deformations in web1-2 in test S-IOF200-t15-S1000-2 at load $F = F_u$.

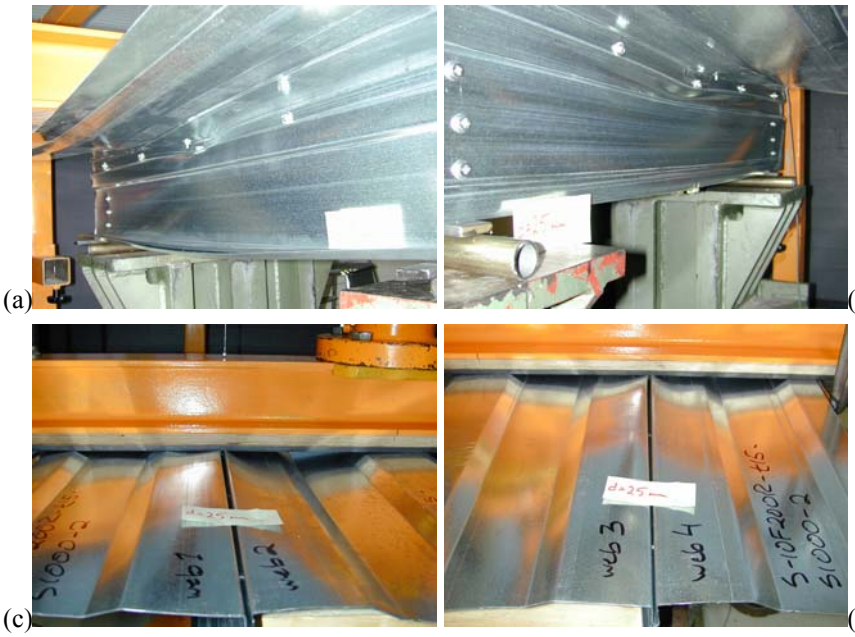

Fig. 3.73 Deformations in test S-IOF200R-t15-S1000-2 at top flange displacement d = 25 mm: web1-2 (a), web3-4 (b), top flange at web1-2 (c), top flange at web3-4 (d).

Test S-IOF200R-t15-S1000-3

Figure 3.74 shows the top and bottom flange displacement curves for the different webs and their calculated averages for test S-IOF200R-t15-S1000-3. Figure 3.75 shows the web crippling deformation curves and their average calculated on the basis of the measurements. Figures 3.72-3.73 show photos of the deformations of test specimen S-IOF200R-t15-S1000-2 during the test. These deformations are demonstrative of the deformations in specimen S-IOF200R-t15-S1000-3 as well.

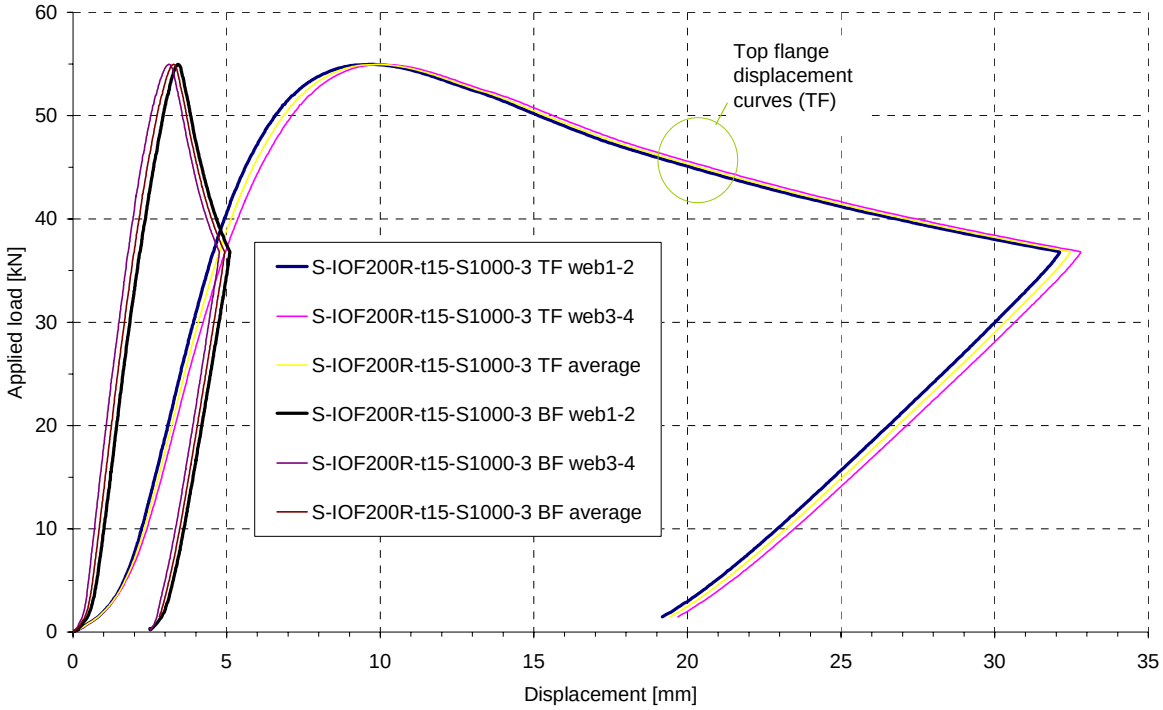

Fig. 3.74 Top and bottom flange displacement curves for test S-IOF200R-t15-S1000-3.

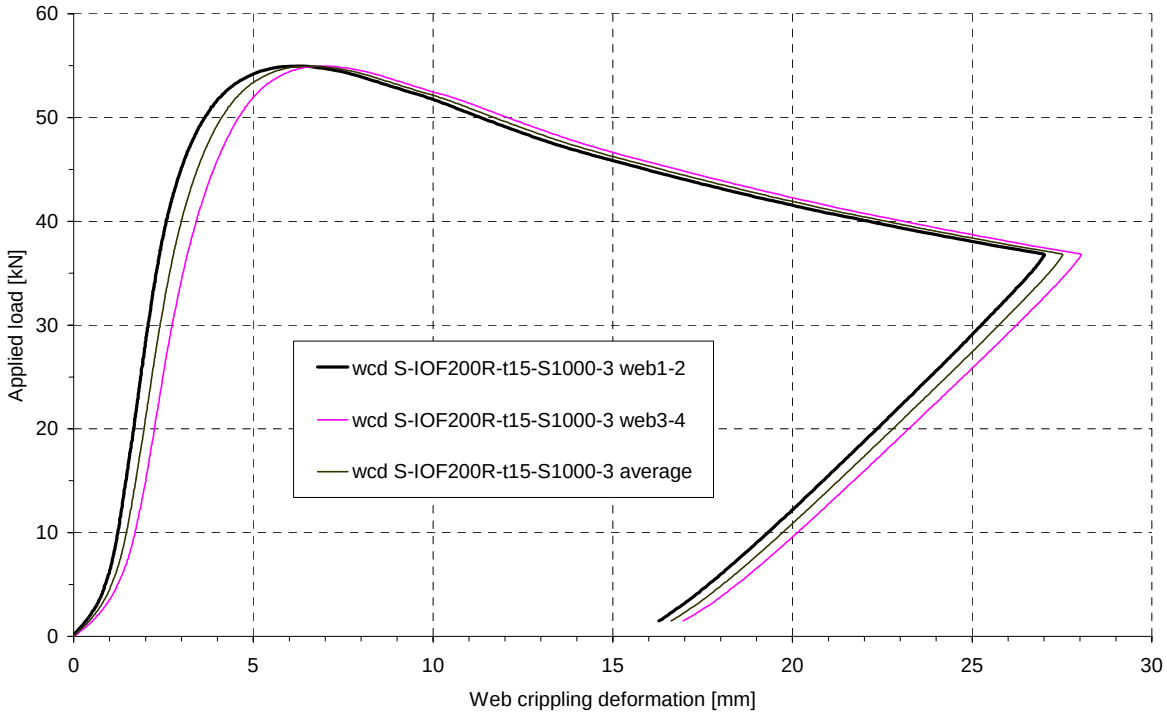

Fig. 3.75 Web crippling deformation curves for test S-IOF200R-t15-S1000-3.

3.6 Comparison of test results and nominal design values

The equations given in the European (ENV 1993-1-3:1996), American (AISI (1996)), Australian (AS/NZS 4600 (1996)) and Finnish (RakMK B6 (1989)) design codes were used to calculate comparison values for the test results in the cases of ITF- and IOF-tests on specimens with single flat webs. The values from tests with longitudinally stiffened webs cannot be directly compared with the design codes, because the codes do not consider the type of stiffeners used in these sections.

For ITF-tests, the design formulae used for the comparisons were the following:

- ENV 1993-1-3:1996: - Eq. (2.9) for cross-sections single webs,
  - Eq. (2.13) for the case with two or more webs (Category 1),
- AISI (1996): - Eq. (2.17),
- AS/NZS 4600 (1996): - Eq. (2.19).

As mentioned in Chapter 2, the National Building code of Finland (RakMK B6 (1989)) does not consider ITF-loading. The partial safety factors were equal to unity in all calculations. When interpreting the results, it should be kept in mind that the design safety factor recommended by ENV 1993-1-3:1996 for this case is γ_{M1} = 1.00, while AISI (1996) and AS/NZS 4600 (1996) both recommend ϕ_w = 0.75 for single unreinforced webs and RakMK B6 (1989) gives a factor γ_m = 1.0.

For ENV 1993-1-3:1996 design values corresponding to ITF-loading were calculated for both nominal and measured cross-sections and material properties. The values for the tested *nominal* cross-sections with single flat webs are given in Table 3.29 along with the corresponding mean ultimate load from tests and the ratios between the test value and the corresponding design value.

The values given by Equations (2.9) and (2.13) for the tested *actual* cross-sections with single flat webs and measured values of yield strength are given in Table 3.30 along with the corresponding mean ultimate load from tests and the ratios between the test value and the corresponding design value.

Table 3.29 Comparison of design values for the tested nominal cross-sections according to ENV 1993-1-3:1996 and test results.

	Mean ultimate load from tests [kN]	Value from Eq. (2.9) [kN]	Ratio between test load and value from Eq. (2.9)	Value from Eq. (2.13), Cat. 1, α=0.057, l_a=10 mm [kN]	Ratio between test load and value from Eq .(2.13)
ITF100-t10	7.45	4.27	1.74	1.23	6.06
ITF150-t10	6.34	3.33	1.90	1.23	5.15
ITF150-t15	16.56	10.19	1.63	2.70	6.13
ITF200-t10	6.51	2.40	2.71	1.23	5.29
ITF200-t15	16.24	8.74	1.86	2.70	6.01

Table 3.30 Comparison of design values for the tested actual cross-sections according to ENV 1993-1-3:1996 and test results.

	Mean ultimate load from tests [kN]	Value from Eq. (2.9) [kN]	Ratio between test load and value from Eq. (2.9)	Value from Eq. (2.13), Cat. 1, α=0.057, l_a=10 mm [kN]	Ratio between test load and value from Eq. (2.13)
ITF100-t10	7.45	4.72	1.58	1.24	6.01
ITF150-t10	6.34	3.39	1.87	1.26	5.03
ITF150-t15	16.56	10.97	1.51	2.78	5.96
ITF200-t10	6.51	2.52	2.58	1.39	4.68
ITF200-t15	16.24	9.29	1.75	2.84	5.72

It can be seen from Tables 3.29 and 3.30 that the use of measured cross-section properties gives slightly higher resistance values than when nominal values are used. This is mostly influenced by the yield strength of the actual cross-section, which is normally higher than the nominal value.

Table 3.31 Comparison of values from Eq. (2.13) when value of l_a is varied.

	Mean ultimate load from tests [kN]	Value from Eq. (2.13), Cat. 1, α=0.057, l_a=10 mm [kN]	Value from Eq. (2.13), Cat. 1, α=0.057, l_a=100 mm [kN]
ITF100-t10	7.45	1.23	2.50
ITF150-t10	6.34	1.23	2.50
ITF150-t15	16.56	2.70	5.18
ITF200-t10	6.51	1.23	2.50
ITF200-t15	16.24	2.70	5.18

Because the values from Eq. (2.13) calculated with α = 0.057 and effective bearing length l_a = 10 mm, as prescribed in ENV 1993-1-3:1996, seemed very conservative (see Tables 3.29 and 3.30), the values were calculated also for l_a = 100 mm, which is equal to the actual bearing length s_s. The calculated capacity values are approximately doubled, but they are still only about one third of the corresponding test result. It could be concluded that for the case of

cassettes under ITF-loading, the current rule given in ENV 1993-1-3:1996 for cross-sections with two or more unstiffened webs is very conservative and the use of the actual bearing length s_s instead of the effective bearing length l_a = 10 mm should be considered in order to avoid extreme conservatism in design. On the other hand, the results obtained by using Eq. (2.9) for cross-sections with single webs gives results that are also quite conservative but not as low as for Eq. (2.13). Therefore the use of Eq. (2.9) could be recommended in this case.

For AISI (1996) and AS/NZS 4600 (1996), design values corresponding to ITF-loading were calculated only for nominal cross-sections and material properties. The values for the tested *nominal* cross-sections with single flat webs are given in Table 3.32 along with the corresponding mean ultimate load from tests and the ratios between the test value and the corresponding design value.

Table 3.32 Comparison of design values for the tested nominal cross-sections according to AISI (1996), AS/NZS 4600 (1996) and test results.

	Tests	AISI (1996)		AS/NZS 4600 (1996)	
	Mean ultimate load from tests [kN]	Value from Eq. (2.17) [kN]	Ratio between test load and value from Eq. (2.17)	Value from Eq. (2.19) [kN]	Ratio between test load and value from Eq. (2.19)
ITF100-t10	7.45	4.85	1.54	4.84	1.54
ITF150-t10	6.34	3.81	1.66	3.80	1.67
ITF150-t15	16.56	11.48	1.44	11.46	1.45
ITF200-t10	6.51	2.76	2.36	2.77	2.35
ITF200-t15	16.24	9.86	1.65	9.84	1.65

For test series IOF200-t15-S1000, the mean failure load obtained in tests was F_{test} = 15.91 kN and the design values were calculated using all four codes according to Table 3.33. The values for RakMK B6 (1989) were calculated for both k_3 = 0.8 and k_3 = 1.0. As explained in Chapter 2, the value k_3 = 0.8 is meant for cassettes in the code, but on the basis of Table 3.33, also the value k_3 = 1.0 gives a sufficiently conservative result.

Table 3.33 Comparison of design codes in the case of tests IOF200-t15-S1000.

Design code	Equation	Design load F_d [kN]	F_{test} / F_d
ENV 1993-1-3:1996	2.12	11.43	1.39
	2.13 with $\alpha = 0.115$	10.45	1.52
AISI (1996)	2.18	12.75	1.25
AS/NZS 4600 (1996)	2.20	12.52	1.27
RakMK B6 (1989)	2.21 with $k_3 = 0.8$	9.06	1.76
	2.21 with $k_3 = 1.0$	11.32	1.41

The AISI (1996) and AS/NZS 4600 (1996) design codes give slightly higher resistance values for the cases of ITF-tests as shown in Tables 3.29 and 3.32 than ENV 1993-1-3:1996 (Eq. (2.9)). The same is true for the IOF-test considered in Table 3.33, while the National Building Code of Finland RakMK B6 (1989) gives quite a conservative value when $k_3 = 0.8$ is used. When $k_3 = 1.0$ is used, the value given by RakMK B6 (1989) is comparable to the ENV 1993-1-3:1996 values.

It can be seen from the comparison results that all examined design codes leave a considerable margin of safety between the design values and the test results. This is understandable, because the actual form and imperfections of the cross-section and the lateral and longitudinal support conditions cannot always be fully guaranteed. Also, the limited amount of tests does not allow statistical comparisons to be made during this study. However, it can be noted that the current design methods for the web crippling of cross-sections with flat webs are conservative, as they should be. As shown above, ITF-results calculated using Eq. (2.13) are considerably conservative.

4. NUMERICAL ANALYSES

4.1 General

The finite element modelling carried out during this research has been done on a multi-purpose commercially available finite element software package ABAQUS Version 6.2 (2001), Version 6.3 (2002) and Version 6.4 (2003). The programme module ABAQUS/Standard was used for static analyses. However, when the number of degrees of freedom was increased, the model became larger and the contact surface areas more complex, and it was necessary to turn to ABAQUS/Explicit for quasi-static dynamic analyses. With ABAQUS/Explicit, it is possible to get accurate results also for highly non-linear and computationally expensive contact analyses. The software's own pre-processor ABAQUS/CAE and postprocessor ABAQUS/Viewer were used throughout. Some keyword cards needed in the analyses are not supported by ABAQUS/CAE and therefore the analysis input file had to be edited using a text editor or CAE's own input data editor. During the research, ABAQUS Versions 6.3 and 6.4 became available and these were used for the modelling described in Section 4.4 and Chapter 5.

The analyses were run using the super computers of the Centre for Scientific Computing (CSC) in Otaniemi, Finland. The computers used were SGI Origin 2000 (cedar.csc.fi) with 128 MIPS R12000 processors and 160 GB total memory and the IBM pSeries 690 with 512 GB total memory.

Section 4.2 presents the creation of reference finite element models using experimental test results found in Hofmeyer (2000). The test results were used to verify the correct behaviour of finite element models. After this initial modelling period was finished, the findings were used for the predictive modelling of the then upcoming ITF-tests on single web cassette sections. Some of the general results of this period are given in Section 4.3 where they are also compared to the corresponding test results. Section 4.4 presents the modelling done on some of the tested cross-sections after the complete test series described in Chapter 3 was finished. These models were used to study the web crippling behaviour of cold-formed steel cassettes further and to carry out a parametric study on the effects of variations in the cross-section and the support and loading conditions. The results of this last part are given in Chapter 5.

4.2 FE-analyses of Hofmeyer experiments

4.2.1 Hofmeyer experiment 25 (yield arc mode)

Cross-section information

As mentioned in Chapter 2.2, Hofmeyer (2000) carried out a series of tests on cold-formed sheet sections of the type shown in Figure 4.1. Hofmeyer's test number 25 was chosen as the first to be modelled in the present work because it is one of the tests best described in Hofmeyer's thesis and the FE-analysis carried out by Hofmeyer using ANSYS was also discussed in more detail. The relevant cross-sectional variables as shown in Figure 4.1 for test specimen number 25 were as shown in Table 4.1. The length of the load bearing plate used in the test was 150 mm.

Table 4.1 Measured and nominal values of cross-section variables for test number 25 (Hofmeyer 2000).

	Symbol	Measured value [mm]	Value used for ABAQUS/Standard analysis [mm]
Bottom flange width	b_{bf}	40.5	40
Web width	b_w	100.1	100
Top flange width	b_{tf}	136.6	140
Corner radius	r_{bf}	2.6	2.6
Steel plate thickness	t	0.680	0.680
Angle between web and flange	θ_w	49.9	50
Specimen length	L	1201.0	1200.0

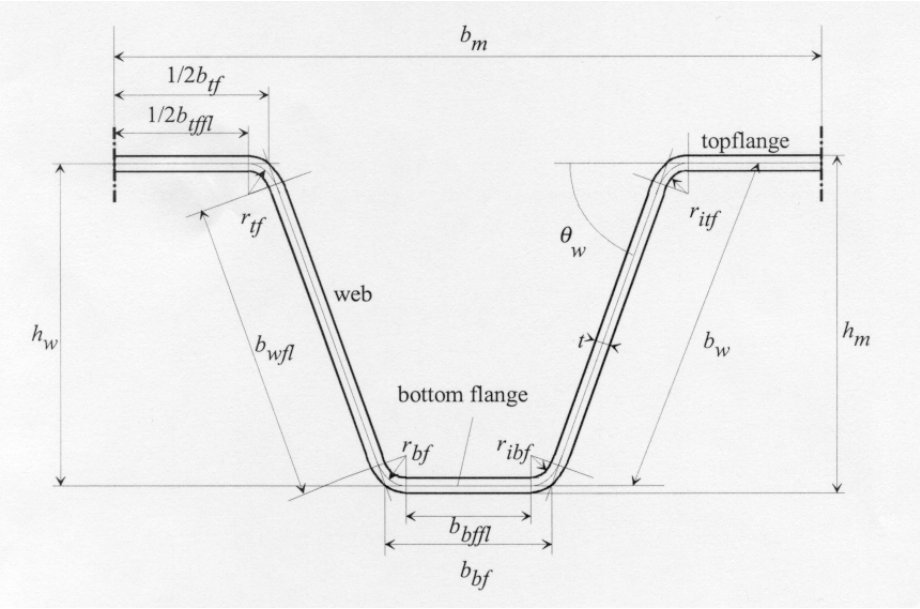

Fig. 4.1 Sheet cross-section used in Hofmeyer's (2000) tests.

Material properties

The material properties used for the analyses were taken as given in Hofmeyer (2000). The stress-strain values are shown in Table 4.2. The real strain values given in the source data had to be transformed into real plastic strain values for the ABAQUS/Standard analyses by subtracting the purely elastic real total strain values 0.00169 at first yield from all subsequent true total strain values. The modulus of elasticity used was E = 210000 N/mm^2 and Poisson's ratio μ = 0.3.

Table 4.2 Real stress-strain values used in the analyses (Hofmeyer 2000).

Real total strain ε_r	Real plastic strain $\varepsilon_{r,p}$	Real stress σ_r [N/mm^2]
0.00169	0.00000	353.9
0.03106	0.02937	362.3
0.05022	0.04853	404.1
0.07511	0.07342	441.9
0.10120	0.09951	468.0
0.15014	0.14845	504.2
0.20008	0.19839	532.9
0.25037	0.24868	554.7

Test arrangement

The test arrangement used by Hofmeyer is shown in Figure 4.2. The test was a three-point bending test where the loading jack was under the sheeting and the loading was applied upwards. This was done to make it easier to make castings of the inner cross-section during the test. Strips were used at regular and sufficient intervals in order to prevent the spreading of the webs.

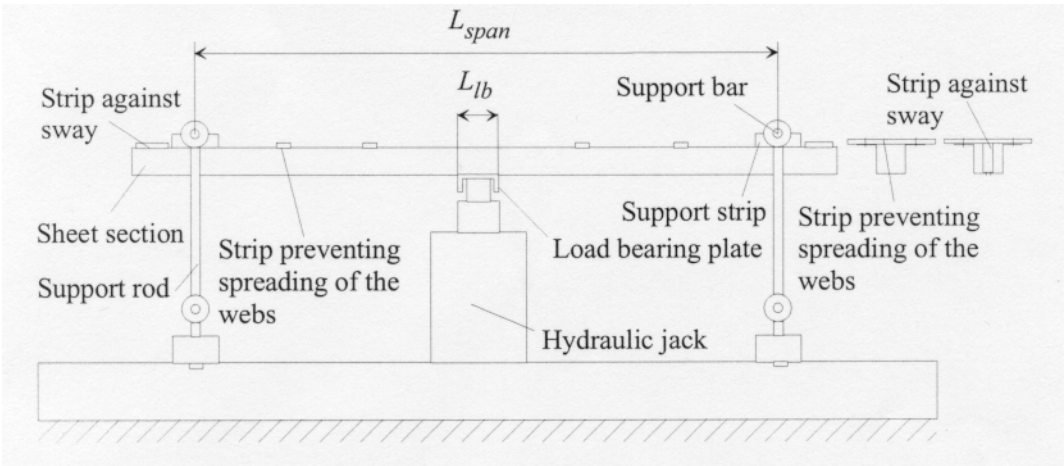

Fig. 4.2 Arrangement for tests by Hofmeyer (2000).

The web crippling deformation was measured as the difference between total mid-span deflection of the top of the sheeting and the movement of the hydraulic loading jack. The load value was measured by recording the support reactions.

Boundary and symmetry conditions

Because of the symmetry of both the test set-up and the expected failure mode, it was sufficient to model only one quarter of the sheet cross-section beam so that symmetry conditions were applied at mid-span and at the middle of the cross-section shown in Figure 4.3. Naturally, the sheeting is assumed to be continuous in the lateral direction and therefore lateral displacements were prevented at the sides of the section and rotational symmetry conditions applied as explained in the following.

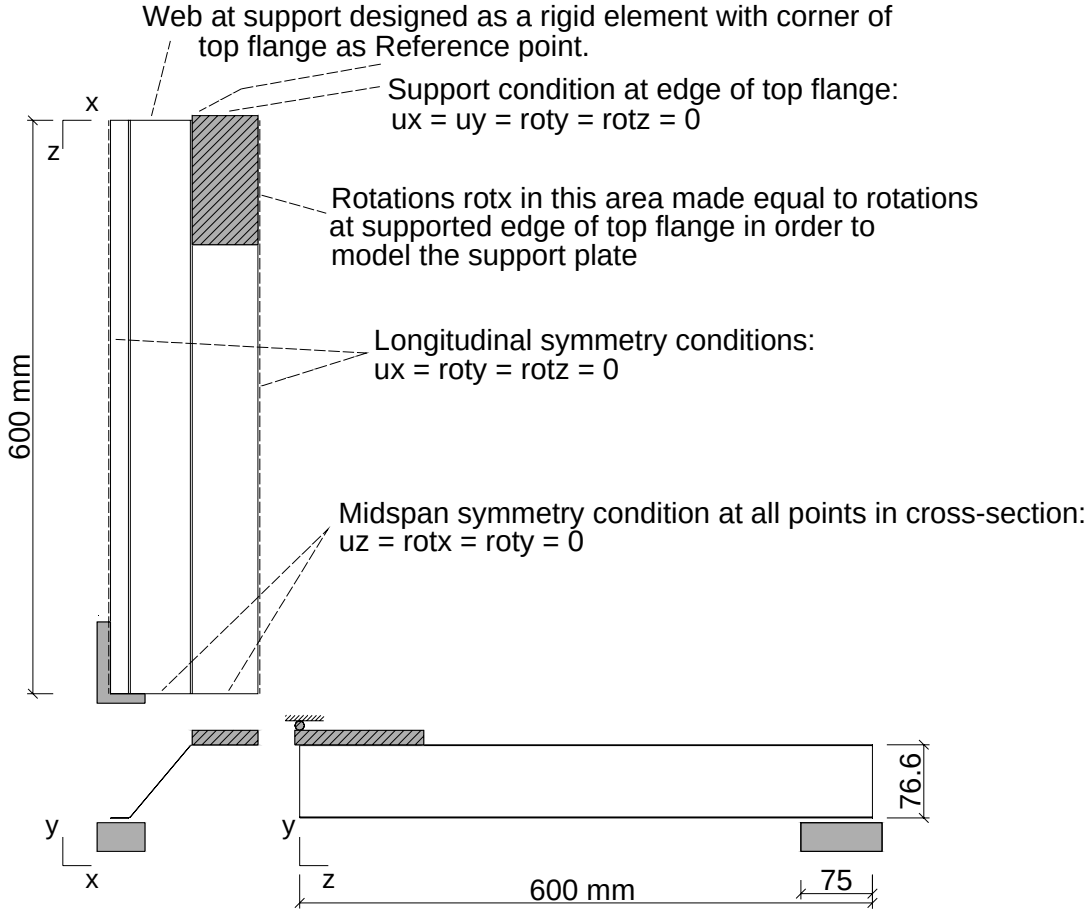

Fig. 4.3 Boundary and symmetry conditions for model hofm25a.inp.

Figure 4.3 shows the support and symmetry boundary conditions used in model hofm25a.inp. At the support, it was actually adequate to prescribe boundary conditions for a single point only, which is named the 'Reference point' in the figure. At this point, vertical (y) and lateral (x) displacements and rotations about the vertical (y) and longitudinal (z) axes were restrained. The vertical (y) displacement of the other points at the end of the top flange were tied to this reference point using the *EQUATION keyword card available in ABAQUS/Standard. The points of the web at the support line were defined as a RIGID BODY with the same 'Reference point' as above. This means that their motion is completely defined by the movement of the 'Reference point', i.e. they can only rotate about the 'Reference point'. This was done in order to prevent the failure of the cross-section at the support area instead of the mid-span area, where the concentrated load is applied. In order to model the actual support conditions of the test set-up as closely as possible, the hinged support strip seen in Figure 4.2 was modelled by tying the rotations about the lateral (x) axis to be the same as the rotation of the 'Reference point'. These support conditions seem relatively complicated, but were necessary, because if only a simple vertical support condition were applied at the end of the profile, strong stress and strain concentration would appear at the support area and this would have an affect on the overall behaviour of the beam.

The continuity of the sheeting in the lateral (x) direction was modelled by setting the lateral (x) displacements and rotations about the vertical (y) and longitudinal (z) axes equal to zero along the outer edges of both flanges. Similarly, in order to model the continuity of the sheeting at midspan, the longitudinal (z) displacements and rotations about the lateral (x) and vertical (z) axes were restrained at all the points of the cross-section.

The loading was applied using a separate loading block with a reference point at one corner of the block. All other degrees of freedom except the vertical (y) displacement were restrained at the reference point. Contact surfaces were modelled at the flanges of the sheeting and the loading block in order to bring the loading onto the structure in a realistic manner.

Mesh

The modelled beam was divided longitudinally in three parts as shown in Figure 4.4. The adjacent edges of the parts were then tied together using *TIE-keywords so that the geometry performs exactly as if it were made of a single piece. This was done in order to give more freedom to the mesh modelling and allow variations in mesh density between different areas of the beam. In this way, simple, regular and undistorted square shell elements could be used in all parts of the beam, also at areas of changing mesh density. The length of the end part where the web crippling deformation is expected to happen is 120 mm, the length of the middle part is 340 mm and the length of the other end part at the support is 140 mm.

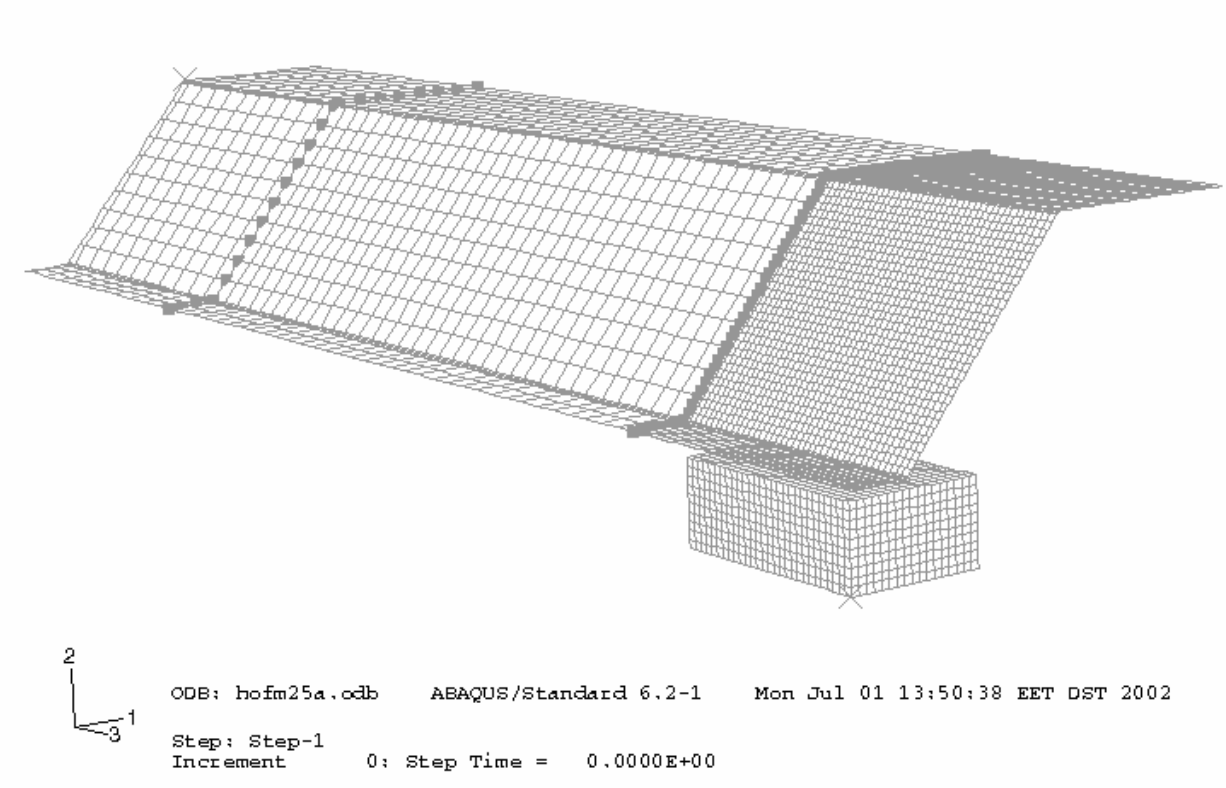

Fig. 4.4 Mesh design for model hofm25a.inp.

All shell elements used for the sheeting were of type S4R, which is a linear four-node general-purpose shell element using reduced integration and allowing for finite (large) strains and changes in thickness. In the web and flanges, the size of the elements was 3 mm × 3 mm in the part where the loading was applied and about 10 mm × 10 mm elsewhere. Four elements were used at the rounded corners. A single element is not sufficient to model the corner area adequately, as shown in Figure 4.5. The loading block was made up of

3 mm × 3 mm R3D4 rigid elements. The total number of nodes in the model was 11575 and the total number of elements 7614.

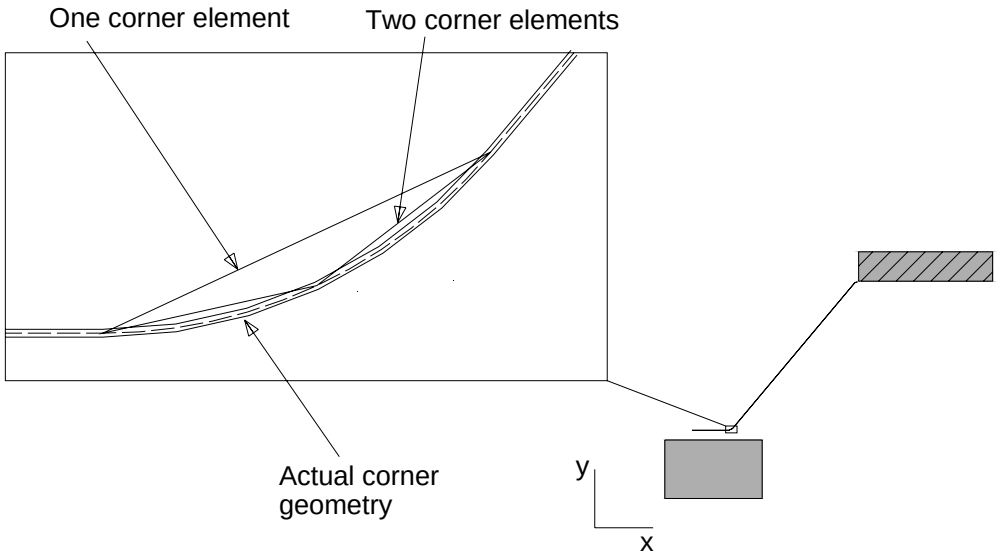

Fig. 4.5 Influence of mesh refinement in corner area.

Results

The load-deflection curve for the finite element analysis performed using ABAQUS/Standard is shown in Figure 4.6 together with the test results (Hofmeyer 2000). As can be seen, the finite element model gives fairly good results in comparison with the test situation. The initial stiffness of the cross-section is higher in the model than in the test, which can be partly explained by the rigid web design at the support and the normal initial imperfections occurring in practice.

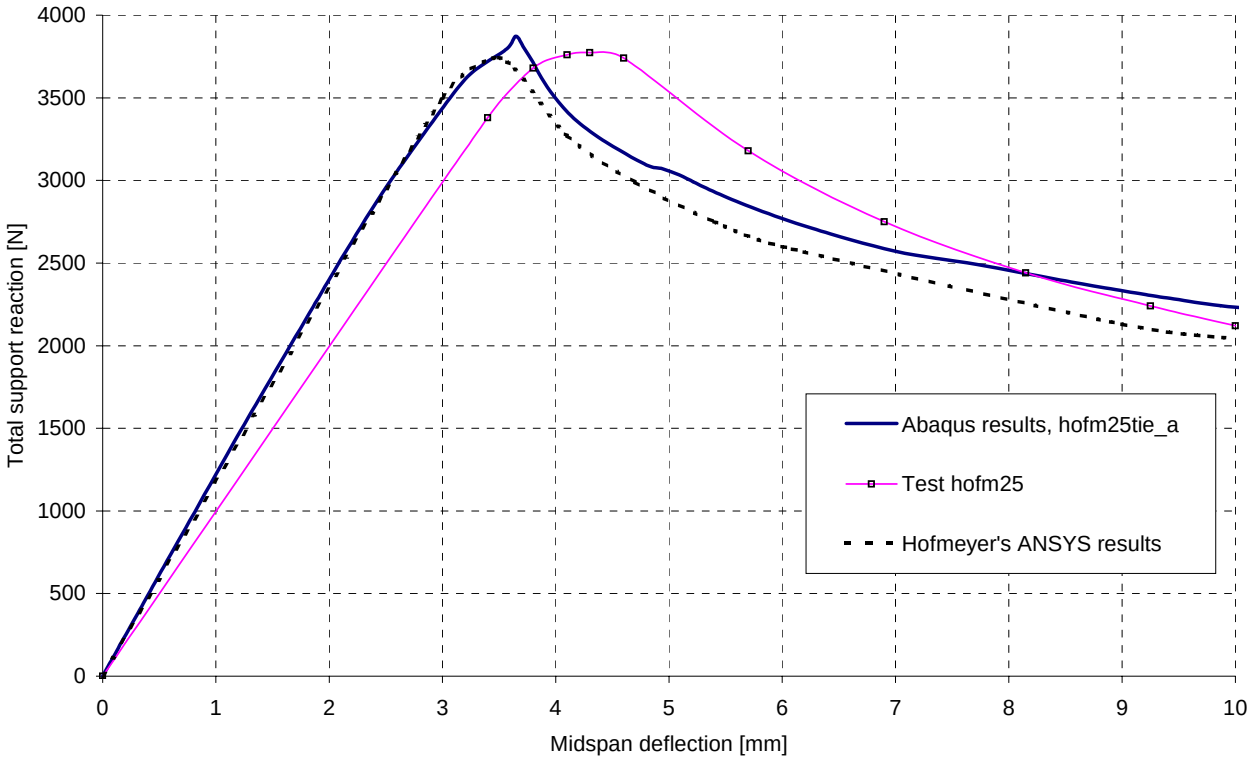

Fig. 4.6 Load-deflection curves for test specimen hofm25.

The test and analysis values for the ultimate load F_u, web crippling deformation Δh_w at F_u and beam deflection w at F_u are given in Table 4.3. The ultimate load given by the ABAQUS/Standard analysis is 2.6 % higher than the test value, the deflection is 15 % smaller and the web crippling deformation is 37 % smaller than measured in the test.

Table 4.3 Ultimate loads and deformation values from test and FE-simulations.

	Test hofm25	ABAQUS analysis results	ANSYS analysis results (Hofmeyer 2000)
F_u [N]	3773	3870	3743
Δh_w [mm]	0.31	0.195	0.23
w [mm]	4.28	3.65	3.50

The yield line formation at the surface of the shell elements obtained from the ABAQUS/Standard analysis is shown in Figure 4.7. When the patterns are compared to those obtained by Hofmeyer (2000) from the corresponding ANSYS analysis (Figure 4.8), it can be seen that the results are very similar to each other. If the yield line formation from the ABAQUS/Standard analysis were drawn at the mid-surface of the shell elements, the patterns would not be as obvious as they are in Figure 4.7. This is due to the fact that the yielding starts from the shell surfaces.

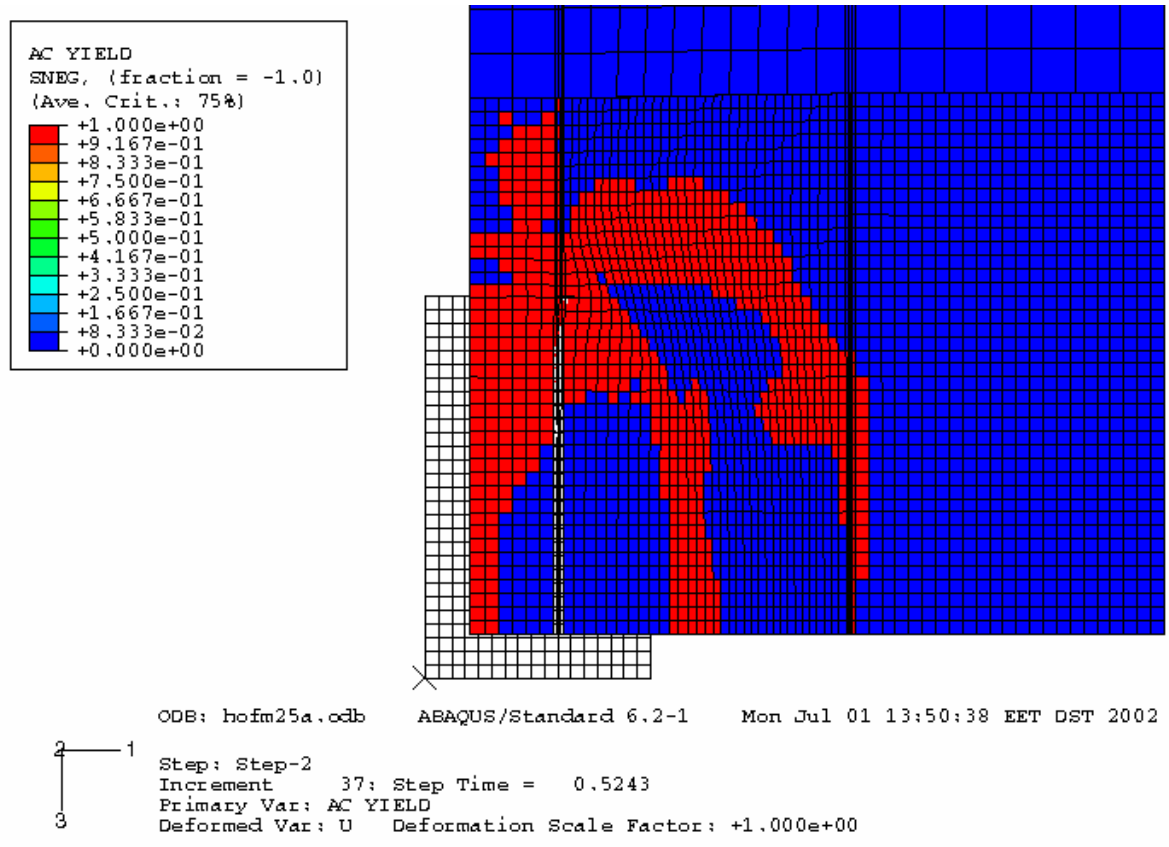

Fig. 4.7 Plasticity after ultimate load for ABAQUS model hofm25a.inp (step 2, increment 37, total deflection 10.5 mm), top view.

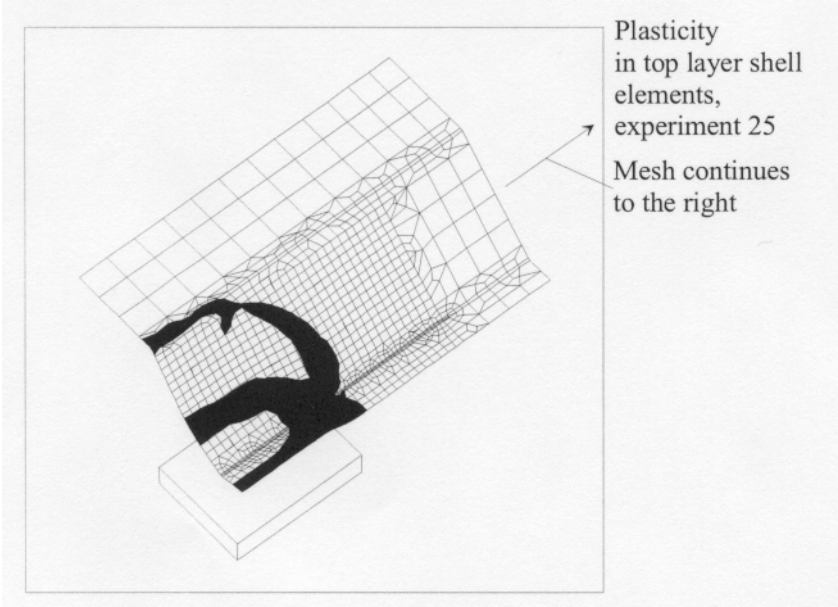

Fig. 4.8 Plasticity after ultimate load for ANSYS model of test hofm25, isometric view (Hofmeyer 2000).

Variation of model

After the above analyses had already been completed, an attempt was made to simplify the boundary conditions at the support and to get an even more realistic model of the tested beam. The model was changed so that the beam was extended 150 mm beyond the actual support line, as shown in Figure 4.2 of the actual test set-up. This permitted the support boundary conditions to be applied only to the nodes at the "support line" in the top flange. The rotational boundary conditions describing the influence of the "support plate" and the rigid body condition of the web at the support could be deleted. This simplification increased the stiffness of the beam cross-section at the support and rationalised the model.

A similar analysis to the one described above was run on this new model named *hofm25a_extsup.inp*. The load-displacement curve given in Figure 4.9 shows that the new curve runs closer to the test curve when compared to the previous analysis curve *hofm25a.inp*. However, the value of the ultimate load is not influenced by the change.

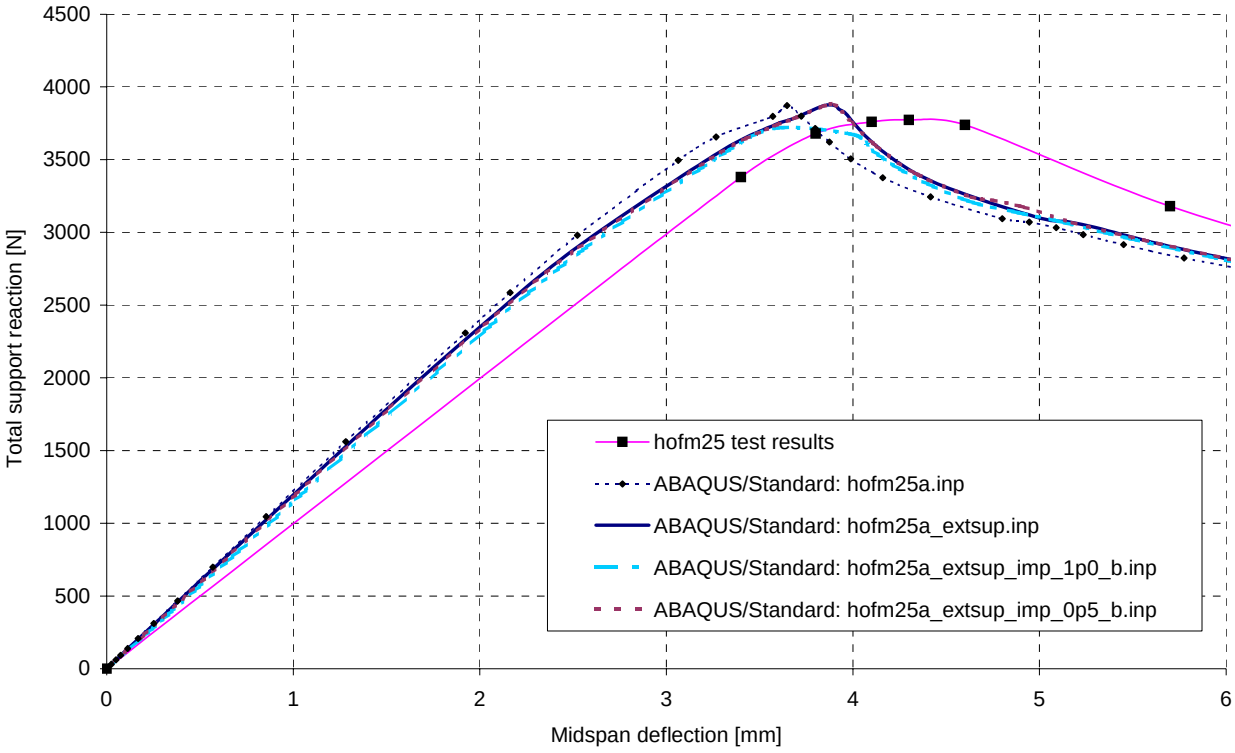

Fig. 4.9 Load-deflection curves for test *hofm25*.

A further approach for the analysis included a linear elastic buckling analysis used to obtain an eigenmode for the beam. The mesh and profile remained unchanged for the buckling

analysis. However, the rigid loading block was removed and replaced by a pressure load in the bottom flange covering the same area as the load block. The lowest eigenmode thus obtained was then used as the basis for initial imperfections in the profile. These initial imperfections, as shown in Figure 4.10, may not be the most common forms obtained during the manufacturing process, but they nevertheless make the otherwise ideal cross-section more realistic by introducing local node displacements along the beam. It should be noted that the deformation scale factor in Figure 4.10 is set so that the maximum nodal displacement is equal to 10 mm, while the length of the model is 600 mm. This means that the deformations are highly exaggerated in the Figure.

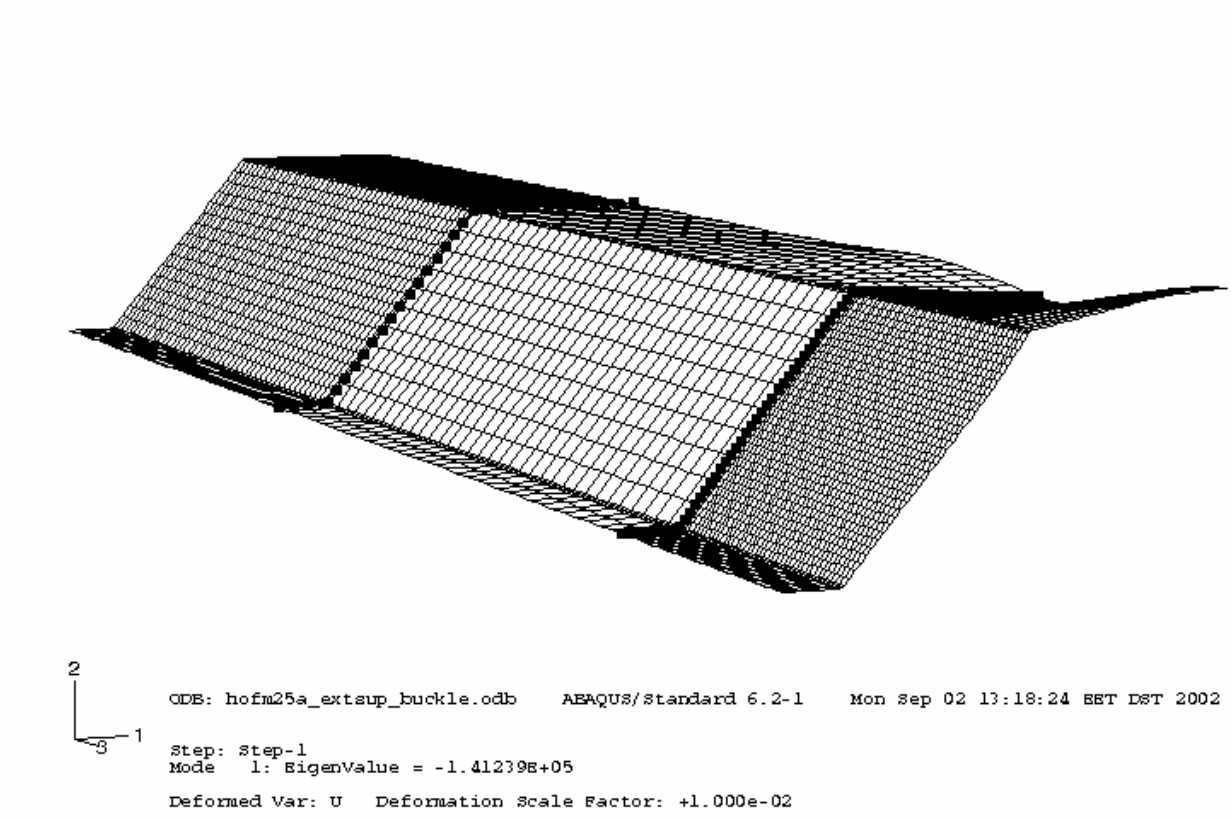

Fig. 4.10 Buckling mode used as basis for initial imperfections for analyses of test *hofm25*.

The buckling mode was scaled so that the largest nodal displacement (at the corner of the top flange) was equal to 1.0 mm or 0.5 mm in models *hofm25a_extsup_imp_1p0_b.inp* and *hofm25a_extsup_imp_0p5_b.inp*, respectively. As can be seen from the curves in Figure 4.9, the smaller magnitude of imperfection has a negligible effect on the behaviour of the profile, but the larger initial imperfection reduces the ultimate load to 3715 N, which is 1.5 % lower than the test value.

The measured web crippling deformation is shown in Figure 4.11 with two ABAQUS/Standard analysis results. The results are qualitatively satisfactory, but the linearity of the web crippling deformation in the test is not accurately repeated in the analyses. The maximum web crippling deformation is reached at approximately the same time in the test and the analyses, but the magnitude of the deformation is smaller in the analyses. This is not considered to be a serious defect of the model, because the web crippling deformation is very sensitive to imperfections in the model.

It can be concluded that the created ABAQUS/Standard model gives a good description of the behaviour of the tested beam *hofm25*, and especially of the failure load value.

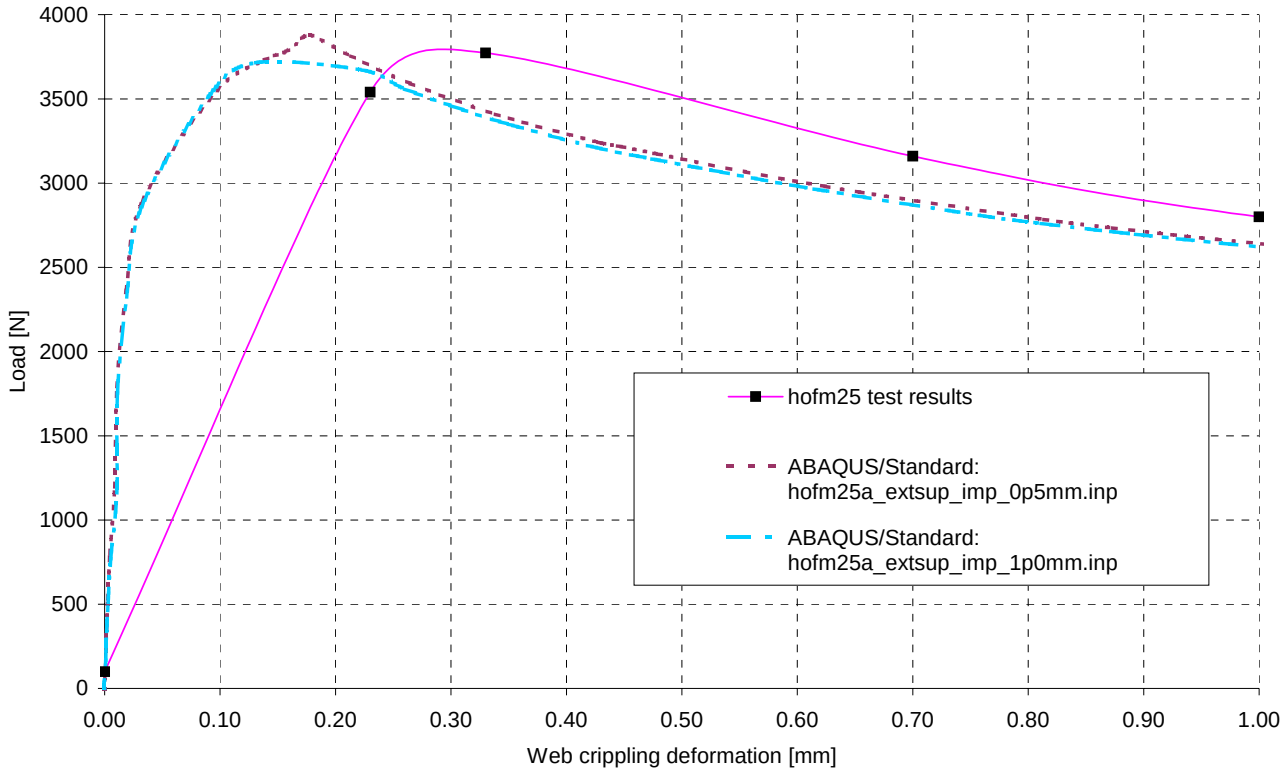

Fig. 4.11 Web crippling deformation for the yield arc mode.

4.2.2 Hofmeyer experiment 61 (yield eye mode)

Experiment information

The second experiment used in the development of FE-models was test number 61 carried out by Hofmeyer (2000). The cross-section was basically similar to that of test specimen 25 above, but some cross-sectional values varied as given in Table 4.4. The failure mode observed in the test was the unsymmetrical yield eye mode. The ultimate load observed in the test was 1614 N.

Table 4.4 Measured and nominal values of cross-section variables for test number 61 (Hofmeyer 2000).

	Symbol	Measured value [mm]	Value used for ABAQUS/Standard analysis [mm]
Bottom flange width	b_{bf}	39.0	39.0
Web width	b_w	100.5	100.5
Top flange width	b_{tf}	141.0	141.0
Corner radius	r_{bf}	5.8	5.8
Steel plate thickness	t	0.680	0.680
Angle between web and flange	θ_w	44.2	44.2
Specimen length	L	2400.0	2400.0

The material properties were the same as for the previous model, as given in Table 4.2. The test set-up was also fundamentally the same as for test 25 above. The main structural difference between the two tests is that the span is twice as long in test 61 as in test 25 and the length of the load bearing plate was only 100 mm in test 61, while in test 25 it was 150 mm. This makes the ratio between the length of the load bearing plate and the length of the beam considerably smaller than in test 25.

Creation of finite element models

The same approach that was used above for modelling test number 25 was at first adopted also for test number 61. However, it was clear from the beginning that a quarter model would not be adequate in this case due to the unsymmetrical failure mode observed in the test. At least a half model would therefore be necessary. In order to have a more complete structure, however, it was decided that the complete basic cross-section of the sheeting should be

modelled, as shown thematically in Figure 4.1. This, together with the increased length of the beam in comparison to test 25 and the relatively dense mesh, meant that the number of degrees of freedom (DOF's) was radically increased. The total number of nodes in the model was 36835 and the number of elements 26448.

The high number of DOF's made the calculation too demanding for the static analysis procedure in ABAQUS/Standard and lead to unsurpassable convergence difficulties. The mesh had to be made very scarce in order for the analysis to work, but this made the whole profile far too stiff and analysis results unrealistic. Therefore a switch to using ABAQUS/Explicit was made. ABAQUS/Explicit is a general-purpose analysis module that uses an explicit dynamic finite element formulation. It is mostly used for the modelling of dynamic events with a short duration, but is also very efficient for analyses including changing contact problems and considerable nonlinearities.

The idea, then, was to carry out a quasi-static analysis using a dynamic analysis procedure. In order to accomplish this, the load introduction period has to be long enough for the inertia effects of the structure to be negligible.

The steel density needed in the dynamic analysis was set equal to the usual value 7850 kg/m^3. The load bearing plate was moved against the profile using displacement control with an end displacement equal to 20 mm. The displacement is applied using the AMPLITUDE - option under the *BOUNDARY keyword. The displacement amplitude is thus applied using the SMOOTH STEP amplitude definition option, which allows the displacement to be ramped up smoothly from the initial zero value to the end value.

Although the test arrangement as shown in Figure 4.2 is basically a simply supported three-point bending test, the support arrangement can be assumed to provide also axial restraints of non-negligible magnitude. The rotation of the sheeting at support seems to be free, but the axial movement does not. This conclusion is strongly supported also by the results of the finite element analyses, as given below, where the stiffness of an axially unrestrained beam is much smaller than that observed in the test. However, if the axial restrain condition is applied at the supports, the stiffness corresponds quite closely to the test result.

A number of analyses were run using different average element sizes, different load application periods and different support boundary conditions. Figure 4.12 shows results for ABAQUS/Explicit - analyses using an average element size equal to 10 mm (referring to the length of the edge of a rectangular shell element). The curves' names show the element size and the load application period ("0p1sek" stands for 0.1 seconds, "1p0sek" stands for 1.0 seconds). In the first two (basic) models, the axial displacement of the beam was not restrained anywhere in the model. This means that as the loading presses the beam down at midspan, the supports can translate towards the loading area. As can be seen, the analyses give a very good estimate of the ultimate load for this model, but the stiffness is considerably lower than observed in the test. When the axial displacement of just one of the supports is prevented (models tagged with "_onesup_u3"), the results are practically the same. However, when the axial displacement of both supports is restrained (models tagged with "_sup_u3") the stiffness is very close to that observed in the test. For some reason, though, the ultimate load is then reached a little earlier. For instance, the ultimate load for curve "u2_rf2_10mm_1p0sek_sup_u3" was 1517 N, i.e. 6 % less than that observed in the test. This is still a very good estimate.

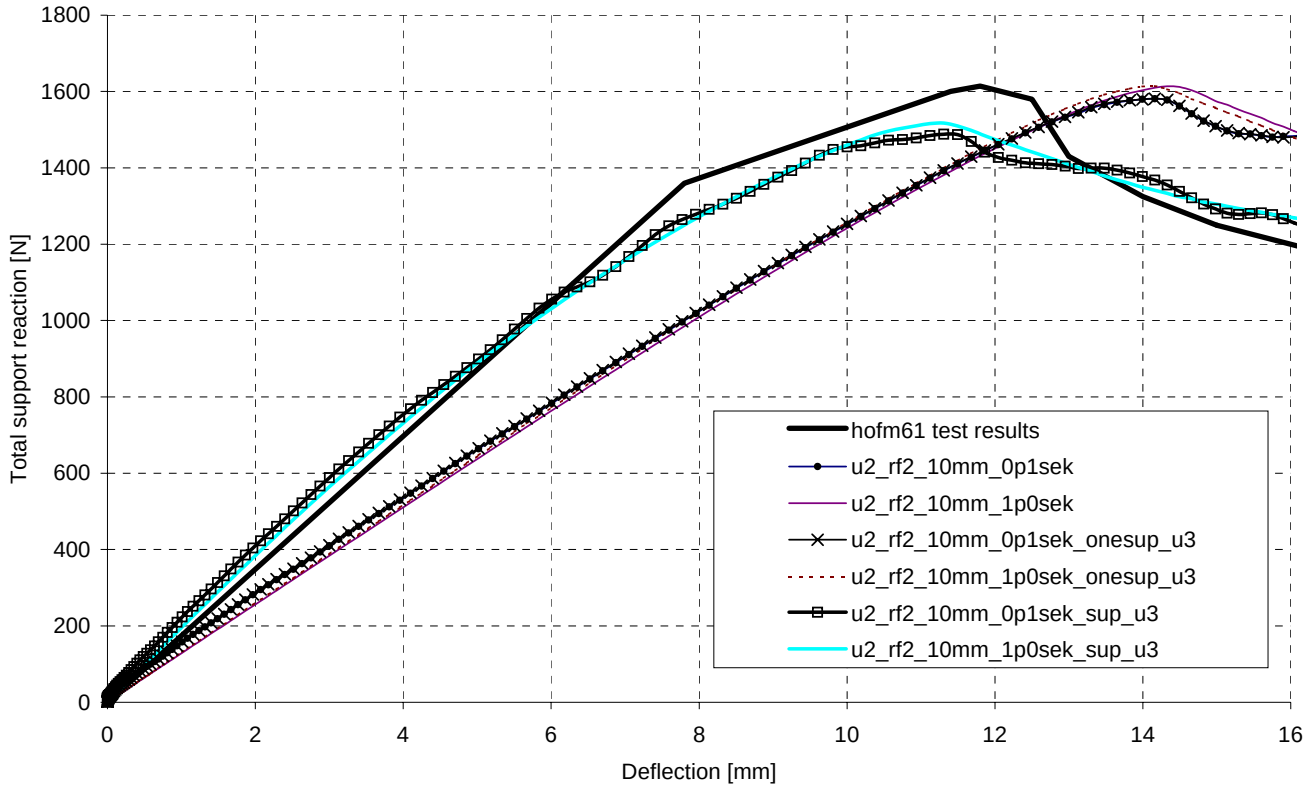

Fig. 4.12 ABAQUS/Explicit results for test hofm61 using an average element size equal to 10 mm.

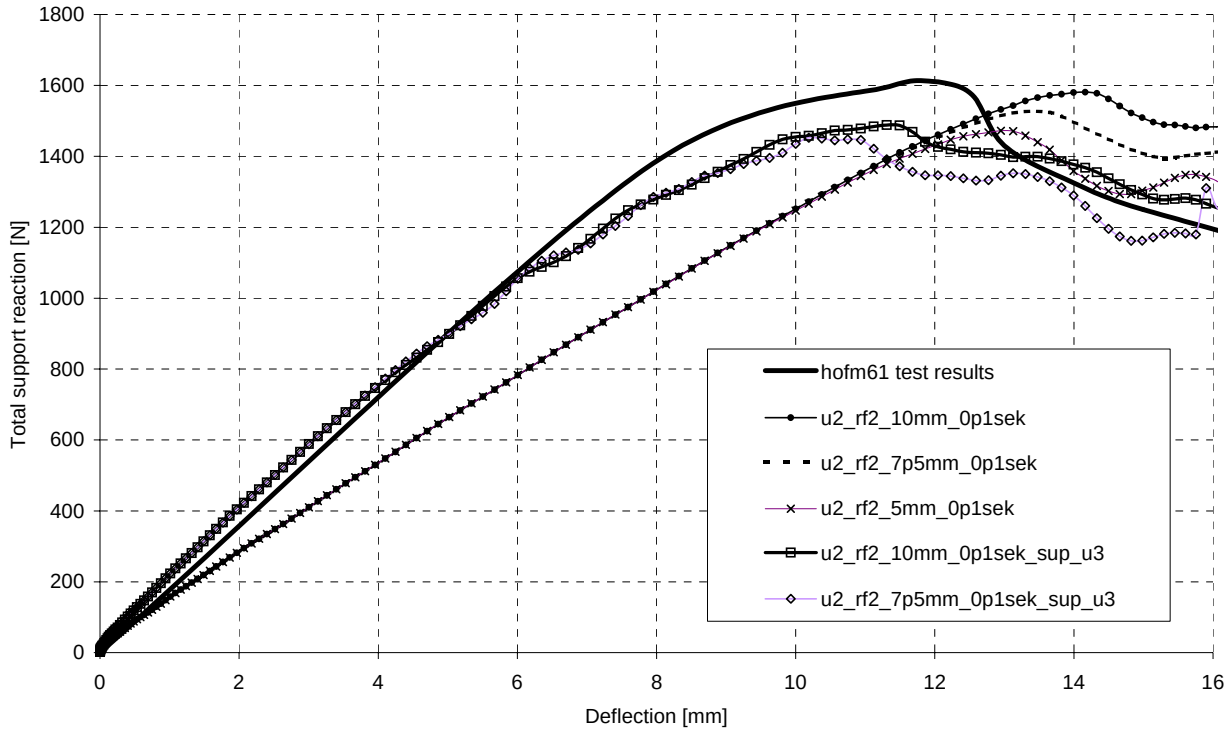

Fig. 4.13 ABAQUS/Explicit results for test hofm61 using different average element sizes, load application times and support boundary conditions.

Figure 4.13 shows another comparison among different ABAQUS/Explicit analysis models. These curves show the effects of varying the mesh density for models with axially unrestrained or axially restrained support boundary conditions. It can be seen that changing the mesh density does not influence the initial stiffness of the models, but that the ultimate load is slightly decreased when the mesh is made denser. For instance, the ultimate load for the model using an average element size equal to 5 mm is 7 % smaller than that for the model using an average element size equal to 10 mm and 8.8 % smaller than the test result for the case where all axial displacements are free.

The web crippling deformations of different models are compared to the test curve in Figure 4.14. The form of the web crippling deformation curve obtained from test hofm61 is rather interesting in that after the ultimate load has been reached, the web crippling deformation starts to decrease strongly and at the end of the test, the value of the deformation changes sign and becomes negative, i.e. the height of the profile actually seems to increase. This effect is due to the measurement technique used in the test and the unsymmetrical deformation form, as shown in Figure 4.15. In the finite element models, the web crippling deformation was in

fact measured in the same way ("a-b" in Figure 4.15), but the failure deformation mode was symmetric, so the aforementioned effect is not seen.

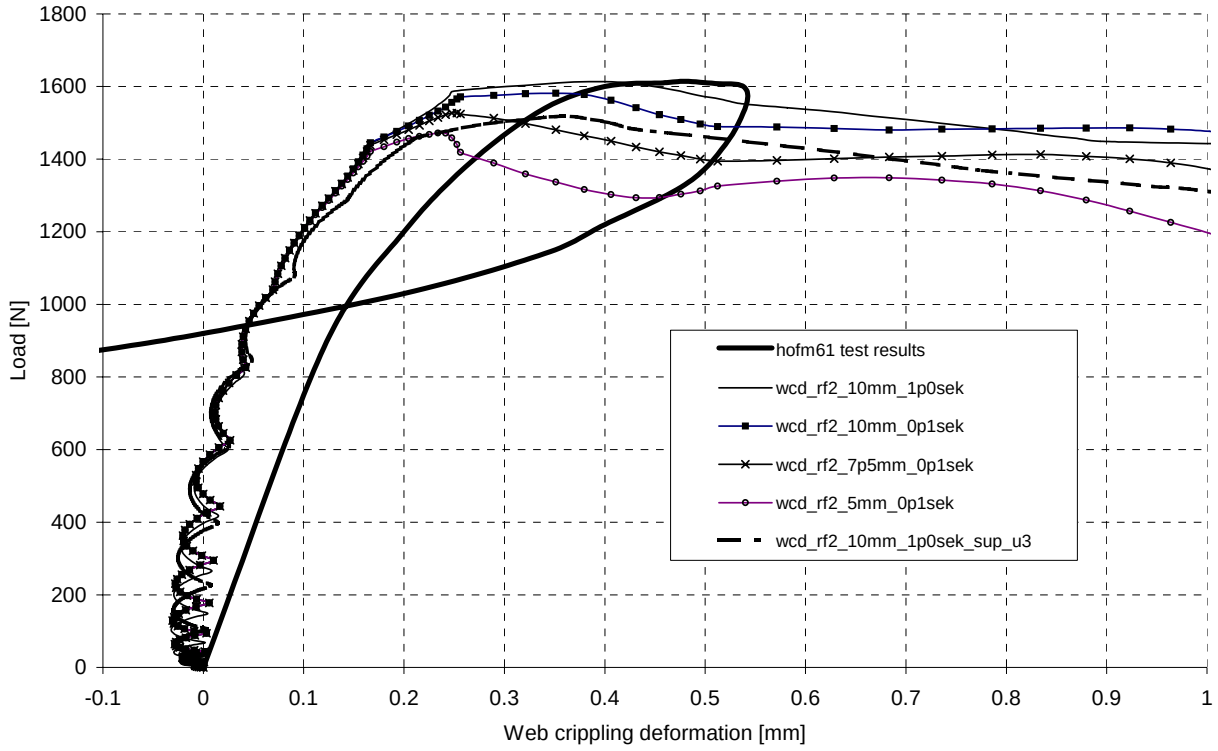

Fig. 4.14 Web crippling deformation from ABAQUS/Explicit results for test hofm61 using different average element sizes, load application times and support boundary conditions.

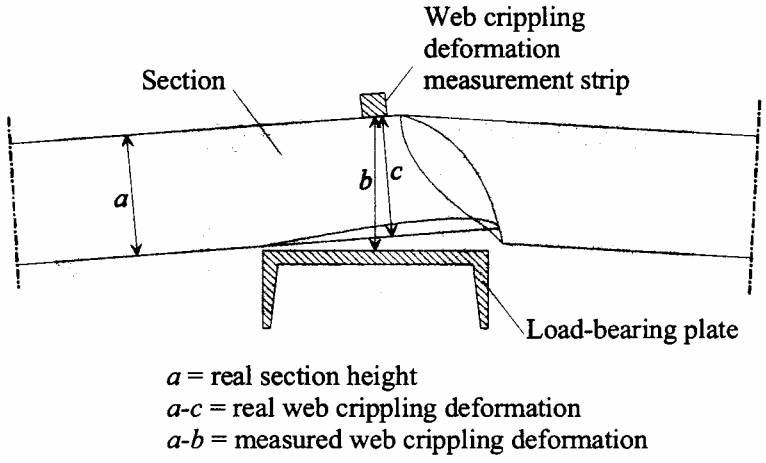

Fig. 4.15 Measured vs. real web crippling deformation for the yield eye post-failure mode of test hofm61 (Hofmeyer 2000).

The differences in web crippling deformation among different models are not too important, as seen in Figure 4.14. Although the web crippling stiffness is not exactly the same as

measured in the test, the curves are all qualitatively fairly similar up to the ultimate load and the changes in stiffness are modelled rather accurately. The existence or non-existence of the axial boundary condition at the supports does not seem to have an important influence. The small fluctuations at the start of the analyses are most likely due to the dynamic damping effects in the analysis procedure. It should be noticed that the scale of the graph is quite large and that the actual magnitude of the fluctuations is in fact about 0.03 mm.

It is the author's strong belief that the unsymmetrical post-failure deformation mode, i.e. the yield-eye failure mode, is a consequence of initial imperfections in the actual structures. Its occurrence is clearly more likely in longer beam elements with a relatively narrow concentrated load area than with shorter beams with a relatively large loading area. If the ideal structure and situation are considered, there can be found nothing unsymmetrical in either. The structure itself, the loading conditions, and the support conditions are all symmetrical about a plane drawn at the midspan of the beam. The material of the beam is homogenous throughout. Therefore an unsymmetrical failure mode should only occur in case of small initial non-symmetries in the actual structures. These could be modelled in ABAQUS using for instance different buckling modes as bases for imperfection shapes, but the results obtained using the ideal model are very consistent with the test results, and therefore the inclusion of imperfection modes was deemed unnecessary. It is assumed that their influence on the stiffness and ultimate load behaviour of the structure is not important, even if they may cause the non-symmetry of post-failure modes. Cases, where the loading is applied centrically in the plane of the web, these initial imperfection modes may prove to be essential for the correct modelling of the structure.

4.3 Preliminary FE-models on cassette sections

Before the tests described in Chapter 3 were carried out, some preliminary FE-analyses were run using ABAQUS/Explicit on models similar to the tested specimens in order to obtain an approximate prediction of the behaviour of the specimens during ITF-tests. A type drawing of the modelled sections is shown in Figure 4.16. It should be noted that in these initial models, the flanges of the section point to the same direction, while in the tested specimens (Chapter 3), the flanges pointed in opposite directions.

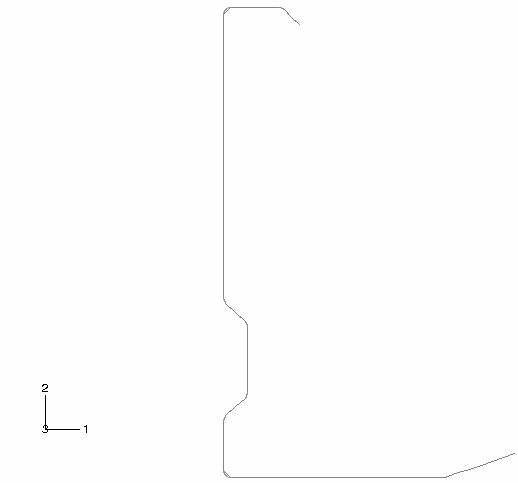

Fig. 4.16 Type drawing of cross-section modelled during the preliminary analyses.

The loading and support pads were modelled using rigid elements of type R3D4 and the cassette section using shell elements S4R. The connections between the pads and the flanges of the structure were modelled using contact surfaces in order to reproduce the real structural behaviour as closely as possible, although the complexity of the approach makes it not the most economical on CPU-time. However, this approach allows the separation of the contact surfaces also after initial contact, making the behaviour of the local contact area more realistic. The contact surfaces had zero friction and were modelled as hard surfaces. The loading was applied by using a prescribed displacement of the loading pad pressing on the wide flange. The application of the displacement was done using the smooth step function in ABAQUS, which makes the initial phase of the displacement slower and thus allows for the structure to smoothly deform from its original state.

The lateral (U1) and longitudinal (U3) displacements were restrained at the mid-length at both flanges of the cassette similarly to what was done in the test set-up as described in Chapter 3.

The rotation about axis 3 (UR3) was restrained along lines at each flange as shown in Figure 4.17. This was done in order to prevent the bending of the flanges that was observed in initial models where this boundary condition was not present.

Figure 4.18 shows a comparison between the FE-analysis results and the corresponding test results for tests ITF100-t10-2 and ITF200R-t15-3. When the curves are analysed, it should be kept in mind that the preliminary FE-models were based on the ideal nominal cross-section without any imperfections and nominal material data, i.e. a value of yield stress equal to 350 N/mm^2 and a value of the modulus of elasticity equal to 210000 N/mm^2. Double precision was used for the ABAQUS/Explicit analyses.

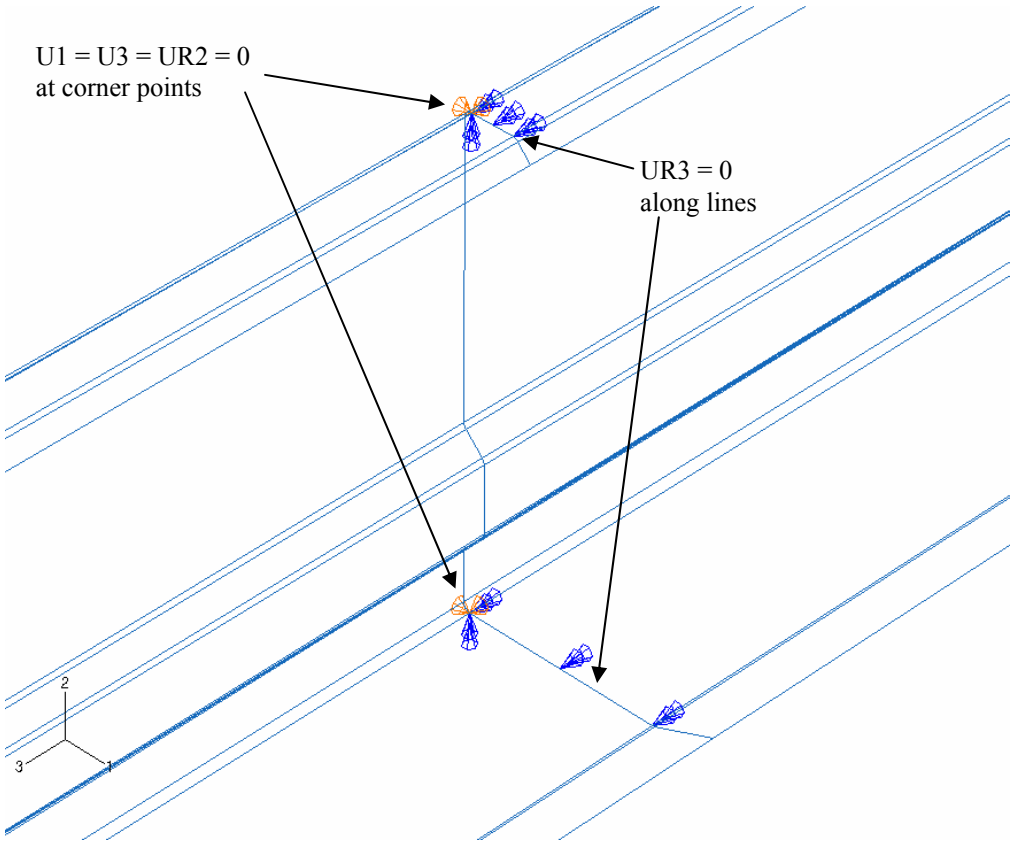

Fig. 4.17 Boundary conditions at load application area.

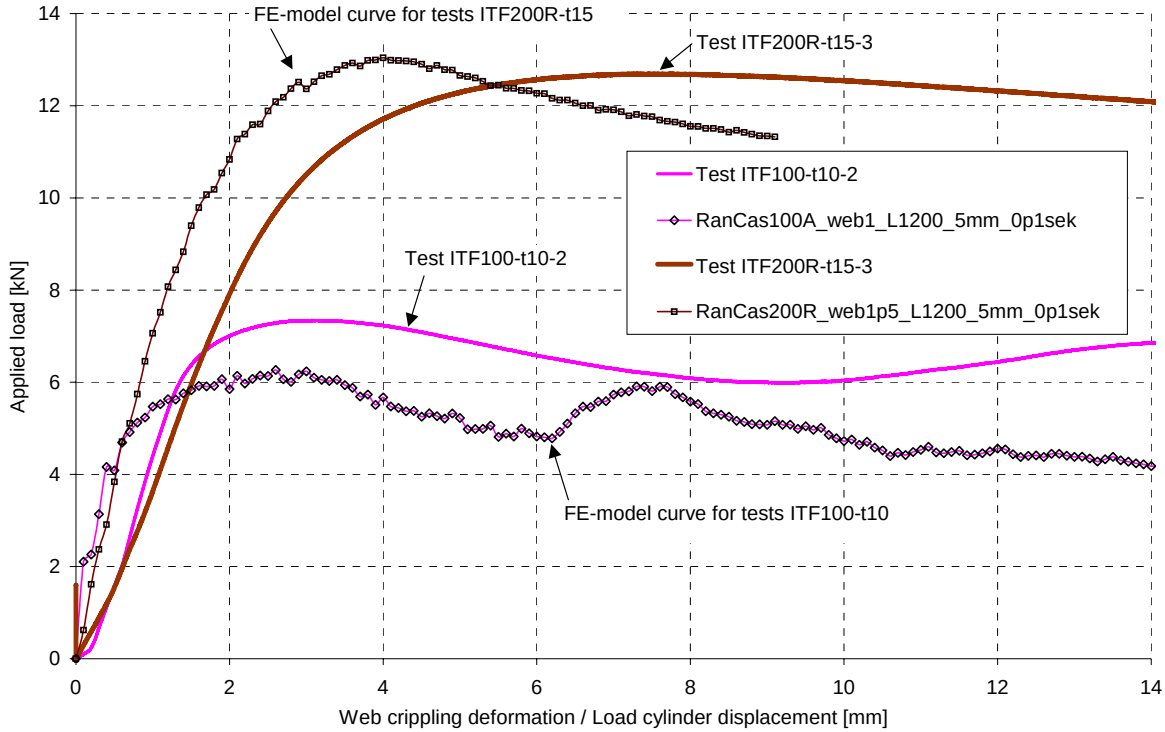

Fig. 4.18 Comparison of preliminary FE-analysis results and ITF-test results.

The first set of curves corresponds to 100 mm high flat web sections with t_{nom} = 1.0 mm. The preliminary load-deformation curve from the FE-analysis for test ITF100-t10-2 has a slightly higher initial stiffness than the test result, but does not quite reach the same failure load. It seems likely that the pre-buckling stiffness of the tested element with a flat web was lowered by the initial imperfections in the cross-section. The higher ultimate load, on the other hand, is mostly influenced by the yield strength, which was determined as 396 N/mm^2 in the direction of cold forming and 437 N/mm^2 in the direction perpendicular to the direction of cold forming, as seen from Tables 3.1.

The second set of curves corresponds to longitudinally stiffened 200 mm high web sections with t_{nom} = 1.5 mm. Here again the initial stiffness recorded during the FE-analysis is higher than that obtained from the test. However, the ultimate load is close to the value obtained in the test. The yield strength of the test specimen was determined as 397 N/mm^2 in the direction of cold forming and 429 N/mm^2 in the direction perpendicular to the direction of cold forming, as seen from Tables 3.5. The height of the web measured for specimen ITF200R-t15-3 was 203.9 mm, as seen from ANNEX A, while the total nominal web height is 201.5 mm, as modelled for the FE-analysis. It is possible that the initial imperfections and

the slightly greater web height of the tested specimen compensate the higher yield strength, which together lead to a lower ultimate load than would otherwise be expected for an ideally straight specimen.

Table 4.5 presents the ultimate load values $F_{FE\text{-}PRE}$ evaluated using FE-analysis before testing for all tested sections. When compared with the corresponding average test results F_{Test}, also presented in the Table, it can be seen that the preliminary analyses were able to predict the failure load with about 20 % accuracy for all models. For the 200 mm high sections, the predictions were within 3 % of the test result. The predictions for 150 mm high sections were within 15 % and the weakest agreement could be obtained for the 100 mm high sections. Larger differences can be seen in the force displacement values w at failure load.

Table 4.5 Comparison of preliminary FE-results with test results

Section type	t_{nom} [mm]	$F_{FE\text{-}PRE}$ [kN]	Average F_{Test} [kN]	$F_{FE\text{-}RPE}$ / F_{Test}	w at $F_{FE\text{-}PRE}$ [mm]	w at F_{Test} [mm]
100	1.0	6.20	7.45	0.83	1.7	3.08
100R	1.0	4.75	6.02	0.79	4.0	7.52
150	1.0	5.80	6.34	0.91	2.0	5.34
	1.5	14.00	16.56	0.85	2.0	3.42
150R	1.0	4.70	5.27	0.89	4.0	8.68
	1.5	12.00	12.90	0.93	3.6	7.34
200	1.0	6.70	6.51	1.03	1.0	6.16
	1.5	16.00	16.24	0.99	0.6	4.67
200R	1.0	5.30	5.14	1.03	6.0	8.94
	1.5	12.70	12.71	1.00	4.0	7.70

Regardless of the differences in stiffness and ultimate load values between the preliminary FE-models and the test results, it can be concluded that a fairly good estimate of the behaviour of the test specimens could be obtained already before the testing using the modelling assumptions that had been studied during the modelling of the Hofmeyer (2000) experiments in Section 4.2. The shapes of the load-deformation curves are very descriptive of those recorded during tests and even the second local maximum of the curve for the flat web specimen was successfully modelled.

4.4 FE-analyses on tested cassette sections

General

A substantial amount of development work was put into the refinement of the FE-models described in Section 4.3 in order to obtain an even closer correspondence to the test results. The work was begun with the modelling of test ITF200-t15-3 with a flat web, continued with tests ITF200R-t15-3, ITF200R-t10-2 and ITF100R-t10-1 with longitudinally stiffened webs, and concluded with test IOF200R-t15-S1000-2 with a longitudinally stiffened web and IOF-loading with a span equal to 1000 mm.

The material model used for these analyses was based on the actual material tests on specimens cut in the direction perpendicular to the direction of cold forming as given in Section 3.2. The tables giving the basic material data corresponding to different modelled tests are given in Table 4.6. The values of stress and strain from the material test data were transformed into true plastic stress and true strain values according to the ABAQUS/Standard Getting Started User's Manual. Double precision was used for all the analyses.

Table 4.6 Material data used for numerical models.

Nominal web height b_w (mm)	Nominal steel sheet thickness t_{nom} (mm)	Steel coil number	Table number
200	1.5	KH089002	Table 3.5b
200	1.0	KF943005	Table 3.4b
100	1.0	FT019002	Table 3.1b

The support conditions were similar to what was described in Section 4.3, except that at both flanges, boundary conditions were applied at the locations where the screw connections were situated in the tests (Chapter 3). Thus, in each flange, there were two points at 20 mm distance from the web, where U1 = U3 = UR2 = 0 and two lines where UR3 = 0 – otherwise as shown in Figure 4.17. The models were based on the measured cross-sections of the tested specimens as given in ANNEX B.

A parametric study was carried out in order to see the influence of different analysis settings and model characteristics on the results. The parameters varied during the development work were:

- the length of the load application period {0.1 sec; 0.5 sec; 1.0 sec; 2.0 sec; 3.0 sec; 5.0 sec},
- the magnitude of the maximum imperfection value {0.001 m; 0.002 m; 0.003 m}, and
- the average element edge length {10 mm; 5.0 mm; 2.5 mm}.

It is noted that initial imperfections were applied also to the models on longitudinally stiffened web sections despite the inherent eccentricity in the section due to the stiffener. This was done in order to qualitatively reproduce the actual measured shape of the tested specimens (see Chapter 3).

Modelling of test ITF200-t15-3

Figure 4.19 shows the influence of the load application period on the results of the finite element analyses corresponding to test ITF200-t15-3. It can be seen that the influence of the variation of the load application period between 0.1 seconds and 5.0 seconds has a negligible influence on the results. Therefore it was decided that it would be most practical to use a load application period equal to 0.1 seconds, as this is the most economical on CPU-time.

Figure 4.20 shows the influence of the magnitude of the maximum value of the geometric initial imperfection for models with average element edge length 5 mm. It can be seen that the increase of the magnitude of the initial imperfection slightly lowers the stiffness and the ultimate load values reached in the analysis, which seems intuitively correct. It is considered that the use of maximum initial imperfection magnitude equal to 0.001 m is adequate for the analyses.

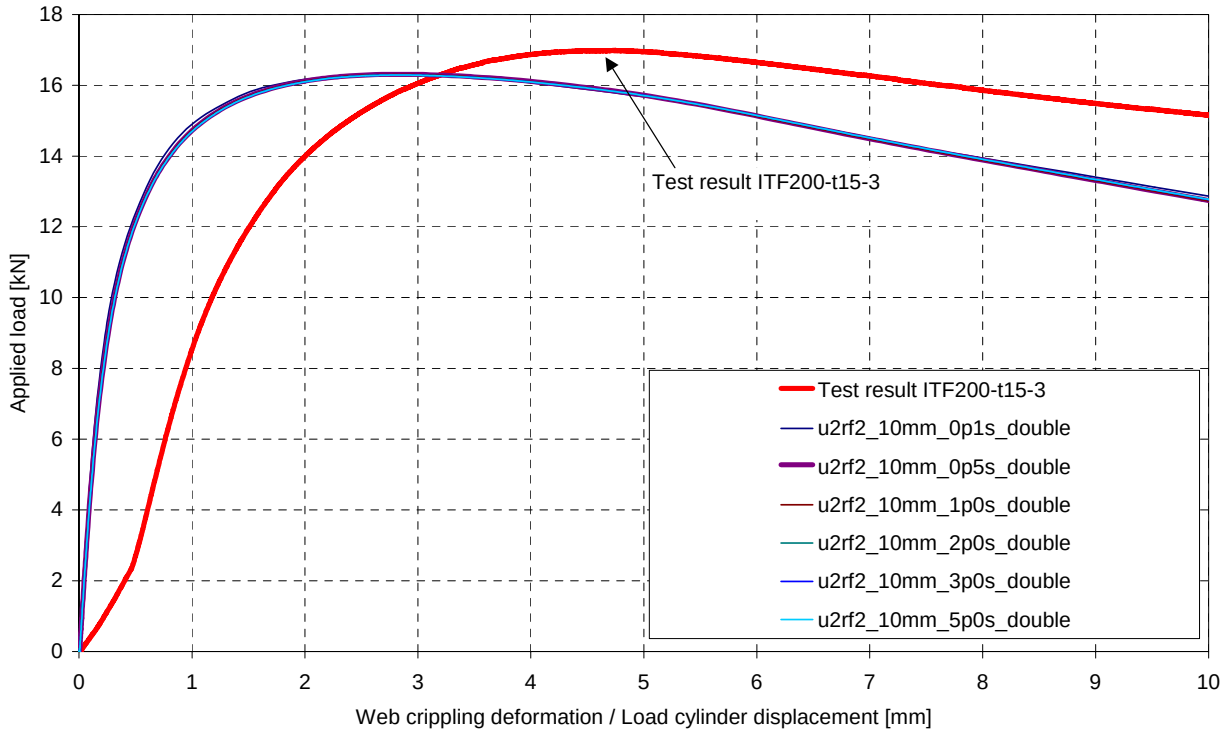

Fig. 4.19 Influence of load application period on FE-models.

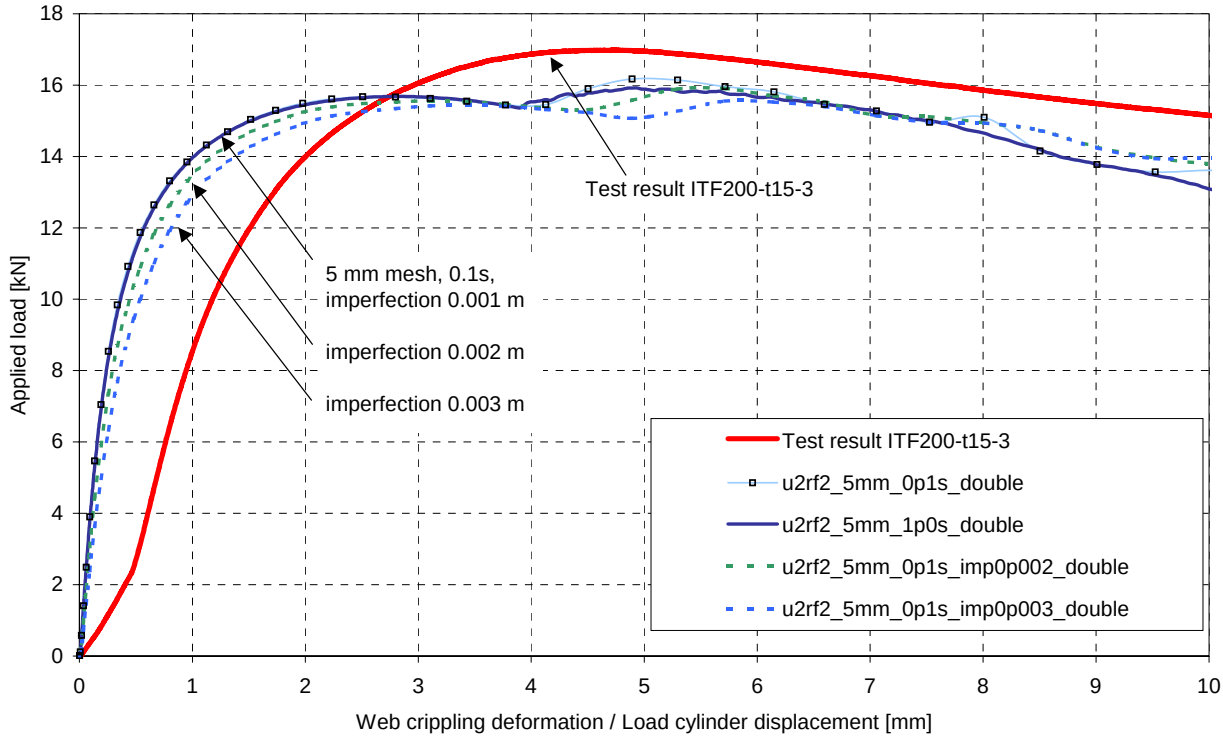

Fig. 4.20 Influence of initial imperfection magnitude on FE-models.

The influence of the average element edge length on the FE-analysis results can be seen in Figure 4.21. Of the three parameters (load application period, initial imperfection magnitude and average element edge length) varied during the development of the finite element models, these results are the most difficult to interpret and make definite conclusions from. It can be seen that the initial stiffness of the three models with different element sizes is practically the same, but that after the first elastic linear phase, the curves start to divert from each other so that the smaller the element size, the lower its stiffness is during the latter part of load increase. This is in fact to be expected, because a coarser mesh generally leads to a stiffer model, as is the case here. In all three cases, however, the stiffness is greater than was measured during the test.

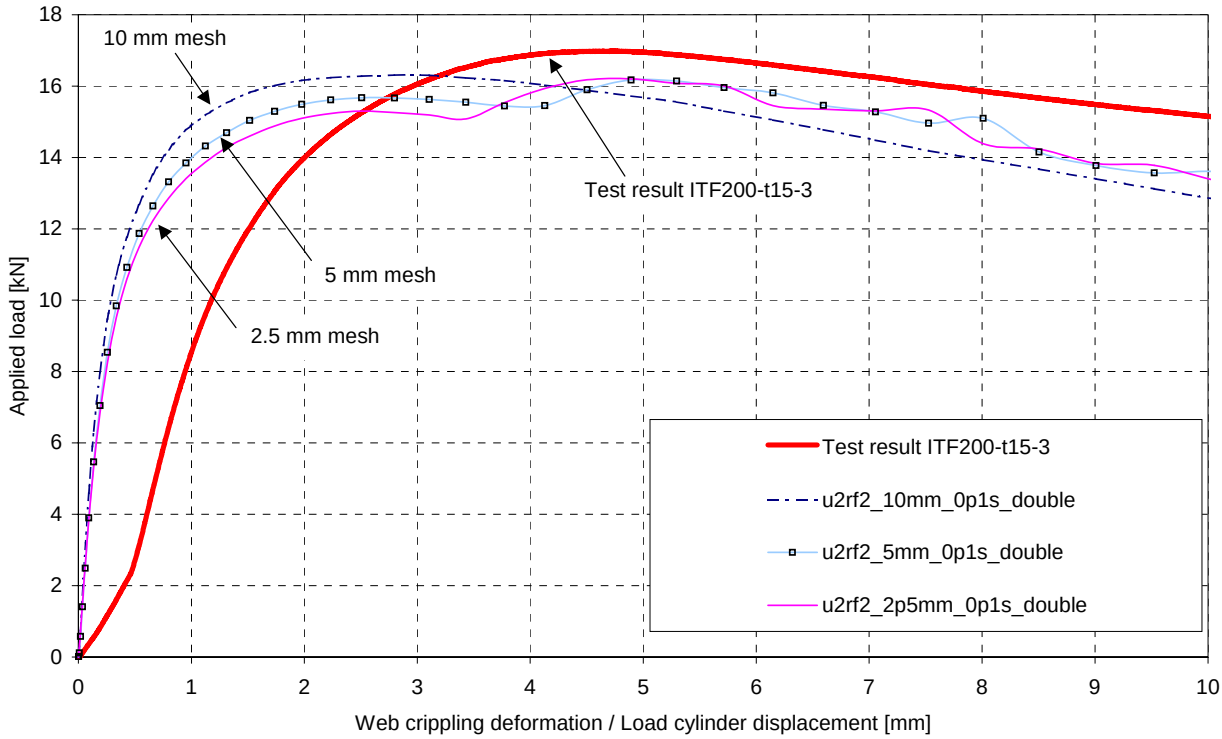

Fig. 4.21 Influence of average element edge length on FE-models.

Another conclusion to be made on the basis of Figure 4.21 is that the coarser the mesh, the higher the ultimate load reached during the analysis, although the differences here are not so large either. However, there are slight differences in the shapes of the curves after the first local maximum load. The model with element edge length equal to 10 mm appears to be most similar to the test curve, while the load in the models with element edge sizes equal to 5 mm

and 2.5 mm seems to first decrease just a little after the local maximum after which it suddenly starts to increase again, reaching a higher load value than the first local maximum.

The higher stiffness of the model with element edge length 10 mm is exemplified by the value of the lowest buckling load. Although the shapes of the lowest buckling modes for models with 10 mm and 2.5 mm edge length are similar (see Figure 4.22), the corresponding buckling load for the model with 10 mm element size is 11.57 kN, while it is 10.80 kN for the model with 2.5 mm element size.

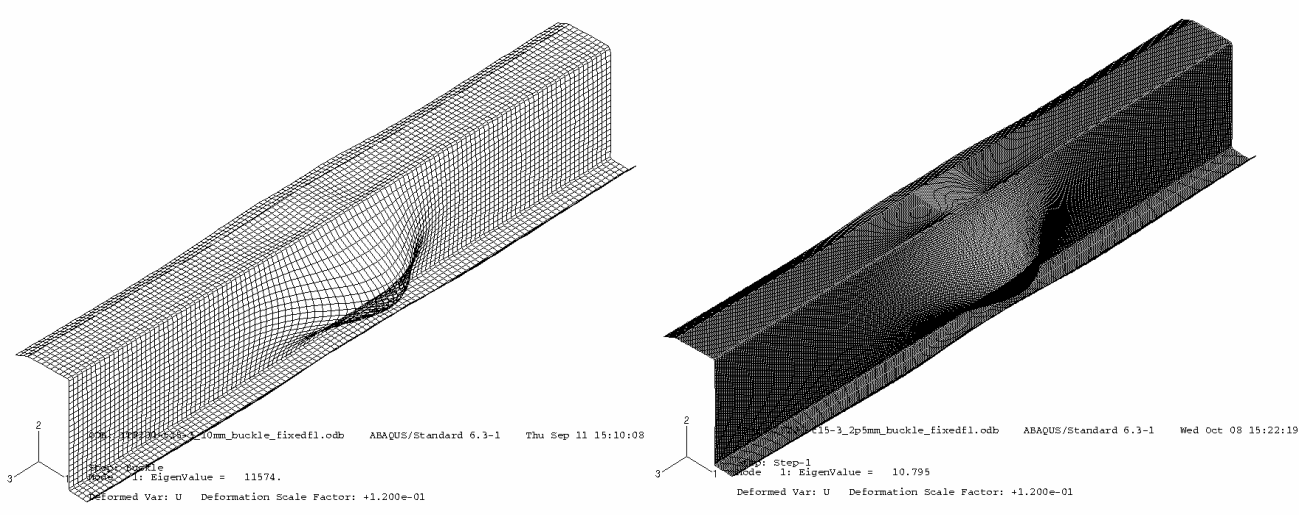

Fig. 4.22 Lowest buckling modes for ITF200-t15-3 models with average element edge length 10 mm (left) and 2.5 mm (right). The deformations are scaled in the picture so that the largest displacement is equal to 120 mm.

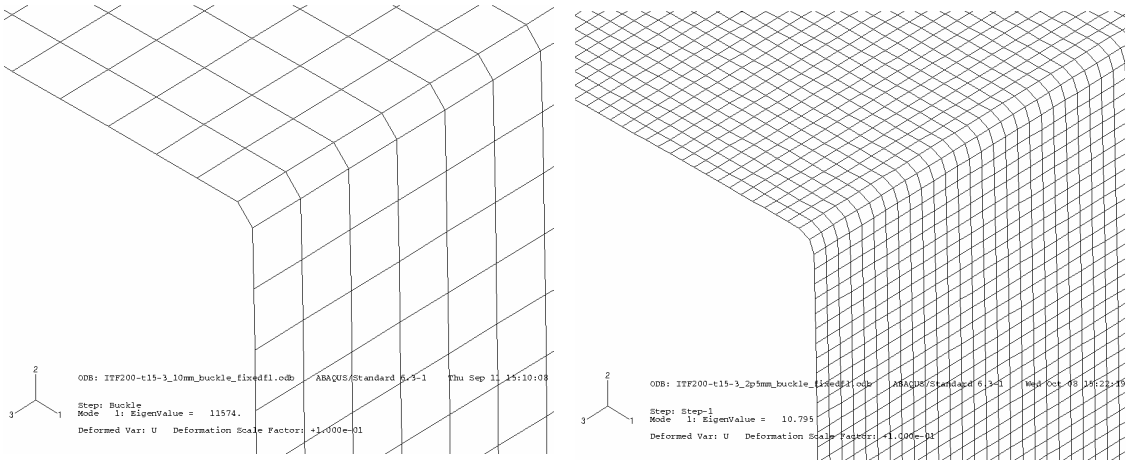

Fig. 4.23 Detail of corner area for ITF200-t15-3 models with average element edge length 10 mm (left) and 2.5 mm (right).

Another factor in the modelling is the precision of the mesh in the corner area, as shown in Figure 4.23 for the models with average element edge length 10 mm and 2.5 mm. The corner is modelled with a single element in the coarser mesh, while two elements are used in the denser mesh. The stresses and strains will be more precisely modelled using the denser mesh.

It is likely that the differences in the load-displacement curves in Figure 4.21 are due to the factors explained above. Furthermore, especially local buckling phenomena are more precisely modelled using the denser element mesh. The question arises therefore, why does the shape of the load-displacement curve from the model with the coarser mesh (10 mm edge length) seem to be closest to the shape of the test curve. No clear answer has been found. However, it should be kept in mind that the geometric initial imperfections in the actual test specimen cannot be modelled precisely. Also, possible residual stresses in the test specimen and stresses due to the fitting of the specimen onto the test rig (see Chapter 3) have not been modelled. Nevertheless, it is considered that all of the above models give a fair estimate of the web crippling behaviour of the structure at hand. Therefore an element mesh based on an average element size equal to 5 mm is chosen for further analyses while the corners are modelled using two elements.

Modelling of test ITF200R-t15-3

The load-displacement curves for test ITF200R-t15-3 on a longitudinally stiffened web section and three corresponding finite element models are given in Figure 4.24. The element edge length was varied from 5 mm to 2.5 mm, but hardly any effect of this can be seen in the resulting curves. All in all the correspondence with the test is quite satisfactory, although the FE-models again show higher values of initial stiffness and lower values of ultimate load. The shapes of the curves are very similar, however, and the differences in the values of ultimate load are within the 10 % range of the test result.

The influence of the lateral support in the plane of the flanges (x-direction) was studied by introducing a spring element to the points where the screws were connected in the test. In the tests and in all the finite element models so far, the x-displacements of the flanges were fully restrained. This is not necessarily the case in all practical cases, however, which is why the

influence of elastic springs was considered. The spring constant was taken equal to 350 N/mm, which corresponds to a common value used for gypsum boards connected with screws (Kesti 2000). A model with only one spring per flange and no other lateral restraints was also run (curve u2_rf2_5mm_0p1s_onespring350). As can be seen from Figure 4.24, the influence of the spring supports on the web crippling behaviour is negligible.

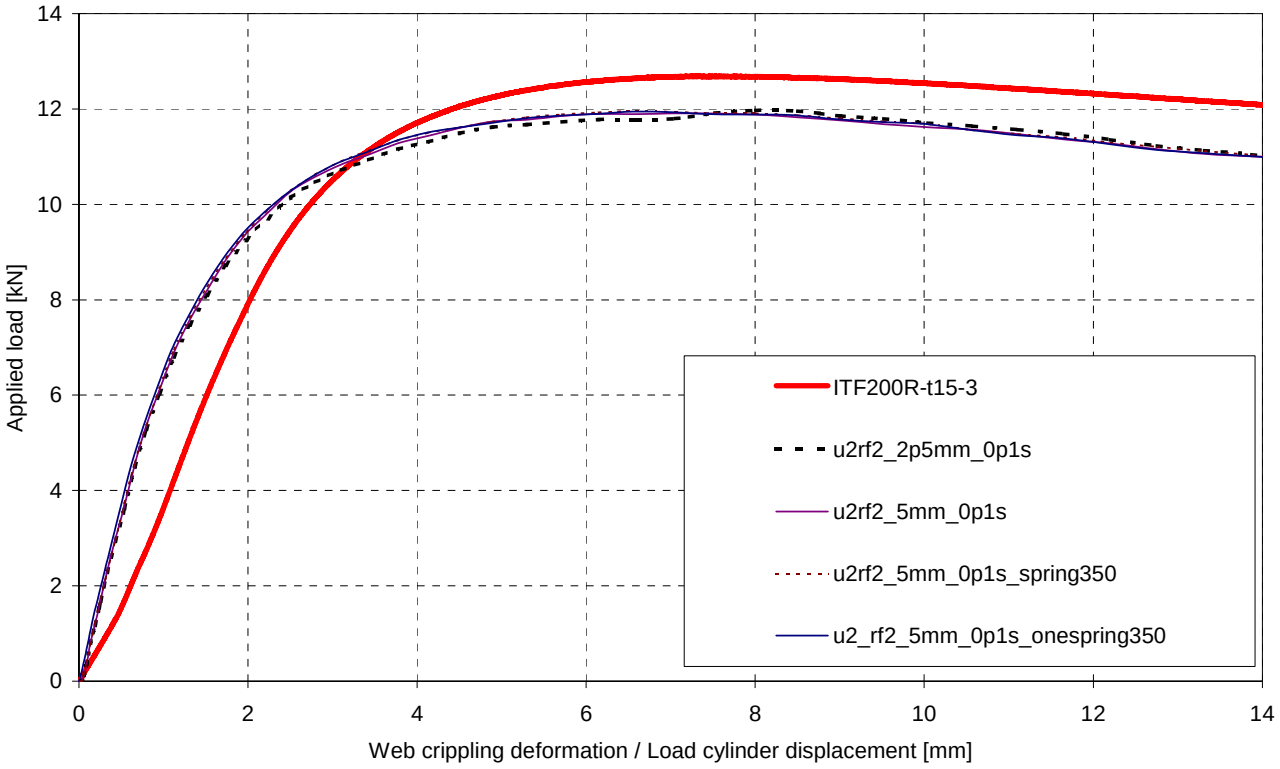

Fig. 4.24 Load-displacement curves for test ITF200R-t15-3 and corresponding FE-models.

Modelling of test ITF200R-t10-2

The load-displacement curves for test ITF200R-t10-2 and the corresponding finite element model are given in Figure 4.25. The element edge length was 5 mm and the model included an initial imperfection of maximum amplitude 1.0 mm based on the lowest buckling mode. The agreement between the curves is quite good overall. The ultimate load reached during the analysis was 5.00 kN (at 8.0 mm displacement) and the ultimate load reached in the test was 5.08 kN (at 8.8 mm). The stiffness values and the curve shapes are also similar. The failure mode can be seen in Figure 4.26. It is similar to the failure mode observed during the test (see Figure 4.27).

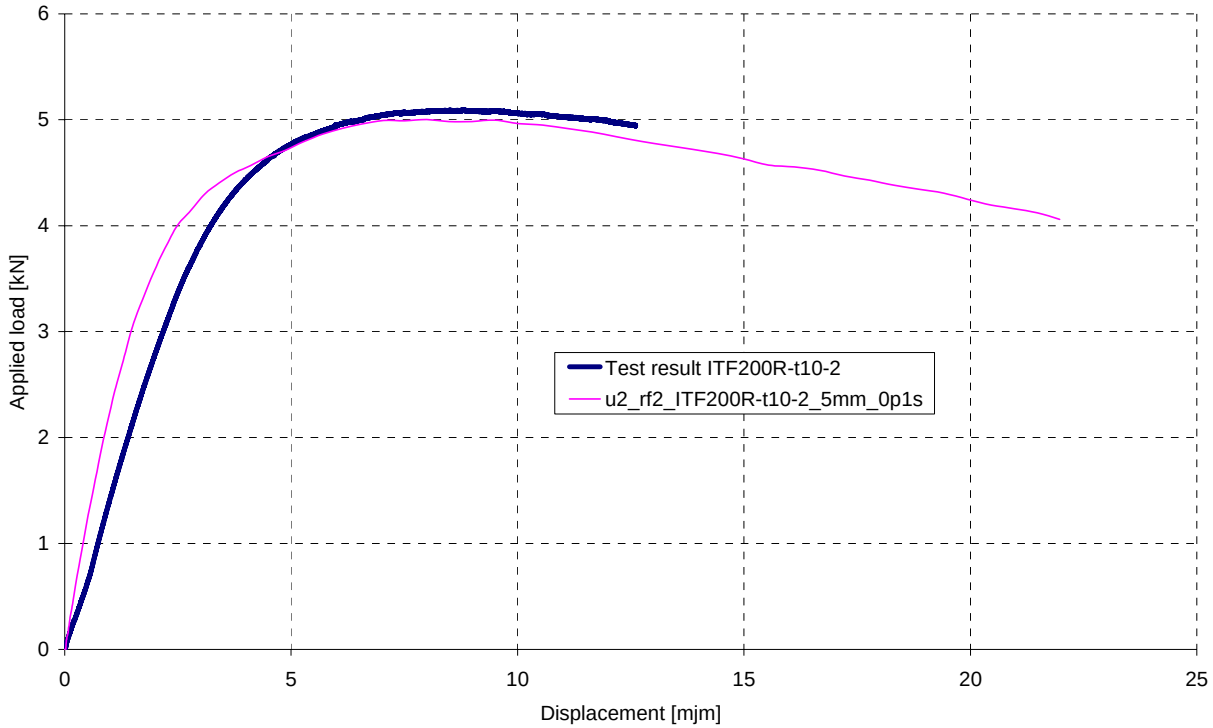

Fig. 4.25 Load-displacement curves for test ITF200R-t10-2 and corresponding FE-model.

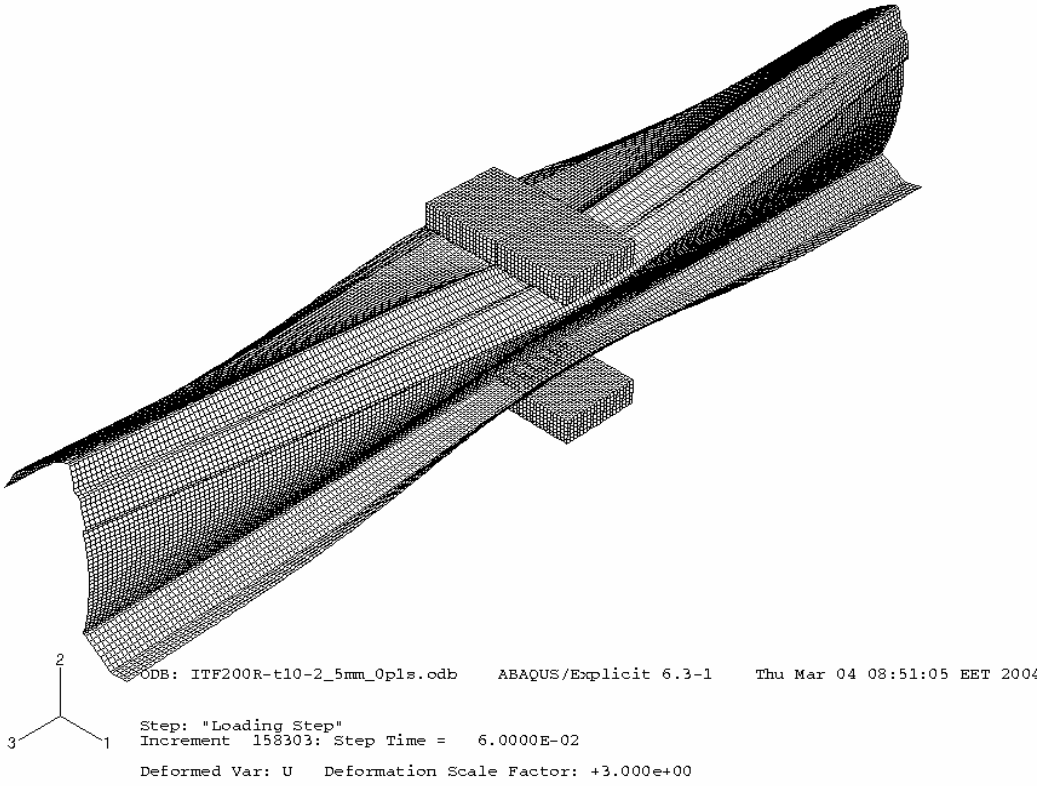

Fig. 4.26 Failure mode for model ITF200R-t10-2_5mm_0p1s, deformation scale factor 3.0.

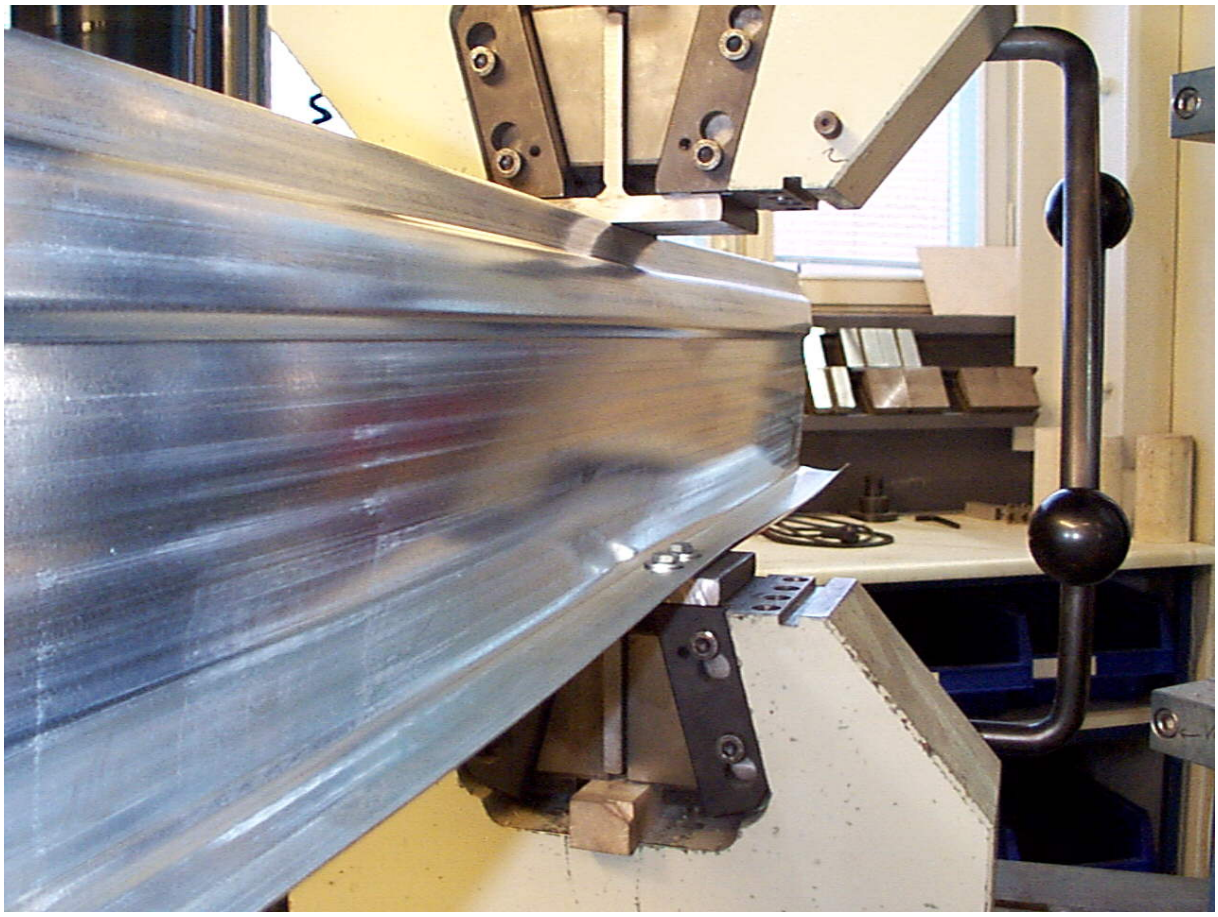

Fig. 4.27 Failure mode for test ITF200R-t10-2.

Modelling of test ITF100R-t10-1

The load-displacement curves for test ITF100R-t10-1 and the corresponding finite element model are given in Figure 4.28. The element edge length was 5 mm and the model included an initial imperfection of maximum amplitude 1.0 mm based on the lowest buckling mode. The agreement between the curves is very good overall. The ultimate load reached during the analysis was 6.23 kN (at 8.5 mm displacement) and the ultimate load reached in the test was 6.01 kN (at 7.5 mm). The stiffness values and the curve shapes are also very similar. The failure mode can be seen in Figure 4.29. It is quite similar to the failure mode observed during the test (see Figure 3.9).

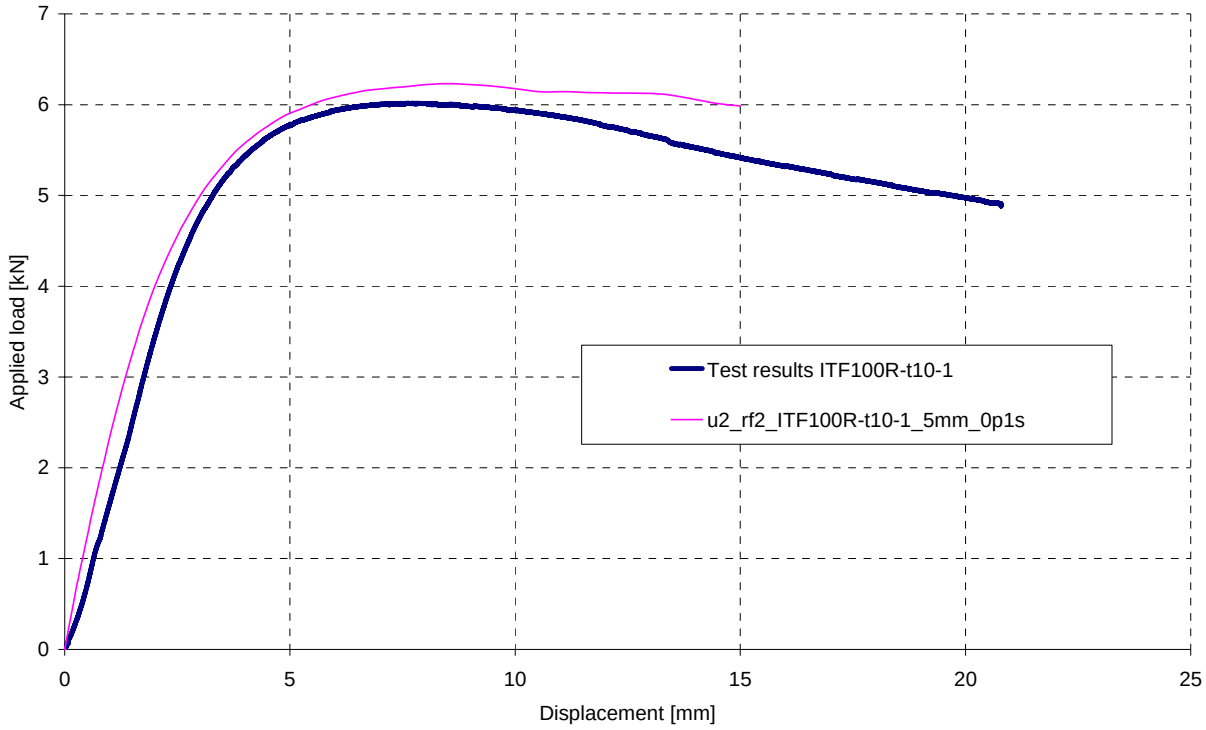

Fig. 4.28 Load-displacement curves for test ITF100R-t10-1 and corresponding FE-model.

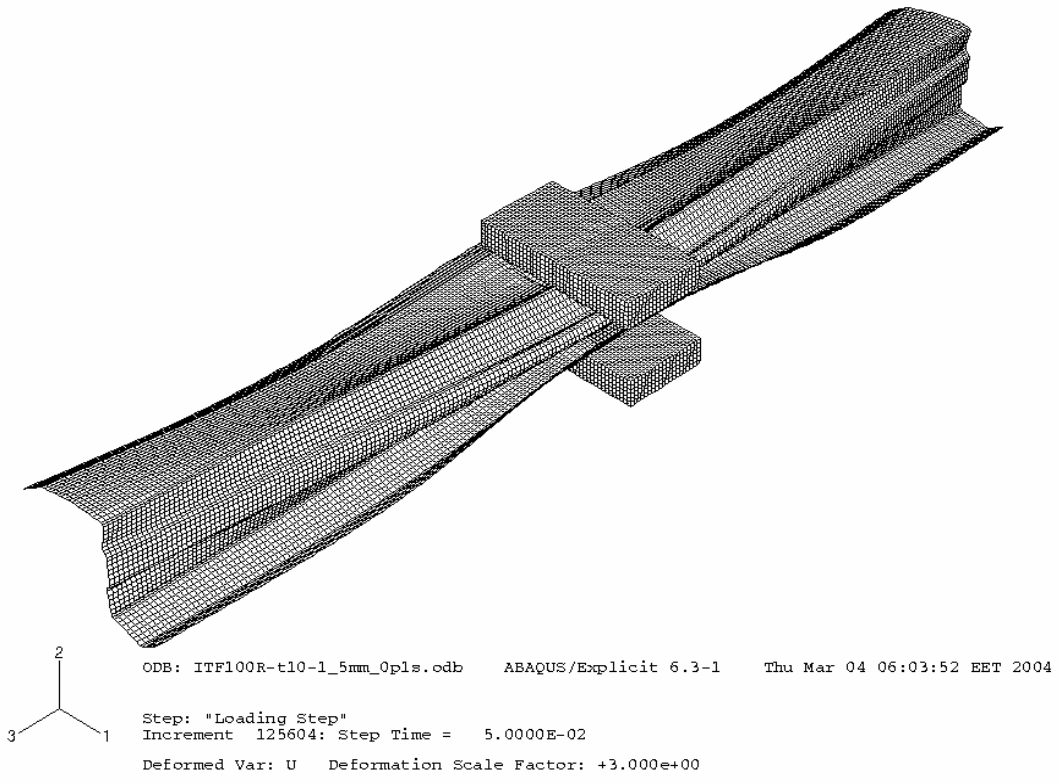

Fig. 4.29 Failure mode for model ITF100R-t10-1_5mm_0p1s, deformation scale factor 3.0.

Modelling of test IOF200R-t15-S1000-2

An attempt was also made to model the internal one-flange test IOF200R-t15-S1000-2. This model was edited from the corresponding ITF-model by removing the support block at mid-span and modelling 40 mm long support strips at the ends of the beam using a stronger material with modulus of elasticity $E = 3.5 \cdot 10^{15}$ N/m^2 and $f_y = 3.5 \cdot 10^{11}$ N/m^2 as shown in Figure 4.30. Vertical displacement boundary conditions (U2 = 0) were applied at the bottom flange nodes at $z = 0.100$ m and $z = 1.100$ m. Lateral displacement boundary conditions (U1 = 0) were applied at the webs from the bottom flange to the lower edge of the stiffener at the same z-locations. These boundary conditions were used to model the T-shaped support rods described in Section 3.4.1.

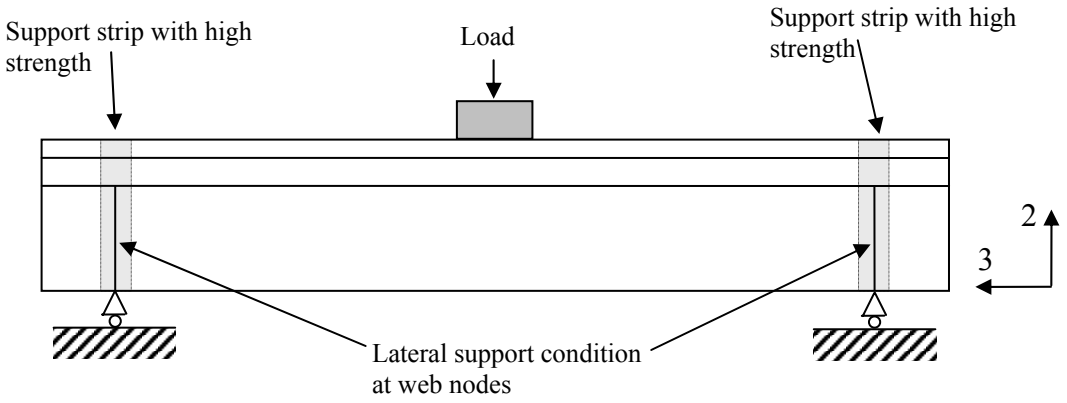

Fig. 4.30 Set-up of IOF-model.

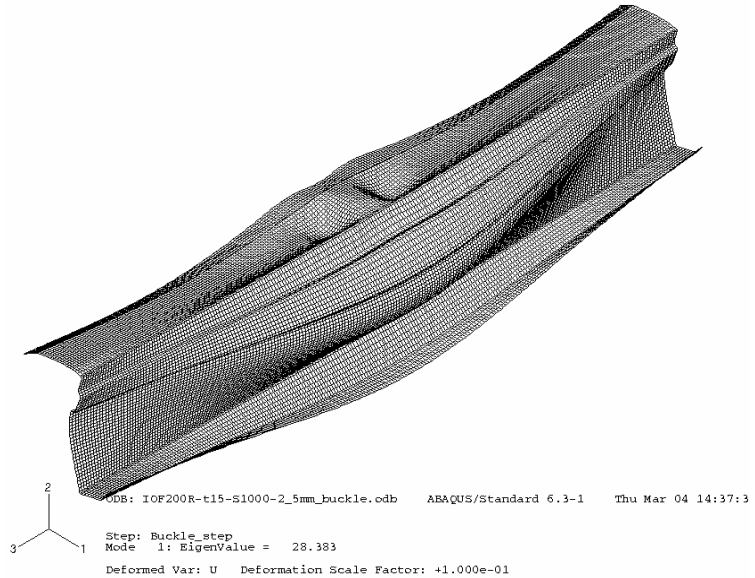

Fig. 4.31 Lowest buckling mode for model IOF200R-t15-S1000-2.

Otherwise the modelling was done as described earlier for ITF-models. An initial imperfection with maximum amplitude 1.0 mm was used for the model based on the lowest buckling mode shown in Figure 4.31. The buckling load was 28.383 kN.

Figure 4.32 shows the load-displacement curves for the top flange and the bottom flange for test IOF200R-t15-S1000-2 and the corresponding FE-model. Figure 4.33 shows the corresponding web crippling deformations (bottom flange displacement subtracted from the top flange displacement). It can be seen that the ultimate load reached during the analysis was only 10.76 kN while the ultimate load recorded during the test was 12.39 kN. The analysis load was thus 13 % lower than the test load. However, the curve shapes are very similar to each other.

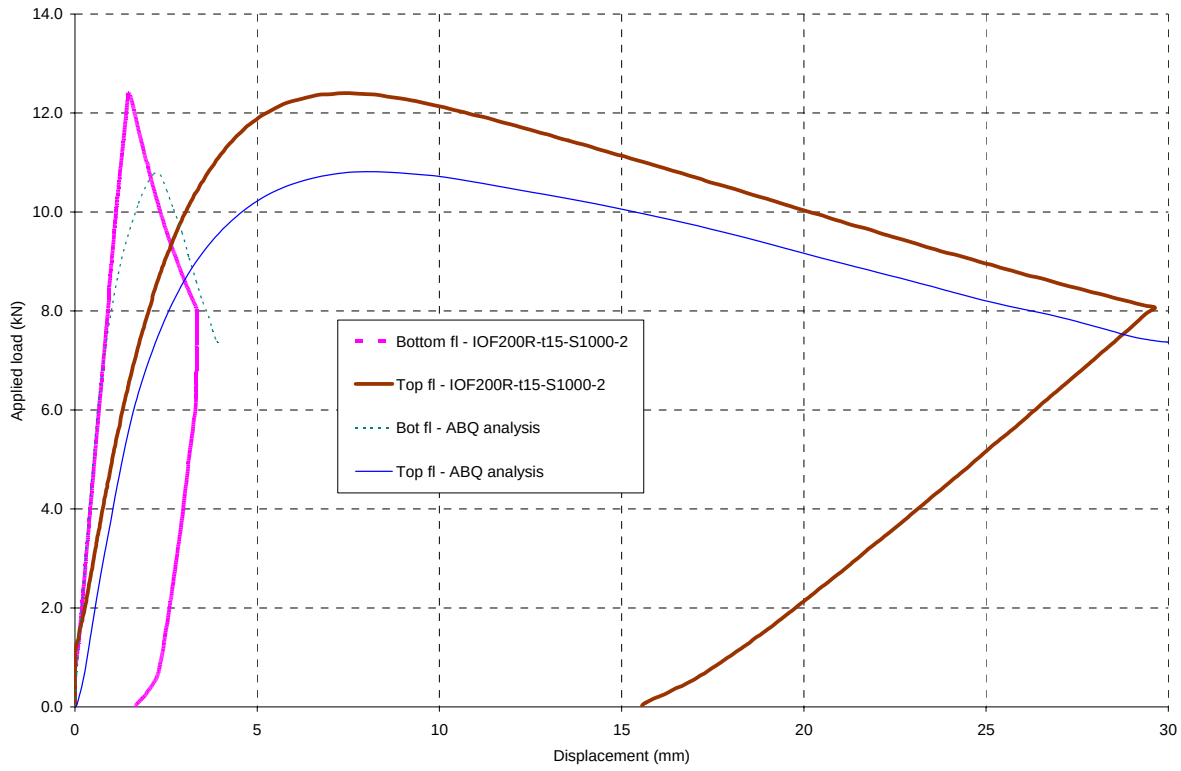

Fig. 4.32 Load-displacement curves for test IOF200R-t15-S1000-2 and the corresponding analysis model.

Two different views of the failure mode are shown in Figure 4.34. The mode is similar to that observed during the test, as shown in Figure 4.35.

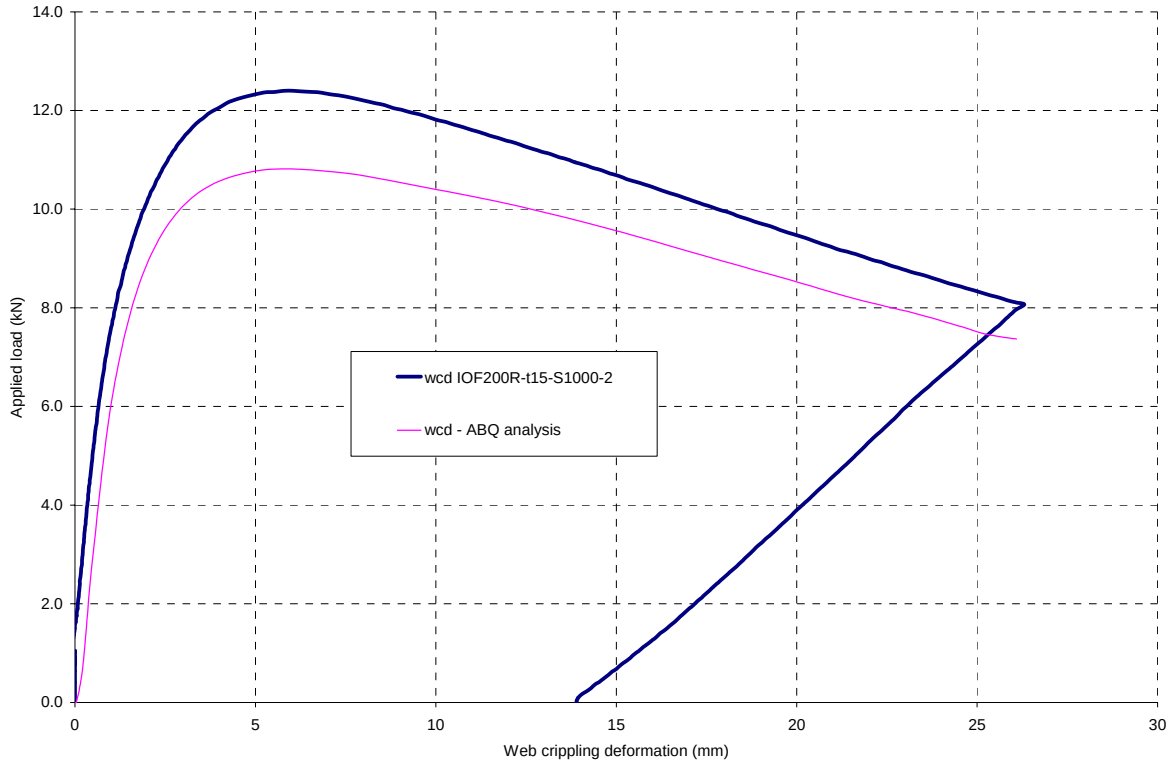

Fig. 4.33 Load-web crippling deformation curves for test IOF200R-t15-S1000-2 and the corresponding analysis model.

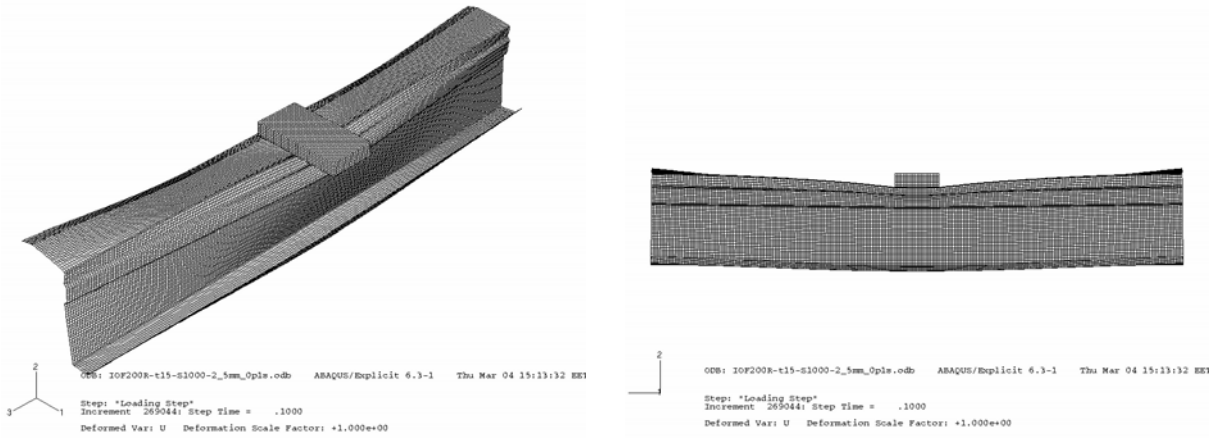

Fig. 4.34 Failure mode obtained from the analysis.

The reasons for the lower failure mode of the numerical model are not known. It is possible that there is some extra stiffness in the test set-up that has not been reproduced numerically using the current modelling assumptions. Despite this, the numerical model can be considered to reasonably reproduce the test result, as the load-displacement curve shapes and failure modes are quite similar. Further development of the numerical model could lead to a better reproduction of the failure load as well, but this work was not continued in this thesis because it is not considered to be the main focus of the work.

Fig. 4.35 Failure modes observed during test at failure load (top row) and at top flange displacement value 30 mm (bottom row).

Mises stress distributions at the mid-surface of the shell elements are shown in Figure 4.36 at the time of the ultimate load and in Figure 4.37 at the end of the analysis. By comparison of the Figures, it can be seen how the bulging of the web under the loading block causes a redistribution of stresses and the tension field is developed in the web between the supports and the load application area.

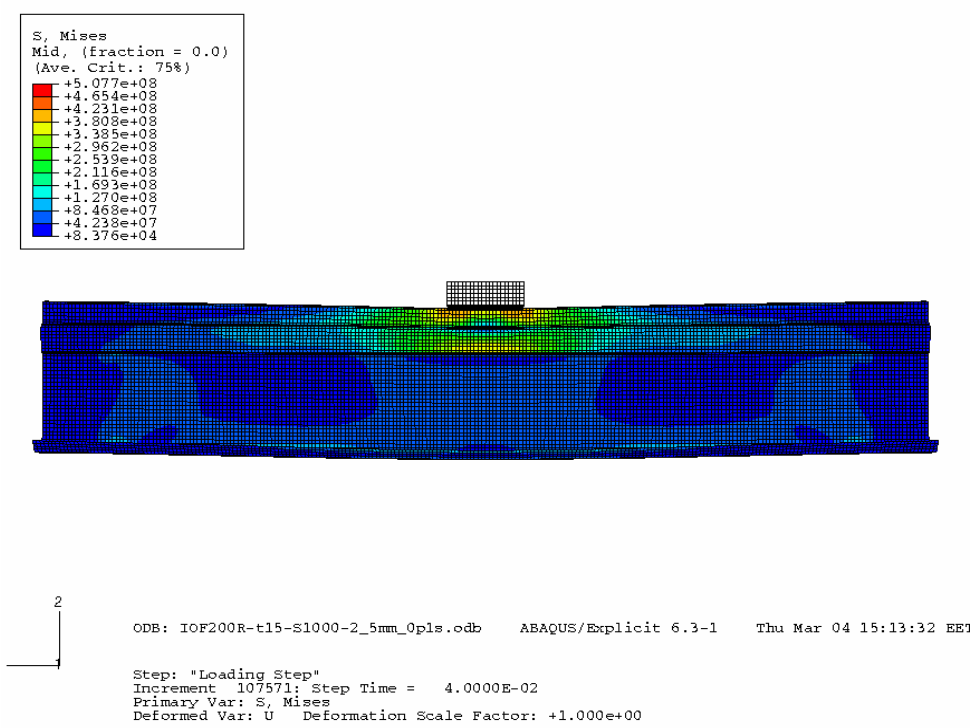

Fig. 4.36 Mises stress distribution at ultimate load
for model IOF200R-t15-S1000-2_5mm_0p1s.

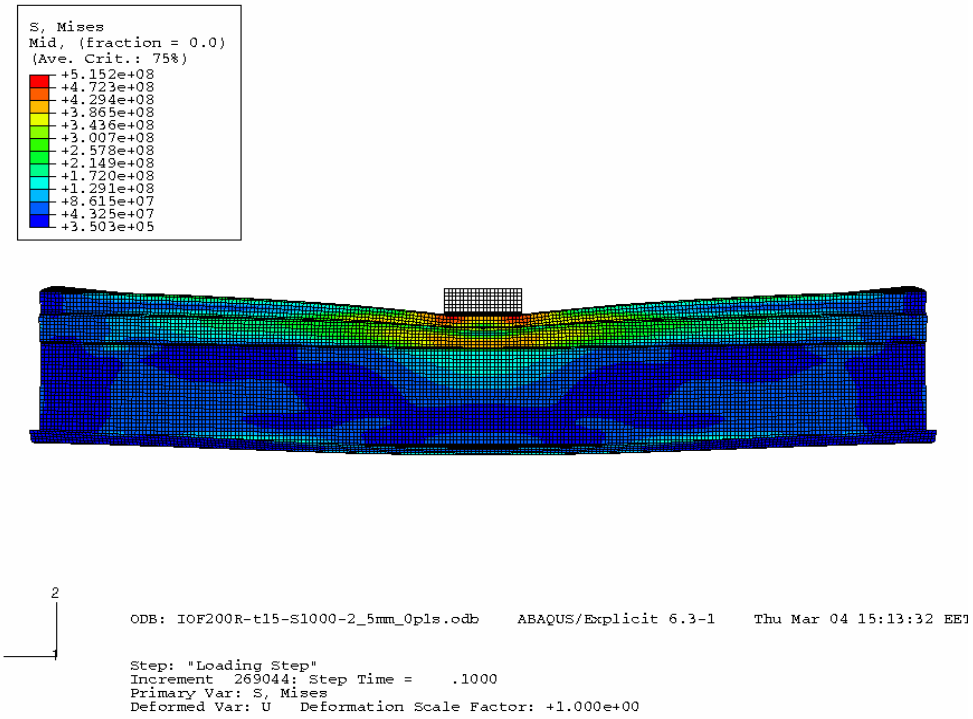

Fig. 4.37 Mises stress distribution at end of analysis
for model IOF200R-t15-S1000-2_5mm_0p1s.

5. PARAMETRIC STUDY ON THE WEB CRIPPLING CAPACITY OF LONGITUDINALLY STIFFENED THIN-WALLED CASSETTE WEBS

5.1 Scope of the parametric study

A parametric study was carried out using finite element analysis in order to find out the influence of the geometry of the longitudinal stiffener on the capacity of the cassette web against local transverse loading. The study was limited to ITF-loading conditions and the influence of bending moment was thus ignored.

The height of the profile b_w was taken as 200 mm, 150 mm or 100 mm, which are commonly used web heights for actual cassette cross-sections. The steel thickness was taken as either $t = 1.46$ mm or $t = 0.96$ mm, which correspond to nominal thicknesses $t_{nom} = 1.5$ mm and $t_{nom} = 1.0$ mm, respectively, reduced by the zinc layer thickness 0.04 mm (according to ENV 1993-1-3: 1996). Only the single web profile was studied as shown in Figure 5.1. The wide flange was cut longitudinally in the same way as was done for the ITF-tests described in Chapter 3. The figure also shows the three main parameters that were varied during the analysis. They are

d the distance of the longitudinal stiffener from the wide flange,
e the out-of-plane height (eccentricity) of the longitudinal stiffener, and
f the in-plane height (width) of the longitudinal stiffener.

The distance of the stiffener from the wide flange *d* was varied between 20 and 75 mm, the out-of-plane eccentricity of the stiffener *e* was varied between 5 and 16 mm and the in-plane height of the stiffener *f* was varied between 20 and 100 mm. Comparisons to similar models with flat webs are also presented. The mid-surface corner radius *R* at the web-flange junctions was equal to 3 mm and the corner radius R_s of the stiffener folds was approximately 4 mm. The influence of the corner radii was not included in this parametric study.

The influence of the bearing length s_s was studied with the help of a few models. For most analyses, the bearing length was 100 mm, but two section geometries were analysed also with

bearing lengths 150 mm and 50 mm. The loading pad and the support pad were always of equal length in each model.

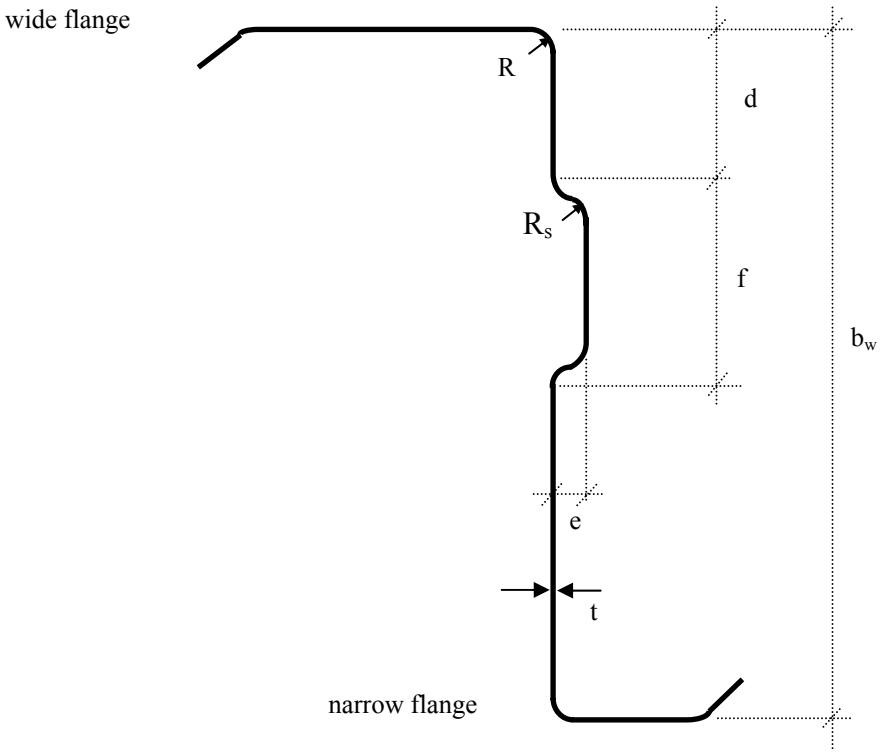

Fig. 5.1 Main parameters studied.

5.2 Set-up of numerical models

The numerical models were constructed by modifying the previously built models validated using test results (Section 4.4). However, the length of the single-web beam was increased from 1200 mm to 3000 mm in order to minimise the influence of the free ends of the beam. This was done after noticing that for some model geometries, the ends of the beam were strongly deformed due to the local transverse load applied at mid-length, similarly to what can be seen to happen during the buckling of the model on test IOF200R-t15-S1000-2 in Figure 4.31. The downside of increasing the length was that this resulted in an increase of the number of nodes and elements in the model by a factor of 2.5 and the required CPU-time increased accordingly. This in turn limited the number of analyses that could be run. However, it was considered more important to have a limited amount of good results than a larger amount of results that leave more questions open.

The element types used were S4R for the cassette section and R3D4 for the loading and support pads. The boundary conditions and contact surface conditions were the same as in the validation models. The load application period was equal to 0.1 seconds in all models, during which a forced displacement equal to 30 mm was introduced to the structure via the rigid loading pad and the contact surfaces. In a few analyses, the displacement was set to 20 mm instead. This does not appear to have any notable influence on the results, as can be noted by comparing curves for models 100R-t15_d40_e12_f20 and 100R-t15_d40_e12_f30 in Figure 5.7. The "smooth step" function in ABAQUS was used for the load application in order to give the structure more time to respond to the loading. The displacement boundary conditions were similar to what was explained in Section 4.4.

All parametric models had a general element edge length of 5 mm, except at rounded corners of the cross-section, where two smaller elements were generally used in a similar way to what is shown in Figure 4.23 for the models with element edge length 2.5 mm. However, an attempt was made not to have an element aspect ratio larger than about 5.0, because a very large aspect ratio or even a single relatively small element in the model can cause the stable time increment used in the dynamic analysis to decrease substantially, leading to a large increase in required CPU-time. The stable time increment in the parametric models turned out to be of the order of $4 \cdot 10^{-7}$ seconds. As a consequence, the CPU-time needed for one analysis was of the order of 20 to 40 CPUh depending on the model, which is already quite high and was considered to be the maximum that is acceptable for the practical research work, even though the wall clock time used for the analyses was reduced by the use of 4 parallel processors.

5.3 Results of the parametric study

The full results of the parametric study are distributed into groups according to web height and steel thickness in Tables 5.2-5.8 in the order given in Table 5.1, where also the total number of models in each group is shown. The total number of parametric models is 71 (+ 5 models with flat webs). The results are organised inside the tables according to failure load values.

The force-displacement curves for all models are given in Figures 5.2-5.10. The curves for the corresponding flat web models are also shown. Some curves end before the full prescribed displacement 30 mm is reached, because in these cases the analysis was interrupted by the user in order to save CPU-time. In all cases, however, the analysis has been continued well past the failure load.

The bearing length s_s was equal to 100 mm in all models except where noted (Tables 5.7 and 5.8). In Tables 5.7 and 5.8, which give results dealing with the effect of bearing length, the results for the models with bearing length s_s = 100 mm are reproduced from Tables 5.2 and 5.6, respectively, in order to facilitate the comparison of the results.

Table 5.1 Grouping of parametric model results.

Table number	Results group	Figures showing corresponding load-displ. curves	Number of models in group
Table 5.2	Models with web height 200 mm, t_{nom} = 1.5 mm	Figures 5.2-5.3	16
Table 5.3	Models with web height 200 mm, t_{nom} = 1.0 mm	Figures 5.4-5.5	15
Table 5.4	Models with web height 150 mm, t_{nom} = 1.5 mm	Figure 5.6	9
Table 5.5	Models with web height 100 mm, t_{nom} = 1.5 mm	Figure 5.7	11
Table 5.6	Models with web height 100 mm, t_{nom} = 1.0 mm	Figure 5.8	12
Table 5.7	Models with different bearing lengths and web height 200 mm	Figure 5.9	4
Table 5.8	Models with different bearing lengths and web height 100 mm	Figure 5.10	4

Table 5.2 Models with web height 200 mm, t_{nom} = 1.5 mm; *d*, *e* and *f* in [mm].

Model tag	d	e	f	Buckling load (kN)	Failure load (kN)	Reduction in failure load compared to flat web (%)	Displ. at failure load (mm)	Material
200-t15_flat				11.34	16.24		4.50	KH089002
200R-t15_d75_e8_f20	75	8	20	19.07	14.54	10.5	5.68	KH089002
200R-t15_d50_e8_f20	50	8	20	18.36	14.30	11.9	5.72	KH089002
200R-t15_d75_e8_f50	75	8	50	23.37	13.71	15.6	6.96	KH089002
200R-t15_d50_e8_f50	50	8	50	22.28	13.42	17.4	8.41	KH089002
200R-t15_d50_e12_f20	50	12	20	20.87	13.36	17.7	10.05	KH089002
200R-t15_d20_e8_f20	20	8	20	15.62	12.84	20.9	6.60	KH089002
200R-t15_d50_e8_f100	50	8	100	25.70	12.56	22.7	10.39	KH089002
200R-t15_d50_e12_f50	50	12	50	23.80	12.40	23.6	10.58	KH089002
200R-t15_d20_e8_f35	20	8	35	18.42	12.10	25.5	5.72	KH089002
200R-t15_d20_e8_f50	20	8	50	20.35	12.05	25.8	7.06	KH089002
200R-t15_d20_e8_f50_EC3	20	8	50	21.00	11.88	26.8	4.89	EC3-1-3
200R-t15_d20_e12_f20	20	12	20	17.72	11.52	29.1	9.01	KH089002
200R-t15_d50_e16_f50	50	16	50	24.51	11.44	29.6	13.32	KH089002
200R-t15_d20_e16_f20	20	16	20	19.28	10.43	35.8	10.58	KH089002
200R-t15_d20_e12_f50	20	12	50	22.40	10.34	36.3	8.51	KH089002
200R-t15_d20_e16_f50	20	16	50	23.65	9.15	43.7	10.58	KH089002

The material used for the analyses was based on the ENV 1993:1-3: 1999 (EC3-1-3) material model with yield strength f_y = 350 N/mm2 and modulus of elasticity E = 210000 N/mm2, except for the models with web height 200 mm and steel thickness 1.5 mm, for which the material was the same as for the test analyses, i.e. material KH089002 as described in Chapter 4). The reason for this was that the author failed to think of changing the material parameters when the parametric study was begun by modifying the model based on test ITF200R-t15-3. The mistake was only noticed after a number of analyses had been run, and the relatively high cost in CPU-time prevented the models to be re-run with the EC3-1-3 material model. However, the influence of the material was studied by running one ITF200R-t15-analysis using the EC3-1-3 material model and it can be seen from the results in Table 5.2 (models 200R-t15_d20_e8_f50 and 200R-t15_d20_e8_f50_EC3) that the material has but a small influence on the failure load (11.88 kN for material EC3-1-3 and 12.05 kN for the test material KH089002). The difference is of the order of 1.4 %. A greater difference can be seen in the value of the displacement of the loading pad at failure load, which is 7.06 mm for the test material KH089002 and only 4.89 mm for the EC3-1-3 material model. The stiffness of the EC3-1-3 material model as described by the value of the modulus of elasticity used (E = 210000 N/mm^2 for EC3-1-3 and E = 203418 N/mm^2 for the test material KH089002) is only slightly higher than that of the test material. However, when the force-displacement curves of the two models, as given in Figure 5.2, are compared, it can be seen that there is not much difference in their shapes. The difference in the displacement value at failure load is due to the low stiffness of the model near the failure load, causing the tangent of the curves to be close to horizontal for some time already before the moment of failure. Therefore already a small increase in failure load will lead to a larger increase in the displacement value.

As can be seen from the parametric results for models 200R-t15 in Table 5.2, the failure load varies between 9.15 kN and 14.54 kN when the size and shape of the longitudinal stiffener are varied. The failure load of the model with a flat web was 16.24 kN. It is also shown that the decrease in % for this and the other model groups are the following:

- 10-44 % for models 200R-t15
- 9.5-42 % for models 200R-t10
- 12-35 % for models 150R-t15
- 13-38 % for models 100R-t15
- 13-29 % for models 100R-t10

The highest reduction percentages are due to high values of stiffener eccentricity *e*. It can be concluded that all of the stiffener geometries reduce the resistance to local transverse forces by at least 10 % in comparison to a similar cross-section without a stiffener.

The maximum value of the failure load for models 200R-t15 with longitudinally stiffened webs is about 59 % larger than the minimum value. For the other model groups with different web heights and steel thicknesses, the increase in failure load from the minimum to the maximum value is 56 % for models 200R-t10, 35 % for 150R-t15, 40 % for 100R-t15 and 22 % for 100R-t10 (see Tables 5.3-5.6). However, these values should not be directly compared among each other, because the ratios of the studied parameters to web height are different for the different groups. Nevertheless, they are a clear indicator that the size and the location of the longitudinal stiffener have an important influence on the section's resistance against local transverse forces.

Tables 5.2-5.8 also show the elastic buckling load corresponding to the lowest buckling mode of the structure. This buckling mode was used as a basis for the initial imperfection introduced into the subsequent ABAQUS/Explicit failure analysis model. The maximum imperfection amplitude was 1.0 mm in all models. Because the failure of the structure under local transverse forces happens through yielding, the elastic buckling load usually has a higher value than the failure load of the same structure. There is only one exception to this rule in the present analyses. As can be seen from Table 5.3, model 200R-t10_d20_e8_f20 has a slightly lower buckling load (5.38 kN) than its failure load (5.68 kN) is. This is explained by the fact that this particular model has the most slender web of those analysed, where the longitudinal stiffener is relatively small and situated close to the wide flange, and thus leaves a large flat area at the lower part of the web. However, it is difficult to find a clear correlation between the failure load and the elastic buckling load for the profiles.

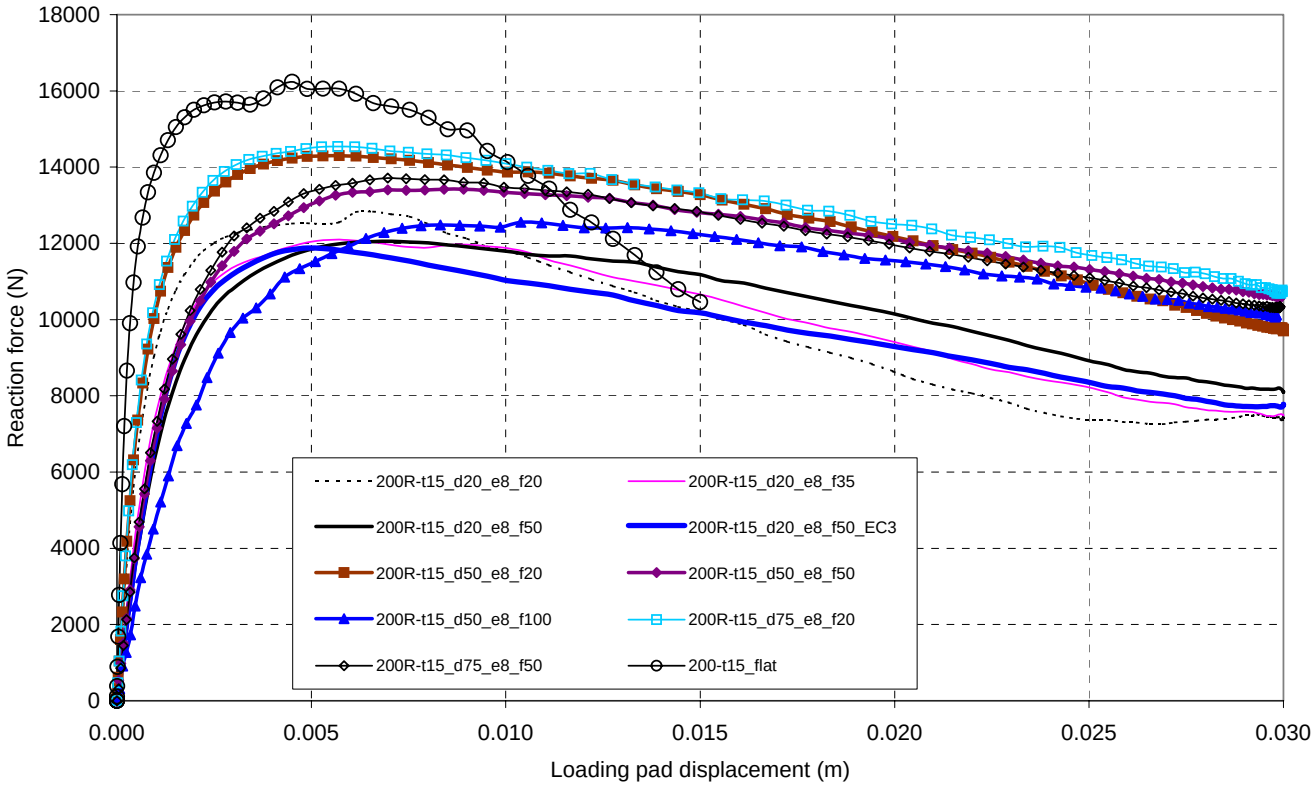

Fig. 5.2 Load-displacement curves for models 200R-t15 with e = 8 mm.

The force-displacement curves in Figures 5.2 and 5.3 for models 200R-t15 all have a similar shape where the initial phase shows a rapid increase in support reaction. The failure load is reached smoothly without any sudden buckling taking place, as was observed during tests on longitudinally stiffened webs. In some curves, most notably those for models 200R-t15_d20_e8_f20, ITF200R-t15_d20_e12_f20 and 200R-t15_d20_e16_f20, there is a small additional increase in the support reaction after the first local maximum is reached. This is due to the local stiffening of the web when the top part of the flange is pressed against the stiffener and the deformations of the rounded corners below the load application area. A similar pattern can be observed in some of the other models as well, but it usually appears a little later during the analysis, because the stiffener is further down from the wide flange. The same phenomenon can be seen in the force-displacement curves for models with 150 mm and 100 mm high webs.

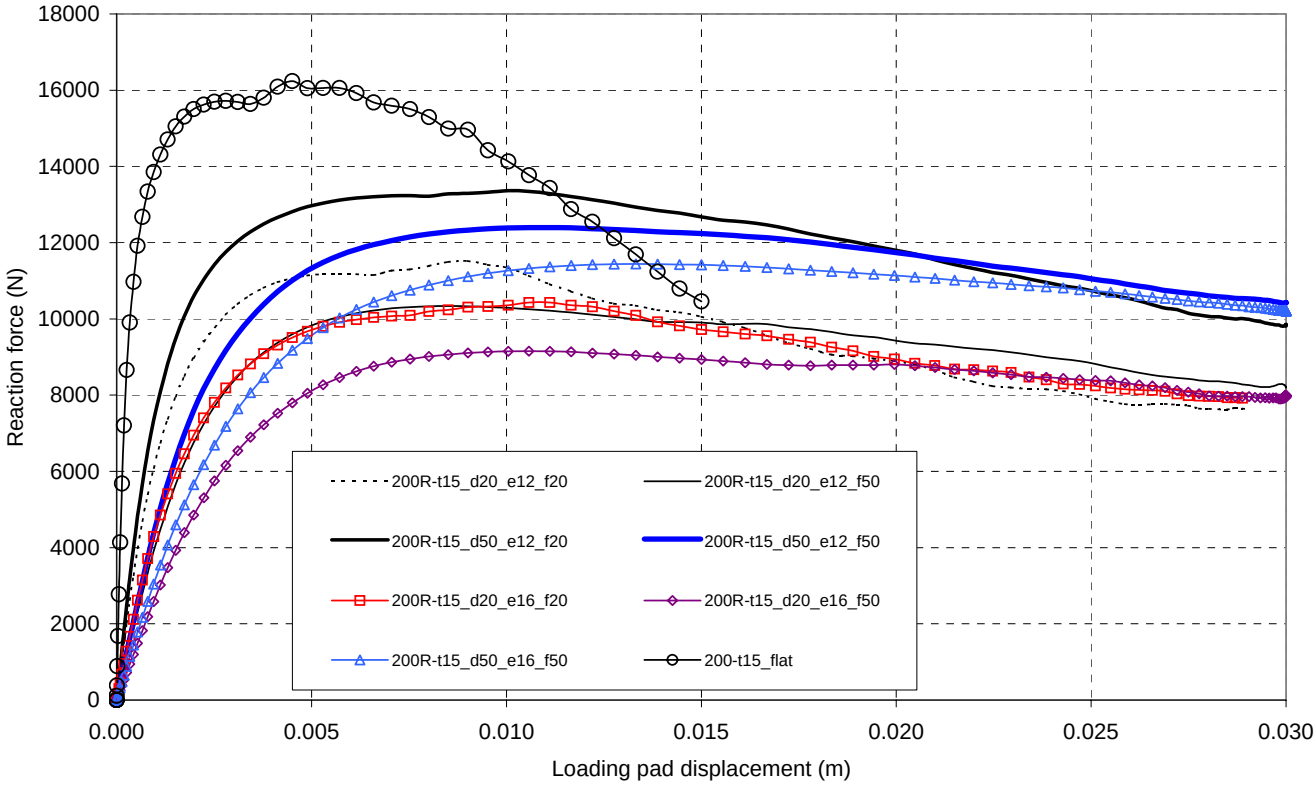

Fig. 5.3 Load-displacement curves for models 200R-t15 with e = 12-16 mm.

The force-displacement curves in Figures 5.4 and 5.5 for models 200R-t10 show a somewhat different behaviour in comparison to those for models 200R-t15. Due to the slenderness of the web, the curves are not so smooth and several local buckling phenomena can be clearly seen to take place during the whole analysis as the deformations progress through the section. Nevertheless, the general shape of the curves is similar to those of models with less slender webs. Also, these effects are reduced when the eccentricity e of the stiffener and/or the distance from the wider flange d are increased, as can be seen most clearly from Figure 5.5 for models 200R-t10_d50_e12_f20, 200R-t10_d50_e12_f50 and 200R-t10_d50_e16_f50. This is intuitively correct.

Table 5.3 Models with web height 200 mm, t_{nom} = 1.0 mm; *d*, *e* and *f* in [mm].

Model tag	d	e	f	Buckling load (kN)	Failure load (kN)	Reduction in failure load compared to flat web (%)	Displ. at failure load (mm)	Material
200-t10_flat				3.47				EC3-1-3
200R-t10_d75_e8_f20	75	8	20	6.79	6.22	9.5	5.53	EC3-1-3
200R-t10_d50_e8_f20	50	8	20	6.52	6.19	9.9	4.46	EC3-1-3
200R-t10_d75_e8_f50	75	8	50	8.34	5.93	13.7	9.86	EC3-1-3
200R-t10_d50_e8_f50	50	8	50	7.95	5.91	14.0	8.41	EC3-1-3
200R-t10_d50_e12_f20	50	12	20	7.44	5.76	16.2	11.47	EC3-1-3
200R-t10_d20_e8_f20	20	8	20	5.38	5.68	17.3	4.56	EC3-1-3
200R-t10_d50_e8_f100	50	8	100	9.21	5.63	18.0	9.92	EC3-1-3
200R-t10_d50_e12_f50	50	12	50	8.44	5.40	21.4	9.86	EC3-1-3
200R-t10_d20_e8_f35	20	8	35	6.44	5.35	22.1	4.46	EC3-1-3
200R-t10_d20_e8_f50	20	8	50	7.26	5.28	23.1	7.10	EC3-1-3
200R-t10_d20_e12_f20	20	12	20	6.16	4.94	28.1	4.96	EC3-1-3
200R-t10_d50_e16_f50	50	16	50	8.64	4.94	28.1	13.32	EC3-1-3
200R-t10_d20_e12_f50	20	12	50	7.96	4.51	34.4	10.58	EC3-1-3
200R-t10_d20_e16_f20	20	16	20	6.70	4.40	36.0	10.86	EC3-1-3
200R-t10_d20_e16_f50	20	16	50	7.88	3.99	41.9	12.78	EC3-1-3

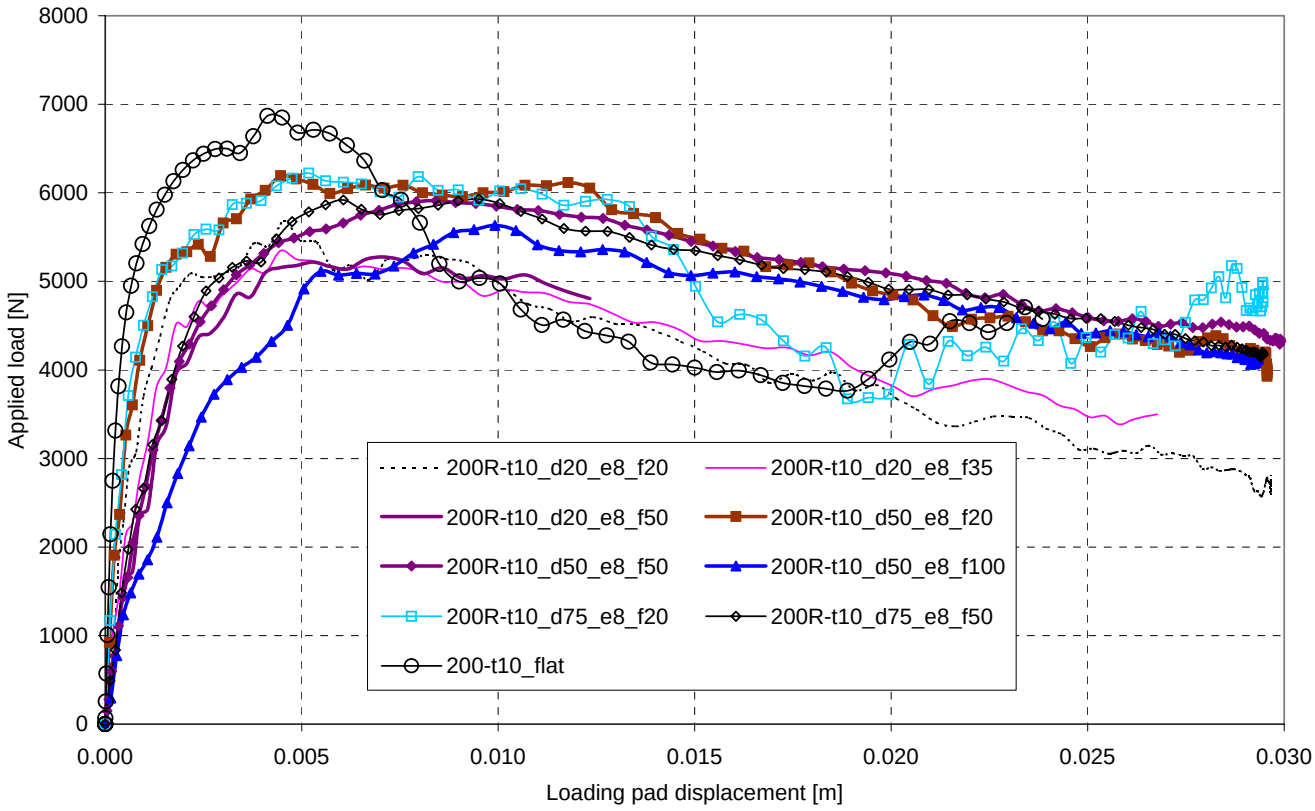

Fig. 5.4 Load-displacement curves for models 200R-t10 with *e* = 8 mm.

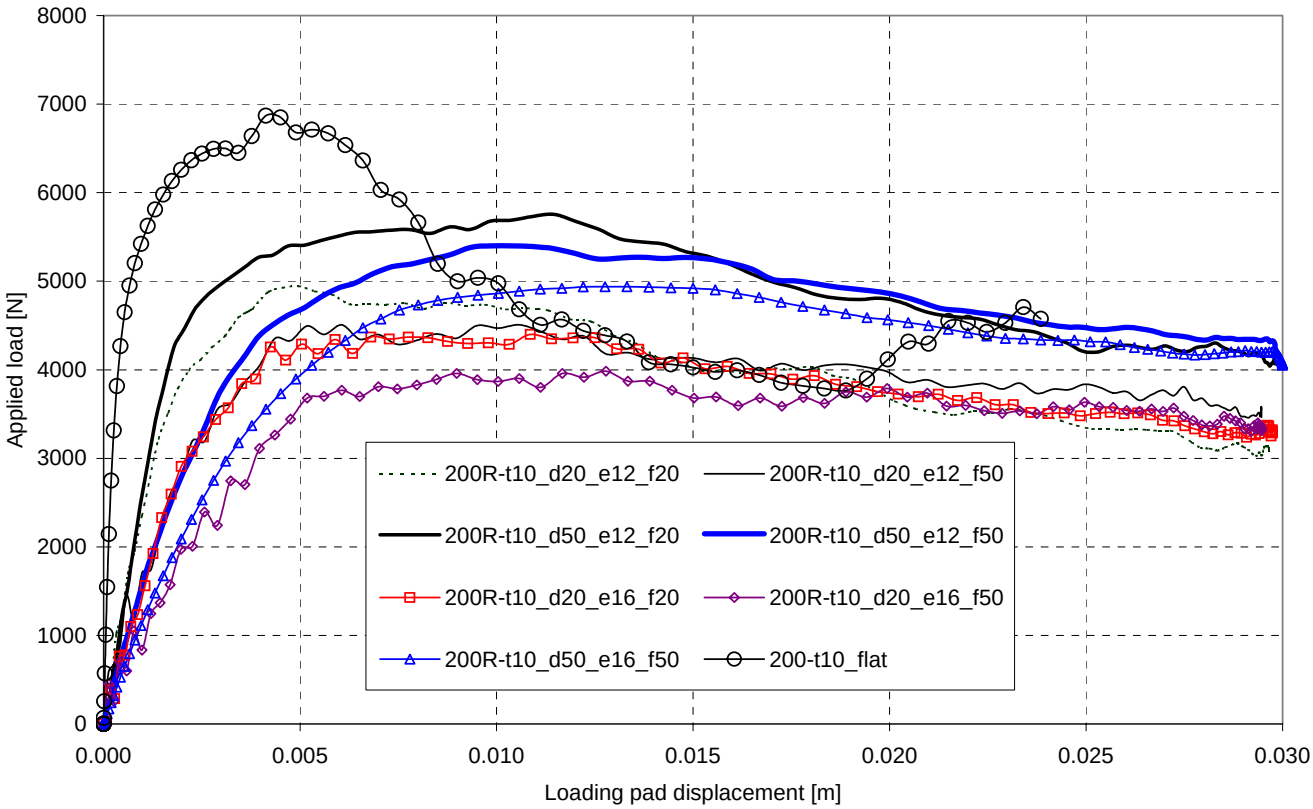

Fig. 5.5 Load-displacement curves for models 200R-t10 with e = 12-16 mm.

In the start and the end of the analyses, the density of data collection points is increased, as can be seen from the curves with markers. This is due to the "smooth step"-setting used in the analyses, which causes the load application speed to be slower at the start and at the end of the analysis. The data is collected at regular time intervals during analysis, so when the application of the forced displacement happens slower, there are more points per unit displacement. The time interval between data collection points was set to 0.001 seconds in most analyses, which means that there are a total of 100 data points collection points during a 0.1 second long analysis.

Table 5.4 Models with web height 150 mm, t_{nom} = 1.5 mm; *d*, *e* and *f* in [mm].

Model tag	d	e	f	Buckling load (kN)	Failure load (kN)	Reduction in failure load compared to flat web (%)	Displ. at failure load (mm)	Material
150-t15_flat				17.06	16.60		1.52	EC3-1-3
150R-t15_d50_e8_f20	50	8	20	29.77	14.63	11.9	5.24	EC3-1-3
150R-t15_d50_e8_f50	50	8	50	36.75	14.22	14.3	6.51	EC3-1-3
150R-t15_d50_e12_f50	50	12	50	39.07	13.67	17.7	7.53	EC3-1-3
150R-t15_d50_e12_f20	50	12	20	32.10	13.55	18.4	6.96	EC3-1-3
150R-t15_d20_e8_f50	20	8	50	32.30	12.62	24.0	5.20	EC3-1-3
150R-t15_d20_e8_f35	20	8	35	30.56	12.19	26.6	5.24	EC3-1-3
150R-t15_d20_e8_f20	20	8	20	26.62	12.05	27.4	4.12	EC3-1-3
150R-t15_d20_e12_f50	20	12	50	34.50	10.86	34.6	7.34	EC3-1-3
150R-t15_d20_e12_f20	20	12	20	29.89	10.85	34.6	5.29	EC3-1-3

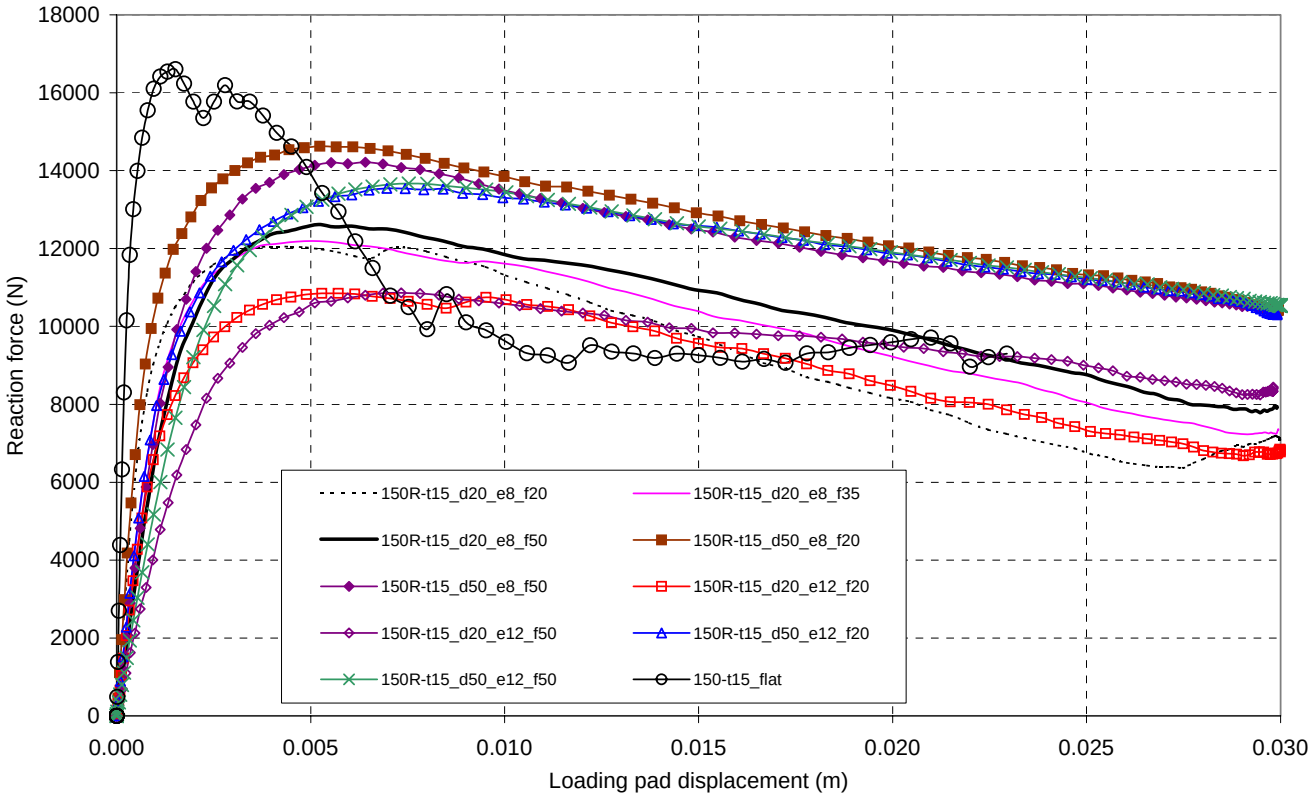

Fig. 5.6 Load-displacement curves for models 150R-t15.

Table 5.5 Models with web height 100 mm, t_{nom} = 1.5 mm; *d*, *e* and *f* in [mm].

Model tag	d	e	f	Buckling load (kN)	Failure load (kN)	Reduction in failure load compared to flat web (%)	Displ. at failure load (mm)	Material
100-t15_flat				28.63	17.01		9.45	EC3-1-3
100R-t15_d50_e8_f20	50	8	20	48.60	14.77	13.2	4.31	EC3-1-3
100R-t15_d40_e12_f20	40	12	20	52.89	13.13	22.8	6.87	EC3-1-3
100R-t15_d20_e8_f50	20	8	50	61.66	12.86	24.4	5.65	EC3-1-3
100R-t15_d20_e8_f20	20	8	20	47.34	12.73	25.2	7.92	EC3-1-3
100R-t15_d40_e12_f30	40	12	30	58.27	12.66	25.6	7.97	EC3-1-3
100R-t15_d20_e8_f35	20	8	35	54.20	12.63	25.7	5.11	EC3-1-3
100R-t15_d50_e16_f20	50	16	20	56.51	12.10	28.9	8.71	EC3-1-3
100R-t15_d20_e16_f20	20	16	20	49.29	10.96	35.6	12.76	EC3-1-3
100R-t15_d20_e12_f50	20	12	50	58.31	11.95	29.7	12.21	EC3-1-3
100R-t15_d20_e12_f20	20	12	20	51.61	11.29	33.6	10.44	EC3-1-3
100R-t15_d20_e16_f35	20	16	35	45.73	10.52	38.2	8.88	EC3-1-3

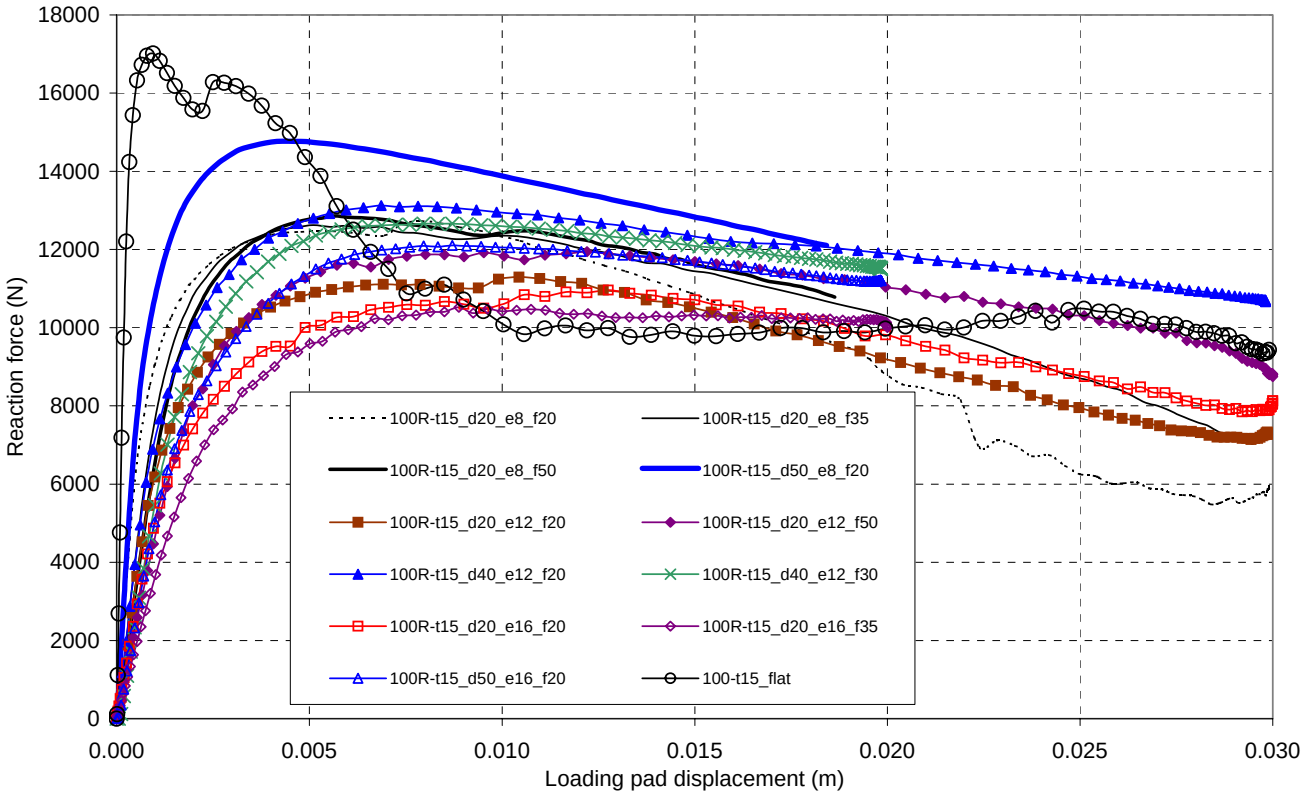

Fig. 5.7 Load-displacement curves for models 100R-t15.

Table 5.6 Models with web height 100 mm, t_{nom} = 1.0 mm; *d*, *e* and *f* in [mm].

Model tag	d	e	f	Buckling load (kN)	Failure load (kN)	Reduction in failure load compared to flat web (%)	Displ. at failure load (mm)	Material
100-t10_flat				8.22	7.44		2.79	EC3-1-3
100R-t10_d40_e8_f20	40	8	20	16.33	6.49	12.8	6.54	EC3-1-3
100R-t10_d40_e8_f30	40	8	30	17.98	6.36	14.5	6.14	EC3-1-3
100R-t10_d20_e5_f35	20	5	35	16.44	6.28	15.6	4.41	EC3-1-3
100R-t10_d20_e8_f35	20	8	35	17.27	6.20	16.7	8.01	EC3-1-3
100R-t10_d20_e5_f50	20	5	50	18.29	6.17	17.1	5.53	EC3-1-3
100R-t10_d20_e5_f20	20	5	20	14.47	6.15	17.3	7.00	EC3-1-3
100R-t10_d20_e8_f50	20	8	50	17.93	6.08	18.3	9.52	EC3-1-3
100R-t10_d40_e12_f30	40	12	30	17.51	6.06	18.5	8.51	EC3-1-3
100R-t10_d40_e12_f20	40	12	20	17.05	5.95	20.0	8.47	EC3-1-3
100R-t10_d20_e8_f20	20	8	20	15.54	5.69	23.5	8.50	EC3-1-3
100R-t10_d20_e12_f20	20	12	20	14.60	5.40	27.4	10.05	EC3-1-3
100R-t10_d20_e12_f50	20	12	50	12.93	5.30	28.8	10.05	EC3-1-3

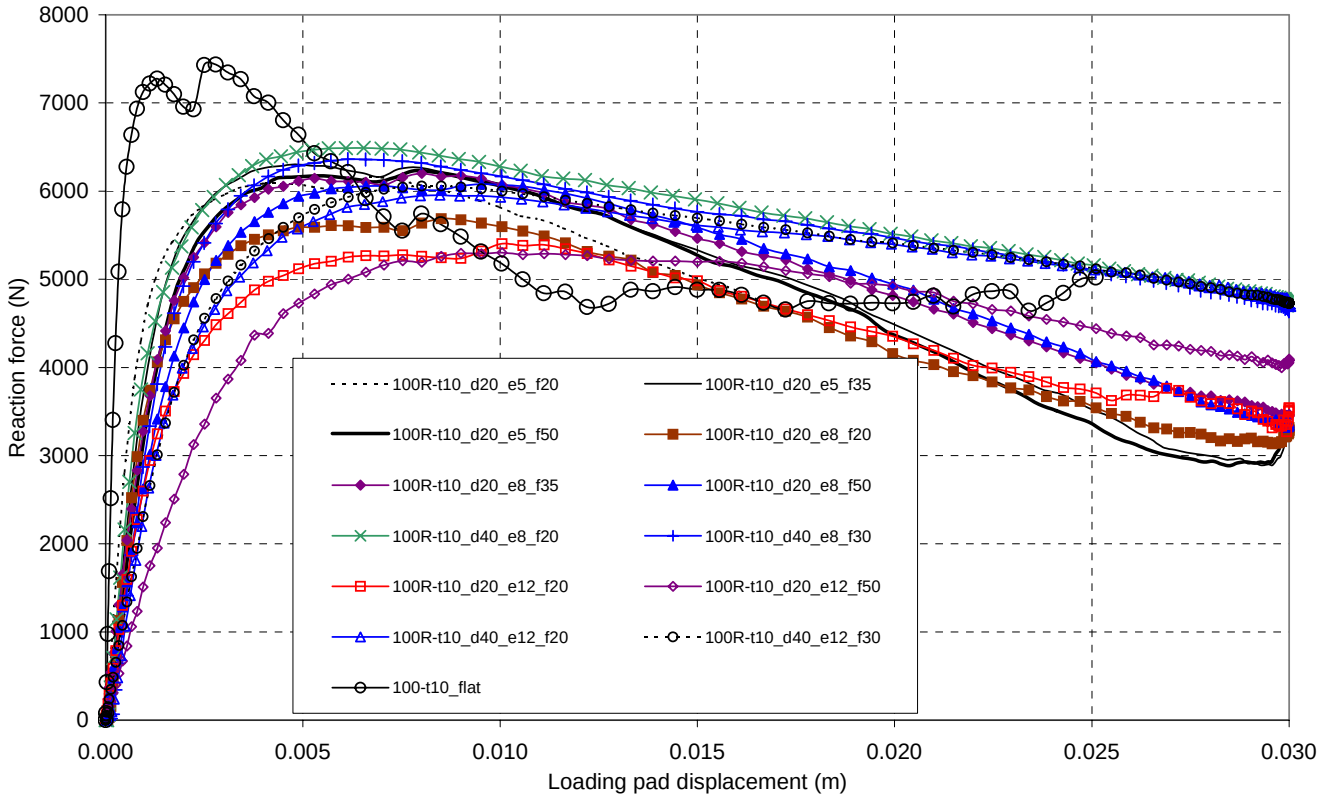

Fig. 5.8 Load-displacement curves for models 100R-t10.

The influence of the bearing length s_s was studied using four different single-web cassette sections with either the 200R-t15 or the 100R-t10 configuration. The results are shown in Tables 5.7-5.8 and Figures 5.9-5.10. The results confirm that the failure load is directly proportional to the bearing length, as expected. Looking at the force-displacement curves more closely, it can be noted that the increase in failure load appears to be fairly linear for each of the four sets of cross-section geometries, at least when the first local maximum is taken as the failure load in each case. The failure loads given in the Tables are the maximum values during the whole analysis, and as can be seen by looking at the graphs, in several cases, these values are somewhat larger than the first maximum.

Table 5.7 Models with different bearing lengths and web height 200 mm.

Model tag	d (mm)	e (mm)	f (mm)	s_s (mm)	Buckling load (kN)	Failure load (kN)	Displ. at failure load (mm)	Material
200R-t15_d20_e8_f20_s50	20	8	20	50	14.72	12.45	4.89	KH089002
200R-t15_d20_e8_f20	20	8	20	100	15.62	12.84	6.60	KH089002
200R-t15_d20_e8_f20_s150	20	8	20	150	23.43	14.69	6.15	KH089002
200R-t15_d50_e8_f20_s50	50	8	20	50	17.40	14.39	8.51	KH089002
200R-t15_d50_e8_f20	50	8	20	100	18.36	14.30	5.72	KH089002
200R-t15_d50_e8_f20_s150	50	8	20	150	27.53	15.00	7.06	KH089002

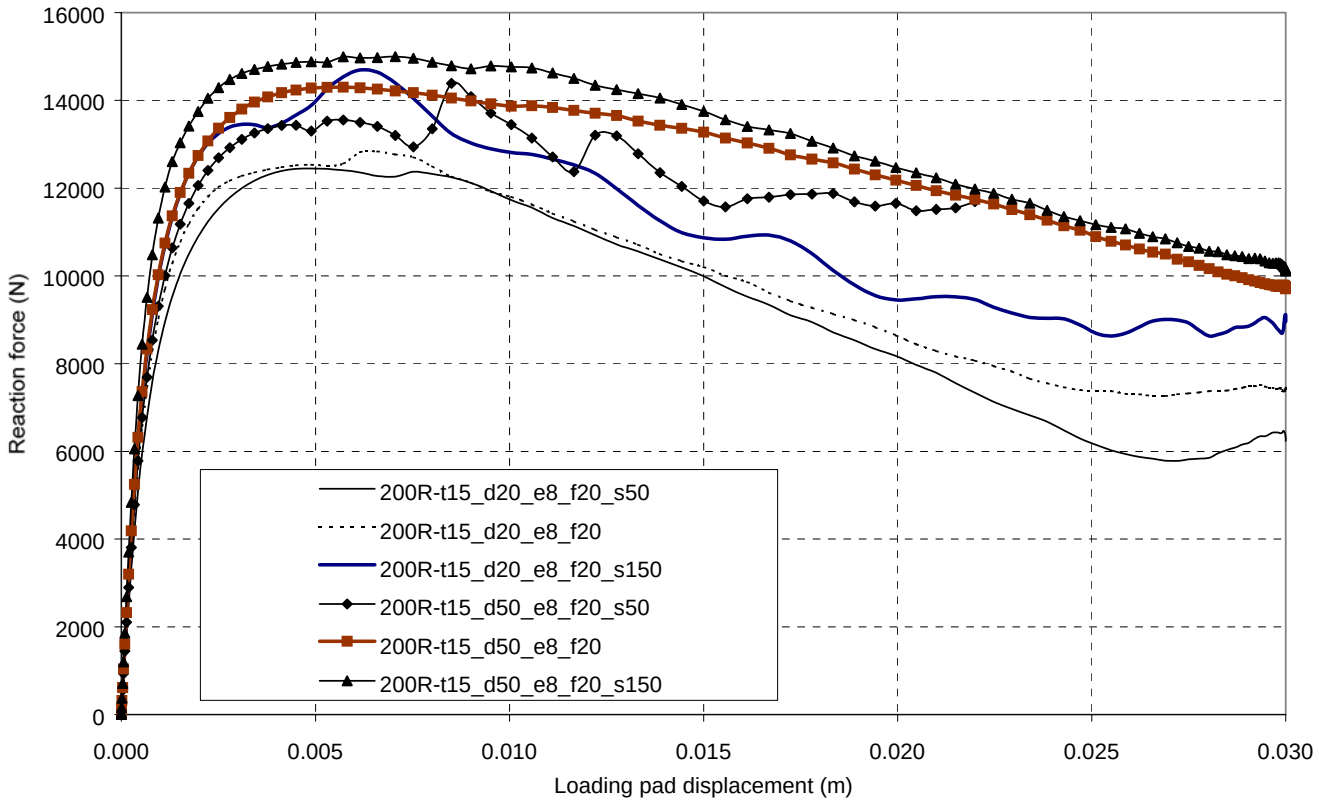

Fig. 5.9 Load-displacement curves for models 200R-t15 with different bearing lengths.

Table 5.8 Models with different bearing lengths and web height 100 mm.

Model tag	d (mm)	e (mm)	f (mm)	s_s (mm)	Buckling load (kN)	Failure load (kN)	Displ. at failure load (mm)	Material
100R-t10_d20_e8_f20_s50	20	8	20	50	14.66	5.44	8.95	EC3-1-3
100R-t10_d20_e8_f20	20	8	20	100	15.54	5.69	8.50	EC3-1-3
100R-t10_d20_e8_f20_s150	20	8	20	150	15.84	5.91	8.47	EC3-1-3
100R-t10_d40_e8_f30_s50	40	8	30	50	17.47	6.01	9.01	EC3-1-3
100R-t10_d40_e8_f30	40	8	30	100	17.98	6.36	6.14	EC3-1-3
100R-t10_d40_e8_f30_s150	40	8	30	150	16.74	7.00	5.72	EC3-1-3

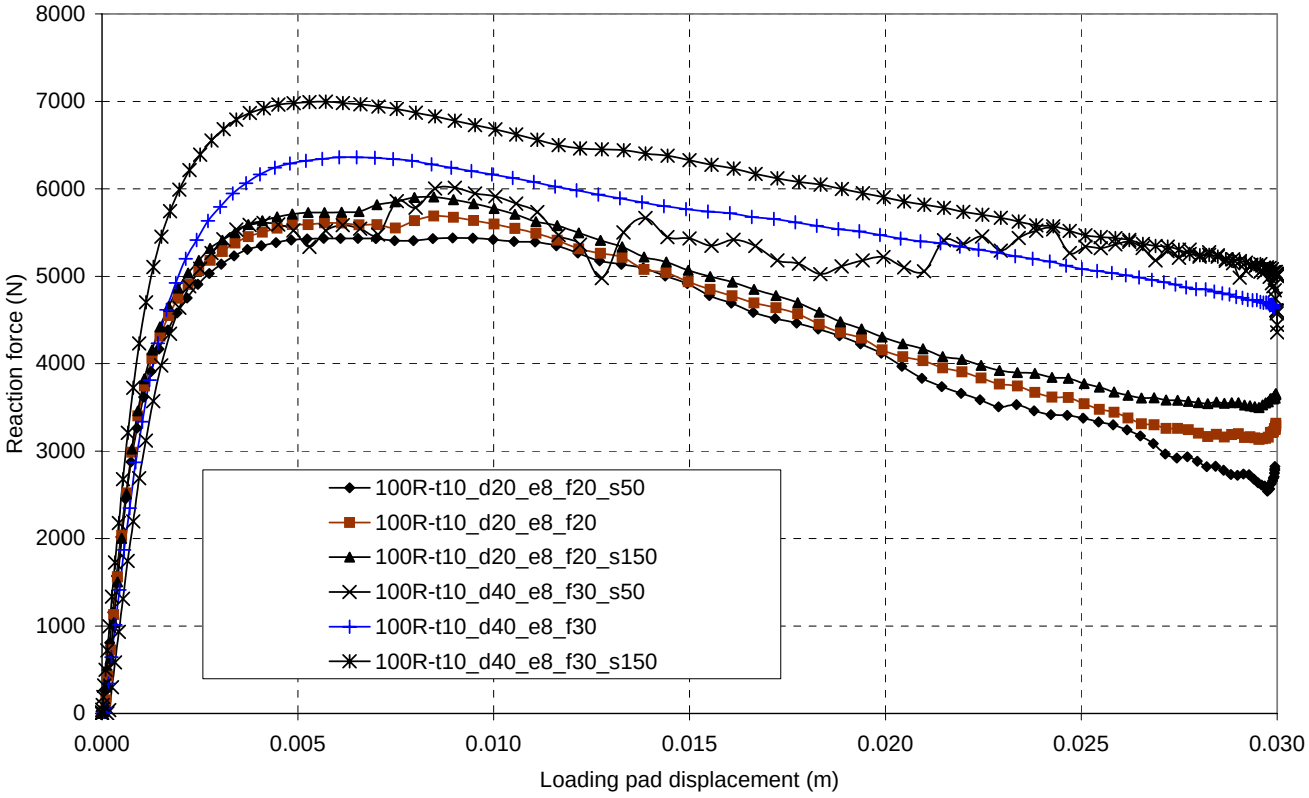

Fig. 5.10 Load-displacement curves for models 100R-t10 with different bearing lengths.

Another conclusion that can be made from Figures 5.9 and 5.10 is that the influence of the bearing length is larger when the longitudinal stiffener is closer to the mid-height of the web, i.e. the value of d is larger. This is concluded from the observation that the curves for models with d = 20 mm are packed together more tightly than the curves for models with d = 50 mm. However, the small number of analysis results does not allow a very thorough analysis of the influence of bearing length, which overall is not considered to be the main focus of the present study. The results can nevertheless be of interest and are therefore included.

In ANNEX F, Mises stress distributions at the mid-level of the shell elements are shown for models 100R-t10_d40_e8_f30 with bearing lengths 50 mm and 150 mm at time of failure and at the end of the analyses. The differences in stress distribution can be seen clearly in these pictures. Higher stress peaks are experienced in the model with s_s = 50 mm. The smaller bearing length also causes the web to crushed at both flanges, while the larger bearing length has the web crushing concentrated at the lower flange in this case.

5.4 Analysis of the influence of the studied parameters *d, e* and *f*

5.4.1 Overview

In this section, comparisons among the analysis results are presented. The results given in Tables 5.2-5.8 are reorganised according to Table 5.9 to show the influence of the distance of the longitudinal stiffener from the wide flange *d*, the out-of-plane height (eccentricity) of the longitudinal stiffener *e* and the in-plane height (width) of the longitudinal stiffener *f* (see Figure 5.1).

Table 5.9 Reorganisation of results for analysis.

Studied parameter	Tables	Figures
d	Tables 5.10-5.14	Figures 5.11-5.14
e	Tables 5.15-5.19	Figures 5.15-5.16
f	Tables 5.20-5.24	Figures 5.17-5.18

5.4.2 Influence of the distance of the stiffener from the wide flange (*d*)

The results of the parametric study on longitudinally stiffened webs have been rearranged into Tables 5.10-5.14 according to web height and steel thickness. A subdivision inside the tables is made so that horizontal lines separate groups of 2 or 3 models from each other. In each group, the other geometric parameters (*e* and *f*) are kept constant, while the value of *d* is varied. This allows the separation of the studied parameter from the others. Depending on the model group, the parameter *d* is given values 20 mm, 40 mm, 50 mm and 75 mm. The corresponding failure loads are marked with F_{di}, where *i* is the value of *d*, e.g. F_{d50} is the failure load for a model with *d* = 50 mm. The ratio F_{di}/F_{d20} is then calculated for

i = {40 mm, 50 mm, 75 mm}. Maximum, minimum and average values of the ratios F_{di}/F_{d20} are finally collected at the bottom of each table.

Table 5.10 Influence of d for 200 mm high webs with t_{nom} = 1.5 mm.

Model name	d (mm)	Failure load F (kN)	F_{di} / F_{d20}
200R-t15_d20_e8_f20	20	12.84	
200R-t15_d50_e8_f20	50	14.30	1.11
200R-t15_d75_e8_f20	75	14.54	1.13
200R-t15_d20_e12_f20	20	11.52	
200R-t15_d50_e12_f20	50	13.36	1.16
200R-t15_d20_e8_f50	20	12.05	
200R-t15_d75_e8_f50	75	13.71	1.14
200R-t15_d20_e12_f50	20	10.34	
200R-t15_d50_e12_f50	50	12.40	1.20
200R-t15_d20_e16_f50	20	9.15	
200R-t15_d50_e16_f50	50	11.44	1.25
		Minimum F_{d50} / F_{d20}	1.11
		Maximum F_{d50} / F_{d20}	1.25
		Average F_{d50} / F_{d20}	1.18
		Minimum F_{d75} / F_{d20}	1.13
		Maximum F_{d75} / F_{d20}	1.14
		Average F_{d75} / F_{d20}	1.14

Table 5.11 Influence of d for 150 mm high webs with t_{nom} = 1.5 mm.

Model name	d (mm)	Failure load F (kN)	F_{di} / F_{d20}
150R-t15_d20_e8_f20	20	12.05	
150R-t15_d50_e8_f20	50	14.63	1.21
150R-t15_d20_e8_f50	20	12.62	
150R-t15_d50_e8_f50	50	14.22	1.13
150R-t15_d20_e12_f20	20	10.85	
150R-t15_d50_e12_f20	50	13.55	1.25
150R-t15_d20_e12_f50	20	10.86	
150R-t15_d50_e12_f50	50	13.67	1.26
		Minimum F_{d50} / F_{d20}	1.13
		Maximum F_{d50} / F_{d20}	1.26
		Average F_{d50} / F_{d20}	1.21

Table 5.12 Influence of d for 100 mm high webs with t_{nom} = 1.5 mm.

Model name	d (mm)	Failure load F (kN)	F_{di} / F_{d20}
100R-t15_d20_e8_f20	20	12.73	
100R-t15_d50_e8_f20	50	14.77	1.16
100R-t15_d20_e12_f20	20	11.29	
100R-t15_d40_e12_f20	40	13.13	1.16
100R-t15_d20_e16_f20	20	10.96	
100R-t15_d50_e16_f20	50	12.10	1.10
		Minimum F_{d40} / F_{d20}	1.16
		Maximum F_{d40} / F_{d20}	1.16
		Average F_{d40} / F_{d20}	1.16
		Minimum F_{d50} / F_{d20}	1.10
		Maximum F_{d50} / F_{d20}	1.16
		Average F_{d50} / F_{d20}	1.13

Table 5.13 Influence of d for 200 mm high webs with t_{nom} = 1.0 mm.

Model name	d (mm)	Failure load F (kN)	F_{di} / F_{d20}
200R-t10_d20_e8_f20	20	5.68	
200R-t10_d50_e8_f20	50	6.19	1.09
200R-t10_d75_e8_f20	75	6.22	1.10
200R-t10_d20_e12_f20	20	4.94	
200R-t10_d50_e12_f20	50	5.76	1.16
200R-t10_d20_e8_f50	20	5.28	
200R-t10_d50_e8_f50	50	5.91	1.12
200R-t10_d75_e8_f50	75	5.93	1.12
200R-t10_d20_e12_f50	20	4.51	
200R-t10_d50_e12_f50	50	5.40	1.20
200R-t10_d20_e16_f50	20	3.99	
200R-t10_d50_e16_f50	50	4.94	1.24
		Minimum F_{d50} / F_{d20}	1.09
		Maximum F_{d50} / F_{d20}	1.24
		Average F_{d50} / F_{d20}	1.16
		Minimum F_{d75} / F_{d20}	1.10
		Maximum F_{d75} / F_{d20}	1.12
		Average F_{d75} / F_{d20}	1.11

Table 5.14 Influence of d for 100 mm high webs with t_{nom} = 1.0 mm.

Model name	d (mm)	Failure load F (kN)	F_{di} / F_{d20}
100R-t10_d20_e8_f20	20	5.69	
100R-t10_d40_e8_f20	40	6.49	1.14
100R-t10_d20_e12_f20	20	5.40	
100R-t10_d40_e12_f20	40	5.95	1.10
		Minimum F_{d40} / F_{d20}	1.10
		Maximum F_{d40} / F_{d20}	1.14
		Average F_{d40} / F_{d20}	1.12

Graphic representations of the results are shown in Figures 5.11 and 5.12 for t_{nom} = 1.5 mm and t_{nom} = 1.0 mm, respectively. Dotted lines (····) are used for b_w = 100 mm, dash lines (---) for b_w = 150 mm and full lines (—) for b_w = 200 mm. Different markers and colours are used to separate the model types from each other (a certain marker stands for a certain combination of *e* and *f*).

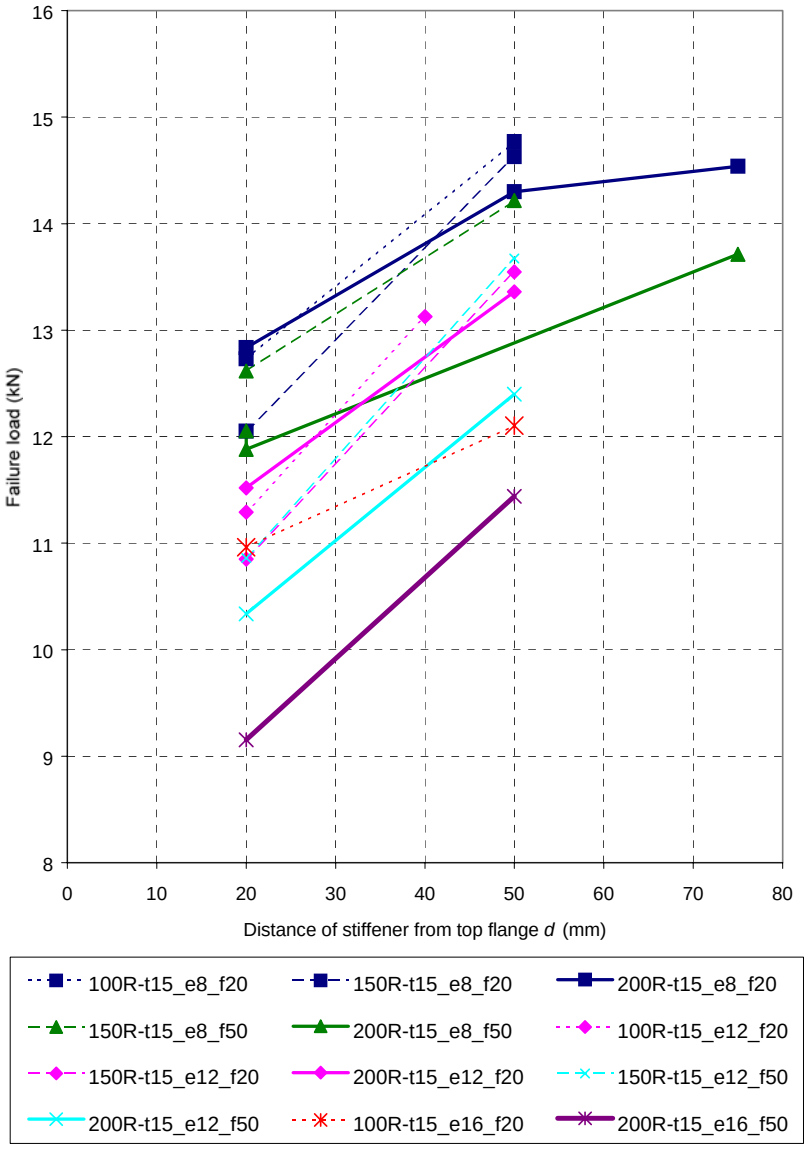

Fig. 5.11 Influence of *d* for t_{nom} = 1.5 mm.

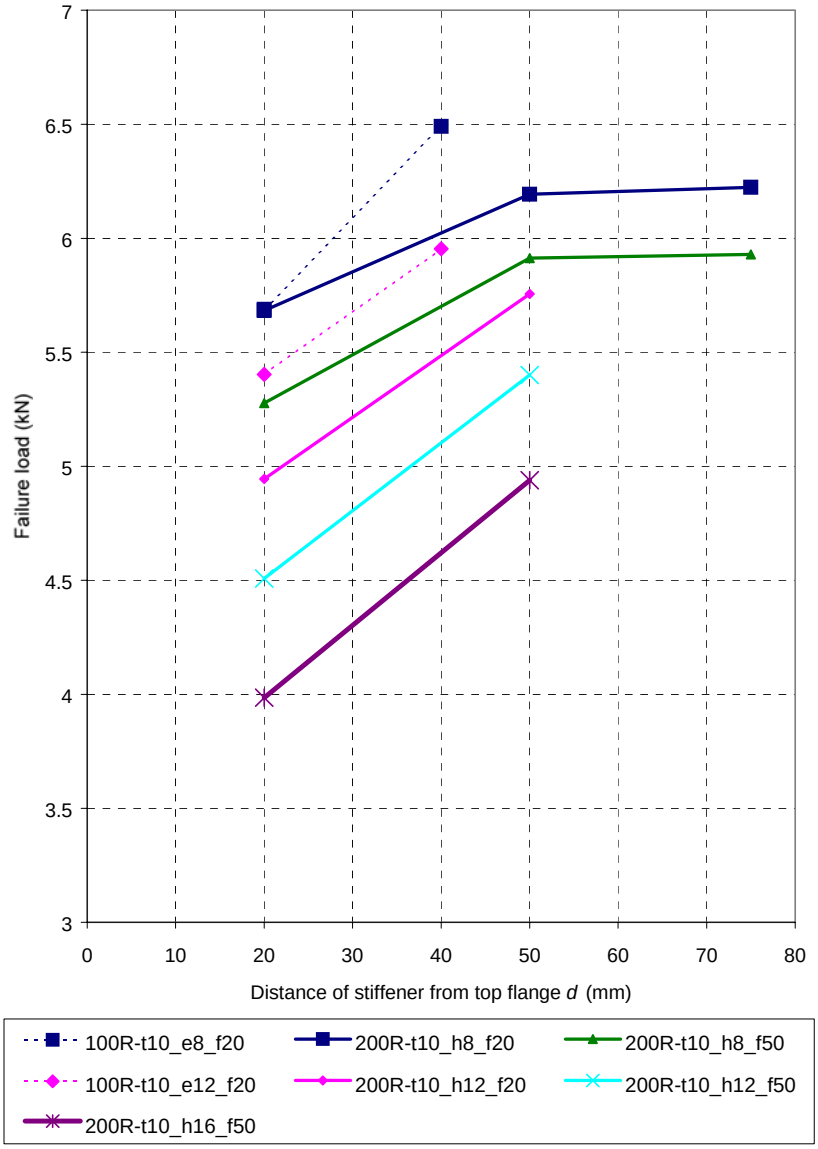

Fig. 5.12 Influence of d for t_{nom} = 1.0 mm.

It is clearly seen from the graphs that the increase of d from 20 mm to 40 mm or 50 mm increases the failure load. From Tables 5.10-5.14, it can be read that this increase is of the order of 11-25 % for b_w = 200 mm, 13-26 % for b_w = 150 mm and 10-16 % for b_w = 100 mm. However, for models with b_w = 200 mm, a further increase of d to 75 mm does not appear to have much influence. The effect seems to be slightly more pronounced for models with t_{nom} = 1.5 mm, for which the average of ratios F_{d40}/F_{d20} or F_{d50}/F_{d20} is 1.18, while for models with t_{nom} = 1.0 mm, it is 1.15, but it is difficult to draw a clear conclusion on this because of the relatively small amount of results.

It should be noted that the increase of d from 20 mm to 40 mm or 50 mm brings the longitudinal stiffener to different relative heights in different cross-sections, as demonstrated in Figure 5.13. For b_w = 100 mm, d = 40 mm means that the stiffener is symmetrically at mid-height of the web, when f = 20 mm, like in all models in Table 5.14. For b_w = 200 mm, however, the stiffener is still clearly in the upper part of the web when d = 50 mm. Only when d = 75 mm and f = 50 mm, is the stiffener symmetrically at mid-height of the 200 mm high web.

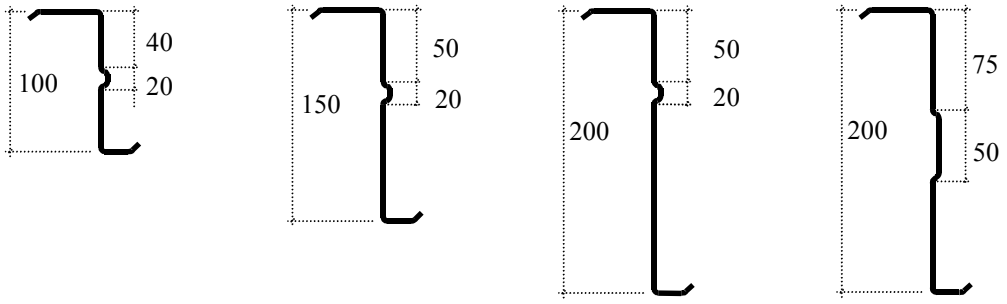

Fig. 5.13 Location of stiffener in cross-sections with b_w = 100 mm, b_w = 150 mm and b_w = 200 mm, when d = 40 mm, 50 mm or 75 mm.

For this reason, the influence of the location of the stiffener relative to web height was analysed by setting the ratio d / b_w on the x-axis and the ratio of the failure load of the longitudinally stiffened web F_{di} to the failure load of the corresponding flat web section F_{flat} on the y-axis, as shown in Figure 5.14. All models from figures 5.11 and 5.12 are combined here so that models with t_{nom} = 1.5 mm have larger markers than models with t_{nom} = 1.0 mm.

It can be seen that the lines from models with t_{nom} = 1.0 mm run a little higher than the lines from otherwise similar models with t_{nom} = 1.5 mm, which means that the influence of the longitudinal stiffener is slightly smaller for thinner webs. Otherwise, the lines show similar behaviour depending on the ratio d/b_w. It is once more seen that increasing the ratio d / b_w to at least 0.25 has a very positive effect on the resistance against ITF-loading, regardless of the other parameters in these models. A further increase of the ratio does not appear to lead to large increases in resistance, while not being detrimental either.

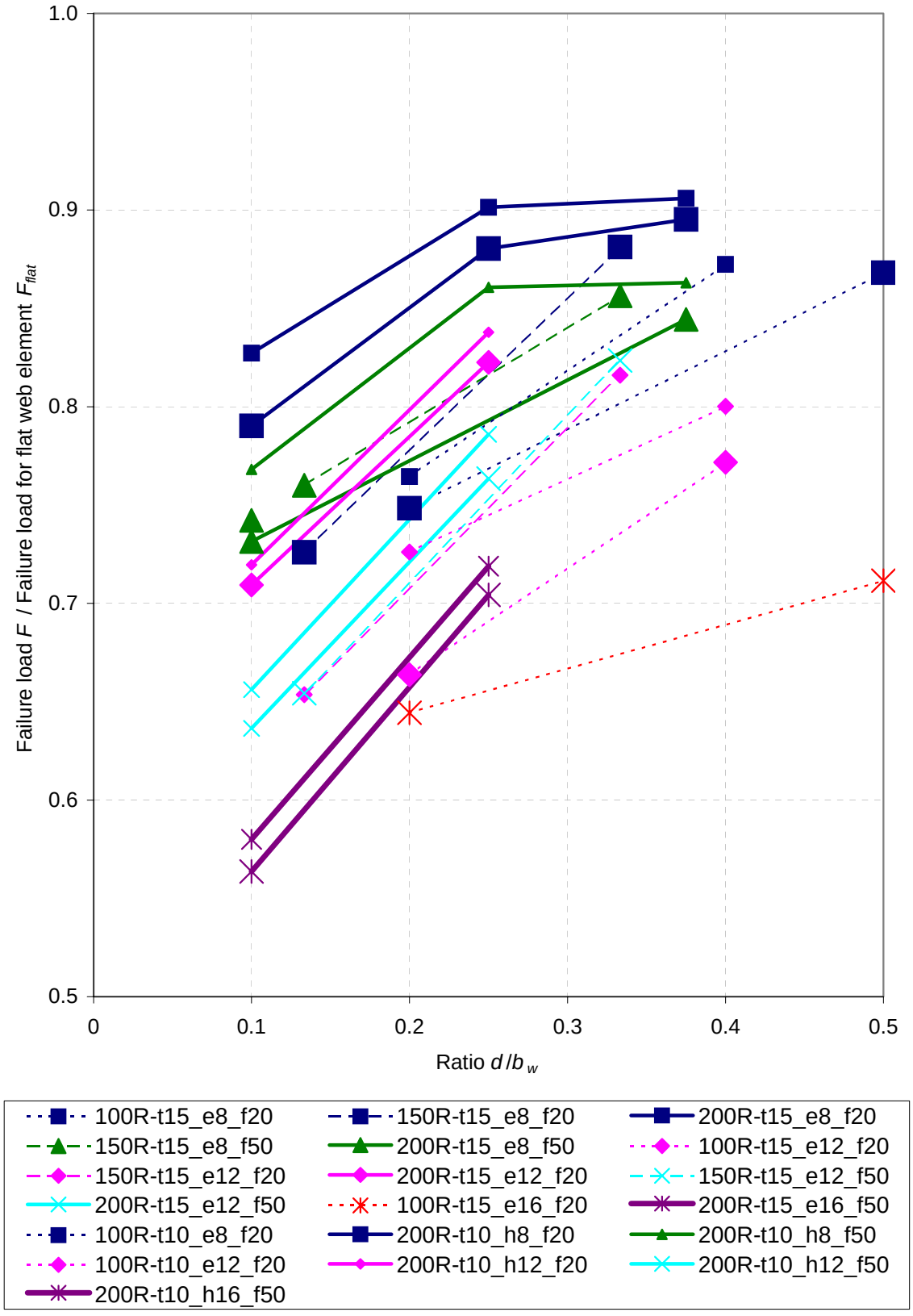

Fig. 5.14 Influence of the ratio d / b_w on failure load.

5.4.3 Influence of the eccentricity of the stiffener (*e*)

A second reorganisation of results into groups has been carried out in Tables 5.15-5.19 according to web height and steel thickness in order to find out the influence of the eccentricity *e* of the longitudinal stiffener on failure load. A subdivision inside the tables is again made so that horizontal lines separate groups of 2 or 3 models from each other. In each group, the other geometric parameters (*d* and *f*) are kept constant, while the value of *e* is varied. Depending on the model group, the parameter *e* is given values 5 mm, 8 mm, 12 mm and 16 mm. The corresponding failure loads are marked with F_{ei}, where *i* is the value of *e*, e.g. F_{e12} is the failure load for a model with *e* = 12 mm. The ratio F_{ei}/F_{e8} is then calculated for *i* = {5 mm, 12 mm, 16 mm}. Maximum, minimum and average values of the ratios F_{ei}/F_{e8} are finally collected at the bottom of each table.

Table 5.15 Influence of *e* for 200 mm high webs with t_{nom} = 1.5 mm.

Model name	*e* (mm)	Failure load *F* (kN)	F_{ei} / F_{e8}
200R-t15_d20_e8_f20	8	12.84	
200R-t15_d20_e12_f20	12	11.52	0.90
200R-t15_d20_e16_f20	16	10.43	0.81
200R-t15_d20_e8_f50	8	12.05	
200R-t15_d20_e12_f50	12	10.34	0.86
200R-t15_d20_e16_f50	16	9.15	0.76
200R-t15_d50_e8_f20	8	14.30	
200R-t15_d50_e12_f20	12	13.36	0.93
200R-t15_d50_e16_f50	16	11.44	0.80
200R-t15_d50_e8_f50	8	13.42	
200R-t15_d50_e12_f50	12	12.40	0.92
		Minimum F_{e12} / F_{e8}	0.86
		Maximum F_{e12} / F_{e8}	0.93
		Average F_{e12} / F_{e8}	0.90
		Minimum F_{e16} / F_{d20}	0.76
		Maximum F_{e16} / F_{d20}	0.81
		Average F_{e16} / F_{d20}	0.79

Graphic representations of the results are shown in Figures 5.15 and 5.16 for t_{nom} = 1.5 mm and t_{nom} = 1.0 mm, respectively. Dotted lines (····) are again used for b_w = 100 mm, dash lines (---) for b_w = 150 mm and full lines (—) for b_w = 200 mm. Different markers and colours are used to separate the model types from each other (a certain marker stands for a certain combination of *d* and *f*).

Table 5.16 Influence of e for 150 mm high webs with t_{nom} = 1.5 mm.

Model name	e (mm)	Failure load F (kN)	F_{ei} / F_{e8}
150R-t15_d20_e8_f20	8	12.05	
150R-t15_d20_e12_f20	12	10.85	0.90
150R-t15_d20_e8_f50	8	12.62	
150R-t15_d20_e12_f50	12	10.86	0.86
150R-t15_d50_e8_f20	8	14.63	
150R-t15_d50_e12_f20	12	13.55	0.93
150R-t15_d50_e8_f50	8	14.22	
150R-t15_d50_e12_f50	12	13.67	0.96
		Minimum F_{e12} / F_{e8}	0.86
		Maximum F_{e12} / F_{e8}	0.96
		Average F_{e12} / F_{e8}	0.91

Table 5.17 Influence of e for 100 mm high webs with t_{nom} = 1.5 mm.

Model name	e (mm)	Failure load F (kN)	F_{ei} / F_{e8}
100R-t15_d20_e8_f20	8	12.73	
100R-t15_d20_e12_f20	12	11.29	0.89
100R-t15_d20_e16_f20	16	10.96	0.86
100R-t15_d20_e8_f35	8	12.63	
100R-t15_d20_e16_f35	16	10.52	0.83
100R-t15_d20_e8_f50	8	12.86	
100R-t15_d20_e12_f50	12	11.95	0.93
100R-t15_d50_e8_f20	8	14.77	
100R-t15_d50_e16_f20	16	12.10	0.82
		Minimum F_{e12} / F_{e8}	0.89
		Maximum F_{e12} / F_{e8}	0.93
		Average F_{e12} / F_{e8}	0.91
		Minimum F_{e16} / F_{d20}	0.82
		Maximum F_{e16} / F_{d20}	0.86
		Average F_{e16} / F_{d20}	0.84

As is intuitively correct, increasing the value of e decreases the failure load of otherwise similar structures. Looking at the lines in Figures 5.14 and 5.15, it can be observed that the decrease happens fairly linearly with the increase of e. The phenomenon is quite similar to simply having an eccentric loading on a column. As in the case of d in the previous section, the steel thickness does not appear to have a notable influence on the results.

From Tables 5.15-5.19, it can be concluded that an increase of the value of e from 8 mm to 12 mm decreases the failure load by 4-14 % with an average decrease of about 9 % for all the studied models. When the eccentricity is further increased to e = 16 mm, the failure load decreases by 11-24 % from the situation with e = 8 mm, with an average decrease of about 18 %.

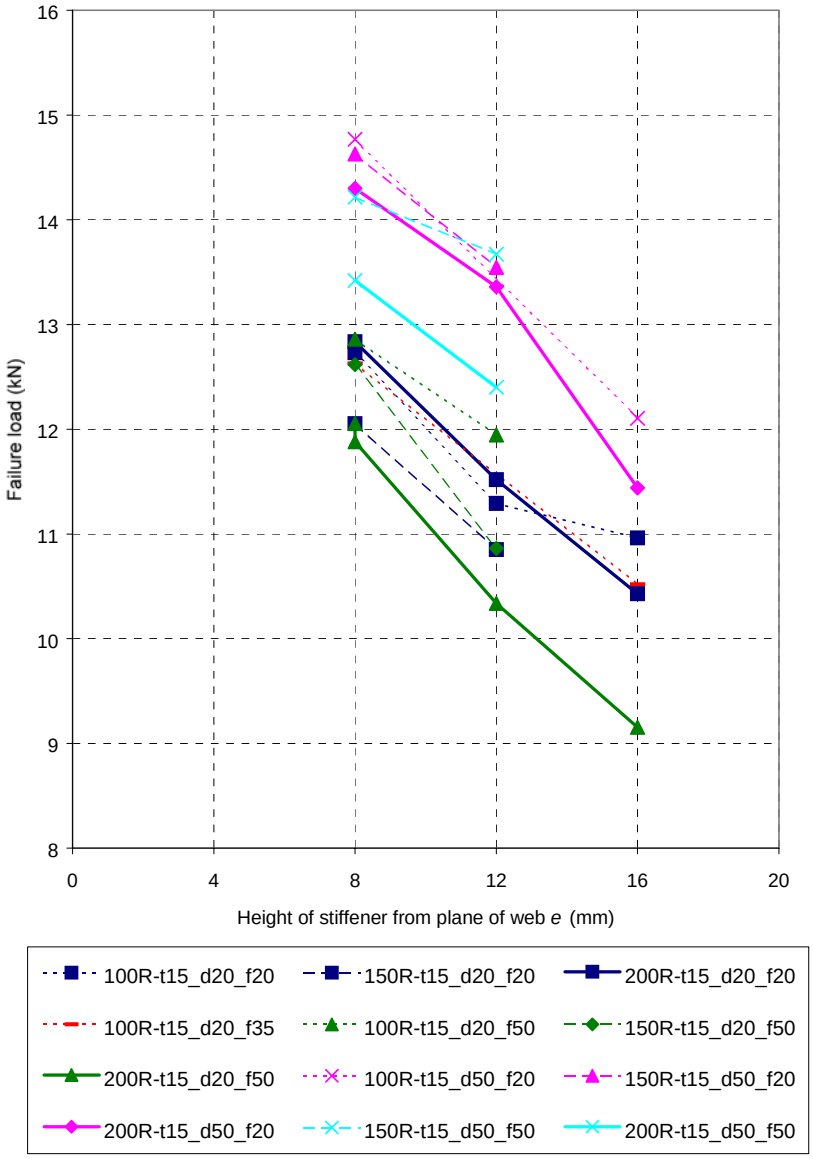

Fig. 5.15 Influence of e for t_{nom} = 1.5 mm.

Table 5.18 Influence of e for 200 mm high webs with t_{nom} = 1.0 mm.

Model name	e (mm)	Failure load F (kN)	F_{ei} / F_{e8}
200R-t10_d20_e8_f20	8	5.68	
200R-t10_d20_e12_f20	12	4.94	0.87
200R-t10_d20_e16_f20	16	4.40	0.89
200R-t10_d20_e8_f50	8	5.28	
200R-t10_d20_e12_f50	12	4.51	0.85
200R-t10_d20_e16_f50	16	3.99	0.76
200R-t10_d50_e8_f20	8	6.19	
200R-t10_d50_e12_f20	12	5.76	0.93
200R-t10_d50_e8_f50	8	5.91	
200R-t10_d50_e12_f50	12	5.40	0.91
200R-t10_d50_e16_f50	16	4.94	0.84
		Minimum F_{e12} / F_{e8}	0.85
		Maximum F_{e12} / F_{e8}	0.93
		Average F_{e12} / F_{e8}	0.89
		Minimum F_{e16} / F_{d20}	0.76
		Maximum F_{e16} / F_{d20}	0.89
		Average F_{e16} / F_{d20}	0.83

Table 5.19 Influence of e for 100 mm high webs with t_{nom} = 1.0 mm.

Model name	e (mm)	Failure load F (kN)	F_{ei} / F_{e8}
100R-t10_d20_e5_f20	5	6.15	1.08
100R-t10_d20_e8_f20	8	5.69	
100R-t10_d20_e12_f20	12	5.40	0.95
100R-t10_d20_e5_f35	5	6.28	1.01
100R-t10_d20_e8_f35	8	6.20	
100R-t10_d20_e5_f50	5	6.17	1.02
100R-t10_d20_e8_f50	8	6.08	
100R-t10_d20_e12_f50	12	5.30	0.87
100R-t10_d40_e8_f20	8	6.49	
100R-t10_d40_e12_f20	12	5.95	0.92
100R-t10_d40_e8_f30	8	6.36	
100R-t10_d40_e12_f30	12	6.06	0.95
		Minimum F_{e5} / F_{e8}	1.01
		Maximum F_{e5} / F_{e8}	1.08
		Average F_{e5} / F_{e8}	1.04
		Minimum F_{e12} / F_{e8}	0.87
		Maximum F_{e12} / F_{e8}	0.95
		Average F_{e12} / F_{e8}	0.92

As can be seen from Table 5.19 showing the results for the case with b_w = 100 mm and t_{nom} = 1.0 mm, three models with d = 20 mm were also computed with the eccentricity e equal to 5 mm, while f = {20 mm, 35 mm 50 mm}. Depending on the value of f, the failure load increased by 1-8 % in comparison to the case with e = 8 mm. The increase was greatest with f = 20 mm, which seems intuitively correct, as in this case the stiffener is most compact and can probably offer a higher stiffness than when f has a larger value.

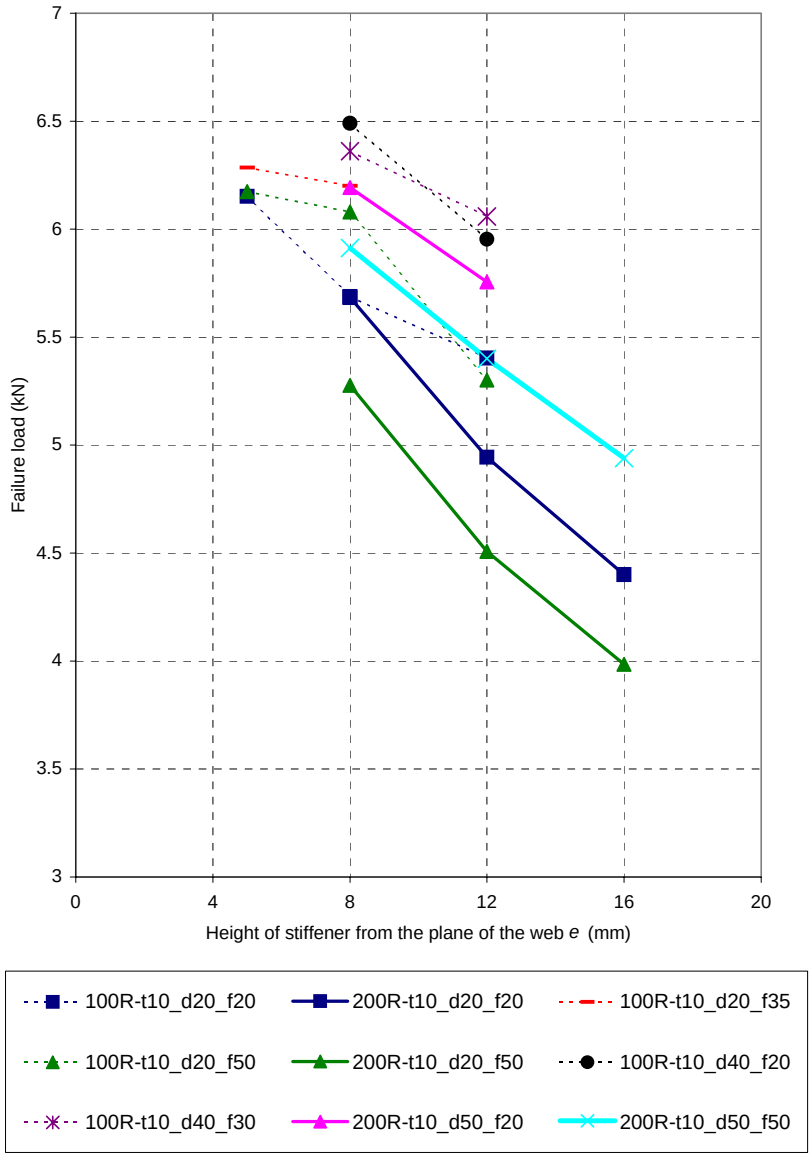

Fig. 5.16 Influence of e for t_{nom} = 1.0 mm.

As was done with d above, the influence of the eccentricity of the longitudinal stiffener relative to web height was analysed by setting the ratio e / b_w on the x-axis and the ratio of the failure load of the longitudinally stiffened web F_{di} to the failure load of the corresponding flat web section F_{flat} on the y-axis, as shown in Figure 5.17. All models from figures 5.15 and 5.16 are combined here so that models with t_{nom} = 1.5 mm have larger markers than models with t_{nom} = 1.0 mm. It can be seen again that the lines from models with t_{nom} = 1.0 mm run a little higher than the lines from otherwise similar models with t_{nom} = 1.5 mm. Besides this, the lines show similar behaviour depending on the ratio e/b_w. It is once more seen that decreasing the ratio e / b_w has a strong influence on the failure load.

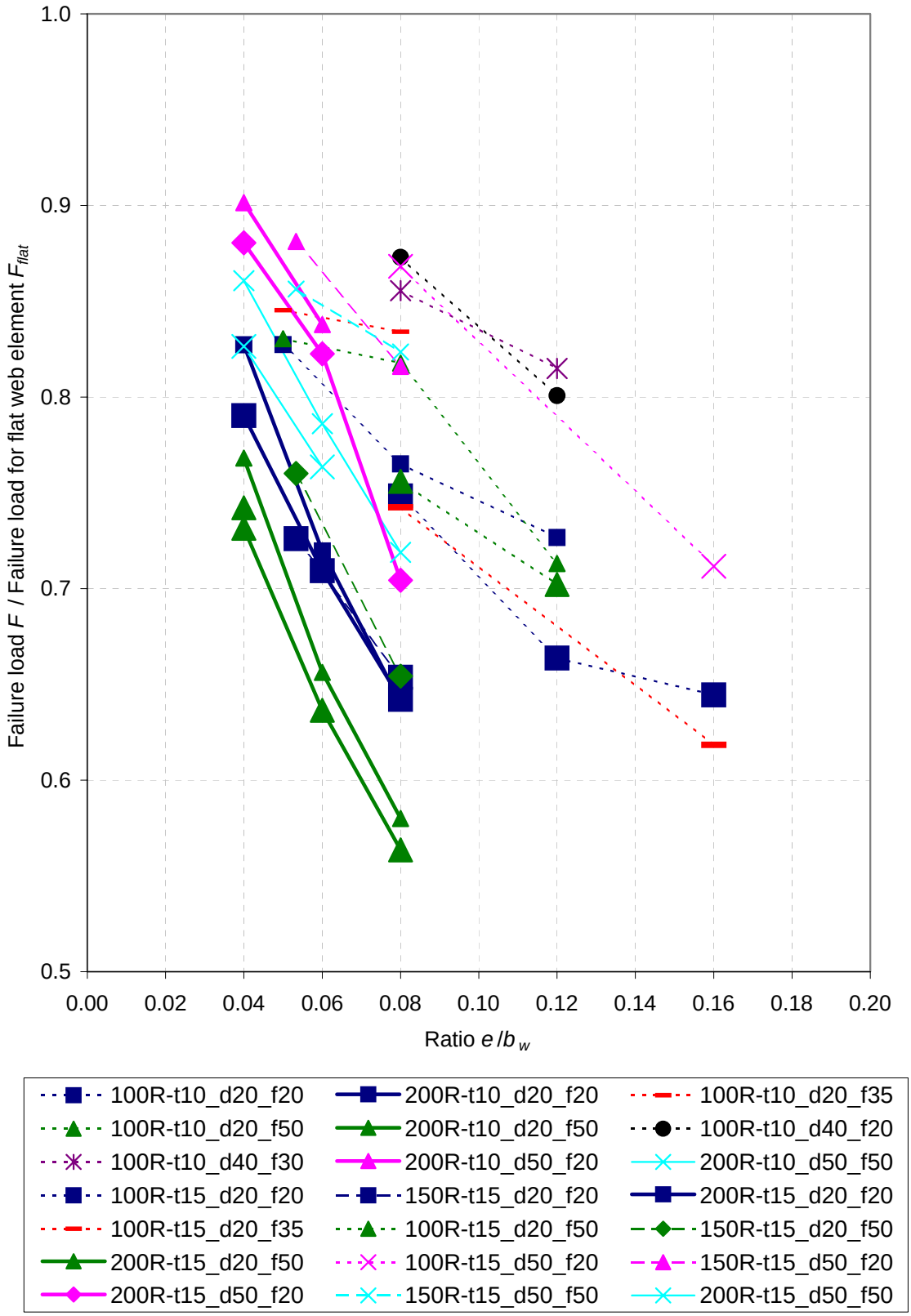

Fig. 5.17 Influence of the ratio e / b_w on failure load.

5.4.4 Influence of in-plane length of the stiffener (*f*)

A third reorganisation of results into groups has been carried out in Tables 5.20-5.24 according to web height and steel thickness in order to find out the influence of the in-plane length *f* of the longitudinal stiffener on failure load. A subdivision inside the tables is once again made so that horizontal lines separate groups of 2 or 3 models from each other. In each group, the other geometric parameters (*d* and *e*) are kept constant, while the value of *f* is varied. Depending on the model group, the parameter *f* is given values 20 mm, 30 mm, 35 mm, 50 mm and 100 mm. The corresponding failure loads are marked with F_{fi}, where *i* is the value of *f*, e.g. F_{f50} is the failure load for a model with *f* = 50 mm. The ratio F_{fi}/F_{f20} is then calculated for *i* = {30 mm, 35 mm, 50 mm, 100 mm}. Maximum, minimum and average values of the ratios F_{fi}/F_{f20} are finally collected at the bottom of each table.

Table 5.20 Influence of *f* for 200 mm high webs with t_{nom} = 1.5 mm.

Model name	*f* (mm)	Failure load *F* (kN)	F_{fi} / F_{f20}
200R-t15_d20_e8_f20	20	12.835	
200R-t15_d20_e8_f35	35	12.097	0.94
200R-t15_d20_e8_f50	50	12.054	0.94
200R-t15_d50_e8_f20	20	14.299	
200R-t15_d50_e8_f50	50	13.421	0.94
200R-t15_d50_e8_f100	100	12.556	0.88
200R-t15_d75_e8_f20	20	14.539	
200R-t15_d75_e8_f50	50	13.713	0.94
200R-t15_d20_e12_f20	20	11.519	
200R-t15_d20_e12_f50	50	10.336	0.90
200R-t15_d50_e12_f20	20	13.359	
200R-t15_d50_e12_f50	50	12.399	0.93
200R-t15_d20_e16_f20	20	10.429	
200R-t15_d20_e16_f50	50	9.154	0.88
		Minimum F_{f35} / F_{f20}	0.94
		Maximum F_{f35} / F_{f20}	0.94
		Average F_{f35} / F_{f20}	0.94
		Minimum F_{f50} / F_{f20}	0.88
		Maximum F_{f50} / F_{f20}	0.94
		Average F_{f50} / F_{f20}	0.92
		Minimum F_{f100} / F_{f20}	0.88
		Maximum F_{f100} / F_{f20}	0.88
		Average F_{f100} / F_{f20}	0.88

Graphic representations of the results are shown in Figures 5.18 and 5.19 for t_{nom} = 1.5 mm and t_{nom} = 1.0 mm, respectively. Dotted lines (····) are again used for b_w = 100 mm, dash lines (---) for b_w = 150 mm and full lines (—) for b_w = 200 mm. Different markers and

colours are used to separate the model types from each other (a certain marker stands for a certain combination of *d* and *e*).

Table 5.21 Influence of *f* for 150 mm high webs with t_{nom} = 1.5 mm.

Model name	*f* (mm)	Failure load *F* (kN)	F_{fi} / F_{f20}
150R-t15_d20_e8_f20	20	12.05	
150R-t15_d20_e8_f35	35	12.19	1.01
150R-t15_d20_e8_f50	50	12.62	1.05
150R-t15_d50_e8_f20	20	14.63	
150R-t15_d50_e8_f50	50	14.22	0.97
150R-t15_d20_e12_f20	20	10.85	
150R-t15_d20_e12_f50	50	10.86	1.00
150R-t15_d50_e12_f20	20	13.55	
150R-t15_d50_e12_f50	50	13.67	1.01
		Minimum F_{f35} / F_{f20}	1.01
		Maximum F_{f35} / F_{f20}	1.01
		Average F_{f35} / F_{f20}	1.01
		Minimum F_{f50} / F_{f20}	0.97
		Maximum F_{f50} / F_{f20}	1.05
		Average F_{f50} / F_{f20}	1.01

Table 5.22 Influence of *f* for 100 mm high webs with t_{nom} = 1.5 mm.

Model name	*f* (mm)	Failure load *F* (kN)	F_{fi} / F_{f20}
100R-t15_d20_e8_f20	20	12.73	
100R-t15_d20_e8_f35	35	12.63	0.99
100R-t15_d20_e8_f50	50	12.86	1.01
100R-t15_d20_e12_f20	20	11.29	
100R-t15_d20_e12_f50	50	11.95	1.06
100R-t15_d20_e16_f20	20	10.96	
100R-t15_d20_e16_f35	35	10.52	0.96
100R-t15_d40_e12_f20	20	13.13	
100R-t15_d40_e12_f30	30	12.66	0.96
		Minimum F_{f30} / F_{f20}	0.96
		Maximum F_{f30} / F_{f20}	0.96
		Average F_{f30} / F_{f20}	0.96
		Minimum F_{f35} / F_{f20}	0.96
		Maximum F_{f35} / F_{f20}	0.99
		Average F_{f35} / F_{f20}	0.98
		Minimum F_{f50} / F_{f20}	1.01
		Maximum F_{f50} / F_{f20}	1.06
		Average F_{f50} / F_{f20}	1.04

Table 5.23 Influence of f for 200 mm high webs with t_{nom} = 1.0 mm.

Model name	f (mm)	Failure load F (kN)	F_{fi} / F_{f20}
200R-t10_d20_e8_f20_EC3	20	5.68	
200R-t10_d20_e8_f35_EC3	35	5.35	0.94
200R-t10_d20_e8_f50_EC3	50	5.28	0.93
200R-t10_d50_e8_f20_EC3	20	6.19	
200R-t10_d50_e8_f50_EC3	50	5.91	0.95
200R-t10_d50_e8_f100_EC3	100	5.63	0.91
200R-t10_d75_e8_f20_EC3	20	6.22	
200R-t10_d75_e8_f50_EC3	50	5.93	0.95
200R-t10_d20_e12_f20_EC3	20	4.94	
200R-t10_d20_e12_f50_EC3	50	4.51	0.91
200R-t10_d50_e12_f20_EC3	20	5.76	
200R-t10_d50_e12_f50_EC3	50	5.40	0.94
200R-t10_d20_e16_f20_EC3	20	4.40	
200R-t10_d20_e16_f50_EC3	50	3.99	0.91
		Minimum F_{f35} / F_{f20}	0.94
		Maximum F_{f35} / F_{f20}	0.94
		Average F_{f35} / F_{f20}	0.94
		Minimum F_{f50} / F_{f20}	0.91
		Maximum F_{f50} / F_{f20}	0.95
		Average F_{f50} / F_{f20}	0.93
		Minimum F_{f100} / F_{f20}	0.91
		Maximum F_{f100} / F_{f20}	0.91
		Average F_{f100} / F_{f20}	0.91

Overall, the steel thickness does not appear to have a notable influence on these results either. Other than that, it is more difficult to draw general conclusions about the results concerning the influence of f than it was in the cases of d and e above. Some of the lines in Figures 5.18 and 5.19 are increasing, some decreasing, some staying practically the same as the value of f is increased from the base value of 20 mm. However, some trends can be observed.

For all models with b_w = 200 mm, the failure load decreases when f is increased from the base value of 20 mm. Furthermore, the decrease appears to be fairly linear and of equal magnitude when f is increased from 20 mm to 50 mm in all cases. Model groups 200R-t15_d20_e8 and 200R-t10_d20_e8 show, however, that the larger part of this decrease in failure load happens at values f = 20...35 mm than at values f = 35...50 mm. When this result is combined with what was noted in the previous section about models with e = 5 mm, it can be concluded that the compactness (low values of e and f) of the stiffener is a positive factor for the web section's resistance against local transverse forces.

The overall decrease in failure load is of the order of 9-12 % when the value of f is increased from the base value of 20 mm up to 100 mm, with about 30-50 % of the change taking place between 20 mm and 35 mm and the rest between 35 mm and 100 mm.

For models with b_w = 150 mm, the results are not quite as straightforward. As the value of f is increased from 20 mm to 50 mm, some of the corresponding failure loads in Figure 5.16 decrease, some increase and some remain the same. No correlation with the values of d and/or e can be seen. The same is true for b_w = 100 mm.

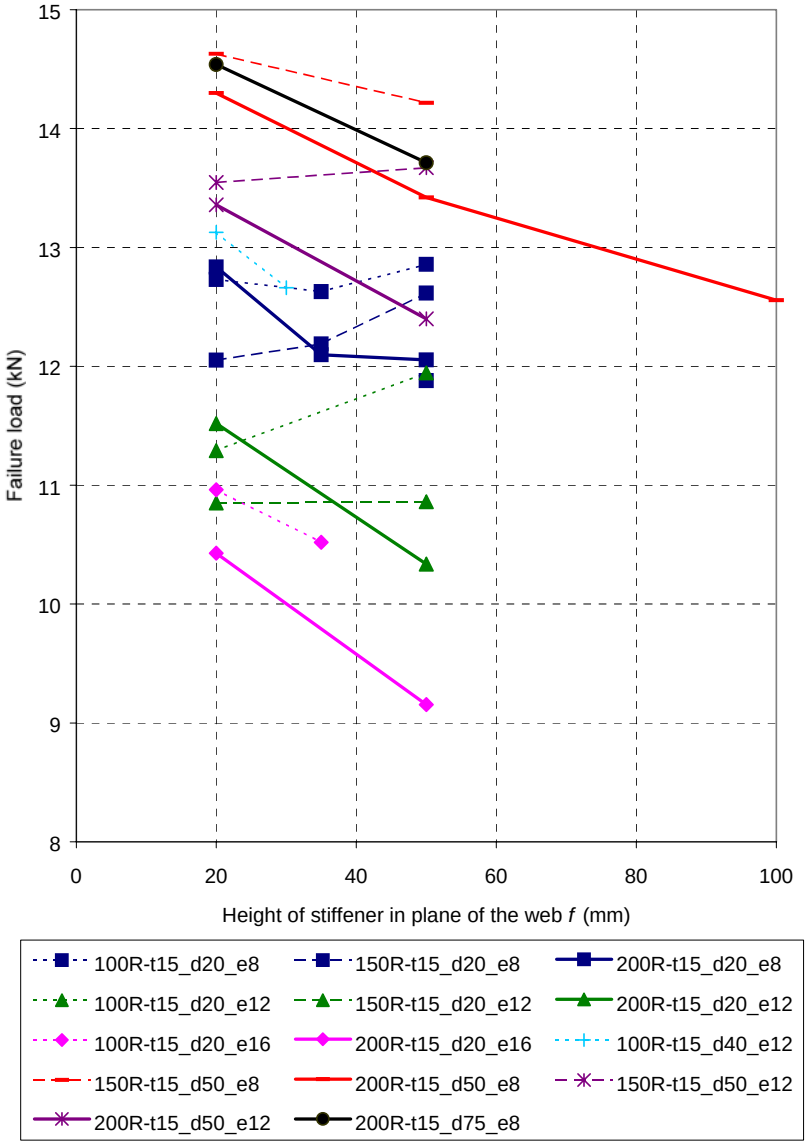

Fig. 5.18 Influence of f for t_{nom} = 1.5 mm.

Table 5.24 Influence of f for 100 mm high webs with t_{nom} = 1.0 mm.

Model name	f (mm)	Failure load F (kN)	F_{fi} / F_{f20}
100R-t10_d20_e5_f20	20	6.15	
100R-t10_d20_e5_f35	35	6.28	1.02
100R-t10_d20_e5_f50	50	6.17	1.00
100R-t10_d20_e8_f20	20	5.69	
100R-t10_d20_e8_f35	35	6.20	1.09
100R-t10_d20_e8_f50	50	6.08	1.07
100R-t10_d40_e8_f20	20	6.49	
100R-t10_d40_e8_f30	30	6.36	0.98
100R-t10_d20_e12_f20	20	5.40	
100R-t10_d20_e12_f50	50	5.30	0.98
100R-t10_d40_e12_f20	20	5.95	
100R-t10_d40_e12_f30	30	6.06	1.02
		Minimum F_{f30} / F_{f20}	0.98
		Maximum F_{f30} / F_{f20}	1.02
		Average F_{f30} / F_{f20}	1.00
		Minimum F_{f35} / F_{f20}	1.02
		Maximum F_{f35} / F_{f20}	1.09
		Average F_{f35} / F_{f20}	1.06
		Minimum F_{f50} / F_{f20}	0.98
		Maximum F_{f50} / F_{f20}	1.07
		Average F_{f50} / F_{f20}	1.02

As was done with d and e above, the influence of the in-plane width of the longitudinal stiffener f relative to web height was analysed by setting the ratio f / b_w on the x-axis and the ratio of the failure load of the longitudinally stiffened web F_{di} to the failure load of the corresponding flat web section F_{flat} on the y-axis, as shown in Figure 5.20. All models from figures 5.18 and 5.19 are again combined here so that models with t_{nom} = 1.5 mm have larger markers than models with t_{nom} = 1.0 mm. It can be seen once more that the lines from models with t_{nom} = 1.0 mm run a little higher than the lines from otherwise similar models with t_{nom} = 1.5 mm. For some cases, the inclinations of the lines for similar models with different steel thicknesses are slightly different. As seen above, no clear overall trend can be seen from this graph either.

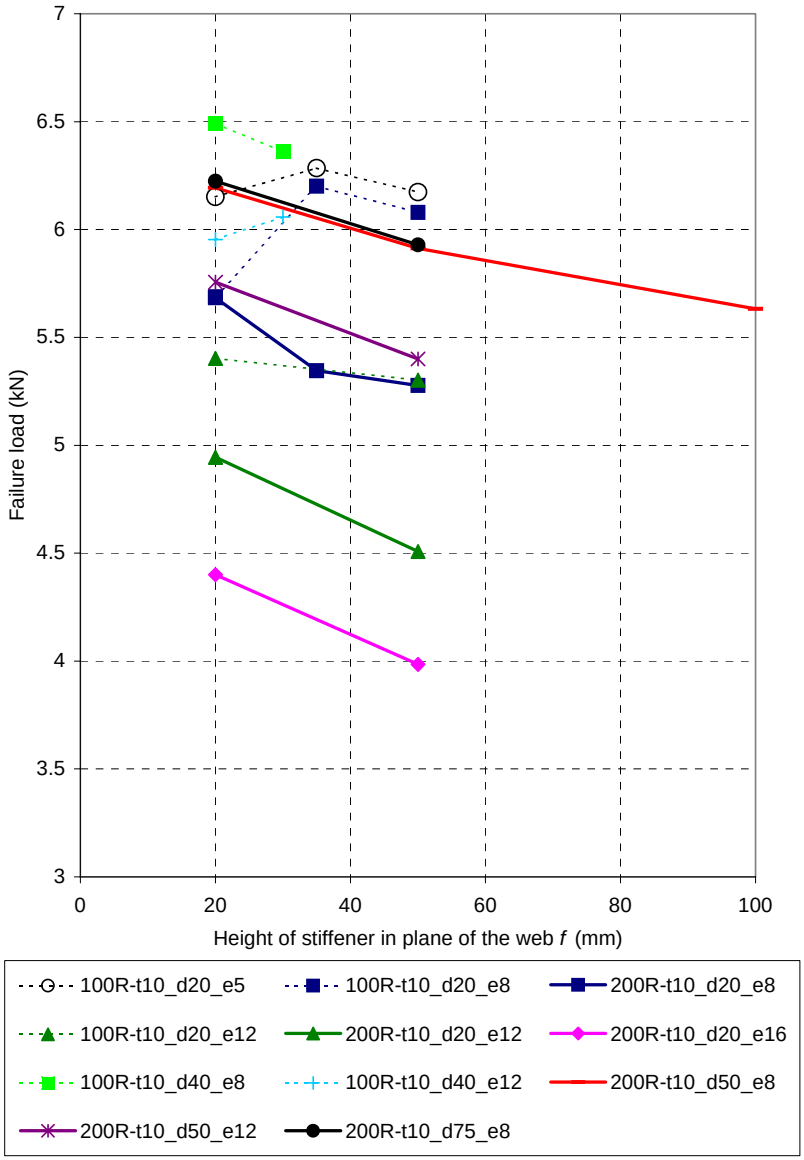

Fig. 5.19 Influence of f for t_{nom} = 1.0 mm.

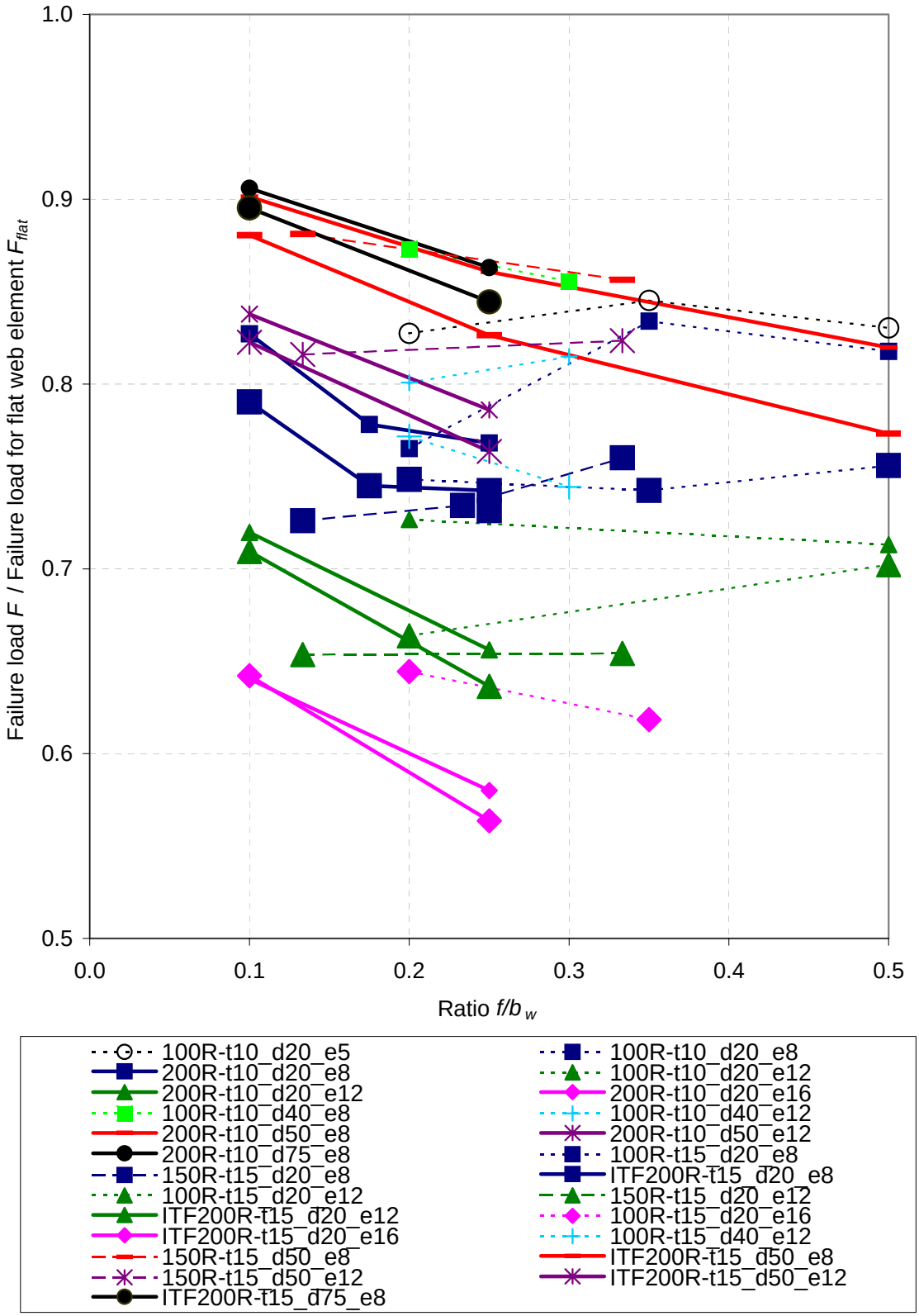

Fig. 5.20 Influence of the ratio f / b_w on failure load.

6. DISCUSSION OF THE RESULTS AND CONCLUSIONS

6.1 General

This research has focused on the resistance against local transverse forces, or web crippling capacity, of thin-walled steel cassettes. These types of structures have previously been designed as single-span structures and web crippling at the support area has usually not been a critical factor in design. Instead, sagging moment capacity has determined the design level. However, if the cassette is to be installed as a continuous structure over two or more spans, the capacity against local transverse forces at the inner support has to be determined.

Although design codes have since long included design formulae for the determination of resistance against local transverse forces, the type of longitudinally stiffened web often used in cassette cross-sections is not included in the current design codes. This study therefore had the following objectives, which effectively divided the research work into separate sub-projects:

- The determination of the web crippling strength of both flat and longitudinally stiffened cassette webs and constructions experimentally;
- The development and validation of numerical models on the basis of the experimental data;
- The numerical study of the influence of different geometrical parameters on the resistance against local transverse forces of longitudinally stiffened cassette webs;
- The provision of design recommendations concerning the resistance to local transverse forces of longitudinally stiffened cassettes webs.

The following sections summarize the methodologies used in the study, the principal results obtained and the conclusions, and propose further research for the continued development of the solutions to the problems.

6.2 Methodology

The problem was initially approached by carrying out a thorough literature study on the existing research work and design codes on cassette sections in general and web crippling in particular. The lack of information on the web crippling of longitudinally stiffened webs of the type studied was thus established.

A test programme was designed in order to gain necessary and valid results to be used directly in the verification of existing design rules and indirectly by using the results to validate numerical models for parametric studies of cassette geometries. Non-linear finite element modelling was already effectively used in the planning of the test programme after similar models had been developed for test results found in literature. The preliminary FE-models were able to predict the test results with acceptable accuracy.

After testing, the material test data and the actual measured cross-section dimensions were available and the numerical models could be developed further. Very good agreement between numerical analyses and test results was obtained. This allowed the initiation of a parametric study on longitudinally stiffened cassette web sections, during which the influence of different cross-section dimensions on the resistance against local transverse forces was investigated.

6.3 Experimental results

The experimental results showed that the existence of a longitudinal stiffener of the type that was tested reduces the resistance of the web section against local transverse forces by about 17-22 % in comparison to a similar flat web section.

The load-displacement graphs of the tested sections show a clear difference between the behaviour of flat and longitudinally stiffened web sections. While the stiffness and ultimate load of the flat web section are higher than those of the similar longitudinally stiffened web, also the failure happens more quickly for the flat web section. When the slenderness of the flat web is high, a clear buckling phenomenon takes place. When the slenderness is lower and the section is more compact, a gradual yielding leads to failure. For the longitudinally

stiffened web sections, the yielding happens slower and near the failure load, the displacements increase relatively quickly, i.e. the load-displacement curve's tangent is nearly horizontal. Once the failure load is reached and the test is continued, the load decreases slowly, while the load for the flat web sections starts to increase again after a short while. This is due to the redistribution of stresses and the development of a tension field in the web section. As the loading is continued, the tension field extends further away from the load application area.

Interior one-flange - tests were carried out with spans 600 mm and 1000 mm. The results showed that the influence of the bending moment on web crippling capacity at these short spans is not very important. The average failure load of the tested sections with L_{span} = 1000 mm was reduced only by about 2-4 % in comparison to the corresponding interior two-flange - tests. For the sections with L_{span} = 600 mm, the failure load was actually slightly increased from the ITF-tests. This is most likely due to the development of a tension field between the stiffened support areas and the load application area, which helps a larger area of the cassette web to carry the load.

Tests on built-up structures comprised of two full cassette sections and a total of four webs were carried out to study the difference between web sections acting alone and together with an adjacent web. According to the tests, the failure load per web increased by about 28 % for flat web sections and 12 % for longitudinally stiffened webs when compared to similar single-web specimens. The increase is greater for structures with flat webs, because these benefit more from the extra support due to the higher slenderness (greater height) of the plate area. However, the overall stiffness per web section was not increased.

The test results were compared with nominal design values calculated according to the European, American (U.S.), Australian and Finnish structural design codes. It was noticed that all codes give conservative values in comparison to the test results and that the American and Australian codes give slightly higher strength values than the European code, while the Finnish code is most conservative of the four. However, the American and Australian design codes prescribe a factor of safety equal to 0.75 (to be multiplied with nominal web crippling strength to obtain design resistance), while the European and Finnish codes are satisfied with a safety factor equal to unity.

Concerning the European design code, large discrepancies were noticed in design values depending on whether the equation for single webs or two or more webs was used. On the basis of the present results, it is recommended that the equation for single webs be used.

6.4 Numerical studies

A large number of finite element modelling has been carried out during this research. The functioning of the numerical models was validated on the basis of test results found in literature and the tests carried out during the present study. Overall, very good correlation was obtained between numerical models and tests after a substantial amount of experimenting on different modelling schemes and options. Among the modelling factors studied were the element sizes, the influence of initial imperfections, the length of the load application period and the number of elements used to model the rounded corners. Also the effect of having elastic spring supports at the flanges instead of screw connections was studied. The validity of the models was given a lot of attention in this study, because that was essential for the credibility of the subsequent parametric study.

In the end, a quasi-static dynamic analysis type was chosen as the basis for the parametric modelling. This made possible the realistic modelling of the support and loading pads using contact surfaces, which allows the separation and individual deformations of the flanges at the loading area. This would not be possible if prescribed displacement boundary conditions were applied. The drawback of this method was the high cost in CPU-time, which was increased so much that the number of different parametric models had to be limited for practical reasons.

In order to study the influence of the size and position of the longitudinal stiffener in the web on the resistance against local transverse forces, a total of 71 parametric numerical models (+ 5 comparison models with flat webs) were run using the model configuration validated on the basis of test results. Three main parameter, i.e. the distance of the stiffener from the wide flange d, the out-of-plane eccentricity of the stiffener e and the in-plane height of the stiffener f were varied, and an additional few models were run to see the influence of the load bearing length on resistance. The web height was chosen as 200 mm, 150 mm or 100 mm and the steel sheet thickness was 0.96 mm or 1.46 mm.

It was concluded that the existence of a longitudinal stiffener of the studied type decreases the resistance of the cross-section against local transverse forces by at least 10 % and much more if it is unfavourably situated or shaped. The relative decrease of resistance is slightly smaller for cross-sections with steel thickness 0.96 mm than for cross-sections with thickness 1.46 mm.

It was found that the placing of the stiffener very close to the flange is unfavourable for the resistance against local transverse forces. It is better to place the stiffener at least a distance equal to 0.25 b_w away from the flange. If the stiffener is moved closer than 0.25 b_w to the mid-height of the web (up to 0.5 b_w), the further influence on resistance is slight but positive. However, if the practical design case and the original purpose of the longitudinal stiffener (increasing bending resistance) are considered, it is probably favourable that the stiffener be closer to the compressed flange than to the mid-height of the web. Therefore it could be concluded that the distance d = 0.25 b_w from the flange can be recommended, although this should be verified in analyses where the combined effects of local transverse forces and bending moment are considered.

The eccentricity of the stiffener e was found to be inversely proportional to the resistance, as could well be expected. Furthermore, the influence appeared to be fairly linear. The influence of the in-plane length of the stiffener f was less coherent than those of d and e. However, it would appear that the compactness (low values of f and e) of the stiffener is favourable for the resistance. Concerning load bearing length, the analyses confirmed that the resistance against local transverse forces is directly proportional to load bearing length.

Although the idea of developing a new design formula or a new resistance factor to be used similarly to Eq. (2.16) of ENV 1993-1-3:1996 for the case of a stiffened webs with two folds on opposite sides of the web was set as a possible objective of the present study, it had to be accepted during the course of the work that this objective was too ambitious due to the considerable number of statistical data needed and the relatively high cost of the numerical modelling work. However, it is hoped that the test and analysis results and the general guidelines and conclusions given in the present study will be of help in the optimisation of the cross-section geometries of cold-formed steel structures and the formulae used in design.

A reduction factor equal to 0.7 - 0.9 should be used for the type of longitudinally stiffened webs considered in this study in connection with the design code formulae for the resistance of unreinforced webs against local transverse forces, depending on the cross-section geometry.

6.5 Further research

Each study has to be limited to a certain scope - otherwise the work would never be finished. Further research is needed on the following aspects.

Numerical parametric studies should be carried out under different loading conditions, namely IOF-, ETF- and EOF-conditions. This would lead to a better understanding of the influence of the different geometrical parameters on the resistance against local transverse forces and naturally lead to the inclusion of the combined effects of hogging bending moment and support reaction in the study. Some further testing may be necessary to validate the numerical models with different loading conditions. The accuracy of the numerical models could be improved further - or other modelling options could be developed.

Different types of stiffeners and cross-sections should be considered in order to widen the field of application of the research. Once a sufficient amount of data has been gathered, a design formula could be developed and used within prescribed limits.

The current design equations for unreinforced webs give relatively conservative values on the basis of this research. Work for their optimisation should be continued.

REFERENCES

ABAQUS Version 6.2 (2001), *User's Manual*, Hibbitt, Karlsson & Sorensen, Inc., U.S.A.

ABAQUS Version 6.3 (2002), *User's Manual*, Hibbitt, Karlsson & Sorensen, Inc., U.S.A.

ABAQUS Version 6.4 (2003), *User's Manual*, Hibbitt, Karlsson & Sorensen, Inc., U.S.A.

AISI (1996), *Specification for the Design of Cold-Formed Steel Members with Commentary*, Cold-Formed Steel Design Manual - Part V, American Iron and Steel Institute, 1996 Edition, Washington, DC, U.S.A.

ANSYS 5.4 (1999), User's Manual, University High Option, ANSYS, Inc., Southpointe 275 Technology Drive, Canonsburg, PA 15317, U.S.A.

AS/NZS 4600 (1996), Australian / New Zealand Standard for Cold-Formed Steel Structures, Standards Australia, Sydney, Australia.

Baehre, R. (1975), Sheet Metal Panels of Use in Building Construction - Current Research Projects in Sweden, *Proceedings of the Third International Specialty Conference on Cold-Formed Steel Structures*, St.Louis, MO, U.S.A., 24-25.11.1975, University of Missouri-Rolla.

Baehre, R., Buca, J. (1986), Die wirksame Breite des Zuggurtes von biegebeanspruchten Kassetten (Effective Width of the Tension Flange of Thin-Walled C-Shaped Panels), *Stahlbau* 9/1986, pp. 276-285, Wilhelm Ernst & Sohn Verlag, Berlin, Germany (in German).

Baehre, R. (1987), Zur Schubfeldwirkung und –bemessung von Kassettenkonstruktionen (Longitudinal Shear Effects and Dimensioning of Waffle-Structures), *Stahlbau* 7/1987, pp. 197-202, Wilhelm Ernst & Sohn Verlag, Berlin, Germany (in German).

Baehre, R., Holz, R., Voß, R.P. (1988), Befestigung von Trapezprofiltafeln auf Stahlkassettenprofilen (Fastening of Trapezoidal Sheetings to Thin-Walled C-Shaped Panels), *Stahlbau*10/1988, pp.309-311, Wilhelm Ernst & Sohn Verlag, Berlin, Germany (in German).

Bakker, M.C.M. (1992), *Web Crippling of Cold-Formed Steel Members*, PhD Thesis, Eindhoven University of Technology, The Netherlands.

Davies, J.M., Bryan, E.R. (1981), *Manual of stressed skin diaphragm design*, Granada, U.K.

Davies, J.M., Leach, P. and Heinz, D. (1994), Second-Order Generalized Beam Theory, *Journal of Constructional Steel Research*, Vol. 31, Nos. 2-3, 1994, pp. 221-241, Elsevier Science Ltd, U.K.

Davies, J.M. (1998), Light gauge steel cassette wall construction, *Proceedings of the Nordic Steel Construction Conference*, Bergen, Norway, 14-16.9.1998, Norwegian Steel Association, Oslo, Norway.

Davies, J.M., Fragos, A.S. (2001), Shear Strength of Empty and Infilled Cassettes, *Proceedings of the Third International Conference on Thin-Walled Structures, Advances and Developments,*, Crakow, Poland, 5-7 June 2001, Elsevier Science Ltd, U.K.

ECCS (1978), *The Stressed Skin Design of Steel Structures*, ECCS 19, TC7, Constrado, Croydon, England.

ECCS (1995), *European Recommendations for the Application of Metal Sheeting acting as a Diaphragm*, ECCS 88, TC7, Brussels, Belgium.

ENV 1993-1-3:1996 European Committee for Standardisation: *Eurocode 3: Design of Steel Structures, Part 1.3: Supplementary rules for cold formed thin gauge members and sheeting*, CEN, Brussels, Belgium.

ENV 1999-1-1:1998 European Committee for Standardisation: *Eurocode 9: Design of aluminium structures - Part 1.1: General rules - General rules and rules for buildings*, CEN, Brussels, Belgium.

Fox, S.R., Schuster, R.M. (2000), Lateral Strength of Wind Load Bearing Wall Stud-to-Track Connection, *Proceedings of the Fifteenth International Specialty Conference on Cold-Formed Steel Structures*, St.Louis, MO, U.S.A., 19-20.10.2000, University of Missouri-Rolla.

Hofmeyer, H. (2000), *Combined Web Crippling and Bending Moment Failure of First-Generation Trapezoidal Steel Sheeting: Experiments, Finite Element Models, Mechanical Models*, PhD Thesis, Eindhoven University of Technology, The Netherlands.

Kaitila, O., Mäkeläinen, P. (2003), *Web Crippling Tests on Rannila Cassettes*, Helsinki University of Technology Laboratory of Steel Structures Research Reports TKK-TeRT-03-01, Espoo, Finland.

Kesti, J., (2000), *Local and Distortional Buckling of Perforated Steel Wall Studs*, Doctoral dissertation, Helsinki University of Technology Laboratory of Steel Structures Publications TKK-TER-19, Espoo, Finland.

Laine, T. (1997), *Kantavien teräspoimulevyjen mitoitustutkimus (Design of load-bearing steel sheeting profiles)*, Master's Thesis, Helsinki University of Technology, Laboratory of Steel Structures, Espoo, Finland (in Finnish).

Langan, J.E., LaBoube, R.A., Yu, W.W. (1994), Perforated Webs Subjected to End-One-Flange Loading, *Proceedings of the Twelfth International Specialty Conference on Cold-Formed Steel Structures*, St.Louis, MO, U.S.A., 18-19.10.1994, University of Missouri-Rolla.

Microsoft Excel® (2000), Microsoft Office 2000, Microsoft Corporation, U.S.A.

RakMK B6 (1989), Suomen Rakentamismääräyskokoelma, B6 Teräsohutlevyrakenteet, Ohjeet 1989, (The National Building Code of Finland B6 Light gauge steel structures, Guidelines), Ympäristöministeriö (Ministry of the Environment), (in Finnish).

Rannila Steel Oy (2001), *Rannilan rakennejärjestelmät – käsikirja* (*Rannila construction systems – handbook*), Otavan kirjapaino Oy, Keuruu, Finland (in Finnish).

Salonen, S. (1988), Ohutlevykasetin vedetyn laipan taipuman määrittäminen (Determination of the deflection of the flange in tension of a thin-walled cassette), *Proceedings of the 3rd Finnish Mechanics Days (Matti A. Ranta (ed.))*, Helsinki University of Technology, Faculty of Information Technology, Institute of Mechanics, Otaniemi, Espoo, Finland 2-3.6.1988/26 (in Finnish).

Serrette, R.L., Peköz, T. (1995), Distortional Buckling of Thin-Walled Beams/Panels, I: Theory and II: Design Methods, *Journal of Structural Engineering*, Vol. 121, No. 4, April, 1995, pp. 757-776, ASCE, U.S.A.

SFS-EN 10 002-1 (2002), *Metallic materials. Tensile testing. Part 1: Method of test at ambient temperature (*Metallien vetokoe. Osa 1: Vetokoe huoneenlämpötilassa), Suomen Standardisoimisliitto SFS (In Finnish and in English).

SFS-EN 10147 (2000), *Kuumasinkityt ohutlevyrakenneteräkset. Tekniset toimitusehdot. (Continuously hot-dip zinc coated structural steel strip and sheet. Technical delivery conditions.)*, Suomen Standardisoimisliitto SFS (In Finnish and in English).

StBK-N5 (1980), *Norm för tunnplåtskonstruktioner 79 (Tunnplåtsnorm) (Design code for cold-formed thin-walled structures 79)*, Staten Stålbyggnadskommitté hos AB Svensk Byggtjänst (in Swedish).

Studnička, J. (1990), Web Crippling of Wide Deck Sections, *Proceedings of the Tenth International Specialty Conference on Cold-Formed Steel Structures*, St.Louis, MO, U.S.A., 23-24.10.1990, University of Missouri-Rolla.

TRY (1989), Teräsohutlevyrakenteiden mitoitus, Ohjeiden B6 käsikirja (Design of Cold-Formed Steel Structures, B6 Handbook),Teräsrakenneyhdistys r.y. TRY (Finnish Constructional Steelwork Association FCSA) (in Finnish).

Wing, B.A., Schuster, R.M. (1982), Web Crippling of Decks Subjected to Two Flange Loading, *Proceedings of the Sixth International Specialty Conference on Cold-Formed Steel Structures*, St.Louis, MO, U.S.A., 16-17.11.1982, University of Missouri-Rolla.

Wing, B.A., Schuster, R.M. (1986), Web Crippling of Multi-Web Deck Sections Subjected to Interior One Flange Loading, *Proceedings of the Eighth International Specialty Conference on Cold-Formed Steel Structures*, St.Louis, MO, U.S.A., 11-12.11.1986, University of Missouri-Rolla.

Yu, W.-W. (2000), *Cold-Formed Steel Design*, Third Edition, John Wiley & Sons, Inc., New York, U.S.A.

Material test stress-strain curves for tested specimens (cf. section 3.2)

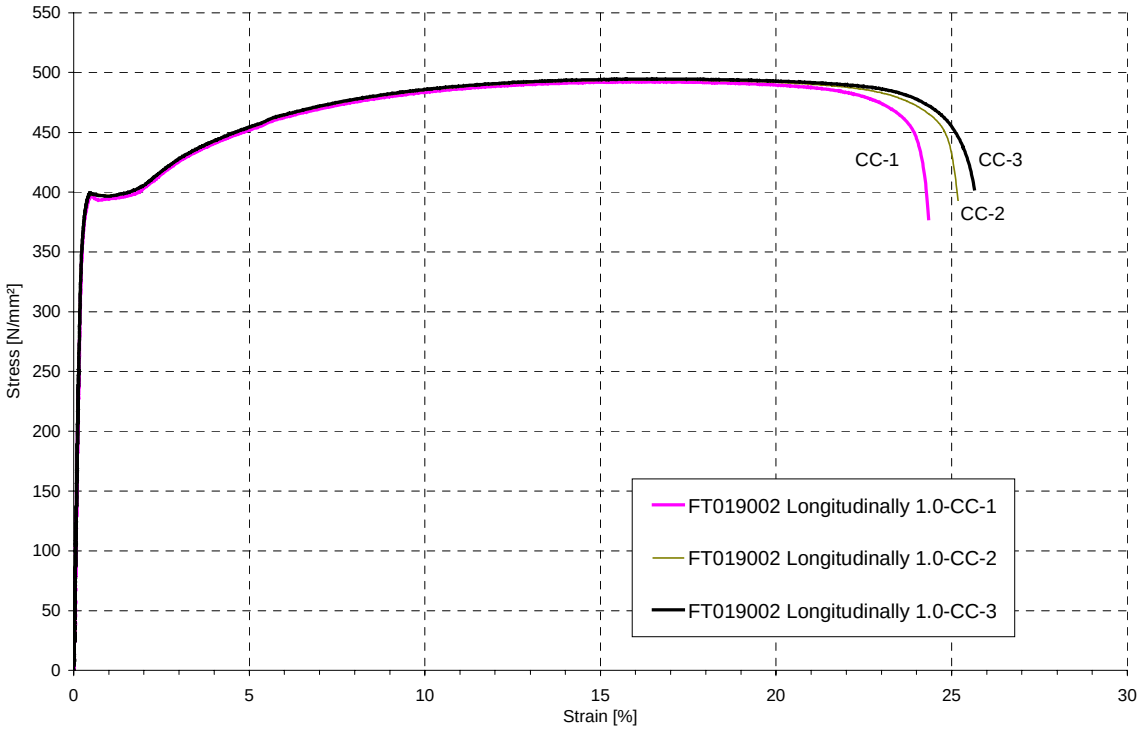

Fig. A1 Complete stress strain curves for material test specimens cut longitudinally from steel coil FT019002 and used for cassettes sections with t_{nom} = 1.0 mm and b_w = 100 mm.

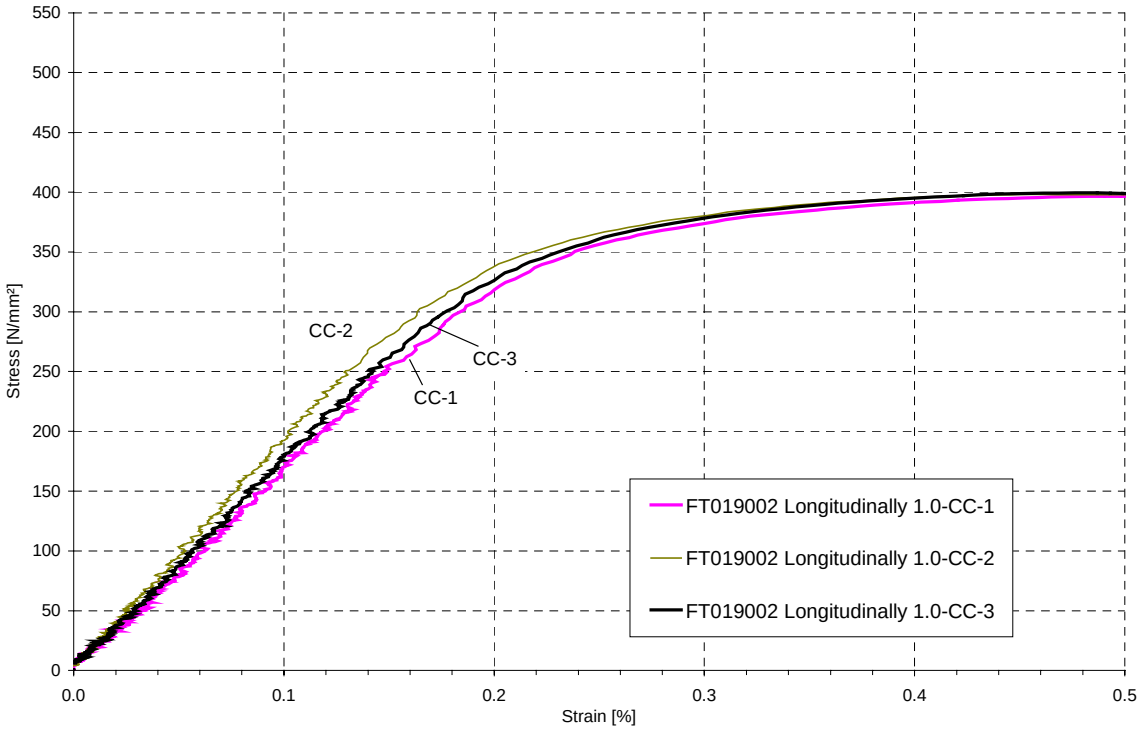

Fig. A2 Initial part of stress strain curves for material test specimens cut longitudinally from steel coil FT019002 and used for cassettes sections with t_{nom} = 1.0 mm and b_w = 100 mm.

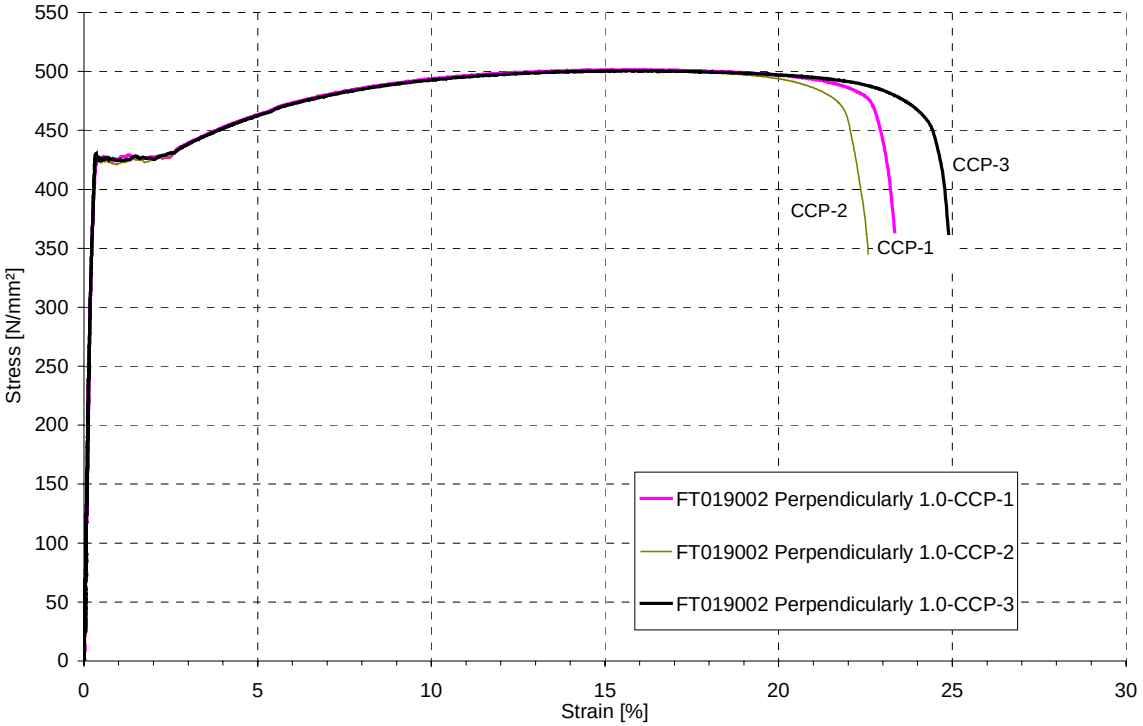

Fig. A3 Complete stress strain curves for material test specimens cut perpendicularly from steel coil FT019002 and used for cassettes sections with t_{nom} = 1.0 mm and b_w = 100 mm.

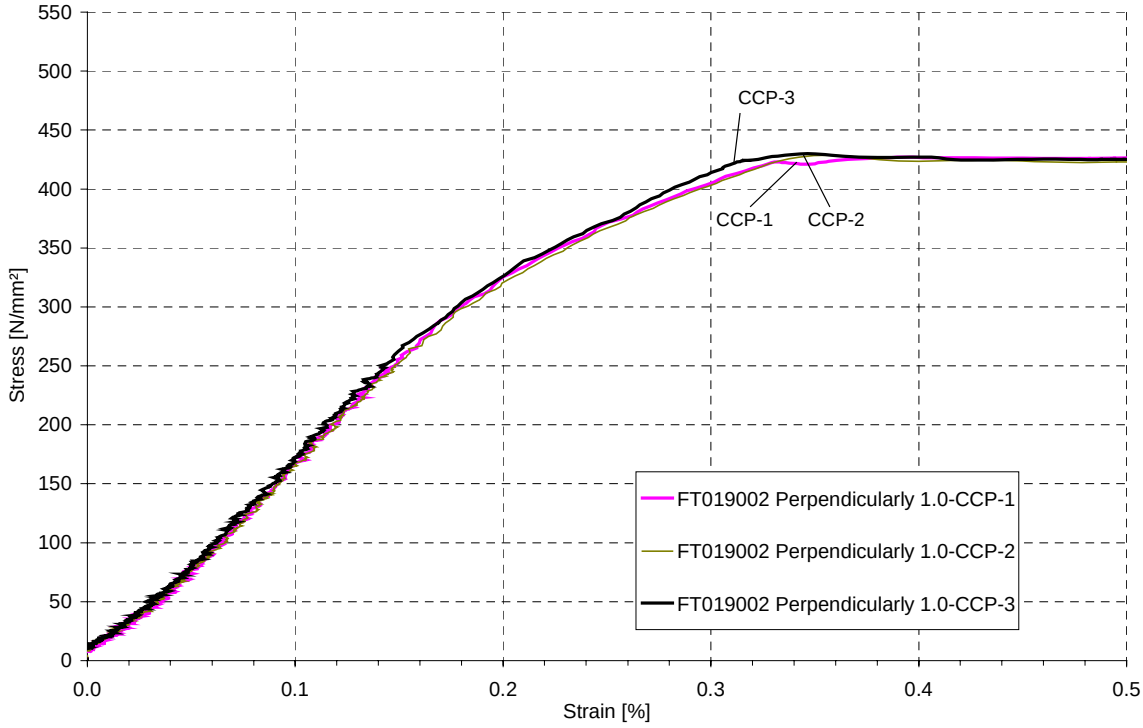

Fig. A4 Initial part of stress strain curves for material test specimens cut perpendicularly from steel coil FT019002 and used for cassettes sections with t_{nom} = 1.0 mm and b_w = 100 mm.

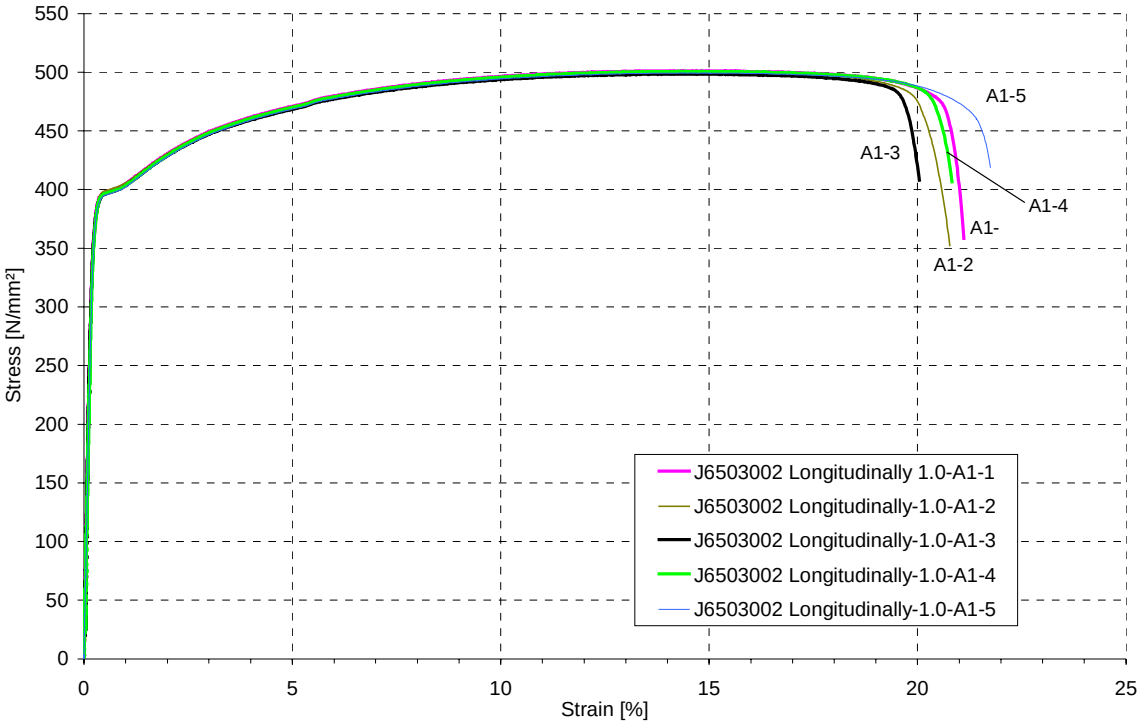

Fig. A5 Complete stress strain curves for material test specimens cut longitudinally from steel coil J6503002 and used for cassettes sections with t_{nom} = 1.0 mm and b_w = 150 mm.

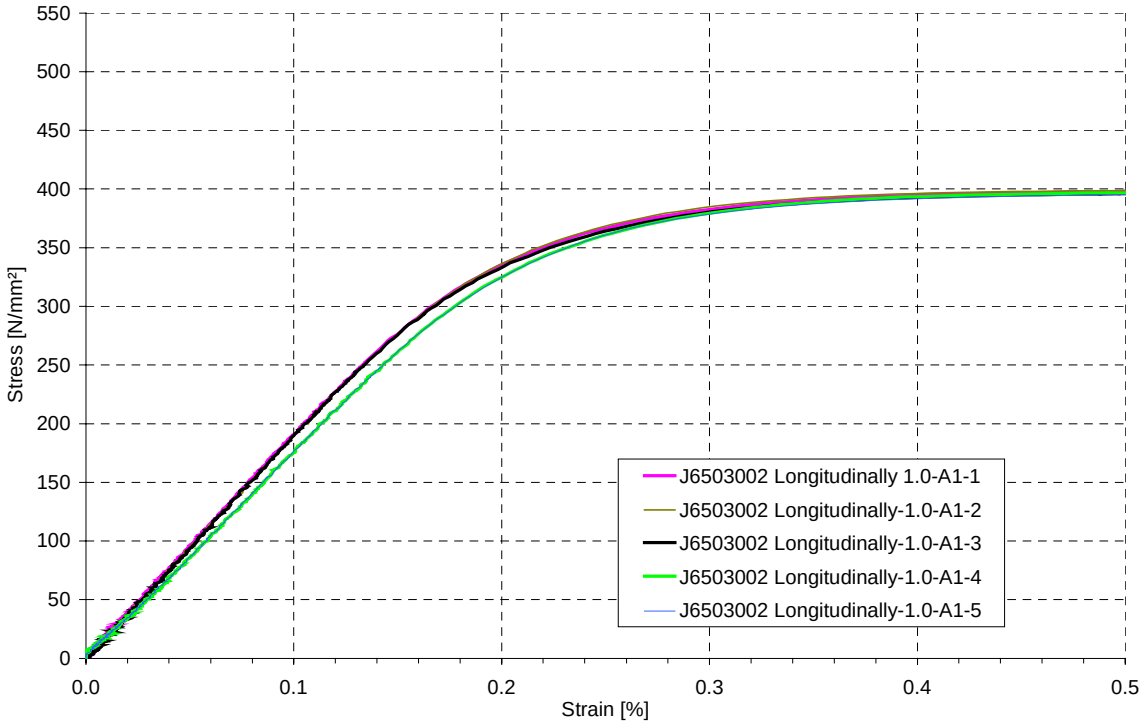

Fig. A6 Initial part of stress strain curves for material test specimens cut longitudinally from steel coil J6503002 and used for cassettes sections with t_{nom} = 1.0 mm and b_w = 150 mm.

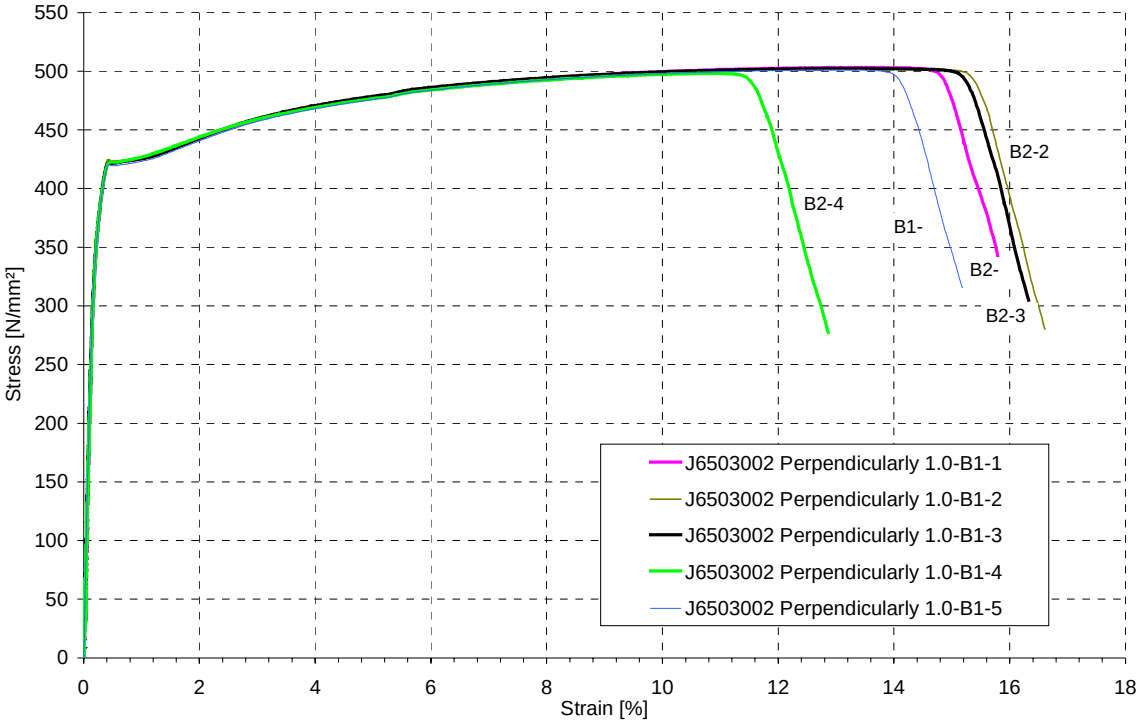

Fig. A7 Complete stress strain curves for material test specimens cut perpendicularly from steel coil J6503002 and used for cassettes sections with t_{nom} = 1.0 mm and b_w = 150 mm.

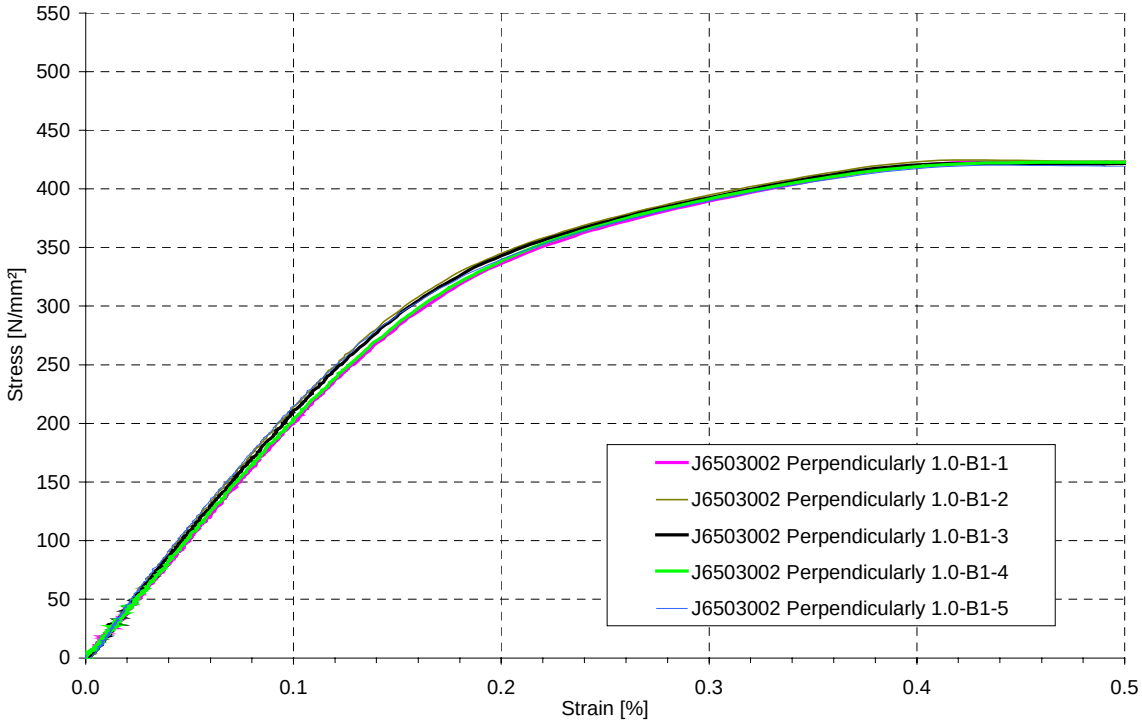

Fig. A8 Initial part of stress strain curves for material test specimens cut perpendicularly from steel coil J6503002 and used for cassettes sections with t_{nom} = 1.0 mm and b_w = 150 mm.

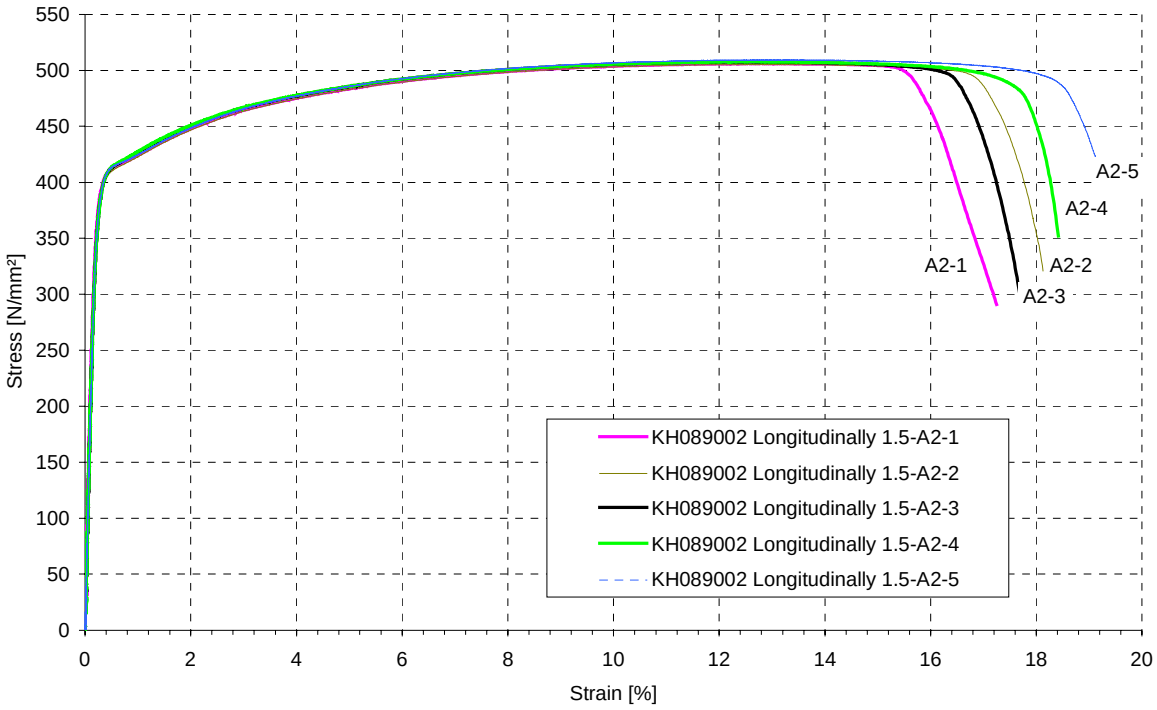

Fig. A9 Complete stress strain curves for material test specimens cut longitudinally from steel coil KH089002 and used for cassettes sections with t_{nom} = 1.5 mm and b_w = 150 mm.

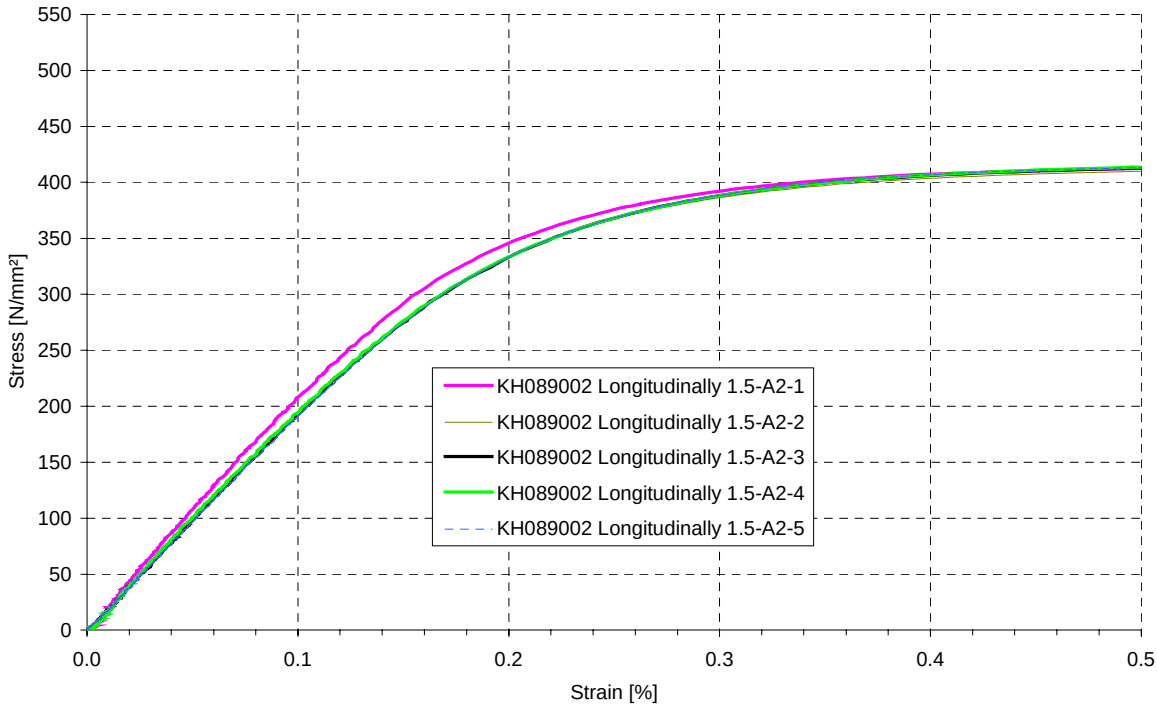

Fig. A10 Initial part of stress strain curves for material test specimens cut longitudinally from steel coil KH089002 and used for cassettes sections with t_{nom} = 1.5 mm and b_w = 150 mm.

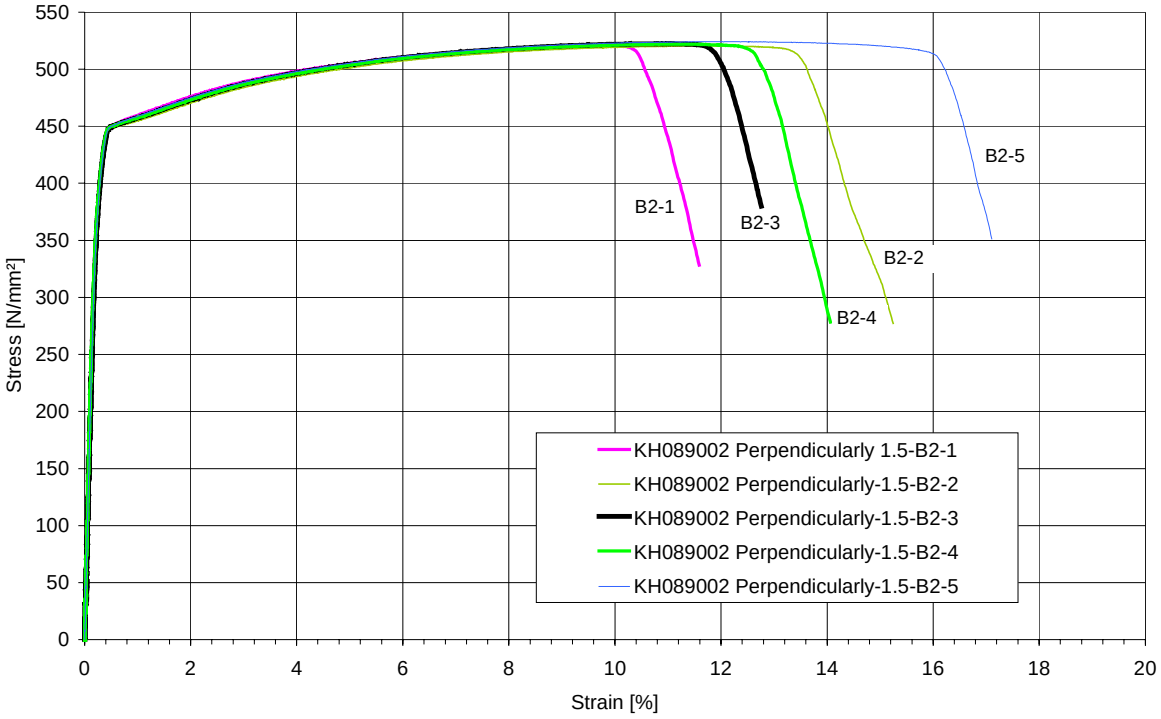

Fig. A11 Complete stress strain curves for material test specimens cut perpendicularly from steel coil KH089002 and used for cassettes sections with t_{nom} = 1.5 mm and b_w = 150 mm.

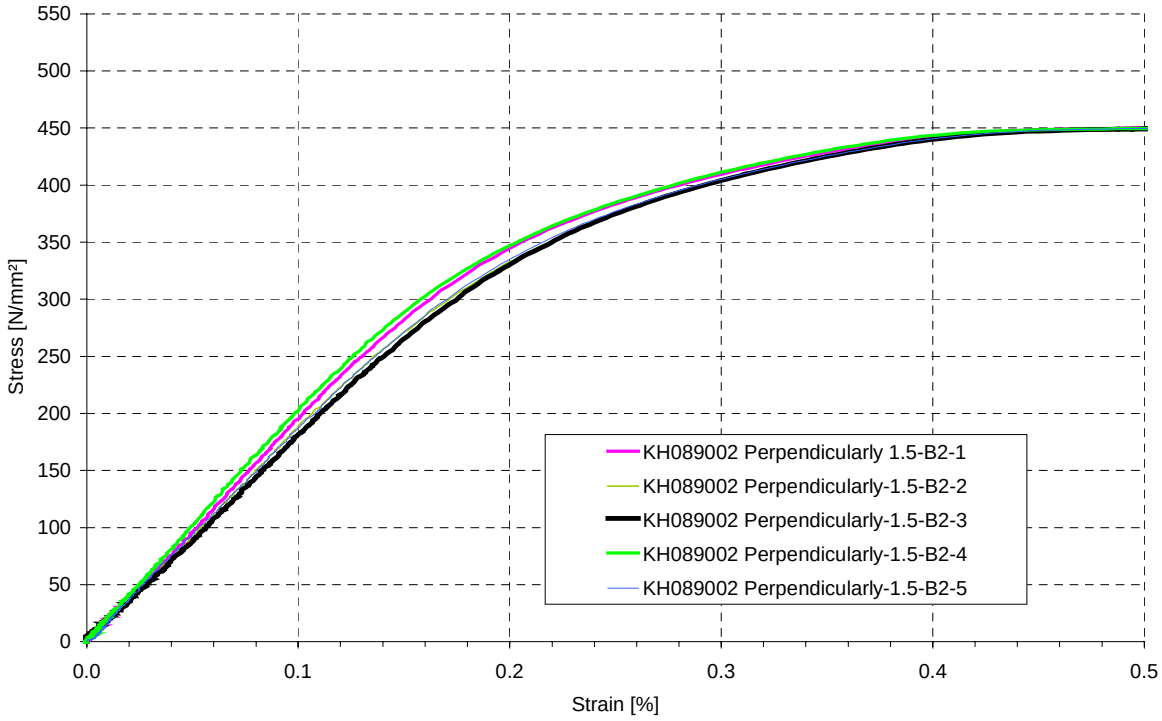

Fig. A12 Initial part of stress strain curves for material test specimens cut perpendicularly from steel coil KH089002 and used for cassettes sections with t_{nom} = 1.5 mm and b_w = 150 mm.

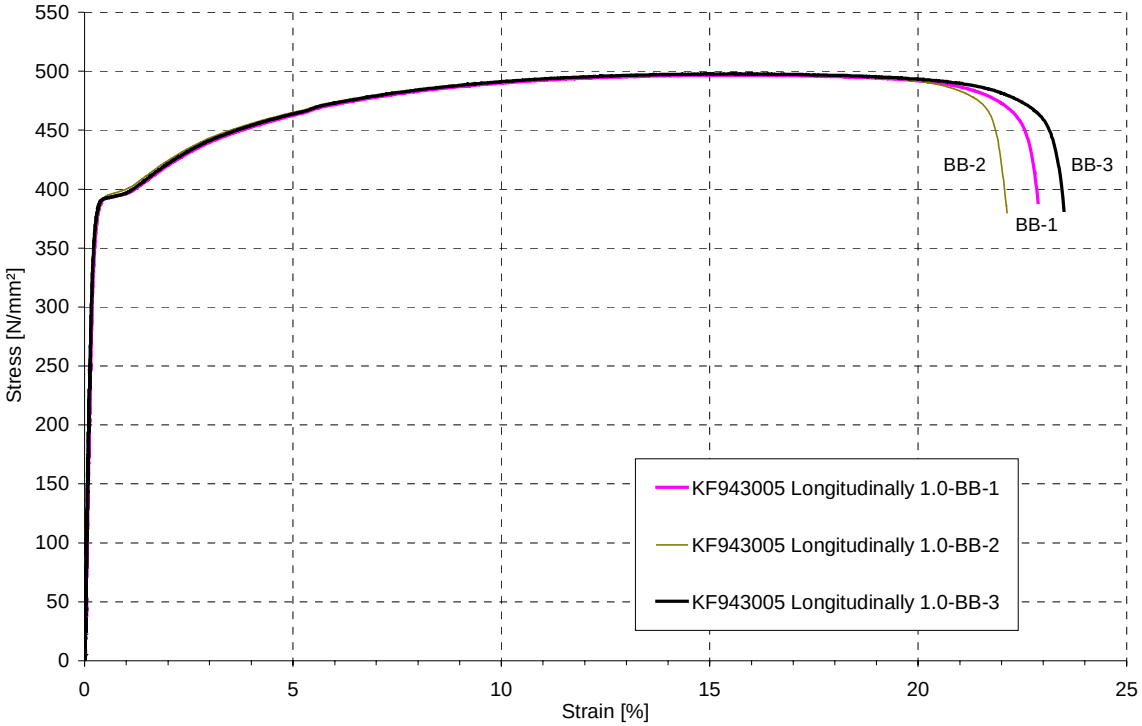

Fig. A13 Complete stress strain curves for material test specimens cut longitudinally from steel coil KF943005 and used for cassettes sections with t_{nom} = 1.0 mm and b_w = 200 mm.

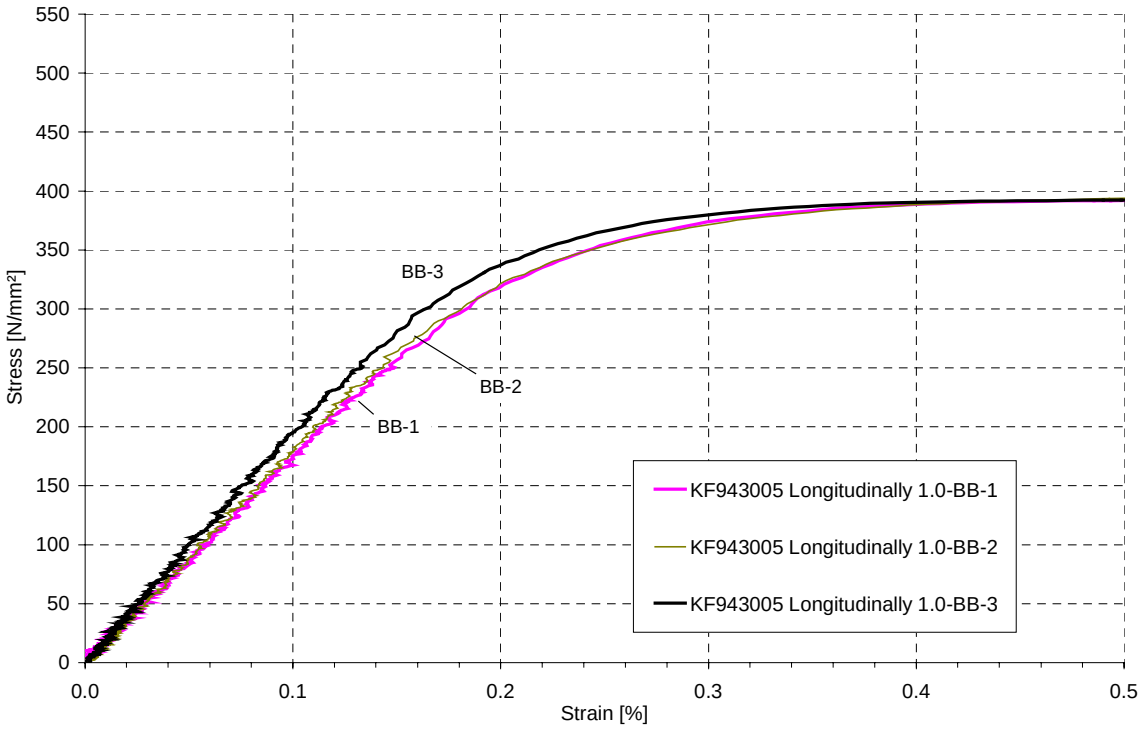

Fig. A14 Initial part of stress strain curves for material test specimens cut longitudinally from steel coil KF943005 and used for cassettes sections with t_{nom} = 1.0 mm and b_w = 200 mm.

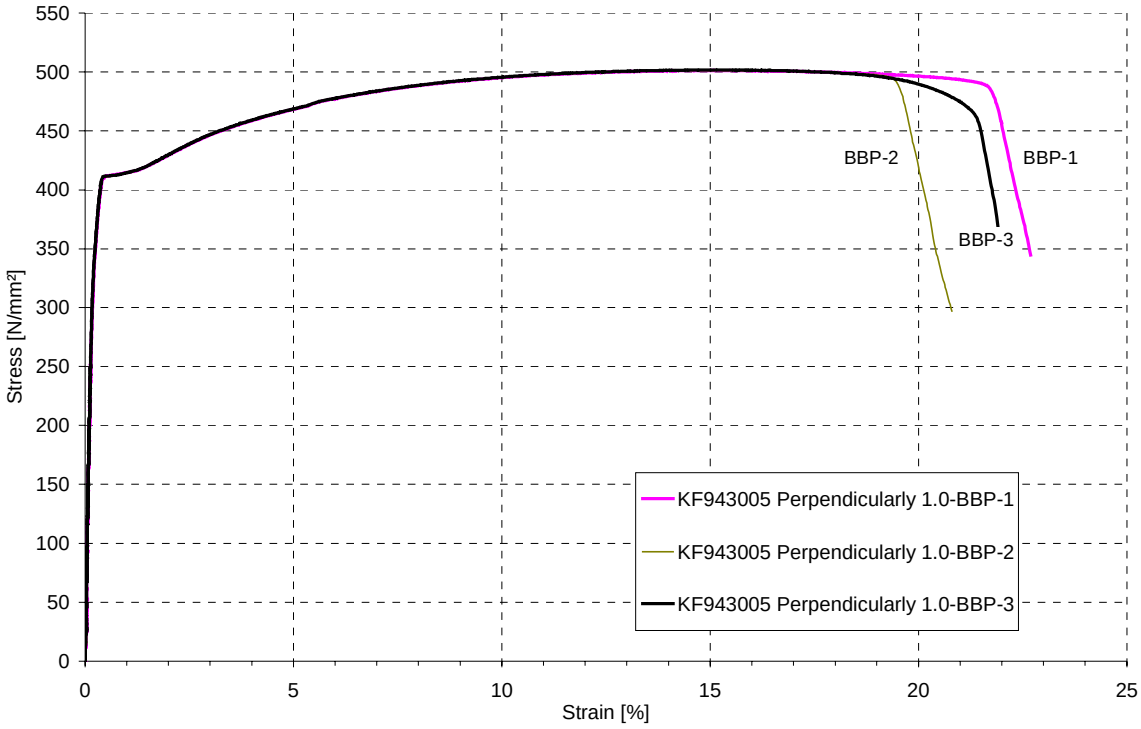

Fig. A15 Complete stress strain curves for material test specimens cut perpendicularly from steel coil KF943005 and used for cassettes sections with t_{nom} = 1.0 mm and b_w = 200 mm.

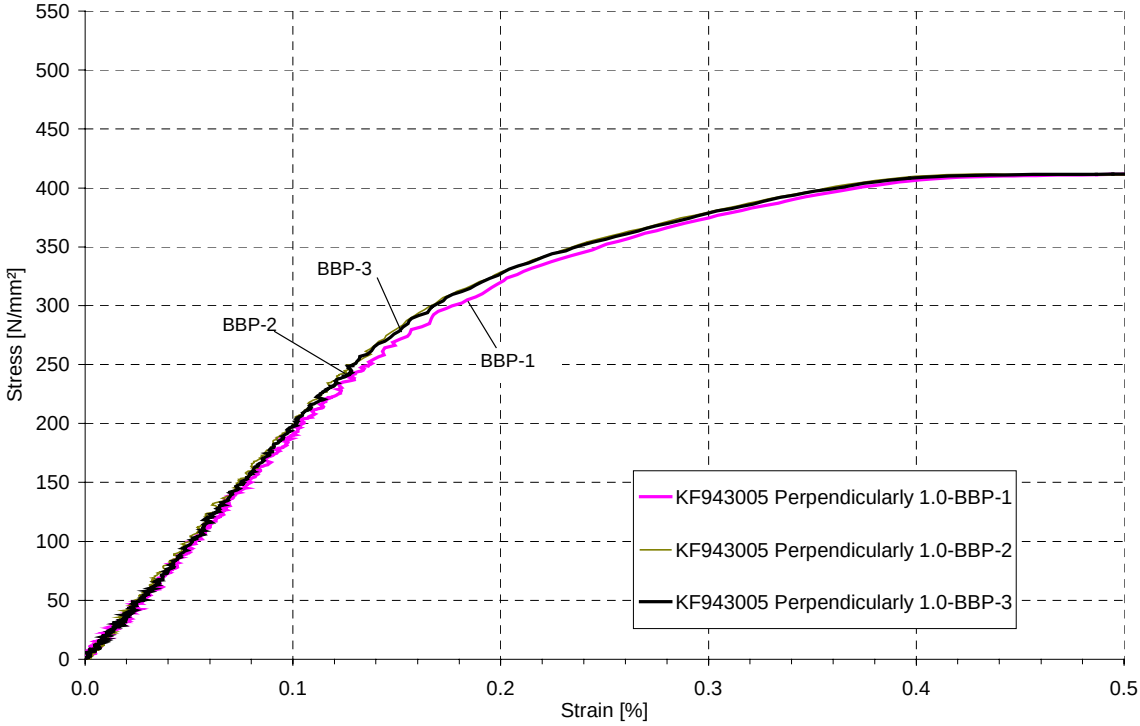

Fig. A16 Initial part of stress strain curves for material test specimens cut perpendicularly from steel coil KF943005 and used for cassettes sections with t_{nom} = 1.0 mm and b_w = 200 mm.

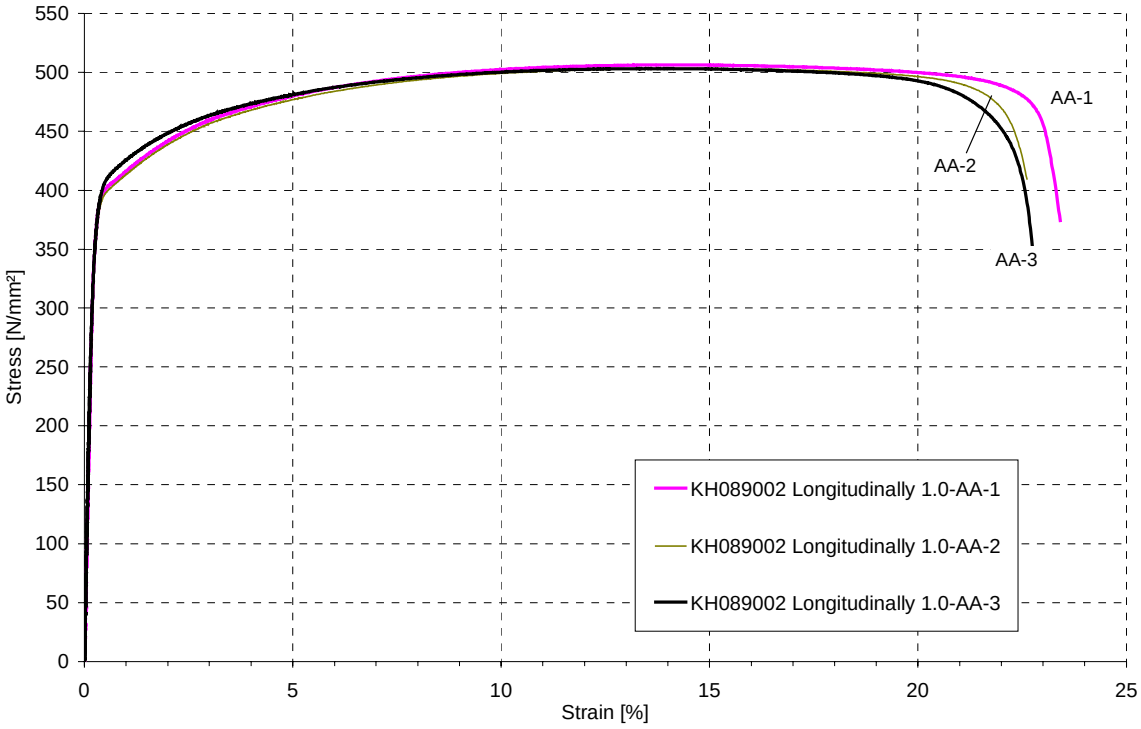

Fig. A17 Complete stress strain curves for material test specimens cut longitudinally from steel coil KH089002 and used for cassettes sections with t_{nom} = 1.5 mm and b_w = 200 mm.

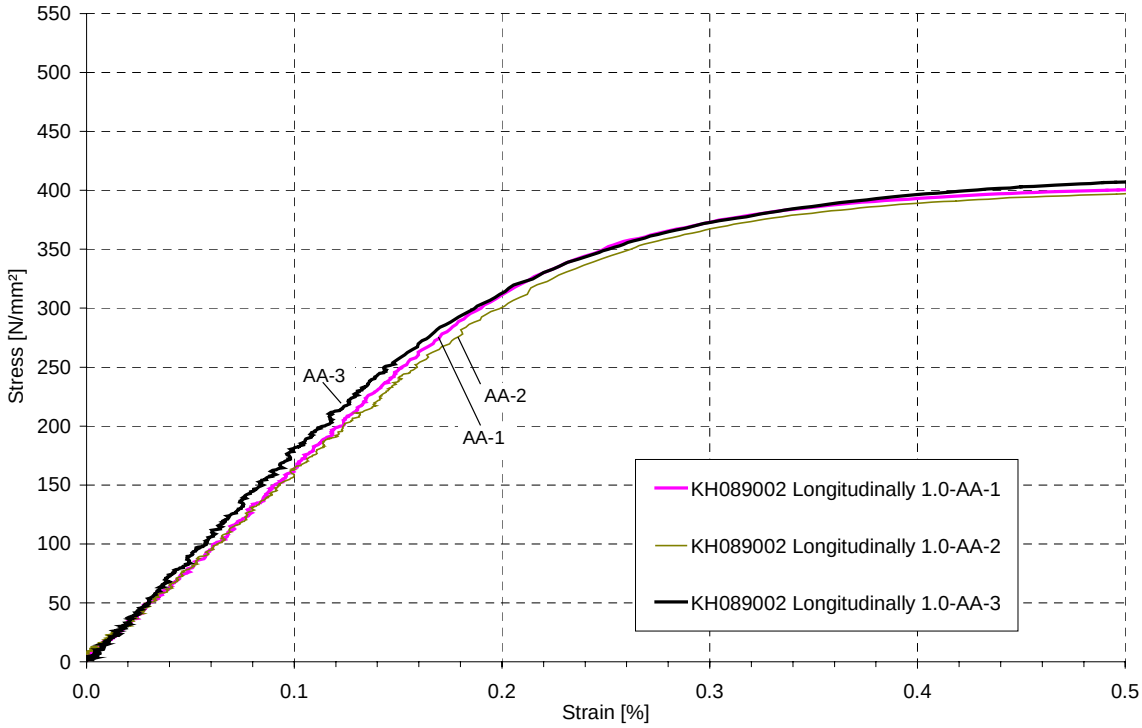

Fig. A18 Initial part of stress strain curves for material test specimens cut longitudinally from steel coil KH089002 and used for cassettes sections with t_{nom} = 1.5 mm and b_w = 200 mm.

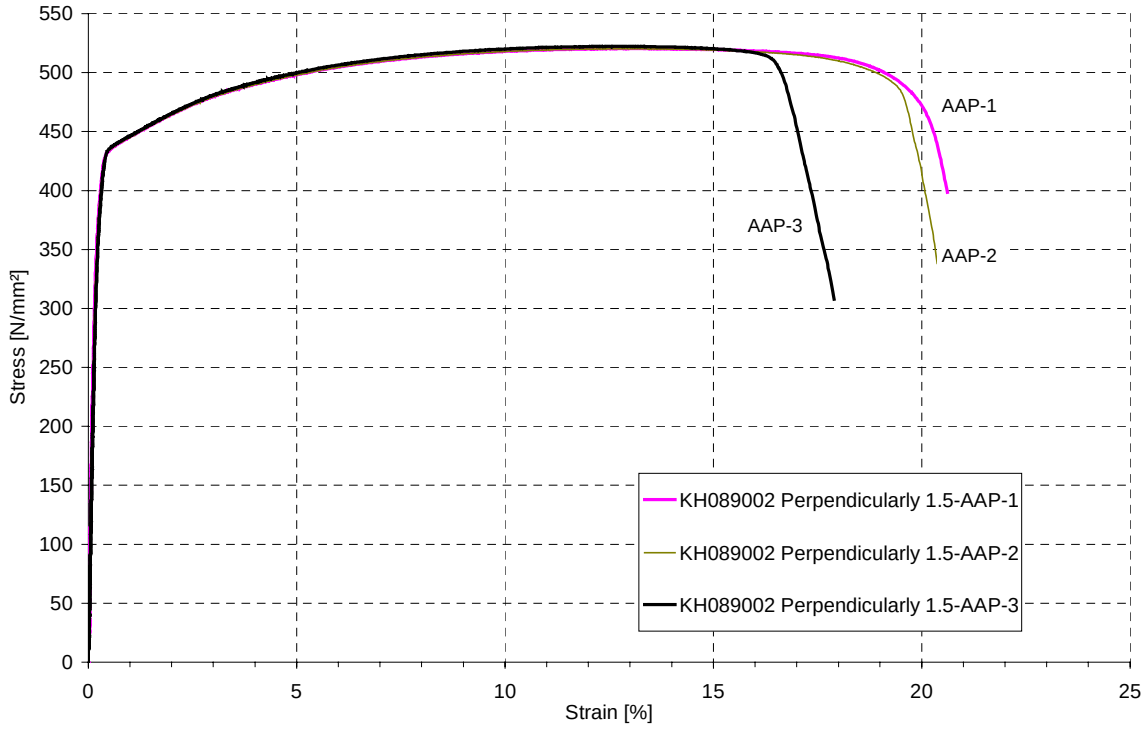

Fig. A19 Complete stress strain curves for material test specimens cut perpendicularly from steel coil KH089002 and used for cassettes sections with t_{nom} = 1.5 mm and b_w = 200 mm.

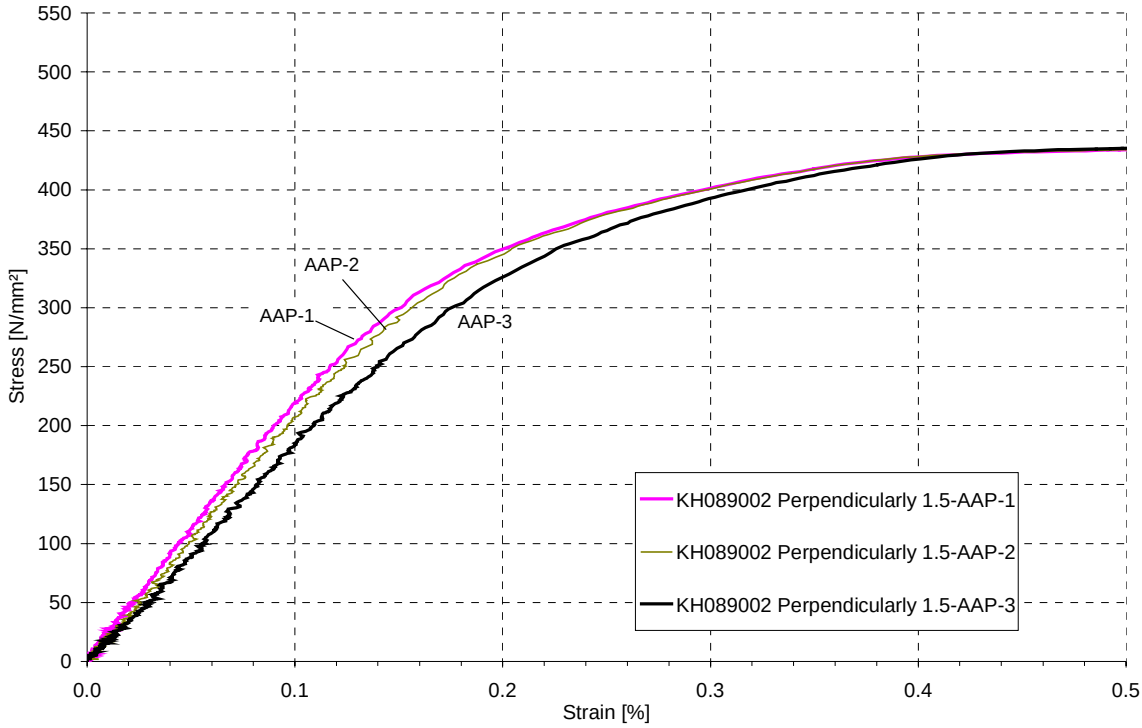

Fig. A20 Initial part of the stress strain curves for material test specimens cut perpendicularly from steel coil KH089002 and used for cassettes sections with t_{nom} = 1.5 mm and b_w = 200 mm.

Measured cross-section dimensions of test specimens

Table B1 Measured cross-sectional dimensions of single web test specimens with flat webs [mm].

	b_{tf}	$b_{tf.fl}$	$b_{tf.st}$	b_w	$b_{w.fl}$	b_{bf}	$b_{bf.fl}$	$b_{bf.st}$	r_{itf}	r_{etf}	r_{tf}	r_{ibf}	r_{ebf}	r_{bf}	L
ITF100-t10-1	97.1	89.0	27.2	101.7	95.6	41.4	37.3	24.3	2.75	4.50	3.63	2.00	3.50	2.75	1199
ITF100-t10-2	97.7	89.1	29.1	101.2	95.5	41.5	36.6	23.3	2.50	4.50	3.50	2.00	3.50	2.75	1199
ITF100-t10-3	97.8	89.8	29.4	101.4	95.9	41.8	37.2	23.5	2.50	4.50	3.50	2.00	3.50	2.75	1201
ITF150-t10-1	97.2	88.3	26.5	152.0	145.1	39.5	32.4	14.0	2.50	5.00	3.75	2.50	5.00	3.75	1198
ITF150-t10-2	96.9	89.4	27.4	151.8	145.7	39.3	33.0	14.9	2.50	4.75	3.63	2.50	5.00	3.75	1194
ITF150-t10-3	96.2	89.0	28.2	152.7	146.5	39.3	32.9	14.4	2.50	5.00	3.75	2.50	5.00	3.75	1195
ITF150-t10-4	98.9	86.2	28.8	153.0	144.1	39.6	32.1	15.5	2.50	4.50	3.50	3.00	5.00	4.00	1196
ITF150-t10-5	95.5	86.3	29.9	153.0	144.4	39.2	32.5	15.2	3.00	4.50	3.75	3.75	5.00	4.38	1199
ITF150-t15-1	91.9	88.1	29.7	153.3	143.3	41.7	35.8	18.9	2.50	4.50	3.50	2.75	5.00	3.88	1200
ITF150-t15-2	94.3	87.3	28.1	152.9	144.7	41.4	35.6	17.3	2.25	4.50	3.38	2.75	4.75	3.75	1202
ITF150-t15-3	94.7	88.4	29.7	152.6	142.4	42.0	36.5	16.9	2.50	4.75	3.63	2.75	5.00	3.88	1201
ITF200-t10-1	93.2	85.6	28.7	201.7	188.0	42.1	33.1	23.5	2.25	5.00	3.63	2.25	5.00	3.63	1198
ITF200-t10-2	92.2	87.7	27.8	200.3	190.5	42.1	33.1	23.9	2.25	4.75	3.50	2.50	4.75	3.63	1198
ITF200-t10-3	93.7	88.0	28.7	200.8	192.2	42.0	34.6	23.6	3.00	5.00	4.00	3.00	4.50	3.75	1199
ITF200-t15-1	93.8	87.0	32.6	203.2	192.3	42.3	35.0	22.3	2.50	5.00	3.75	1.00	4.25	2.63	1199
ITF200-t15-2	94.3	85.0	29.7	203.2	188.9	42.6	32.1	24.7	2.75	5.00	3.88	1.25	4.00	2.63	1203
ITF200-t15-3	94.1	86.1	29.4	202.3	189.8	41.9	33.1	23.1	2.75	4.50	3.63	1.00	4.25	2.63	1201
ITF200-t15-4	94.5	86.3	29.4	203.8	189.2	41.9	33.7	25.6	3.00	5.00	4.00	1.50	4.00	2.75	1203
IOF200-t15-S600-1	93.3	87.3	27.3	202.4	191.0	43.5	35.3	24.6	3.00	5.00	4.00	2.75	4.50	3.63	1198
IOF200-t15-S600-2	95.1	86.4	28.0	203.7	192.9	43.0	35.2	23.4	3.00	5.00	4.00	1.75	4.00	2.88	1207
IOF200-t15-S600-3	94.5	86.9	28.3	203.6	190.6	43.5	35.4	25.9	3.00	5.00	4.00	2.00	4.50	3.25	1199
IOF200-t15-S600-4	94.2	86.7	27.5	203.7	191.1	43.0	35.0	26.0	3.00	5.00	4.00	2.25	4.50	3.38	1198
IOF200-t15-S1000-1	93.1	88.0	28.8	203.7	189.8	43.8	35.3	25.7	2.75	5.00	3.88	2.25	4.50	3.38	1200
IOF200-t15-S1000-2	94.7	86.0	28.2	204.1	193.2	42.9	34.5	26.6	2.50	5.00	3.75	2.25	4.00	3.13	1200
IOF200-t15-S1000-3	92.7	85.3	29.4	204.0	191.3	42.7	34.7	26.0	2.50	5.00	3.75	2.25	4.00	3.13	1198

Table B2 Measured cross-sectional dimensions of single web test specimens with longitudinally stiffened webs [mm].

	b_{tf}	$b_{tf.fl}$	$b_{tf.st}$	b_w	$b_{w.fl}$	b_{bf}	$b_{bf.fl}$	$b_{bf.st}$	r_{itf}	r_{etf}	r_{tf}	r_{ibf}	r_{ebf}	r_{bf}	$b_{w.st}$	$b_{w.st.fl}$	$d_{w.st}$	$h_{w.st}$	L
ITF100R-t10-1	95.2	89.0	27.7	102.7	98.7	39.8	37.7	19.8	2.75	4.50	3.63	1.75	4.00	2.88	45.0	31.2	27.8	8.5	1198
ITF100R-t10-2	95.9	90.0	30.7	101.9	96.9	43.0	35.6	16.6	2.75	4.50	3.63	2.50	3.75	3.13	45.5	30.0	26.2	8.7	1197
ITF100R-t10-3	95.6	89.0	26.4	102.4	97.3	42.0	35.1	17.8	2.75	4.00	3.38	2.50	3.75	3.13	44.9	29.9	25.9	8.7	1202
ITF150R-t10-1	94.7	90.3	27.4	152.1	147.6	41.8	37.2	14.7	2.75	4.50	3.63	2.75	5.00	3.88	45.2	29.3	25.7	8.2	1199
ITF150R-t10-2	96.3	91.3	29.3	151.7	147.5	41.8	35.7	15.2	2.50	4.50	3.50	2.50	4.50	3.50	46.6	29.3	23.8	8.8	1200
ITF150R-t10-3	94.3	89.7	29.4	152.8	142.0	42.1	31.5	14.7	2.50	4.00	3.25	3.00	5.50	4.25	45.7	29.6	25.9	7.3	1200
ITF150R-t15-1	97.0	88.5	30.1	153.2	143.2	41.8	35.7	11.8	2.75	4.75	3.75	2.50	5.00	3.75	45.6	28.7	25.4	8.6	1200
ITF150R-t15-2	96.7	88.5	27.7	152.4	144.3	41.4	36.1	12.2	2.50	4.50	3.50	2.25	4.50	3.38	45.9	28.6	25.6	8.8	1203
ITF150R-t15-3	96.0	89.3	27.0	151.8	144.9	41.4	36.3	12.1	3.00	4.50	3.75	2.75	4.50	3.63	46.0	30.2	26.0	9.0	1203
ITF200R-t10-1	94.0	87.4	30.0	201.9	192.0	43.4	32.7	14.4	3.00	4.50	3.75	2.75	4.50	3.63	45.3	29.6	26.0	7.9	1201
ITF200R-t10-2	94.3	89.4	29.3	201.7	188.0	42.4	33.4	14.6	2.50	4.50	3.50	2.50	4.25	3.38	44.7	30.8	25.6	8.4	1200
ITF200R-t10-3	93.6	89.1	29.8	201.9	189.8	43.3	32.8	15.2	2.50	5.00	3.75	2.25	4.00	3.13	44.9	29.9	25.4	8.3	1199
ITF200R-t15-1	93.9	87.4	28.1	202.6	190.2	41.6	34.5	15.5	2.50	5.00	3.75	1.75	3.75	2.75	47.7	27.2	23.7	8.4	1199
ITF200R-t15-2	95.0	87.9	28.0	202.6	189.0	40.9	31.1	15.3	2.25	4.75	3.50	2.00	4.50	3.25	47.2	28.2	24.0	8.3	1203
ITF200R-t15-3	95.5	88.9	30.3	203.5	191.1	41.0	33.3	15.4	2.00	5.00	3.50	1.00	3.75	2.38	48.1	27.7	23.5	7.9	1199
IOF200R-t15-S600-1	94.9	86.7	30.7	204.2	194.1	41.7	34.7	19.2	3.00	5.00	4.00	2.00	4.00	3.00	47.5	29.1	26.1	9.3	1199
IOF200R-t15-S600-2	94.8	86.5	30.9	203.7	193.7	42.5	34.3	17.5	2.25	5.00	3.63	2.25	4.50	3.38	48.1	29.0	25.9	8.1	1202
IOF200R-t15-S600-3	96.4	87.0	28.9	203.9	192.4	41.8	33.3	18.9	2.25	5.00	3.63	2.25	4.00	3.13	47.4	29.3	25.9	8.2	1201
IOF200R-t15-S600-4	95.0	88.2	29.3	203.8	193.1	41.7	35.1	17.4	2.25	5.00	3.63	2.00	4.00	3.00	47.2	28.4	25.8	8.6	1200
IOF200R-t15-S1000-1	94.8	86.5	29.6	203.5	193.3	42.0	34.9	14.8	2.75	5.00	3.88	2.00	4.00	3.00	48.3	29.6	25.0	8.9	1205
IOF200R-t15-S1000-2	93.1	87.2	29.5	203.7	196.2	42.1	32.2	17.1	3.00	5.00	4.00	2.00	4.00	3.00	47.3	30.0	25.5	8.9	1199
IOF200R-t15-S1000-3	92.7	85.8	30.3	203.2	195.0	42.0	35.0	16.8	2.75	5.00	3.88	2.00	4.00	3.00	47.2	28.7	25.1	8.7	1200

Table B3 Measured initial curvatures of single web test specimens with flat webs [mm].

	$curv_{tf}$	$curv_{w}$	$curv_{bf}$	$curv_{w.vert}$
ITF100-t10-1	0.31	-0.69	-1.90	-0.93
ITF100-t10-2	0.35	-0.46	-1.97	-0.80
ITF100-t10-3	0.33	-0.46	-1.85	-0.79
ITF150-t10-1	-0.59	-1.07	-1.09	-0.26
ITF150-t10-2	-0.55	-1.46	-1.27	-0.64
ITF150-t10-3	-0.54	-1.21	-1.15	-0.37
ITF150-t10-4	-0.21	-1.30	-1.21	-0.54
ITF150-t10-5	-0.27	-1.16	-1.05	-0.33
ITF150-t15-1	-1.00	-1.80	-0.89	-0.57
ITF150-t15-2	-1.27	-1.72	-1.03	-0.68
ITF150-t15-3	-0.96	-2.00	-1.20	-0.57
ITF200-t10-1	-6.40	-6.50	-0.06	-3.13
ITF200-t10-2	-3.05	-5.77	0.00	-2.15
ITF200-t10-3	-5.55	-6.03	0.35	-1.93
ITF200-t15-1	-1.74	-1.83	0.37	-0.56
ITF200-t15-2	-1.89	-2.23	0.84	-0.71
ITF200-t15-3	-1.20	-1.57	0.24	-0.74
ITF200-t15-4	-1.37	-1.66	0.06	-0.31
IOF200-t15-S600-1	-1.57	-2.10	0.41	-1.06
IOF200-t15-S600-2	-2.05	-1.90	0.06	-0.59
IOF200-t15-S600-3	-1.65	-2.11	0.17	-0.72
IOF200-t15-S600-4	-1.37	-1.72	-0.10	-0.79
IOF200-t15-S1000-1	-1.03	-1.76	-0.12	-0.45
IOF200-t15-S1000-2	-1.19	-1.43	-0.38	-0.41
IOF200-t15-S1000-3	-1.32	-1.38	-0.17	-0.52

Table B4 Measured initial curvatures of single web test specimens with longitudinally stiffened webs [mm].

	$curv_{tf}$	$curv_{w}$	$curv_{bf}$	$curv_{w.vert}$
ITF100R-t10-1	0.07	-2.53	-2.48	-8.96*
ITF100R-t10-2	0.23	-2.46	-2.46	-8.61*
ITF100R-t10-3	0.10	-2.04	-2.25	-8.54*
ITF150R-t10-1	-0.13	-0.29	-0.88	-1.43
ITF150R-t10-2	-0.44	-1.57	-1.00	-3.47
ITF150R-t10-3	-0.03	-0.31	-1.32	2.90
ITF150R-t15-1	-0.69	-2.33	-0.97	-1.86
ITF150R-t15-2	-1.18	-2.18	-1.14	-2.47
ITF150R-t15-3	-0.88	-1.84	-1.27	-1.70
ITF200R-t10-1	-0.36	1.45	-0.75	1.80
ITF200R-t10-2	-0.28	1.45	-0.21	1.92
ITF200R-t10-3	0.70	2.60	-1.70	8.30
ITF200R-t15-1	-1.93	-2.78	0.04	-1.98
ITF200R-t15-2	-0.71	-1.74	0.06	-0.28
ITF200R-t15-3	-1.40	-1.90	0.00	-1.08
IOF200R-t15-S600-1	-0.92	-0.74	-0.23	-0.10
IOF200R-t15-S600-2	-0.82	-0.84	-0.03	-0.12
IOF200R-t15-S600-3	-0.79	-0.81	0.13	-0.42
IOF200R-t15-S600-4	-0.85	-0.95	0.10	-0.53
IOF200R-t15-S1000-1	-1.27	-2.23	0.22	-0.90
IOF200R-t15-S1000-2	-1.00	-1.60	-0.19	-0.54
IOF200R-t15-S1000-3	-0.73	-1.44	-0.11	-0.94

Table B5 Measured cross-sectional dimensions of built-up test specimens with flat webs [mm].

		b_{tf}	$b_{tf.fl}$	$b_{tf.st}$	b_w	$b_{w.fl}$	b_{bf}	$b_{bf.fl}$	$b_{bf.st}$	r_{itf}	r_{etf}	r_{tf}	r_{ibf}	r_{ebf}	r_{bf}	L
S-IOF200-t15-S1000-1	web1	96.4	90.6	29.8	199.8	187.2	29.3	22.3	10.5	2.5	5.0	3.75	2.5	4.0	3.25	1201
	web2	93.7	87.2	29.1	203.6	192.5	42.9	35.3	25.6	2.0	5.0	3.50	2.0	4.0	3.00	1198
	web3	96.8	89.4	29.5	199.8	189.6	28.5	21.5	9.3	2.0	5.0	3.50	2.0	5.0	3.50	1198
	web4	93.0	87.5	28.7	203.5	191.6	43.1	34.6	24.9	2.5	5.0	3.75	2.3	3.5	2.88	1201
S-IOF200-t15-S1000-2	web1	96.2	89.2	30.9	199.4	188.6	29.7	22.3	10.4	2.5	4.5	3.50	2.5	4.5	3.50	1200
	web2	92.3	87.2	29.5	204.1	190.4	42.5	35.9	26.5	3.3	4.5	3.88	1.5	4.0	2.75	1199
	web3	97.2	90.3	29.1	199.6	190.1	28.8	21.4	9.7	2.0	5.0	3.50	2.0	4.5	3.25	1199
	web4	94.0	89.7	28.7	203.6	190.8	43.6	36.6	26.2	2.5	5.0	3.75	2.5	3.0	2.75	1200
S-IOF200-t15-S1000-3	web1	98.1	90.6	29.3	199.9	188.4	28.0	22.3	11.1	2.5	4.5	3.50	2.0	4.0	3.00	1200
	web2	92.4	88.7	28.7	203.8	190.8	43.2	35.2	25.4	3.0	4.5	3.75	2.0	3.5	2.75	1196
	web3	96.4	90.2	29.3	200.4	189.3	29.4	19.4	10.5	2.0	5.0	3.50	2.0	4.5	3.25	1196
	web4	94.2	88.6	27.2	204.4	189.7	42.8	34.9	26.1	2.0	5.0	3.50	2.0	4.0	3.00	1200

Table B6 Measured cross-sectional dimensions of built-up test specimens with longitudinally stiffened webs [mm].

		b_{tf}	$b_{tf.fl}$	$b_{tf.st}$	b_w	$b_{w.fl}$	b_{bf}	$b_{bf.fl}$	$b_{bf.st}$	r_{itf}	r_{etf}	r_{tf}	r_{ibf}	r_{ebf}	r_{bf}	$b_{w.st}$	$b_{w.st.fl}$	$d_{w.st}$	$h_{w.st}$	L
S-IOF200R-t15-S1000-1	web1	95.6	89.6	30.0	198.2	191.0	29.5	21.1	10.4	2.5	4.5	3.50	2.5	4.5	3.50	49.7	30.0	26.0	10.8	1201
	web2	94.9	89.5	29.5	204.1	193.9	42.6	33.6	17.9	2.8	5.0	3.88	2.3	4.0	3.13	47.8	27.3	25.2	8.1	1199
	web3	96.1	88.6	31.5	198.8	190.6	29.1	20.8	9.8	2.5	4.5	3.50	2.5	4.5	3.50	49.7	26.4	25.1	10.6	1199
	web4	95.8	89.7	28.5	204.1	193.2	42.3	36.1	16.9	2.8	4.5	3.63	2.0	4.0	3.00	49.7	29.0	26.1	8.0	1201
S-IOF200R-t15-S1000-2	web1	96.4	88.8	30.9	198.4	189.2	30.0	23.0	10.8	2.5	4.5	3.50	2.5	4.0	3.25	47.0	32.1	26.0	10.2	1202
	web2	95.5	90.4	28.7	203.2	192.9	42.9	35.7	14.9	2.5	4.5	3.50	2.0	4.0	3.00	48.1	28.7	25.2	8.8	1204
	web3	96.6	88.2	29.2	199.0	188.6	30.0	22.9	11.7	2.5	4.5	3.50	2.3	4.5	3.38	45.6	30.1	27.0	10.0	1204
	web4	93.9	89.2	28.4	203.7	193.3	41.9	34.9	17.5	2.5	5.0	3.75	2.0	4.0	3.00	46.5	28.8	25.3	8.2	1202
S-IOF200R-t15-S1000-3	web1	96.6	89.5	31.5	198.9	189.6	29.3	21.0	10.7	2.5	4.5	3.50	2.5	4.0	3.25	49.1	29.8	26.4	10.5	1200
	web2	93.3	88.6	28.9	204.4	191.5	42.2	35.2	17.3	2.8	4.5	3.63	2.0	3.5	2.75	47.1	29.5	24.3	8.5	1200
	web3	95.9	87.3	30.5	198.8	188.0	28.5	21.8	10.6	2.5	4.5	3.50	2.5	4.5	3.50	47.2	28.8	26.2	10.1	1200
	web4	95.3	90.7	30.3	204.3	192.9	42.1	35.5	18.0	2.5	4.5	3.50	2.0	3.0	2.50	47.3	28.4	24.9	8.6	1199

Table B7 Measured initial curvatures of built-up test specimens with flat webs [mm].

		$curv_{tf}$	$curv_{w}$	$curv_{bf}$	$curv_{w.vert}$
S-IOF200-t15-S1000-1	web1	-1.02	1.30	0.30	0.00
	web2	-1.00	-2.50	-0.53	-1.23
	web3	-1.28	0.53	0.20	-0.13
	web4	-1.07	-1.77	0.00	-0.60
S-IOF200-t15-S1000-2	web1	-0.50	1.90	0.15	-0.17
	web2	-1.37	-2.78	-0.40	-1.05
	web3	-1.00	0.95	0.00	-0.17
	web4	-0.97	1.70	-0.54	-0.54
S-IOF200-t15-S1000-3	web1	-0.54	0.31	0.28	-0.60
	web2	-1.36	-2.35	0.20	0.82
	web3	-1.40	0.91	0.10	-0.18
	web4	-0.60	1.45	-0.27	-0.88

Table B8 Measured top flange widths of built-up test specimens with flat webs [mm].

	b1	b2	b3
S-IOF200-t15-S1000-1	298	598	299
S-IOF200-t15-S1000-2	299	598	299
S-IOF200-t15-S1000-3	300	598	299

Table B9 Measured initial curvatures of built-up test specimens with longitudinally stiffened webs [mm].

		$curv_{tf}$	$curv_{w}$	$curv_{bf}$	$curv_{w.vert}$
S-IOF200R-t15-S1000-1	web1	0.40	0.80	0.40	1.51
	web2	-1.00	-1.25	-0.15	-0.11
	web3	-0.70	0.70	0.00	1.66
	web4	-1.00	-1.45	-0.38	0.00
S-IOF200R-t15-S1000-2	web1	-0.20	1.45	0.25	1.90
	web2	-1.60	2.75	0.05	-2.50
	web3	-0.95	1.10	0.14	1.10
	web4	-1.04	-1.50	-0.15	0.71
S-IOF200R-t15-S1000-3	web1	-1.30	1.30	0.00	2.06
	web2	-1.00	-1.40	-0.12	-0.14
	web3	-0.65	0.77	0.17	-0.17
	web4	-1.10	-1.32	-0.30	0.00

Table B10 Measured top flange widths of built-up test specimens with longitudinally stiffened webs [mm].

	b1	b2	b3
S-IOF200R-t15-S1000-1	299	598	300
S-IOF200R-t15-S1000-2	299	598	300
S-IOF200R-t15-S1000-3	298	598	299

ANNEX C
1 (1)

Collected load-displacement curves from ITF-tests

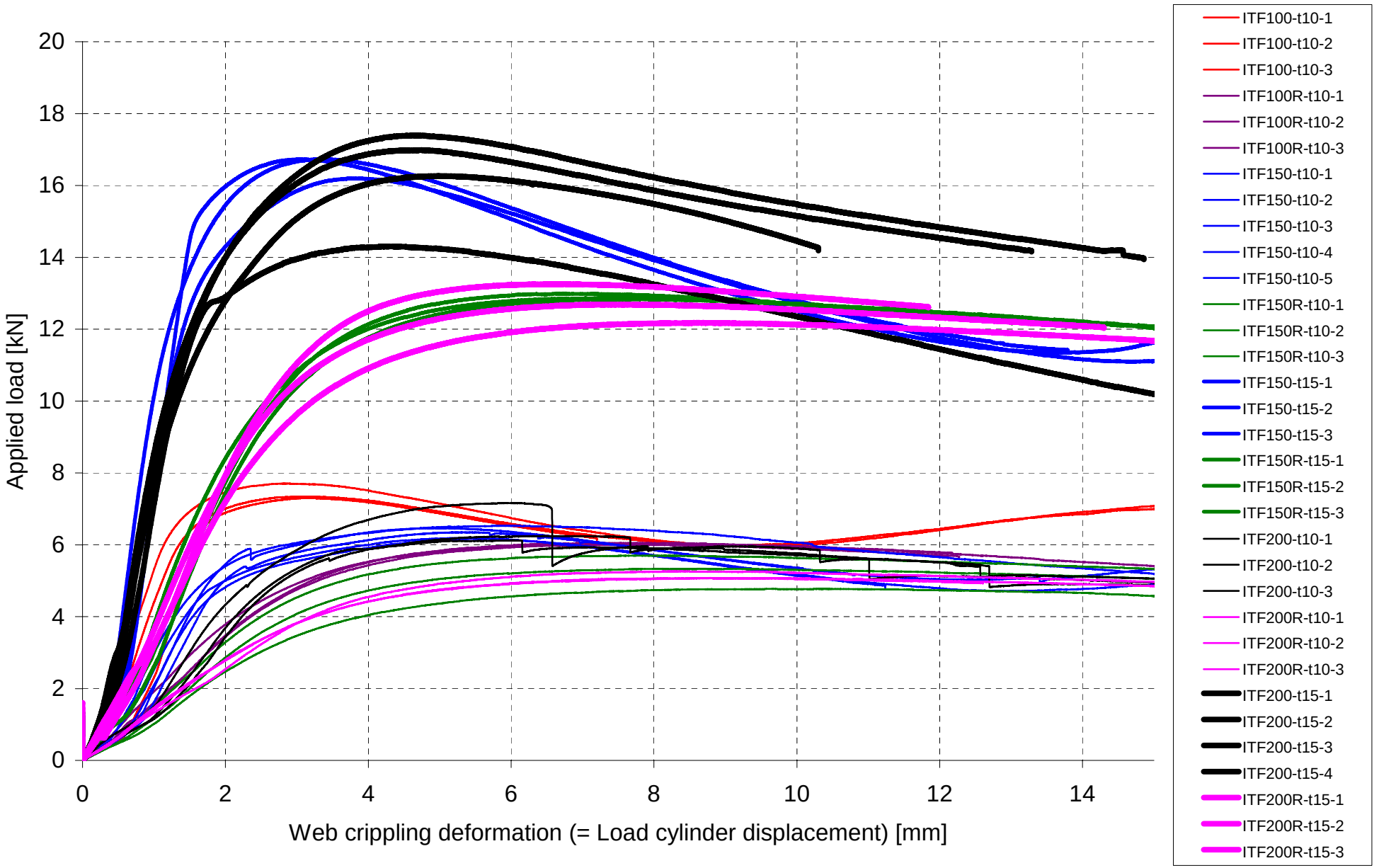

ANNEX D

1 (1)

Collected load-displacement curves from ITF200- and IOF200-tests

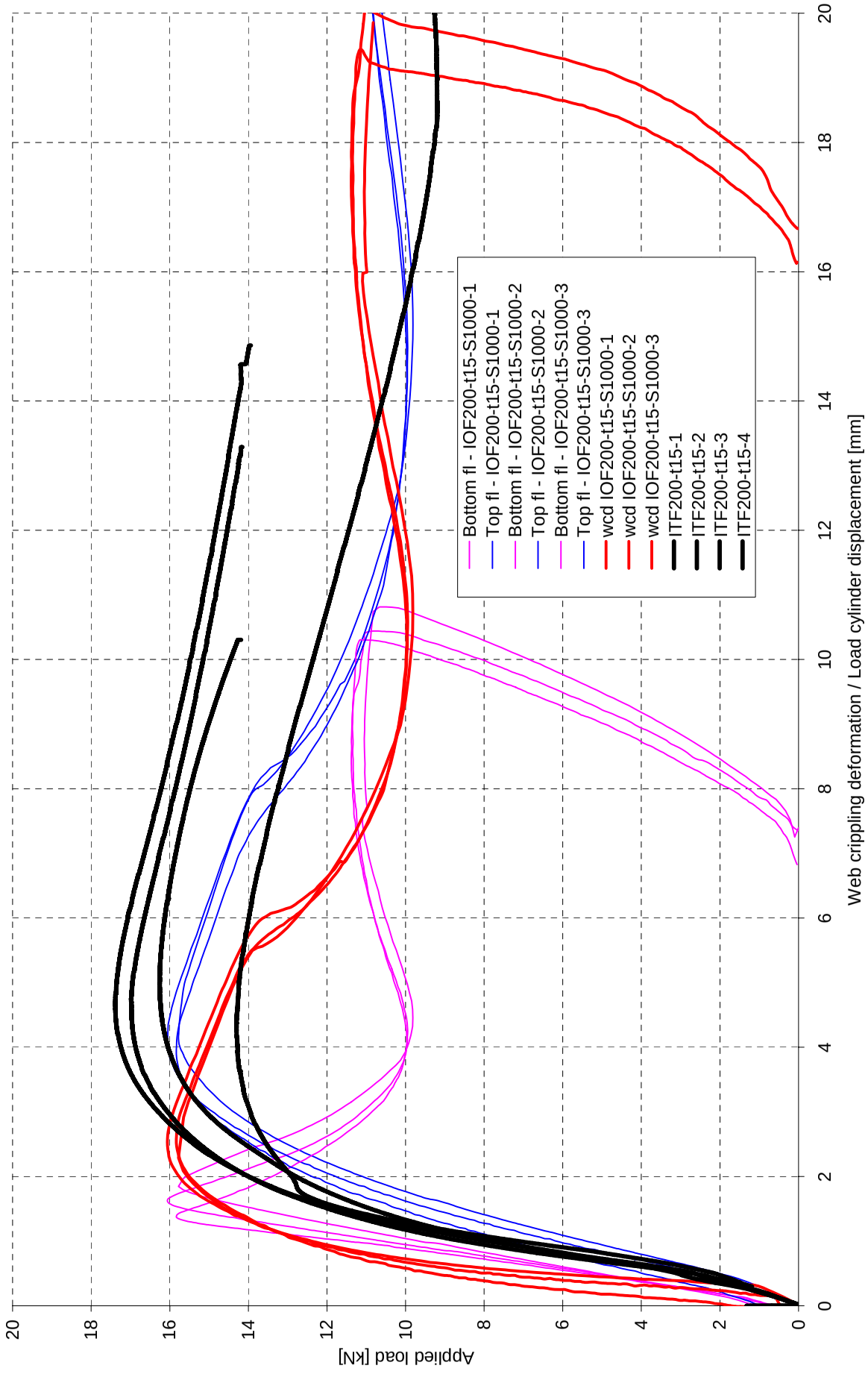

ANNEX E

1 (1)

Collected load-displacement curves from ITF200R- and IOF200R-tests

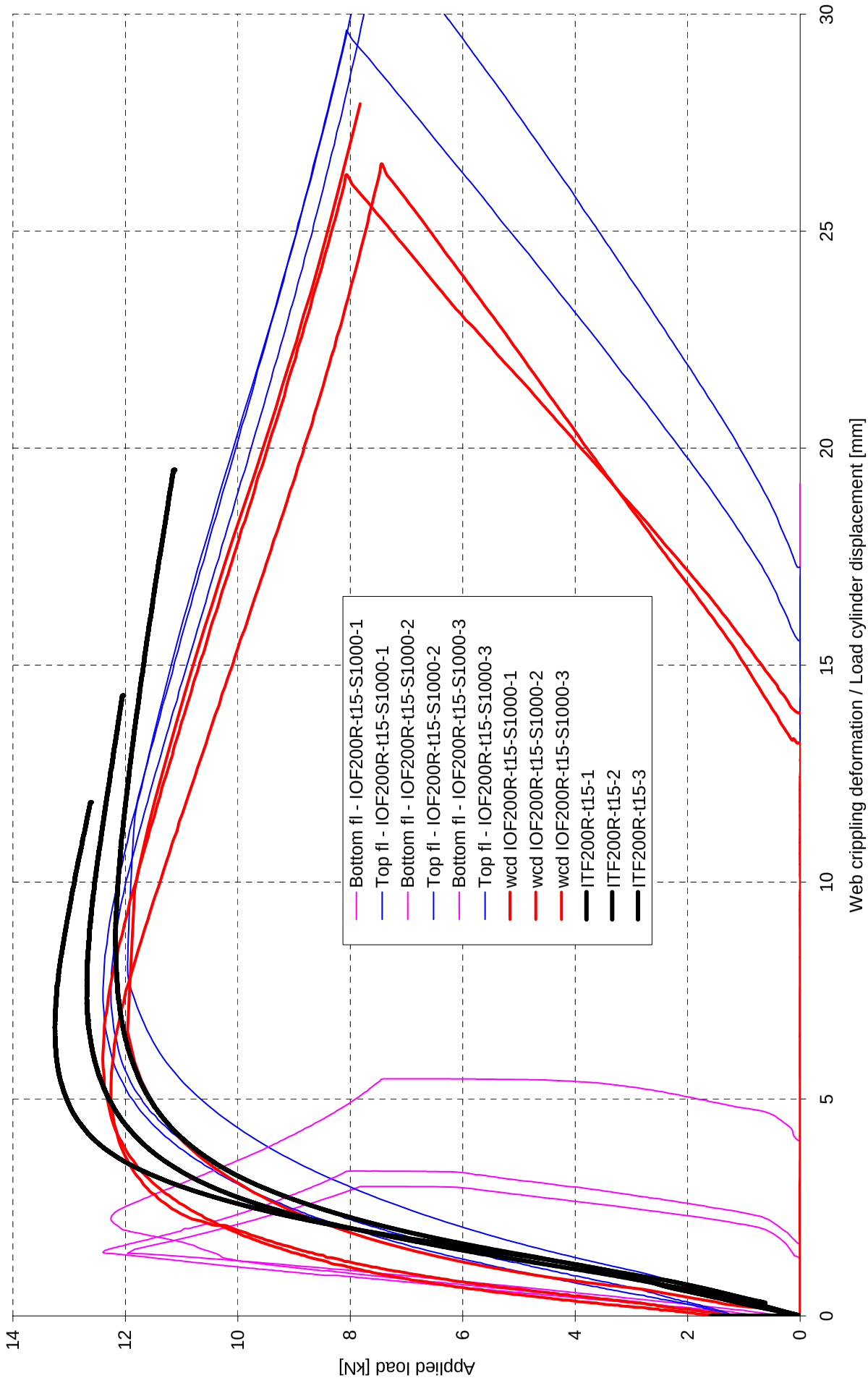

Example of input-file for ABAQUS/Explicit analysis

This annex presents the input file for the model ITF200-t15_flat created for the parametric study. Dash lines "---" replace edited parts (e.g. node and element data). All parametric models followed fundamentally the same scheme. The input file was created using ABAQUS/CAE.

```
*Heading
** Job name: ITF200-t15_flat Model name: ITF200-t15_flat
**
** PARTS
**
*Part, name=CassetteSection
*End Part
*Part, name=LoadingBlock
*End Part
**
** ASSEMBLY
**
*Assembly, name=Assembly
**
*Instance, name=CassetteSection-1, part=CassetteSection
*Node
      1,       -0.003,        0.197,         1.52
      2,        -0.02,        0.197,         1.52
---
  54719,  -0.09985445,    0.1937899,        0.005
  54720,   -0.1087272,     0.190745,        0.005
*Element, type=S4R
 1,    1,   85, 9089,   94
 2,   85,   86, 9090, 9089
---
53924, 54719, 54720,  9087,  9088
53925, 54720,  9086,    84,  9087
** Region: (CasShellSection:Picked)
*Elset, elset=_I1, internal, generate
     1,  53925,      1
** Section: CasShellSection
*Shell Section, elset=_I1, material=S350_testmat
0.001443, 5
*End Instance
**
*Instance, name=LoadingBlock-1, part=LoadingBlock
-0.0970000049989506, -0.0337218462614279,         1.55
-0.0970000049989506, -0.0337218462614279,         1.55, -0.0970000049989508,
0.966278166426624,         1.55, 89.9999992730282
*Node
      1,         0.03,           0.,          0.2
      2,         0.03,         0.03,          0.2
---
   2606,        0.055,         0.01,           0.
   2607,        0.055,        0.005,           0.
*Element, type=R3D4
 1,   1,  51, 676,  70
 2,  51,  52, 677, 676
---
2679, 2606, 2607,  236,  235
2680, 2607,  411,   14,  236
*Node
   2608,         0.05,           0.,          0.1
*Nset, nset=LoadingBlock-1-RefPt_, internal
2608,
*Elset, elset=LoadingBlock-1, generate
    1,  2680,     1
*End Instance
**
*Instance, name=LoadingBlock-2, part=LoadingBlock
      -0.103,  0.197628696,         1.55
      -0.103,  0.197628696,         1.55,       -0.103, 1.19762870868805,         1.55,
89.9999992730282
```

```
*Node
      1,          0.03,           0.,          0.2
      2,          0.03,          0.03,         0.2
---
   2606,         0.055,          0.01,          0.
   2607,         0.055,         0.005,          0.
*Element, type=R3D4
 1,   1,  51, 676,  70
 2,  51,  52, 677, 676
---
2679, 2606, 2607,  236,  235
2680, 2607,  405,   14,  236
*Node
   2608,          0.05,           0.,          0.1
*Nset, nset=LoadingBlock-2-RefPt_, internal
2608,
*Elset, elset=LoadingBlock-2, generate
    1,  2680,     1
*End Instance
*Nset, nset=RP_supportblock, instance=LoadingBlock-1
 2608,
*Nset, nset=RP_LoadBlock, instance=LoadingBlock-2
 2608,
*Nset, nset=Cassette_all, instance=CassetteSection-1, generate
     1,  54720,      1
*Elset, elset=Cassette_all, instance=CassetteSection-1, generate
     1,  53925,      1
*Nset, nset=load_block_left_screw_location, instance=LoadingBlock-2
 12,
*Nset, nset=load_block_right_screw_location, instance=LoadingBlock-2
 37,
*Nset, nset=sup_block_left_screw_location, instance=LoadingBlock-1
10,
*Nset, nset=sup_block_right_screw_location, instance=LoadingBlock-1
 31,
*Nset, nset=bf_left_screw_location, instance=CassetteSection-1
 38,
*Nset, nset=bf_right_screw_location, instance=CassetteSection-1
 15,
*Nset, nset=bf_screw_lines, instance=CassetteSection-1
  13,  15,  17,  36,  38,  40, 201, 202, 208, 209, 210, 378, 379, 387, 388, 389
*Elset, elset=bf_screw_lines, instance=CassetteSection-1
 203, 204, 205, 215, 216, 217, 218, 611, 612, 613, 629, 630, 631, 632
*Nset, nset=tf_left_screw_location, instance=CassetteSection-1
 2,
*Nset, nset=tf_right_screw_location, instance=CassetteSection-1
 6,
*Nset, nset=tf_screw_lines, instance=CassetteSection-1
   1,   2,   5,   6,  28,  50,  85,  86,  95,  96, 247, 248, 249, 250, 251, 252
 253, 254, 255, 256, 257, 258, 259, 432, 433, 434, 435, 436, 437, 438, 439, 440
 441, 442, 443, 444
*Elset, elset=tf_screw_lines, instance=CassetteSection-1
   1,   2,   3,  13,  14,  15, 269, 270, 271, 272, 273, 274, 275, 276, 277, 278
 279, 280, 281, 282, 695, 696, 697, 698, 699, 700, 701, 702, 703, 704, 705, 706
 707, 708
*Elset, elset=_Load_block_bot_surface_SPOS, internal, instance=LoadingBlock-2
   37,   38,   39,   40,   41,   42,   43,   44,   45,   46,   47,   48,   49,   50,   51,
52
---
 2617, 2618, 2619, 2620, 2621, 2622, 2623, 2624, 2625, 2626, 2627, 2628, 2629, 2630, 2631,
2632
*Surface, type=ELEMENT, name=Load_block_bot_surface
_Load_block_bot_surface_SPOS, SPOS
*Elset, elset=_Sup_block_top_surface_SPOS, internal, instance=LoadingBlock-1
  117,  118,  119,  120,  121,  122,  123,  124,  125,  126,  127,  128,  129,  130,  131,
132
---
 2303, 2304, 2305, 2306, 2463, 2464, 2465, 2466, 2467, 2468, 2469, 2470, 2471, 2472, 2473,
2474
*Surface, type=ELEMENT, name=Sup_block_top_surface
_Sup_block_top_surface_SPOS, SPOS
*Elset, elset=_Cas_top_surface_SNEG, internal, instance=CassetteSection-1
    1,    2,    3,    4,    5,    6,    7,    8,    9,   10,   11,   12,   13,   14,   15,
16
---
 9004, 9005, 9006, 9007, 9008, 9009, 9010, 9011
```

```
*Surface, type=ELEMENT, name=Cas_bot_surface
_Cas_bot_surface_SPOS, SPOS
*Rigid Body, ref node=LoadingBlock-1.LoadingBlock-1-RefPt_, elset=LoadingBlock-1.LoadingBlock-
1
*Rigid Body, ref node=LoadingBlock-2.LoadingBlock-2-RefPt_, elset=LoadingBlock-2.LoadingBlock-
2
*End Assembly
*Amplitude, name=Loading_amplitude, definition=smooth step
0., 0., 0.1, 1.
**
** MATERIALS
**
*Material, name=S350_testmat
*Density
7850.,
*Elastic
 2.03418e+11, 0.3
*INCLUDE, INPUT=KH089002_AA-3_ABQ_plastic_input.txt
**
** INTERACTION PROPERTIES
**
*Surface Interaction, name=Contact_properties
*Friction
0.,
*Surface Behavior, pressure-overclosure=HARD
**
** BOUNDARY CONDITIONS
**
** Name: Load_block_bc Type: Displacement/Rotation
*Boundary
RP_LoadBlock, 1, 1
RP_LoadBlock, 2, 2
RP_LoadBlock, 3, 3
RP_LoadBlock, 4, 4
RP_LoadBlock, 5, 5
RP_LoadBlock, 6, 6
** Name: Sup_block_bc Type: Displacement/Rotation
*Boundary
RP_supportblock, 1, 1
RP_supportblock, 2, 2
RP_supportblock, 3, 3
RP_supportblock, 4, 4
RP_supportblock, 5, 5
RP_supportblock, 6, 6
** Name: bf_left_screw_bc Type: Displacement/Rotation
*Boundary
bf_left_screw_location, 1, 1
bf_left_screw_location, 3, 3
bf_left_screw_location, 5, 5
bf_left_screw_location, 6, 6
** Name: bf_right_screw_bc Type: Displacement/Rotation
*Boundary
bf_right_screw_location, 1, 1
bf_right_screw_location, 3, 3
bf_right_screw_location, 5, 5
bf_right_screw_location, 6, 6
** Name: bf_screw_lines_bc Type: Displacement/Rotation
*Boundary
bf_screw_lines, 3, 3
bf_screw_lines, 6, 6
** Name: tf_left_screw_bc Type: Displacement/Rotation
*Boundary
tf_left_screw_location, 1, 1
tf_left_screw_location, 3, 3
tf_left_screw_location, 5, 5
tf_left_screw_location, 6, 6
** Name: tf_right_screw_bc Type: Displacement/Rotation
*Boundary
tf_right_screw_location, 1, 1
tf_right_screw_location, 3, 3
tf_right_screw_location, 5, 5
tf_right_screw_location, 6, 6
**
** Name: tf_screw_lines Type: Displacement/Rotation
*Boundary
tf_screw_lines, 3, 3
tf_screw_lines, 6, 6
```

```
**
*IMPERFECTION, FILE=ITF200-t15_flat_buckle, STEP=1, NSET=Cassette_all
1,0.001
**
** ----------------------------------------------------------------
**
** STEP: Loading Step
**
*Step, name="Loading Step"
*Dynamic, Explicit
, 0.1
*Bulk Viscosity
0.06, 1.2
**
** BOUNDARY CONDITIONS
**
** Name: Load_block_bc Type: Displacement/Rotation
*Boundary, amplitude=Loading_amplitude
RP_LoadBlock, 1, 1
RP_LoadBlock, 2, 2, -0.03
RP_LoadBlock, 3, 3
RP_LoadBlock, 4, 4
RP_LoadBlock, 5, 5
RP_LoadBlock, 6, 6
**
** INTERACTIONS
**
** Interaction: Bot_fl_contact
*Contact Pair, interaction=Contact_properties, mechanical constraint=KINEMATIC
Cas_bot_surface, Sup_block_top_surface
** Interaction: Top_fl_contact
*Contact Pair, interaction=Contact_properties, mechanical constraint=KINEMATIC
Cas_top_surface, Load_block_bot_surface
**
** OUTPUT REQUESTS
**
***Restart, write, number interval=1, time marks=NO
**
** FIELD OUTPUT: F-Output-1
**
*Output, field
*Node Output
U,
*Element Output
S,
**
** HISTORY OUTPUT: H-Output-RP_Load
**
*Output, history, time interval=0.001
*Node Output, nset=RP_LoadBlock
U2,
**
** HISTORY OUTPUT: H-Output-RP_Support
**
*Node Output, nset=RP_supportblock
RF2,
*End Step
```

ANNEX G
1 (2)

Mises stress distributions at shell mid-surface for models ITF100R-t10_0p1s_d40_e8_f30 with bearing lengths 50 mm and 150 mm

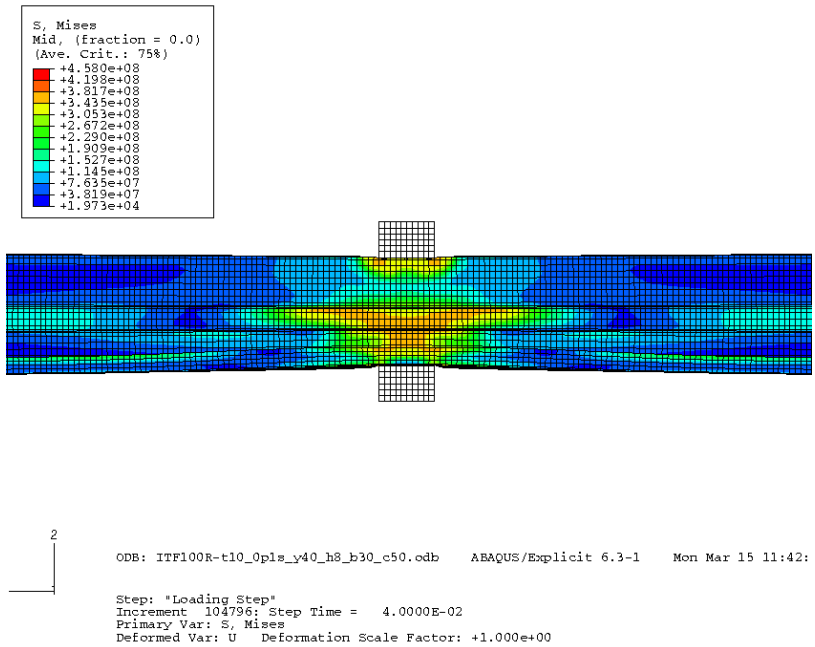

Fig. G1 Mises stress distribution for model ITF100R-t10_0p1s_d40_e8_f30_s50 at time of failure.

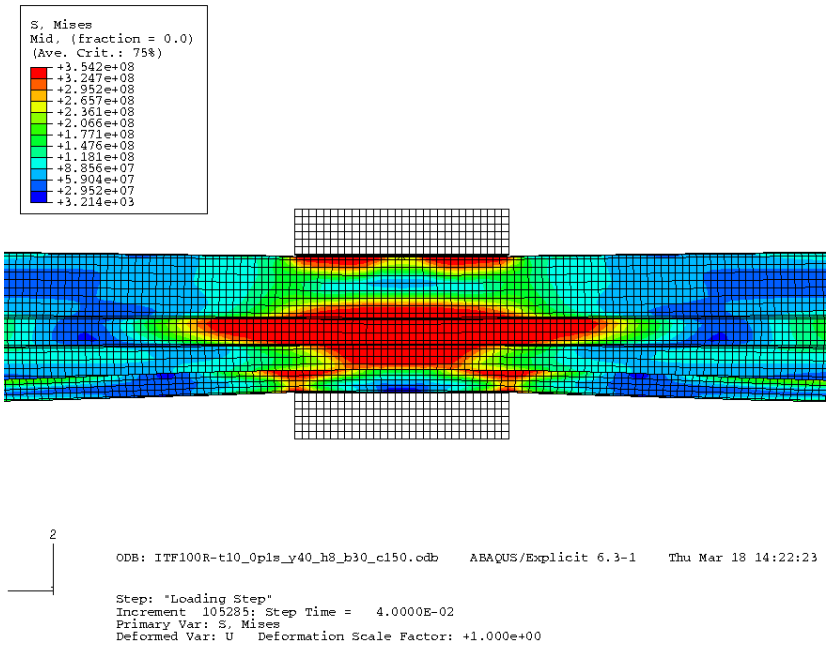

Fig. G2 Mises stress distribution for model ITF100R-t10_0p1s_d40_e8_f30_s150 at time of failure.

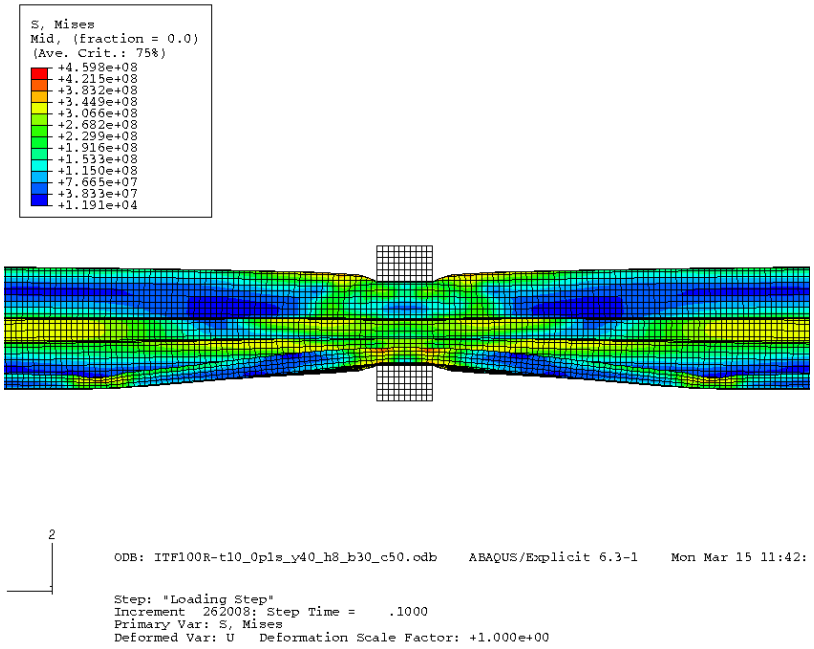

Fig. G3 Mises stress distribution for model ITF100R-t10_0p1s_d40_e8_f30_s50 at end of analysis.

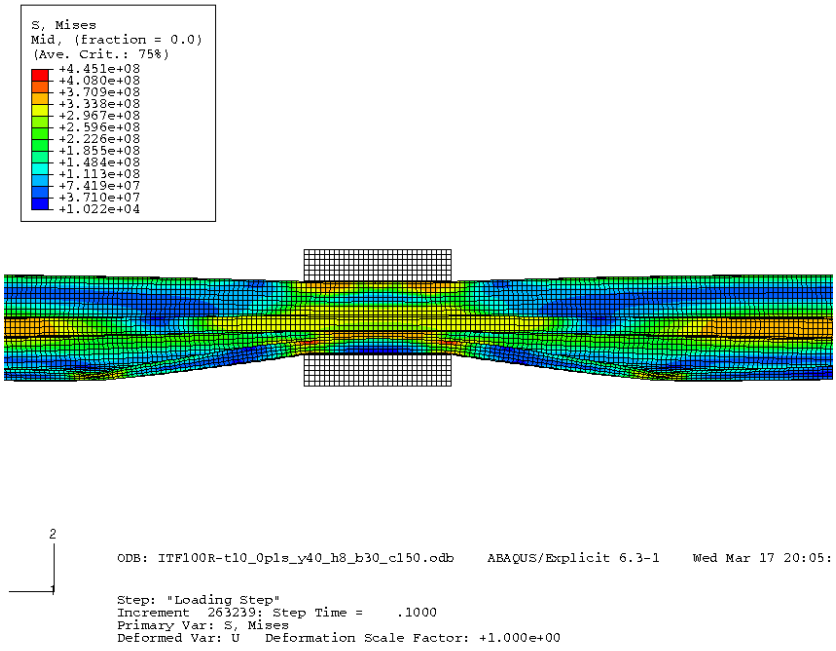

Fig. G4 Mises stress distribution for model ITF100R-t10_0p1s_d40_e8_f30_s150 at end of analysis.

ISBN 951-22-7270-9
ISSN 1456-4327